Advanced Physical Techniques in Inorganic Chemistry: Probing Small Molecule Activation

Advanced Physical Techniques in Inorganic Chemistry: Probing Small Molecule Activation

A dissertation presented

by

Bryce L. Anderson

To

The Department of Chemistry and Chemical Biology

in partial fulfillment of the requirements

for the degree of

Doctor of Philosophy

in the subject of

Chemistry

Harvard University

Cambridge, Massachusetts

May 2016

Dissertation Advisor: Professor Daniel G. Nocera Bryce L. Anderson

Advanced Physical Techniques in Inorganic Chemistry: Probing Small Molecule Activation

Abstract

Robust and efficient catalysts are necessary for realizing chemical energy storage as a solution for the intermittency associated with renewable energy sources. To aid in the development of such catalysts, physical methods are used to probe the photochemistry of small molecule activation in the context of solar-to-fuels cycles. Three systems are studied in the context of HX splitting (X=Br, Cl): polypyridyl nickel complexes, $NiX_3(LL)$ (LL = bidentate phosphine) complexes, and dirhodium phosphazane complexes. Two systems are studied in the context of dioxygen activation: cryptand-encapsulated peroxide dianion and cubane models of cobalt water oxidation catalysts.

Nickel complexes are shown to facilitate photo-driven H_2 evolution from solutions containing HCl. Transient absorption (TA) reveals that polypyridyl ligands act as redox mediators, circumventing the inherently short excited state lifetimes common to first row transition metal complexes. By coupling the one-electron photochemistry of the polypyridyl ligands to disproportionation of reduced nickel complexes, two-electron chemistry is achieved.

Halogen photoelimination is studied in a series of $NiX_3(LL)$ complexes which eliminate halogen in both solution and the solid state. Computation shows that efficient halogen

photoelimination is facilitated by a dissociative LMCT excited state. TA identifies an aryl-halide complex as an intermediate in the photoelimination reaction.

Halogen photoelimination from valence isomeric dirhodium phosphazane complexes, Rh_2[I,III] and Rh_2[II,II], is studied using TA and photocrystallography. TA suggests a common photo-intermediate that is probed by photocrystallography to reveal structural changes associated with transition to the proposed common intermediate.

Oxygen activation chemistry is studied using the first soluble form of peroxide dianion. The kinetics of peroxide dianion oxidation are studied by leveraging the dianion's propensity to form ion pairs with ruthenium polypyridyl complexes. TA kinetic data and DFT calculations facilitate a Marcus analysis which shows that the O–O bond of the peroxide dominates the internal reorganization energy.

Cubane model complexes structurally related to the CoPi water oxidation catalyst are studied using TA and computations. Photooxidation by a covalently linked photosensitizer exhibits fast electron transfer rates. Calculations show extensive delocalization of the cubane molecular orbitals and examination of the excited state manifold implicates d–d excited states as facilitators of rapid charge transfer.

Table of Contents

List of Figures

List of Tables

List of Abbreviations

ANL	Argonne National Laboratory
APS	Advanced Photon Source
bpy	Bipyridine
Btu	British thermal unit
CCD	Charge-Coupled Device
CDA	Charge Decomposition Analysis
CR	Charge Recombination
CS	Charge Separation
DFT	Density Functional Theory
DSA®	Dimensionally Stable Anode
E_{00}	00 Excitation energy
EDTA	Ethylenediaminetetraacetic acid
EPR	Electron Paramagnetic Resonance
ESI	Electrospray Ionization
ET	Electron Transfer
FT-IR	Fourier-Transform Infrared
FT-NIR	Fourier-Transform Near Infrared
FWHM	Full Width Half Max
HAA	Hydrogen Atom Abstraction
HOMO	Highest Occupied Molecular Orbital
I	Intensity
IR	Infrared
K	Boltzmann constant
k_{ET}	Electron transfer rate constant
k_{CR}	Charge recombination rate constant
k_{CS}	Charge separation rate constant
K_{IP}	Ion pair formation equilibrium constant
LCMS	Liquid chromatography mass spectrometry
LED	Light Emitting Diode
LMCT	Ligand-to-Metal Charge Transfer
LUMO	Lowest Unoccupied Molecular Orbital
MLCT	Metal-to-Ligand Charge Transfer
N_{AV}	Avogadro's number
NBO	Natural Bond Order
Nd:YAG	Neodymium-doped Yttrium Aluminum Garnet
NMR	Nuclear Magnetic Resonance
OEC	Oxygen Evolving Complex
OPA	Optical Parametric Amplifier
PCET	Proton Coupled Electron Transfer
PES	Potential Energy Surface
PMT	Photomultiplier Tube
PS	Photosensitizer
PSII	Photosystem II
PTI	Photon Technology International
PVC	Polyvinyl chloride
r_{avg}	Average radius
S	Huang-Rhys factor
SRS	Stanford Research Systems

STP	Standard Temperature and Pressure
T	Temperature
TA	Transient Absorption
TAML	Tetra-amino macrocyclic ligand
TD–DFT	Time Dependent Density Functional Theory
TOF	Time Of Flight
TS	Transition State
TTL	Transistor-Transistor Logic
UV	Ultraviolet
UV-Vis	Ultraviolet-Visible
H_{ab}	Quantum coupling constant
VT	Variable Temperature
WOC	Water Oxidation Catalyst
z	Electric charge
δ	Chemical Shift
$\Delta\varepsilon$	Change in extinction coefficient
ε_{op}	Optical dielectric constant
ε_s	Static dielectric constant
μ_{eff}	Effective magnetic moment
μ	Ionic strength
Φ_p	Photoelimination quantum yield
λ	Total reorganization energy
λ_i	Inner sphere reorganization energy
λ_o	Outer sphere reorganization energy
λ	Wavelength
λ_{exc}	Excitation Wavelength
τ	Time constant
ν	Energy in wavenumbers
ω	Frequency
$\hbar$	Reduced Planck Constant

Acknowledgments

Without the help and support of my family and coworkers I would not have succeeded as a graduate student. This section is intended to honor those who have enabled me to complete this journey.

Although the work in this thesis is about science, my family has been my most important asset during my PhD. First and foremost, the primary contributor to my success is the love of my life, my beautiful wife, Heather**.** She has been my unyielding partner and my best friend since the day we met. Heather is my foundation, my source of stability, and I am so lucky to have her in my life.

My mom and dad, Darla and Lane, have been amazing parents who always encouraged me to shoot for my goals. They have always let me know how much they love me and have been a constant support throughout graduate school, and my entire life for that matter.

The advancement of my technical skills is largely attributable to my labmates. The Nocera laboratory is composed of people with diverse backgrounds and experiences and this diversity leads to a truly special environment where people are naturally encouraged to think in different ways and view problems from different perspectives. While everyone that I have worked with has helped shape who I've become over the past six years, many deserve explicit praise.

Professor Daniel G. Nocera is the architect of the unique lab environment where I, an ex-military high school dropout, was embraced as both a friend and colleague. I've learned a great deal from Dan both as a scientist and as a person. Dan has an uncanny ability to understand your goals, both personal and professional, and subtly pushes you toward them while giving you the freedom and resources to explore science on your terms. I consider myself very lucky that Dan welcomed me into his lab.

Dr. Dilek Doğutan is our labs second in command so to speak. In addition to keeping the lab running, Dilek has been an invaluable friend and colleague who has made the last years immeasurably more enjoyable.

A number of faculty members of MIT and Harvard have had an impact on my PhD. I am grateful to Professor Robert Griffin for his patience, guidance, and providing access to his labs expertise and instrumentation. Professor Andrei Tokmakoff served as my initial thesis chair and showed a genuine interest in my research before we parted ways. Professor JoAnne Stubbe has, almost certainly without knowing it, had a significant impact on my life. Thank you, Professor James Anderson of Harvard for stepping up as a member of my thesis committee when we made the move from MIT to Harvard.

This thesis is the product of extensive collaboration with coworkers. Of said coworkers, Professor David Powers has been particularly instrumental to my professional development in addition to the science in this thesis. Dave has been an amazing collaborator: he has been an important collaborator on the work in this thesis which can be seen in the photo-H_2 evolution discussed in Chapter 2, the NiX_3 work of Chapter 3, and the photocrystallography experiments of Chapter 4. In addition to scientific collaboration, it has been a pleasure to interact with Dave on a personal level. I count myself lucky to have Dave as both a friend and colleague.

Andrew Maher has been an outstanding colleague, office mate, and friend ever since he joined the lab. He has been instrumental to portions of this thesis including the NiX_3 chemistry of Chapter 3 and the electron transfer studies of peroxide in Chapter 5.

Seung Jun Hwang has been another amazing friend and collaborator during my graduate student career. Seung Jun was critical to the NiX_3 work of Chapter 3 and the photocrystallography of Chapter 4. I'll miss our time together at APS sharing military stories, eating popcorn fish, and doing science.

Dr. Andrew Ullman has been a great coworker and was instrumental to the cobalt cubane work of Chapter 6. In addition to his scientific contributions to this thesis, Andrew was a great labmate, always willing to talk science and offer insight into whatever you want to talk about.

Casey Brodsky stepped up and helped me with dangling synthetic and electrochemical aspects of the cubane work After Andrew Ullman graduated.

Dr. Patrick Holder and Dr. Arturo Pizano helped me find my role in the lab during my initial years, serving as both mentors and friends. They fostered my interest in instrumentation and encouraged me to dig in and master it, which turned out to be one of the most rewarding aspects of my PhD.

Dr. Michael Colvin is one of the post-docs from the Griffin lab whose time I've monopolized periodically. His domain specific expertise has helped me out of a bind more than a few times.

Dr. Michael Huynh has been my go-to guy for computation related questions. He's also the one I go to for general software related advice and has really helped me 'level up'.

Dr. Bon June Koo has been a great friend and collaborator over the years. She has also been a great friend to Heather and is certainly the one to blame for my wife's addiction to Settlers of Catan.

Dr. Dan Graham, the remaining member of my cohort, was a great friend and labmate.

Dr. Casandra Cox was the first office mate I had in the sunless basement office of MIT and made me feel welcome as a new member of the group. More importantly, Casandra was one of the few to offer the 'unwritten advice' about graduate school.

Dr. Yu-Sheng Chen of the University of Chicago has been an excellent friend and collaborator on the photocrystallography work of Chapter 4. In another life I would love to find myself at the Advanced Photon Source working with Yu-Sheng.

I've had good times collaborating scientifically with numerous other members of the lab. I've had many a good afternoon (or long days…) doing EPR with Dr. Chris Lemon, Dr. Eric Bloch, Robert Halbach, and probably more.

Dr. Tuncay Ozel and Dave Song have both been great friends and share my passion for the outdoors. I'm going to miss going on hikes and wading into the lake hunting for bass.

There are many others that have come and gone through the Nocera lab during my five plus years of graduate school. While it's impossible to thank all of them individually, they should know that I've enjoyed working with everyone that has come through the lab. The post-docs that come through the Nocera lab have all been exceptional and the students that are attracted to the Nocera lab are always friendly and interesting on both a scientific and personal level.

Thank you everyone for the good times and good memories.

Chapter 1: Introduction

1.1 The Growing Global Demand for Energy

World energy demands are projected to grow by 56% between 2010 and 2040 (Figure 1.1a) to over 800×10^{15} Btu, an average power consumption of 27 TW.[1] This growth is primarily driven by the increasing populations and the modernization of developing countries. Fossil fuels are predicted to be the primary energy sources sustaining this economic growth (Figure 1.1b). Yet, climate scientists have been sounding the alarm about the effect that fossil fuels are having on our global climate: the combustion of fossil fuels is responsible for the rising levels of atmospheric carbon dioxide (CO_2) (Figure 1.2),[2] a leading cause of global warming. The potentially catastrophic effects of global warming have led to unprecedented cooperation among developed and developing countries alike to stymie climate change by decreasing the emission of greenhouse gasses. However, the growing global demand for energy must then be satisfied by alternative carbon-neutral energy sources if the societies of the world ever hope to mitigate global warming.

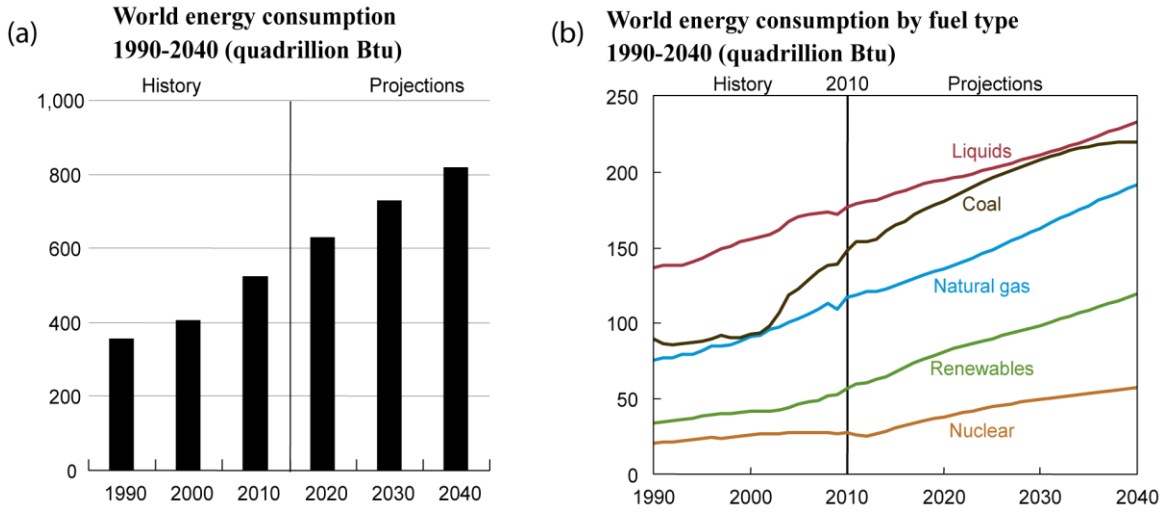

Figure 1.1. (a) Historical and predicted total world energy consumption from 1990 through 2040, (b) world energy consumption by fuel type. Adapted from International Energy Outlook 2013: U.S. Energy Information Administration, ref 1.

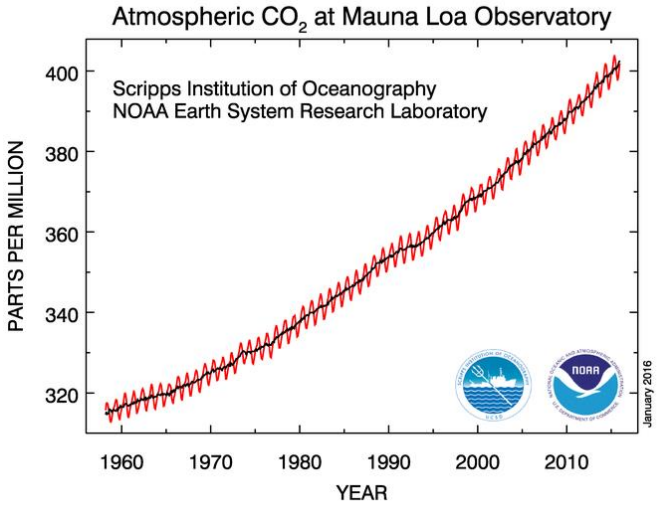

Figure 1.2. Atmospheric CO_2 concentrations measured at Mauna Loa Observatory, Hawaii. Dr. Pieter Tans, NOAA/ESRL (www.esrl.noaa.gov/gmd/ccgg/trends/) and Dr. Ralph Keeling, Scripps Institution of Oceanography (scrippsco2.ucsd.edu/).

While many alternative sources of energy exist, and the carbon-free solution to our energy needs will certainly be a combination of different sources, each has its own unique advantages and limitations. Biomass has the potential to be carbon neutral but is unfeasible on large scales due to the relatively poor efficiency of photosynthesis.[3] Hydropower is well understood, cheap, and exceptionally clean but has essentially been fully exploited in developed countries.[1] Geothermal power is carbon neutral but has a relatively small maximum theoretical power output of 44 TW, the vast majority of which cannot be harnessed.[4] Nuclear fission offers a carbon free solution but is hampered by a myriad of concerns: containment failures such as those at Chernobyl and Three Mile Island have demonstrated the hazards of nuclear waste and soured the public's appetite for more reactors while problems associated with fissile fuel such as availability, reprocessing, and weaponization have proven difficult to resolve.[5,6] Nuclear fusion surmounts many of the issues inherent to nuclear fission but despite continual progress the technology to harness

nuclear fusion for power generation remains beyond our grasp.[7,8] Despite the qualities of these and other alternative energy sources, the most obvious and promising source of clean energy is the sun.

1.2 Solar Energy

The amount of solar power available is a vastly greater than that of all other alternatives combined. The earth surface receives 86 PW of power from the sun,[9] more energy in a single hour than our societies consume in an entire year combined.[10,11] While the merits of a solar powered world have been well established,[5,10,12] there are still

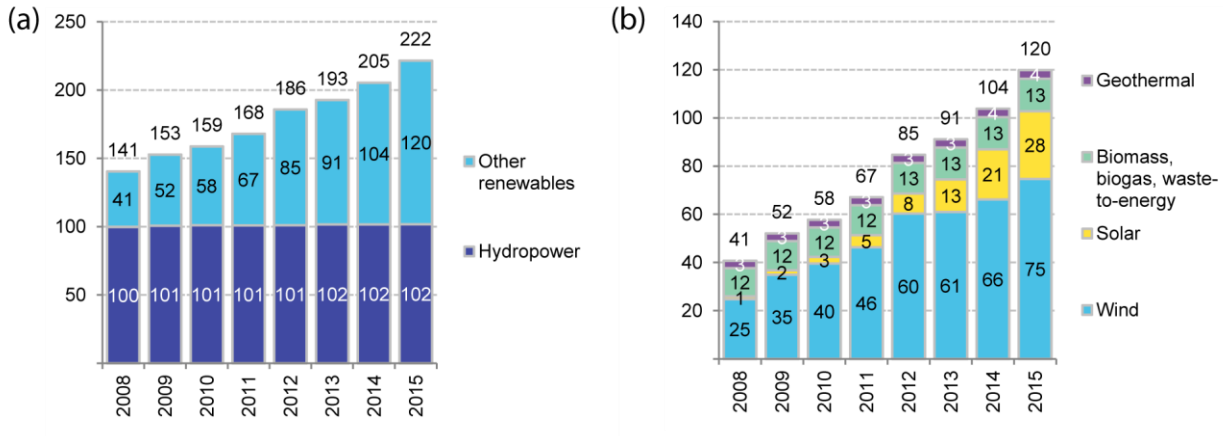

Figure 1.3. Cumulative US generation capacity from renewable sources in GW. (a) The growth of generation from hydropower has been stagnant while other renewable sources have seen significant growth. (b) Solar and wind power compose the bulk of the growth of renewable energy sources. Adapted from Sustainable Energy in America 2016 Factbook: Bloomberg New Energy Finance and The Business Council for Sustainable Energy (Copyright 2016).

technical and economic challenges that need to be surmounted before it can be a viable substitute for fossil fuels. Photovoltaics convert sunlight directly into electricity but have historically been considered too costly to compete with fossil fuels.[13–15] However, the price of silicon based solar panels has plummeted in recent years[16,17] leading to the growth of generation capacity in the US (Figure 1.3) and new photovoltaics such as perovskites have

potential to drive costs even lower.[18,19] The price of harvesting solar energy is on the cusp of being economically competitive with traditional energy sources.

The diurnal nature of solar energy coupled with variations in energy flux due to atmospheric conditions are unfortunately incompatible with our need for a continuous supply of energy. In order to make a solar powered society viable, safe and high-density energy storage solutions are necessary to store energy on unprecedented scales.[14]

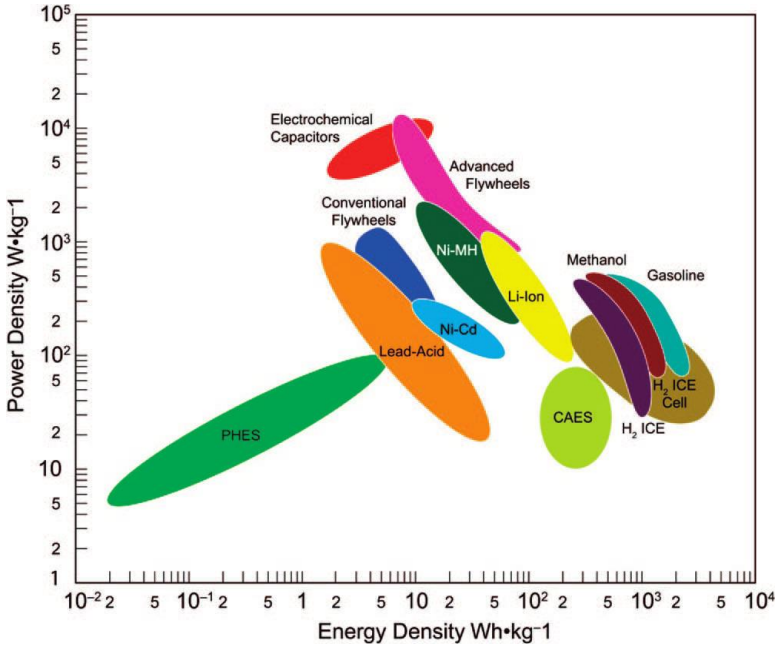

Figure 1.4. Energy and power densities of various energy storage solutions. Chemical energy storage dominates the high energy density region. Reprinted with permission from Cook et al. *Chem. Rev.* **2010**, *110* (11), 6474–6502. Copyright 2010 American Chemical Society.

Chemical fuels offers an attractive solution as they are a high density energy storage solution in comparison to alternatives such as batteries and mechanical methods (Figure 1.4). Fuels can achieve gravimetric energy densities as high as 142 MJ/kg in the form of molecular hydrogen (H_2) and volumetric energy densities of 39 MJ/L in diesel fuel,[20] vastly higher energy densities than can be achieved by alternative storage mechanisms such as pumped hydroelectric (~5–7 J kg^{-1} m^{-1}) and compressed air.[21]

While chemical fuels are an attractive energy storage medium, the current technology for converting solar energy to chemical fuels suffers from inefficiencies that render large scale solar-to-fuels processes economically uncompetitive in today's markets. Efficient, cheap, and abundant catalysts are needed to convert increasingly economical solar energy into chemicals fuels on scales grand enough to continue to power our economies without diminishing our standard of living. A mechanistic understanding of the chemistry of small molecule activation is crucial for directing the development of these catalysts.

1.3 The Challenges of Splitting H_2O

It is convenient to split the chemistry of solar fuels into two half reactions. Hydrogen possesses many qualities that make it a desirable cathodic product of a solar-to-fuels cycle. Hydrogen can be used as fuel in traditional combustion engine designs, in fuel cells for efficient electricity generation, or as a feedstock for the production of other fuels. When paired with water oxidation for the anodic half reaction, the net reaction is water splitting. In many ways, water splitting is an ideal solution for chemical energy storage: the products, H_2 and O_2, are relatively benign yet have highly favorable energy storage properties. The challenge of the water splitting reaction is one of kinetics: the water splitting reaction is a minefield of high energy intermediates (Figure 1.5).[22] The net reaction of water splitting is a proton coupled electron transfer (PCET) process involving four protons and four electrons rendering the reaction very complex from a mechanistic perspective. In addition to the complexity of managing four protons and four electrons, water oxidation catalysts must efficiently promote the formation of an O–O bond. Efficient catalysts must avoid the generation of these high energy intermediates, otherwise they become activation barriers

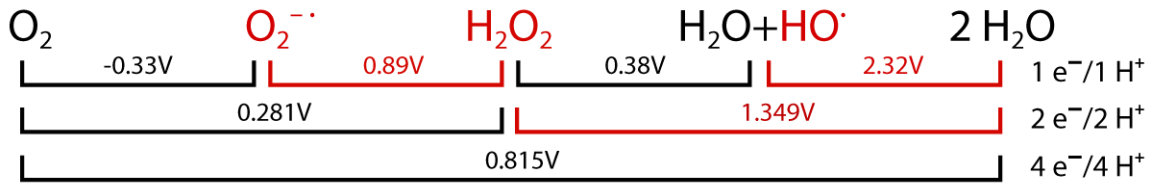

Figure 1.5. Oxygen Latimer diagram. High energy intermediates are highlighted in red. Figure adapted from ref 22.

in the water splitting process requiring the expenditure of extra energy which is ultimately lost as heat.

A mechanistic understanding of the O–O bond is crucial for understanding and developing efficient catalysts for use in an economy based on a H_2O solar-to-fuels cycle. The chemistry of the O–O bond is often the most significant yet poorly understood part of oxygen activation chemistry.[23] Two general mechanisms for O–O bond formation are plausible: an acid-base mechanism consisting of nucleophilic attack of a hydroxide on a high valent terminal-oxo and a radical coupling mechanism where two terminal oxyl radicals couple to form a peroxide (Figure 1.6).[24–26] Oxyl radicals and high valent oxo moieties are generally considered high energy intermediates necessitating careful tuning in order to minimize activation barriers while remaining reactive enough to undergo O–O bond formation.

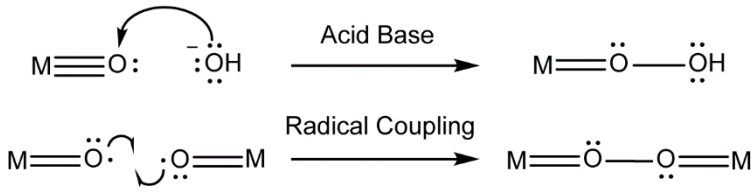

Figure 1.6. Potential mechanisms of O–O bond formation promoted by terminal metal-oxo complexes.

Notwithstanding the challenges of oxygen activation, numerous examples of synthetic and natural water splitting catalysts exist. No photochemical fuel cycle has been as successful as photosynthesis, which is the primary energy harvesting mechanism for life on earth,[27] harvesting energy at a rate of roughly 100 TW.[5,28,29] Despite the relatively poor solar-to-fuel conversion rate for biomass, the unparalleled success of photosynthesis has made it the target of countless studies attempting to unlock the secrets of its catalytic process. Photosynthesis is composed of a series of photochemical and thermal reactions resulting in the net storage of sunlight in the form of carbon-hydrogen bonds. The manganese oxide cubane cofactor of photosystem II (PSII), known as the oxygen evolving complex (OEC), is responsible for the water oxidation half reaction of photosynthesis which is the source of essentially all the oxygen in the atmosphere(Figure 1.7).[30] Efficient oxygen activation is critical for the success of PSII: O–O bond formation is part of the rate liming transition from state S_3 to S_0.[31,32] Inspired by the OEC, metal oxides have been studied extensively for use as water oxidation catalysts. Heterogeneous metal oxides, many of which form extended cubane structures[42–38] reminiscent of the OEC active site, have been shown to be effective water oxidation catalysts including NiO_2,[39,40] Co_3O_4,[41,42] PtO_2,[43] RuO_2,[44] IrO_2,[45] and MnO_2.[46] Molecular OEC mimics consisting of cubane complexes[47–49] have been studied with conflicting results.[50]

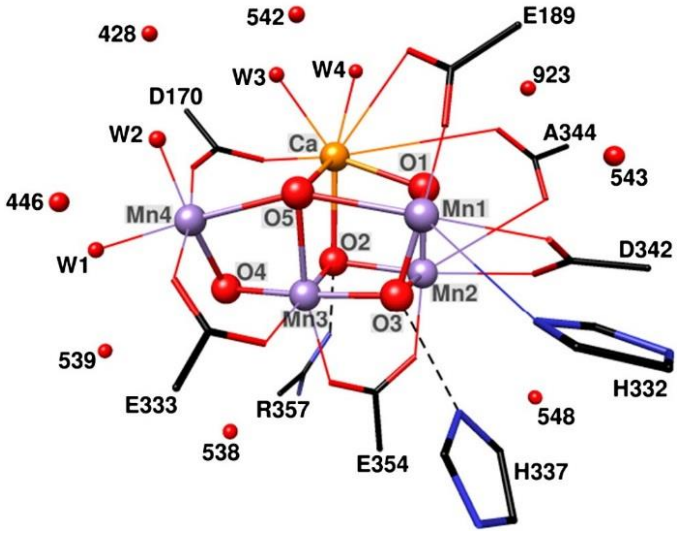

Figure 1.7. The Mn_4CaO_5 cubane structure of the active site of the PSII oxygen evolving complex.[51]

Oxygen reduction chemistry is another challenging facet of a H_2O solar-fuel cycle. As the microscopic reverse of the water oxidation process it must also overcome the challenges associated with PCET and O–O bond cleavage. Current fuel cell technology achieves an energy conversion efficiency of 40–60%,[52] significantly below the theoretical maximum of 83% at STP.[53] The situation is further complicated by the production of the parasitic activated oxygen species peroxide and superoxide which, in addition to decreasing efficiency, can damage fuel cell electrodes and membranes.[54]

The challenges of oxygen activation present an obstacle for the broader adoption of water splitting as a cheap and efficient means of chemical energy storage. A better mechanistic understanding of the chemical transformations inherent to water splitting would aid the development of more efficient and robust catalysts made from abundant materials that can be scaled to meet the growing energy demands of the global society.

1.4 HX (X=Cl, Br) as an Alternative to H_2O for Solar Energy Storage

The chemistry of halide oxidation has a rich history due to the importance of halogens as critical chemical feedstocks in the production of commodity chemicals. Applications range from the production of PVC to the manufacture of pharmaceuticals. State-of-the-art chlorine production is currently dominated by electrolysis of brine in the chloro-alkali process. Chloride oxidation is accomplished using dimensionally stable anodes (DSAs®) consisting of titanium coated with platinum group metal oxides, typically RuO_2 combined with smaller amounts of other oxides such as TiO_2, SnO_2, and IrO_2.[55] By using titanium as the anode substrate, surface corrosion is rapidly passivated by formation of an oxide layer thus limiting damage to the anode.[56,57] The chloro-alkali process is responsible for an annual production capacity of 55 million tons of Cl_2 (2011).[58] Leveraging the technology developed for DSAs®, robust catalysts also exist for X_2 reduction with relatively low precious metal requirements.[59]

In comparison to water oxidation, HX (X=Cl, Br) splitting is mechanistically a much simpler reaction. HX splitting requires the management of only two protons and two electrons, and doesn't come with complexity of forming an O–O bond. These simplifications are manifested in faster kinetics of halide reduction compared with the corresponding oxygen reduction reaction in fuel cells[60] and thermodynamic efficiencies that can be in excess of 75% for a H_2/Cl_2 fuel cell.[61] Additionally, HCl splitting stores more energy per electron than water splitting (Equations 1.1 through 1.3).[62] While an HBr fuel cycle provides less energy storage potential per electron than either HCl or H_2O, it has its own unique advantages. Because bromine is a liquid it doesn't require the high pressure storage

$$2HCl \rightarrow H_2 + Cl_{2\,(g)},\ \Delta G° = 262\ kJ\ mol^{-1}\ (E° = 1.36) \quad (1)$$

$$2HBr \rightarrow H_2 + Br_{2\,(l)},\ \Delta G° = 206\ kJ\ mol^{-1}\ (E° = 1.08) \quad (2)$$

$$2H_2O \rightarrow 2H_2 + O_{2\ (g)},\ \Delta G° = 475\ kJ\ mol^{-1}\ (E° = 1.23) \quad (3)$$

facilities required for O_2 or Cl_2. In addition, H_2/Br_2 fuel cells have been shown to operate at efficiencies of nearly 90% and power densities above 1.5W/cm^2.[63]

Notwithstanding the many thermodynamic and kinetic advantages of HX compared to H_2O for large scale energy storage, it is not without its drawbacks. Both HX and X_2 are highly corrosive and require careful storage considerations which add cost in terms of both engineering and environmental hazards. However, the chemical industries extensive experience managing large quantities of these chemicals demonstrates the technical feasibility of HX splitting as a large scale storage mechanism for the intermittent nature of renewable solar energy.

1.5 Photochemical Solar-to-Fuels Cycles

Direct solar-to-fuels conversion using molecular photo-catalysts has many theoretical advantages over electrolytic systems. By combining the light harvesting and catalytic functionality many engineering aspects can be significantly simplified.[64–66] Even more important than the potential engineering advantages, molecular systems are amenable to a wider array of characterization techniques and more finely focused perturbations than heterogeneous systems. Heterogeneous systems are notoriously difficult to interrogate because of the challenges of isolating or even definitively identifying the active component

of heterogeneous catalytic systems. Conversely, molecular systems are typically very uniform facilitating spectroscopic interrogation. Molecular synthetic techniques can be used to precisely tune molecular systems providing a controlled way to improve molecular catalysts. The ability to probe and perturb molecular solar-to-fuels systems offers the opportunity to gain mechanistic insight that may be difficult or impossible to obtain from heterogeneous systems.

1.5.1. Photochemical Hydrogen Production

The literature contains many examples of photochemical H_2 production under a diversity of conditions. In photosynthesis the process of water splitting is broken down into a multicomponent process consisting of a light harvesting photosensitizer (PS), a redox mediator (M), and a catalyst (Cat).[67–69] In principle, the mediator can be combined with the photosensitizer (PS) to reduce system complexity at the cost of being able to independently tune each component. Many synthetic photochemical H_2 generation schemes employ the multicomponent principle because of the ability to manage each phase of the light harvesting process independently (Figure 1.8). In photosynthesis the macrocycle chlorophyll plays the role of the photosensitizer. While porphyrins have been

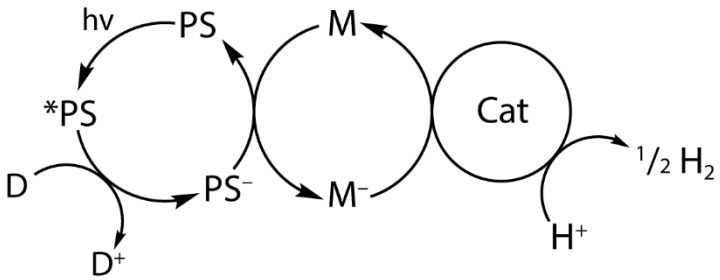

Figure 1.8. Three component system utilizing a sacrificial reductant as a substitute for the anodic reaction. In principle, component D can represent H_2O/OH^-, X^-, or any other source of electrons.

studied in the context of photochemical H_2 generation,[70,71] nanomaterials such as quantum dots[72] and transition metal complexes, in particular ruthenium (II) polypyridyl complexes,[73,74] are more common photosensitizers due to their favorable photophysical properties. The most well-known three-component system for artificial photosynthesis is the triad of $Ru(bpy)_3^{2+}$, methylviologen, and a Pt or Pd catalyst.[75,76] In the vast majority of these catalytic schemes sacrificial electron donors (D) such as EDTA fulfill the role of the anodic process. While the need for a sacrificial electron donor undermines the utility of these systems as photochemical solar-to-fuels cycles, it does facilitate the study of the individual half reactions.

There have also been efforts to achieve photochemical H_2 generation without the need for rare and expensive elements. Utilizing organic dyes as the photosensitizer and a molecular cobaloxime catalyst, catalytic hydrogen generation has been demonstrated.[77,78] This strategy can be extended to employ a semiconductor as the electron transfer mediator (M of Figure 1.8)[79,80] in an architecture similar to that of dye sensitized solar cells. Due to the high extinction coefficients of the dyes employed, many spectroscopic studies have been reported which probe the mechanism of these systems.[81,82]

Bimetallic complexes have also been explored as a way to perform photochemical hydrogen elimination without the complexity of a multicomponent system. Work by Gray and coworkers has demonstrated photochemical H_2 elimination from bimetallic systems with using UV irradiation but under stoichiometric conditions.[83–85] Later reports demonstrated stoichiometric H_2 elimination from dirhodium complexes with isocyanide ligands using visible light.[86–87] The preparation of ground state mixed valence homobimetallics exemplifies the electronic flexibility of bimetallic constructs, and these

have been shown to be catalytic as opposed to stoichiometric.[88] Mixed valence bimetallic complexes could potentially mediate H^+ reduction at one metal center and X^- ($X = Br^-$, Cl^-, OH^-) oxidation at the other.

1.5.2. Photochemical HX Splitting (X = Br, Cl)

The energy storing step of photochemical HX splitting is the cleavage of a halogen bond. The terminal photoproduct of the aforementioned dirhodium complexes studied by Gray and coworkers contains metal–X bonds that are not susceptible to photolysis precluding a closed HX splitting photocycle. Due to the challenges of HX splitting, examples of closed photochemical HX splitting are exceedingly rare. One rare example is $IrCl_6^{3-}$ which undergoes photooxidation to yield $IrCl_6^{2-}$ and ½ H_2 (Equation 1.4) which can then undergo photoreduction to regenerate $IrCl_6^{3-}$ and furnish ½ Cl_2 (Equation 1.5), forming a closed HX photocycle (Equation 1.6).[89] Laser flash photolysis studies by Glebov et. al. studied the photochemical chloride oxidation and provided evidence for the formation of $Cl_2^{\bullet-}$ suggesting that the mechanism of halide oxidation depends on the homolysis of an Ir–Cl bond.[90]

$$IrCl_6^{3-} + H^+ \xrightarrow[HCl(aq)]{h\nu} IrCl_6^{2-} + 1/_2\ H_2 \quad (4)$$

$$IrCl_6^{2-} + Cl^- \xrightarrow[HCl(aq)]{h\nu} IrCl_6^{3-} + 1/_2\ Cl_2 \quad (5)$$

$$HCl(aq) \xrightarrow{h\nu} 1/_2\ H_2 + 1/_2\ Cl_2 \quad (6)$$

With the goal of facilitating the multi-electron chemistry required to perform H_2 and Cl_2 elimination from the same metallic scaffold, bimetallic complexes related to those studied by the Gray group for photo-hydrogen elimination have been developed as platforms

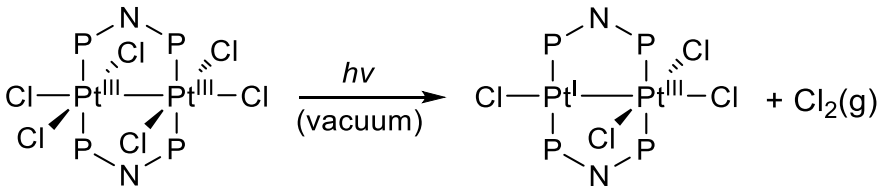

Figure 1.9. Pt_2(III,III) provides the first example of trap free halogen photoelimination. In the solid state Cl_2 can be captured under vacuum to demonstrate authentic halogen elimination.

capable of both photochemical H_2 evolution and halide oxidation. Using binuclear mixed valence rhodium complexes in the presence of a radical trap, Heyduk and Nocera demonstrated photocatalytic H_2 generation from hydrohalic solutions sustained over a period of twelve hours.[87] Related platforms yielded the first example of trap free halogen photoelimination presented by Cook et. al. in 2009 using a phosphazane bridged Pt_2(III,III) complex.[91] Photolysis of the Pt_2(III,III) complex in the solid state under vacuum generates the mixed valence Pt_2(I,III) complex and Cl_2 was collected by condensation (Figure 1.9). In solution the quantum yield of photo-elimination reaches 38%.

Building upon the success of the homobimetallic platinum complexes, heterobimetallic systems have also been shown to promote halogen elimination. Mixed metal gold and iridium complexes in the presence of halogen traps have also been shown to photo-eliminate Cl_2.[92] Like the bimetallic systems studied by Gray and coworkers, the mixed metal gold and iridium complexes exhibit metal-metal bonding character.

1.5.3. Photochemical Water Oxidation

As in photochemical H_2 and Cl_2 cycles, the most successful approaches for photochemical water splitting require the presence of a sacrificial reagent to reach measurable efficiencies. The most well-known systems leverage the ever popular

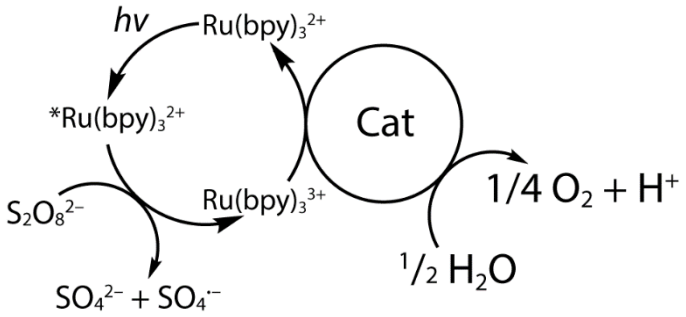

Figure 1.10. The Rubpy/persulfate flash quench reaction is used to photochemically oxidize water to O_2.

ruthenium(II) polypyridyl family of photosensitizers and use persulfate as a sacrificial oxidant (Figure 1.10). Photocycles leveraging this construct have been demonstrated using a variety of catalytic moieties.[93–98] As with multicomponent systems for photochemical H_2 and Cl_2 generation, the necessity of a sacrificial oxidant precludes a closed photochemical water splitting cycle. However, these systems can be useful when studying the mechanism of water oxidation because they provide a common set of conditions with which to study molecular catalysts, facilitating comparison between literature results.[99]

Molecular models of heterogeneous water oxidation catalysts provide a way to study the mechanism of these catalysts without the background noise inherent to heterogeneous systems. Numerous systems have taken design queues from the OEC by mimicking aspects of its ligand scaffold[100,101] or its cubane structure.[30,47] In addition to biomimetic systems, there are some notable synthetic examples such as the ruthenium "blue dimer",[102] iron TAML,[103–105] and tetraaza complexes.[106] While the literature contains many reported water oxidation catalysts, many of the results are clouded with uncertainty due to the propensity of these molecular catalysts to decompose under the harsh conditions of water oxidation, potentially generating the true catalyst in situe.[50,107]

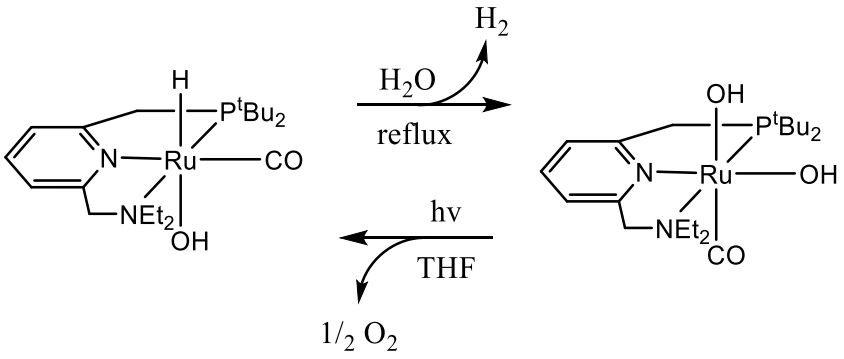

Figure 1.11. Potential H_2O splitting cycle mediated by a ruthenium (II) pincer complex presented by Milstein and coworkers (ref 108).

Recent work by Milstein and coworkers has provided an example of a ruthenium pincer complex which has the potential to form a closed water splitting photocycle (Figure 1.11).[108] The proposed mechanism of oxygen evolution consists of a MLCT transition followed by reductive elimination of H_2O_2 which subsequently undergoes disproportionation to generate O_2. This result is very exciting for the solar-to-fuels community because it performs both the thermodynamically challenging anodic reaction and hydrogen evolution using a single molecular platform.

The dearth of authentic photochemical water oxidation systems reveals the challenge of photochemical water oxidation. The complex choreography needed to efficiently manage four protons and four electrons presents a mechanistic labyrinth that scientists and engineers must navigate in the development of efficient catalysts made from earth-abundant elements. Studies of the thermodynamic and kinetic properties of oxygen activation can aid in navigating this complex catalytic design landscape.

1.6 Probing Small Molecule Activation

A primary advantage of molecular solar-to-fuels catalysts is the ability to identify and characterize the components of the catalytic cycle. While inorganic chemistry enjoys a diverse array of physical techniques for characterizing chemical species, most of these methods are only useful for characterization of isolable species and are incompatible with studying the transient intermediates which are critical to the mechanism of chemical transformations. The work detailed in this dissertation endeavors to apply the atypical techniques outlined below to elucidate the fundamental properties of molecular solar-to-fuels systems. We hope that the insights gleaned can be applied in the development of solar-to-fuels cycles that can free us from our dependence on fossil fuels by providing an efficient mechanism to store solar energy.

1.6.1. Transient Absorption

Studies leveraging transient absorption (TA) will dominate the bulk of this dissertation. Fundamentally, TA leverages electronic absorption spectroscopy in the ultra-violet and visible (UV-Vis) range of the electromagnetic spectrum. The underlying principle of TA is the use of a short duration light pulse to excite the system and monitor its evolution using UV-Vis absorption spectroscopy. Figure 1.12 depicts the two TA experimental configurations used in this dissertation. The vastly different timescales of TA experiments lead to different methods of synchronization: ultrafast experiments must rely on the characteristic speed of light while nanosecond experiments can be electronically timed. The high sensitivity of TA can be partially attributed to the use of well-developed CCD and PMT technologies as the primary methods of detection.

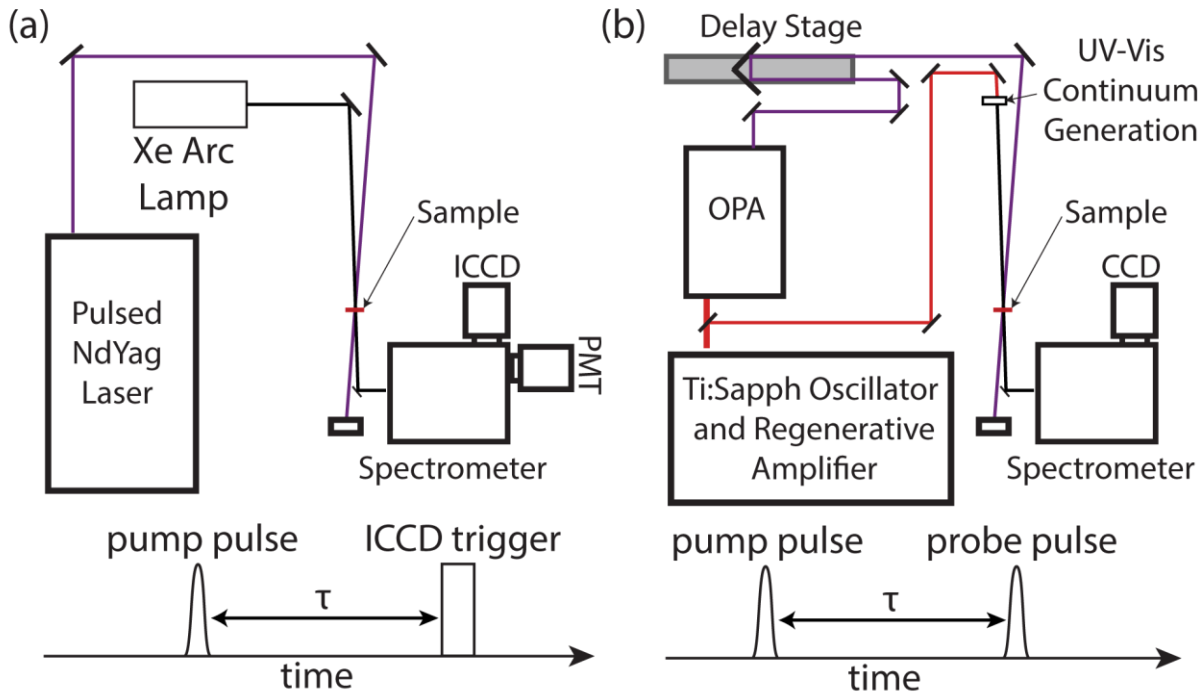

Figure 1.12. Diagram of typical TA experimental configurations. (a) Nanosecond TA often consists of a continuous probe source and a pulsed laser, commonly a Nd:YAG. Timing is performed electronically using a gated CCD camera or recorded on a ADC, typically an oscilloscope. (b) Picosecond and Femtosecond experimental configuration consists of a time-of-flight delay scheme controlled by a translation stage. Both pump and probe are pulses generated from the same Ti:Sapphire oscillator.

TA has been a powerful tool for studying the kinetics of chemical systems due to the sensitivity and high time resolution of the technique. TA has found extensive use in the domain of studying photo-induced charge transfer, enabling the observation of chemical kinetics on timescales that would be impossible to study by other means. Due to TA's high sensitivity and time resolution there are numerous reports leveraging its ability to identify photochemical intermediates. A recent example is a study of the oxidation of bromide by ruthenium(II) excited states.[109] This study found evidence for the formation of bromine radicals which subsequently react with free Br^- in solution to form $Br_2^{\bullet -}$, demonstrating the photo-induced formation of a Br–Br bond. Another interesting example is a study of the

photochemistry of tellurium bromide complexes which yielded a proposed mechanism for Br_2 addition and photoelimination based on evidence obtained by TA.[110–112]

While there have been many studies which demonstrate halogen photoelimintation through characterization of photochemical products, [91,92,113–116] studies probing the mechanism and intermediates of photo-halogen elimination are relatively rare. The Nocera group has led the field in applying TA to the study of HX slitting to better understand the mechanisms underpinning the observed photochemistry. Spectroscopic evidence for a photointermediate in the photolysis of bimetallic systems was first reported by Cook *et. al*. for Pt-Rh complexes.[117] Utilizing TA spectroscopy, a new species was observed immediately following laser flash photolysis which decays over the course of tens of microseconds. It was proposed that this intermediate was either a complex with a chloride in a μ-bridging position or a Cl_2 adduct. Despite the uncertainty as to the nature of this intermediate, the observation of a transient species in photochemical HX splitting process is an exciting step forward for the field.

1.6.2. Photocrystallography

X-ray crystallography is a ubiquitous technique of the inorganic community due to its ability to elucidate structure on the molecular scale. Since the first reported structures determined by X-ray diffraction techniques reported in 1913 by W. L. Bragg[118] (Figure 1.13) X-ray crystallography has been a mainstay of the inorganic chemist's analytical toolbox. Initially only simple structures were achievable but with the advance of structural solving tools,[119] X-ray sources, and detectors X-ray crystallography of molecules as complex as proteins is now common in both academic and industrial settings.[120]

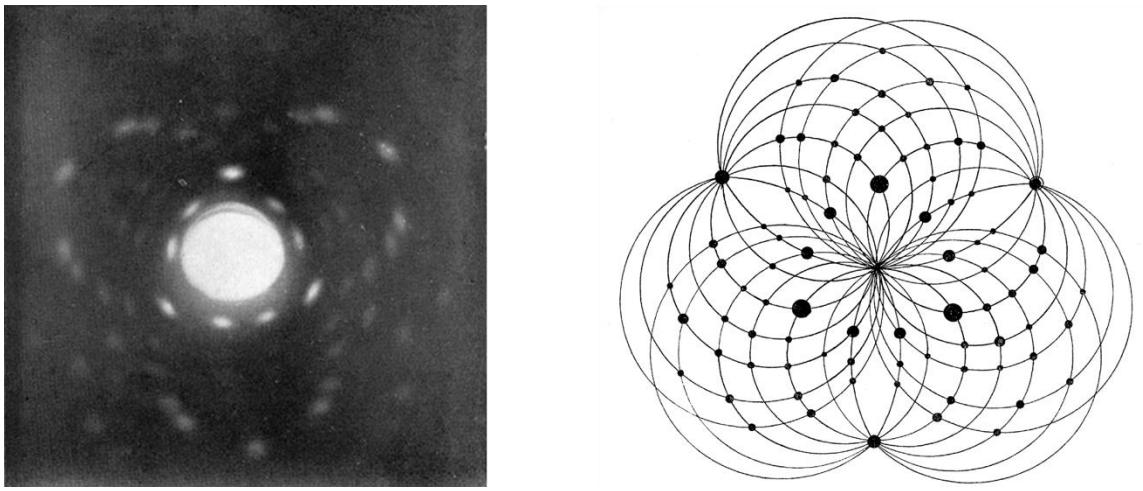

Figure 1.13. Diffraction pattern obtained from Fluorspar crystals and the predicted diffraction pattern. Figures adapted with permission from Bragg, W. L. The Structure of Some Crystals as Indicated by Their Diffraction of X-Rays. *Proceedings of the Royal Society of London A: Mathematical, Physical and Engineering Sciences* **1913**, *89* (610), 248–277.

Photocrystallography, the study of crystal structures in excited states, is a relatively recent development. The first reported example of steady state photocrystallography was in 1991 showing the photoinduced changes in the structure of $Na_2[Fe(CN)_5(NO)]\ 2H_2O$ using neutron diffraction.[121,122] This system was revisited by Coppens and coworkers[123,124] using X-ray crystallography to report the first electron density study of an excited state species. Since that time the field has expanded to include time resolved photocrystallography, enabling the analysis of molecular excited states on time scales as short as picoseconds.[125–127]

Figure 1.14 contains a depiction of a typical photocrystallography experiment. Photocrystallography is typically performed using a UV or visible radiation source to excite the molecules in a crystal and subsequently collecting the X-ray diffraction pattern in order to get structural information about the excited state.[128] Synchrotron radiation sources are commonly used due to their higher X-ray brilliance. The experiment can be either steady

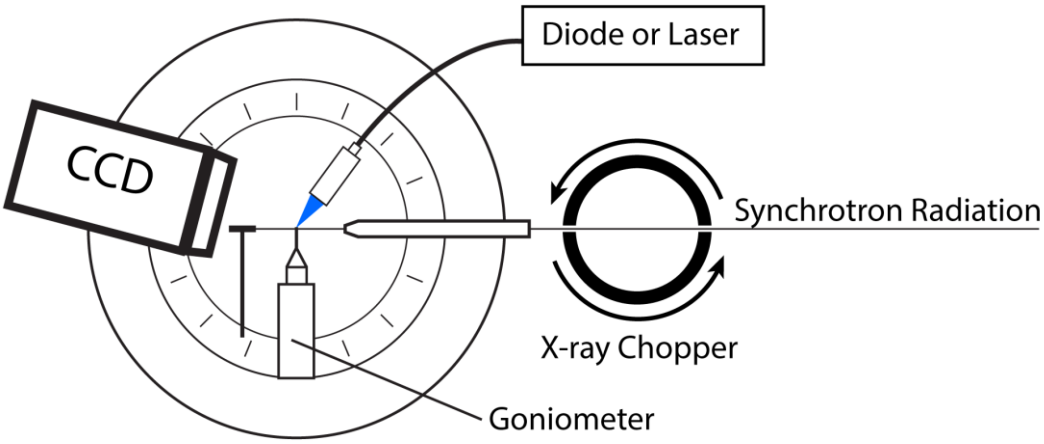

Figure 1.14. Typical photocrystallography experimental apparatus. If the experiment is using continuous irradiation the X-ray chopper is absent or stopped in the 'open' position.

state, using continuous excitation sources such as diode laser, or time resolved by using a pulsed laser and a method of gating the X-ray source. Gating of the X-ray source typically consists of a series of beam 'choppers' synchronized with the electron bunches circling the synchrotron ring. The resultant X-ray diffraction pattern consists of a superposition of structures of the ground state and excited state geometries which can be modeled as a form of disorder.

Photocrystallography presents some unique challenges and possibilities in the context of studying photochemical processes. Like TA, photocrystallography allows the study of intermediates in a photochemical reaction but unlike TA, photocrystallography provides direct evidence for structural changes associated with the photochemical process. Photocrystallography is not without its challenges as samples most be able to maintain their crystallinity for the duration of the experiment.

1.7 Scope of Thesis

In this dissertation we report mechanistic studies of small molecule activation processes which are relevant to the problem of solar energy storage. To probe these reactions TA and photocrystallography are employed to observe intermediates that would have otherwise gone undetected, yielding insight that can be applied to the development of better catalysts. Specifically, we study the two half reactions of HX (X = Cl, Br) splitting, and oxygen activation chemistry through studies of the oxidation of peroxide dianion and a cubane model of the CoPi water oxidation catalyst.

In the first part of this thesis we study the two half reactions of HX splitting. In Chapter 2 we study nickel complexes which are shown to facilitate photo-driven H_2 evolution from solutions containing HCl. TA spectroscopy probes the role of the polypyridyl ligands which are shown to act as redox mediators, providing a method for circumventing the inherently short excited state lifetimes associated with first row transition metal complexes. The two-electron chemistry required for H_2 generation is achieved by coupling the one-electron photochemistry of the polypyridyl ligands to the disproportionation of reduced nickel complexes.

In Chapter 3 we leverage TA to probe halogen photoelimination in a series of $NiX_3(LL)$ (LL = bidentate phosphine) complexes which eliminate halogen in both solution and the solid state. Computational studies examine the nature of the $NiX_3(LL)$ excited states to show that efficient halogen photoelimination is facilitated by a dissociative LMCT excited state. TA identifies an aryl-halide complex as an intermediate in the photoelimination reaction which may enhance the quantum yield of halogen elimination by guiding the

photochemically generated halogen radical away from the nickel center, suppressing the thermodynamically favorable back reaction.

In Chapter 4 photocrystallography is used in tandem with TA to study halogen photoelimination from valence isomeric dirhodium phosphazane complexes, Rh_2[I,III] and Rh_2[II,II]. TA experiments provide spectroscopic evidence for a common photo-intermediate for halogen elimination from the two valence isomers. To evaluate this hypothesis, we employ photocrystallography to reveal structural changes associated with transition to the proposed common intermediate. The insight gained from TA and photocrystallography leads to the synthetic isolation of the proposed intermediate. The observed structural intermediate suggests that halogen elimination proceeds through a binuclear reductive elimination mechanism.

For the remainder of this thesis we study systems important for oxygen activation chemistry. In Chapter 5 we employ TA to study the kinetics of charge transfer in the first soluble form of peroxide dianion. To circumvent the limits of diffusion we leverage the highly charged nature of peroxide dianion to form ion pairs with ruthenium polypyridyl complexes. TA kinetic data and DFT calculations facilitate a Marcus analysis which shows that the O–O bond of the peroxide dominates the internal reorganization energy of the system.

In Chapter 6 we study cubane model complexes structurally related to CoPi water oxidation catalysts using TA and computations. Photooxidation by a covalently linked photosensitizer reveals fast electron transfer from the cubane systems. Calculations show extensive delocalization of the cubane molecular orbitals and examination of the excited

state manifold implicates d–d excited states as facilitators of rapid charge recombination. These results suggest that the delocalized electron structure of the CoPi catalysts may play an important role in facilitating charge transfer and redox leveling.

1.8 References

1. International Energy Outlook 2013: U.S. Energy Information Administration, http://www.eia.gov/forecasts/archive/ieo13/pdf/0484(2013).pdf (Accessed March 2016).

2. Advancing the Science of Climate Change. The National Academies Press. 2010. DOI 10.17226/12782

3. Blankenship, R. E.; Tiede, D. M.; Barber, J.; Brudvig, G. W.; Fleming, G.; Ghirardi, M.; Gunner, M. R.; Junge, W.; Kramer, D. M.; Melis, A.; Moore, T. A.; Moser, C. C.; Nocera, D. G.; Nozik, A. J.; Ort, D. R.; Parson, W. W.; Prince, R. C.; Sayre, R. T. Comparing Photosynthetic and Photovoltaic Efficiencies and Recognizing the Potential for Improvement. *Science* **2011**, *332* (6031), 805–809.

4. Pollack, H. N.; Hurter, S. J.; Johnson, J. R. Heat Flow from the Earth's Interior: Analysis of the Global Data Set. *Rev. Geophys.* **1993**, *31* (3), 267–280.

5. Abbott, D. Keeping the Energy Debate Clean: How Do We Supply the World's Energy Needs? *Proceedings of the IEEE* **2010**, *98* (1), 42–66.

6. Moniz E, Deutch J, eds (2003) The Future of Nuclear Power (Massachusetts Institute of Technology, Cambridge, MA).

7. Li, J.; Guo, H. Y.; Wan, B. N.; Gong, X. Z.; Liang, Y. F.; Xu, G. S.; Gan, K. F.; Hu, J. S.; Wang, H. Q.; Wang, L.; Zeng, L.; Zhao, Y. P.; Denner, P.; Jackson, G. L.; Loarte, A.; Maingi, R.; Menard, J. E.; Rack, M.; Zou, X. L. A Long-Pulse High-Confinement Plasma Regime in the Experimental Advanced Superconducting Tokamak. Nat Phys 2013, 9 (12), 817–821.

8. Herrmann, M. Plasma Physics: A Promising Advance in Nuclear Fusion. Nature 2014, 506 (7488), 302–303.

9. Hermann, W. A. Quantifying Global Exergy Resources. *Energy* **2006**, *31* (12), 1685–1702.

10. Barber, J. Photosynthetic Energy Conversion: Natural and Artificial. *Chem. Soc. Rev.* **2008**, *38* (1), 185–196.

11. Barber, J.; Tran, P. D. From Natural to Artificial Photosynthesis. *Journal of The Royal Society Interface* **2013**, *10* (81), 20120984.

12. Eisenberg, R.; Nocera, D. G. Preface: Overview of the Forum on Solar and Renewable Energy. *Inorg. Chem.* **2005**, *44* (20), 6799–6801.

13. Grätzel, M. Photovoltaic and Photoelectrochemical Conversion of Solar Energy. *Philosophical Transactions of the Royal Society of London A: Mathematical, Physical and Engineering Sciences* **2007**, *365* (1853), 993–1005.

14. Lewis, N. S. Toward Cost-Effective Solar Energy Use. *Science* **2007**, *315* (5813), 798–801.

15. Wadia, C.; Alivisatos, A. P.; Kammen, D. M. Materials Availability Expands the Opportunity for Large-Scale Photovoltaics Deployment. *Environ. Sci. Technol.* **2009**, *43* (6), 2072–2077.

16. Green, M. A. Crystalline and Thin-Film Silicon Solar Cells: State of the Art and Future Potential. *Solar Energy* **2003**, *74* (3), 181–192.

17. Bazilian, M.; Onyeji, I.; Liebreich, M.; MacGill, I.; Chase, J.; Shah, J.; Gielen, D.; Arent, D.; Landfear, D.; Zhengrong, S. Re-Considering the Economics of Photovoltaic Power. *Renewable Energy* **2013**, *53*, 329–338.

18. Snaith, H. J. Perovskites: The Emergence of a New Era for Low-Cost, High-Efficiency Solar Cells. *J. Phys. Chem. Lett.* **2013**, *4* (21), 3623–3630.

19. Park, N.-G. Organometal Perovskite Light Absorbers Toward a 20% Efficiency Low-Cost Solid-State Mesoscopic Solar Cell. *J. Phys. Chem. Lett.* **2013**, *4* (15), 2423–2429.

20. Alternative Fuels and Advanced Vehicles Data Center: U.S. Department of Energy, http://www.afdc.energy.gov/fuels/fuel_comparison_chart.pdf (Accessed March 2016).

21. Cook, T. R.; Dogutan, D. K.; Reece, S. Y.; Surendranath, Y.; Teets, T. S.; Nocera, D. G. Solar Energy Supply and Storage for the Legacy and Nonlegacy Worlds. *Chem. Rev.* **2010**, *110* (11), 6474–6502.

22. Wood, P. M. The Potential Diagram for Oxygen at pH 7. *Biochemical Journal* **1988**, *253* (1), 287–289.

23. Tolman, W. B. Making and Breaking the Dioxygen O–O Bond: New Insights from Studies of Synthetic Copper Complexes. *Acc. Chem. Res.* **1997**, *30* (6), 227–237.

24. Betley, T. A.; Surendranath, Y.; Childress, M. V.; Alliger, G. E.; Fu, R.; Cummins, C. C.; Nocera, D. G. A Ligand Field Chemistry of Oxygen Generation by the Oxygen-Evolving Complex and Synthetic Active Sites. *Phil. Trans. R. Soc. B* **2008**, *363* (1494), 1293–1303.

25. Betley, T. A.; Wu, Q.; Van Voorhis, T.; Nocera, D. G. Electronic Design Criteria for O–O Bond Formation via Metal–Oxo Complexes. *Inorg. Chem.* **2008**, *47* (6), 1849–1861.

26. Wang, L.-P.; Van Voorhis, T. Direct-Coupling O_2 Bond Forming a Pathway in Cobalt Oxide Water Oxidation Catalysts. *J. Phys. Chem. Lett.* **2011**, *2* (17), 2200–2204.

27. Bryant, D. A.; Frigaard, N.-U. Prokaryotic Photosynthesis and Phototrophy Illuminated. *Trends in Microbiology* **2006**, *14* (11), 488–496.

28. Steger, U.; Achterberg, W.; Blok, K.; Bode, H.; Frenz, W.; Gather, C.; Hanekamp, G.; Imboden, D.; Jahnke, M.; Kost, M.; Kurz, R.; Nutzinger, H. G.; Ziesemer, T. *Sustainable Development and Innovation in the Energy Sector*; Springer Science & Business Media, 2005.

29. Nealson, K. H.; Conrad, P. G. Life: Past, Present and Future. *Philosophical Transactions of the Royal Society of London B: Biological Sciences* **1999**, *354* (1392), 1923–1939.

30. Yano, J.; Kern, J.; Yachandra, V. K.; Nilsson, H.; Koroidov, S.; Messinger, J. Light-Dependent Production of Dioxygen in Photosynthesis. In Sustaining Life on Planet Earth: Metalloenzymes Mastering Dioxygen and Other Chewy Gases; Kroneck, P. M. H., Torres, M. E. S., Eds.; Metal Ions in Life Sciences; Springer International Publishing, **2015**; pp 13–43.

31. Carrell, G.; Tyryshkin, M.; Dismukes, C. An Evaluation of Structural Models for the Photosynthetic Water-Oxidizing Complex Derived from Spectroscopic and X-Ray Diffraction Signatures. *J. Biol. Inorg. Chem.* **2002**, *7* (1-2), 2–22.

32. Siegbahn, P. E. M. Water Oxidation Mechanism in Photosystem II, Including Oxidations, Proton Release Pathways, O—O Bond Formation and O2 Release. *Biochimica et Biophysica Acta (BBA) - Bioenergetics* **2013**, *1827* (8–9), 1003–1019.

33. Kanan, M. W.; Nocera, D. G. In Situ Formation of an Oxygen-Evolving Catalyst in Neutral Water Containing Phosphate and Co^{2+}. *Science* **2008**, *321* (5892), 1072–1075.

34. Du, P.; Eisenberg, R. Catalysts Made of Earth-Abundant Elements (Co, Ni, Fe) for Water Splitting: Recent Progress and Future Challenges. *Energy Environ. Sci.* **2012**, *5* (3), 6012–6021.

35. Risch, M.; Khare, V.; Zaharieva, I.; Gerencser, L.; Chernev, P.; Dau, H. Cobalt–Oxo Core of a Water-Oxidizing Catalyst Film. *J. Am. Chem. Soc.* **2009**, *131* (20), 6936–6937.

36. Dincă, M.; Surendranath, Y.; Nocera, D. G. Nickel-Borate Oxygen-Evolving Catalyst That Functions under Benign Conditions. *PNAS* **2010**, *107* (23), 10337–10341.

37. Zaharieva, I.; Najafpour, M. M.; Wiechen, M.; Haumann, M.; Kurz, P.; Dau, H. Synthetic Manganese–calcium Oxides Mimic the Water-Oxidizing Complex of Photosynthesis Functionally and Structurally. *Energy Environ. Sci.* **2011**, *4* (7), 2400–2408.

38. Du, P.; Kokhan, O.; Chapman, K. W.; Chupas, P. J.; Tiede, D. M. Elucidating the Domain Structure of the Cobalt Oxide Water Splitting Catalyst by X-Ray Pair Distribution Function Analysis. *J. Am. Chem. Soc.* **2012**, *134* (27), 11096–11099.

39. Bockris, J. O.; Otagawa, T. Mechanism of Oxygen Evolution on Perovskites. *J. Phys. Chem.* **1983**, *87* (15), 2960–2971.

40. Bediako, D. K.; Lassalle-Kaiser, B.; Surendranath, Y.; Yano, J.; Yachandra, V. K.; Nocera, D. G. Structure–Activity Correlations in a Nickel–Borate Oxygen Evolution Catalyst. *J. Am. Chem. Soc.* **2012**, *134* (15), 6801–6809.

41. Singh, R. N.; Koenig, J.-F.; Poillerat, G.; Chartier, P. Electrochemical Studies on Protective Thin Co3 O 4 and NiCo2 O 4 Films Prepared on Titanium by Spray Pyrolysis for Oxygen Evolution. *J. Electrochem. Soc.* **1990**, *137* (5), 1408–1413.

42. Kanan, M. W.; Yano, J.; Surendranath, Y.; Dincă, M.; Yachandra, V. K.; Nocera, D. G. Structure and Valency of a Cobalt−Phosphate Water Oxidation Catalyst Determined by in Situ X-Ray Spectroscopy. *J. Am. Chem. Soc.* **2010**, *132* (39), 13692–13701.

43. Rasiyah, P.; Tseung, A. C. C. The Role of the Lower Metal Oxide/Higher Metal Oxide Couple in Oxygen Evolution Reactions. *J. Electrochem. Soc.* **1984**, *131* (4), 803–808.

44. Burke, L. D.; Murphy, O. J.; O'Neill, J. F.; Venkatesan, S. The Oxygen Electrode. Part 8. Oxygen Evolution at Ruthenium Dioxide Anodes. *J. Chem. Soc., Faraday Trans. 1* **1977**, *73* (0), 1659–1671.

45. Hu, J.-M.; Zhang, J.-Q.; Cao, C.-N. Oxygen Evolution Reaction on IrO2-Based DSA Type Electrodes: Kinetics Analysis of Tafel Lines and EIS. *International Journal of Hydrogen Energy* **2004**, *29* (8), 791–797.

46. Siegbahn, P. E. M. Recent Theoretical Studies of Water Oxidation in Photosystem II. *Journal of Photochemistry and Photobiology B: Biology* **2011**, *104* (1–2), 94–99.

47. Dimitrou, K.; Folting, K.; Streib, W. E.; Christou, G. Dimerization of the [$Co_2III(OH)_2$] Core to the First Example of a [Co_4IIIO_4] Cubane: Potential Insights into Photosynthetic Water Oxidation. *J. Am. Chem. Soc.* **1993**, *115* (14), 6432–6433.

48. Chakrabarty, R.; Bora, S. J.; Das, B. K. Synthesis, Structure, Spectral and Electrochemical Properties, and Catalytic Use of Cobalt(III)−Oxo Cubane Clusters. *Inorg. Chem.* **2007**, *46* (22), 9450–9462.

49. Dismukes, G. C.; Brimblecombe, R.; Felton, G. A. N.; Pryadun, R. S.; Sheats, J. E.; Spiccia, L.; Swiegers, G. F. Development of Bioinspired Mn4O4−Cubane Water Oxidation Catalysts: Lessons from Photosynthesis. *Acc. Chem. Res.* **2009**, *42* (12), 1935–1943.

50. Ullman, A. M.; Liu, Y.; Huynh, M.; Bediako, D. K.; Wang, H.; Anderson, B. L.; Powers, D. C.; Breen, J. J.; Abruña, H. D.; Nocera, D. G. Water Oxidation Catalysis by Co(II) Impurities in $Co(III)_4O_4$ Cubanes. *J. Am. Chem. Soc.* **2014**, *136* (50), 17681–17688.

51. Reprinted from Biochimica et Biophysica Acta (BBA) - Bioenergetics, 1837 (8), Arturo Robertazzi, Artur Galstyan, Ernst Walter Knapp. PSII manganese cluster: Protonation of W2, O5, O4 and His337 in the S1 state explored by combined quantum chemical and electrostatic energy computations, 1316-1321, **2014**, with permission from Elsevier.

52. Fuel Cell Technologies Program: U.S. Department of Energy, Energy Efficiency & Renewable Energy. http://www1.eere.energy.gov/hydrogenandfuelcells/fuelcells/pdfs/fc_comparison_chart.pdf Accessed March, 2016.

53. Pilatowsky, I.; Romero, R. J.; Isaza, C. A.; Gamboa, S. A.; Sebastian, P. J.; Rivera, W. Thermodynamics of Fuel Cells. In *Cogeneration Fuel Cell-Sorption Air Conditioning Systems*; Green Energy and Technology; Springer London, 2011; pp 25–36.

54. Ramaswamy, N.; Hakim, N.; Mukerjee, S. Degradation Mechanism Study of Perfluorinated Proton Exchange Membrane under Fuel Cell Operating Conditions. *Electrochimica Acta* **2008**, *53* (8), 3279–3295.

55. Couper, A. M.; Pletcher, D.; Walsh, F. C. Electrode Materials for Electrosynthesis. *Chem. Rev.* **1990**, *90* (5), 837–865.

56. Duby, P. The History of Progress in Dimensionally Stable Anodes. *JOM* **1993**, *45* (3), 41–43.

57. Alves, V. A.; Silva, L. A. da; Boodts, J. F. C. Electrochemical Impedance Spectroscopic Studyof Dimensionally Stable Anode Corrosion. *Journal of Applied Electrochemistry* **1998**, *28* (9), 899–905.

58. Gupta, R. C. *Handbook of Toxicology of Chemical Warfare Agents*; Academic Press, 2015.

59. Huskinson, B.; Rugolo, J.; Mondal, S. K.; Aziz, M. J. A High Power Density, High Efficiency Hydrogen–chlorine Regenerative Fuel Cell with a Low Precious Metal Content Catalyst. *Energy Environ. Sci.* **2012**, *5* (9), 8690–8698.

60. Thomassen, M.; Sandnes, E.; Børresen, B.; Tunold, R. Evaluation of Concepts for Hydrogen – Chlorine Fuel Cells. *J Appl Electrochem* **2006**, *36* (7), 813–819.

61. Yeo, R. S.; McBreen, J.; Tseung, A. C. C.; Srinivasan, S.; McElroy, J. An Electrochemically Regenerative Hydrogen-Chlorine Energy Storage System: Electrode Kinetics and Cell Performance. *J Appl Electrochem* **1980**, *10* (3), 393–404.

62. CRC Handbook of Chemistry and Physics. 86th ed. CRC Press: Boca Raton, FL, 2005-2006; p 8-21,23.

63. Livshits, V.; Ulus, A.; Peled, E. High-Power H2/Br2 Fuel Cell. *Electrochemistry Communications* **2006**, *8* (8), 1358–1362.

64. Bard, A. J. Design of Semiconductor Photoelectrochemical Systems for Solar Energy Conversion. *J. Phys. Chem.* **1982**, *86* (2), 172–177.

65. Sivula, K.; Formal, F. L.; Grätzel, M. WO3–Fe2O3 Photoanodes for Water Splitting: A Host Scaffold, Guest Absorber Approach. *Chem. Mater.* **2009**, *21* (13), 2862–2867.

66. Steinmiller, E. M. P.; Choi, K.-S. Photochemical Deposition of Cobalt-Based Oxygen Evolving Catalyst on a Semiconductor Photoanode for Solar Oxygen Production. *Proc Natl Acad Sci U S A* **2009**, *106* (49), 20633–20636.

67. Tollin, G. Model Systems for Photosynthetic Energy Conversion. *J. Phys. Chem.* **1976**, *80* (20), 2274–2277.

68. Harriman, A. 6 - The Role of Porphyrins in Natural and Artificial Photosynthesis A2 - Grätzel, Michael. In *Energy Resources Through Photochemistry and Catalysis*; Academic Press, 1983; pp 163–215.

69. Esswein, A. J.; Nocera, D. G. Hydrogen Production by Molecular Photocatalysis. *Chem. Rev.* **2007**, *107* (10), 4022–4047.

70. Kalyanasundaram, K.; Grätzel, M. Light Induced Redox Reactions of Water Soluble Porphyrins, Sensitization of Hydrogen Generation from Water by Zincporphyrin Derivatives. *HCA* **1980**, *63* (2), 478–485.

71. Persaud, L.; Bard, A. J.; Campion, A.; Fox, M. A.; Mallouk, T. E.; Webber, S. E.; White, J. M. Photochemical Hydrogen Evolution via Singlet-State Electron-Transfer Quenching of Zinc tetra(N-Methyl-4-Pyridyl)porphyrin Cations in a Zeolite L Based System. *J. Am. Chem. Soc.* **1987**, *109* (24), 7309–7314.

72. Han, Z.; Eisenberg, R. Fuel from Water: The Photochemical Generation of Hydrogen from Water. *Acc. Chem. Res.* **2014**, *47* (8), 2537–2544.

73. Meyer, T. J. Chemical Approaches to Artificial Photosynthesis. *Acc. Chem. Res.* **1989**, *22* (5), 163–170.

74. Balzani, V.; Juris, A. Photochemistry and Photophysics of Ru(II)□polypyridine Complexes in the Bologna Group. From Early Studies to Recent Developments. *Coordination Chemistry Reviews* **2001**, *211* (1), 97–115.

75. Kiwi, J.; Graetzel, M. Projection, Size Factors, and Reaction Dynamics of Colloidal Redox Catalysts Mediating Light Induced Hydrogen Evolution from Water. *J. Am. Chem. Soc.* **1979**, *101* (24), 7214–7217.

76. Miller, D. S.; Bard, A. J.; McLendon, G.; Ferguson, J. Catalytic Water Reduction at Colloidal Metal "Microelectrodes". 2. Theory and Experiment. *J. Am. Chem. Soc.* **1981**, *103* (18), 5336–5341.

77. Zhang, P.; Wang, M.; Dong, J.; Li, X.; Wang, F.; Wu, L.; Sun, L. Photocatalytic Hydrogen Production from Water by Noble-Metal-Free Molecular Catalyst Systems Containing Rose Bengal and the Cobaloximes of BFx-Bridged Oxime Ligands. *J. Phys. Chem. C* **2010**, *114* (37), 15868–15874.

78. Lazarides, T.; McCormick, T.; Du, P.; Luo, G.; Lindley, B.; Eisenberg, R. Making Hydrogen from Water Using a Homogeneous System Without Noble Metals. *J. Am. Chem. Soc.* **2009**, *131* (26), 9192–9194.

79. Abe, R.; Hara, K.; Sayama, K.; Domen, K.; Arakawa, H. Steady Hydrogen Evolution from Water on Eosin Y-Fixed TiO2 Photocatalyst Using a Silane-Coupling Reagent under Visible Light Irradiation. *Journal of Photochemistry and Photobiology A: Chemistry* **2000**, *137* (1), 63–69.

80. Patsoura, A.; Kondarides, D. I.; Verykios, X. E. Enhancement of Photoinduced Hydrogen Production from Irradiated Pt/TiO2 Suspensions with Simultaneous Degradation of Azo-Dyes. *Applied Catalysis B: Environmental* **2006**, *64* (3–4), 171–179.

81. Sabatini, R. P.; McCormick, T. M.; Lazarides, T.; Wilson, K. C.; Eisenberg, R.; McCamant, D. W. Intersystem Crossing in Halogenated Bodipy Chromophores Used for Solar Hydrogen Production. *J. Phys. Chem. Lett.* **2011**, *2* (3), 223–227.

82. Sabatini, R. P.; Eckenhoff, W. T.; Orchard, A.; Liwosz, K. R.; Detty, M. R.; Watson, D. F.; McCamant, D. W.; Eisenberg, R. From Seconds to Femtoseconds: Solar Hydrogen Production and Transient Absorption of Chalcogenorhodamine Dyes. *J. Am. Chem. Soc.* **2014**, *136* (21), 7740–7750.

83. Trogler, W. C.; Erwin, D. K.; Geoffroy, G. L.; Gray, H. B. Production of Hydrogen by Ultraviolet Irradiation of Binuclear molybdenum(II) Complexes in Acidic Aqueous Solutions. Observation of Molybdenum Hydride Intermediates in octahalodimolybdate(II) Photoreactions. *J. Am. Chem. Soc.* **1978**, *100* (4), 1160–1163.

84. Tyler, D. R.; Gray, H. B. Studies of the Photochemical Behavior of (undecacarbonyl)triferrate(2-) in Solution. *J. Am. Chem. Soc.* **1981**, *103* (7), 1683–1686.

85. Gray, H. B.; Maverick, A. W. Solar Chemistry of Metal Complexes. *Science* **1981**, *214* (4526), 1201–1205.

86. Mann, K. R.; Lewis, N. S.; Miskowski, V. M.; Erwin, D. K.; Hammond, G. S.; Gray, H. B. Solar Energy Storage. Production of Hydrogen by 546-Nm Irradiation of a Dinuclear rhodium(I) Complex in Acidic Aqueous Solution. *J. Am. Chem. Soc.* **1977**, *99* (16), 5525–5526.

87. Heyduk, A. F.; Nocera, D. G. Hydrogen Produced from Hydrohalic Acid Solutions by a Two-Electron Mixed-Valence Photocatalyst. *Science* **2001**, *293* (5535), 1639–1641.

88. Heyduk, A. F.; Macintosh, A. M.; Nocera, D. G. Four-Electron Photochemistry of Dirhodium Fluorophosphine Compounds. *J. Am. Chem. Soc.* **1999**, *121* (21), 5023–5032.

89. Eidem, P. K.; Maverick, A. W.; Gray, H. B. Production of Hydrogen by Irradiation of Metal Complexes in Aqueous Solutions. *Inorganica Chimica Acta* **1981**, *50*, 59–64.

90. Glebov, E. M.; Plyusnin, V. F.; Tkachenko, N. V.; Lemmetyinen, H. Laser Flash Photolysis of $IrCl_6^{2-}$ in Aqueous Solutions. *Chemical Physics* **2000**, *257* (1), 79–89.

91. Cook, T. R.; Surendranath, Y.; Nocera, D. G. Chlorine Photoelimination from a Diplatinum Core: Circumventing the Back Reaction. *J. Am. Chem. Soc.* **2009**, *131* (1), 28–29.

92. Teets, T. S.; Lutterman, D. A.; Nocera, D. G. Halogen Photoreductive Elimination from Metal–Metal Bonded Iridium(II)–Gold(II) Heterobimetallic Complexes. *Inorg. Chem.* **2010**, *49* (6), 3035–3043.

93. Yin, Q.; Tan, J. M.; Besson, C.; Geletii, Y. V.; Musaev, D. G.; Kuznetsov, A. E.; Luo, Z.; Hardcastle, K. I.; Hill, C. L. A Fast Soluble Carbon-Free Molecular Water Oxidation Catalyst Based on Abundant Metals. *Science* **2010**, *328* (5976), 342–345.

94. Shevchenko, D.; Anderlund, M. F.; Thapper, A.; Styring, S. Photochemical Water Oxidation with Visible Light Using a Cobalt Containing Catalyst. *Energy Environ. Sci.* **2011**, *4* (4), 1284–1287.

95. Natali, M.; Orlandi, M.; Berardi, S.; Campagna, S.; Bonchio, M.; Sartorel, A.; Scandola, F. Photoinduced Water Oxidation by a Tetraruthenium Polyoxometalate Catalyst: Ion-Pairing and Primary Processes with $Ru(bpy)_3^{2+}$ Photosensitizer. *Inorg. Chem.* **2012**, *51* (13), 7324–7331.

96. Liu, H.; Moré, R.; Grundmann, H.; Cui, C.; Erni, R.; Patzke, G. R. Promoting Photochemical Water Oxidation with Metallic Band Structures. *J. Am. Chem. Soc.* **2016**, *138* (5), 1527–1535.

97. Panda, C.; Debgupta, J.; Díaz Díaz, D.; Singh, K. K.; Sen Gupta, S.; Dhar, B. B. Homogeneous Photochemical Water Oxidation by Biuret-Modified Fe-TAML: Evidence of FeV(O) Intermediate. *J. Am. Chem. Soc.* **2014**, *136* (35), 12273–12282.

98. Mukhopadhyay, S.; Singh, R. S.; Biswas, A.; Pandey, D. S. Photochemical Water Oxidation by Cyclometalated iridium(III) Complexes: A Mechanistic Insight. *Chem. Commun.* **2016**, *52* (19), 3840–3843.

99. Fukuzumi, S.; Jung, J.; Yamada, Y.; Kojima, T.; Nam, W. Homogeneous and Heterogeneous Photocatalytic Water Oxidation by Persulfate. *Chem. Asian J.* **2016**, ASAP DOI: 10.1002/asia.201501329.

100. Duan, L.; Bozoglian, F.; Mandal, S.; Stewart, B.; Privalov, T.; Llobet, A.; Sun, L. A Molecular Ruthenium Catalyst with Water-Oxidation Activity Comparable to that of Photosystem II. *Nat Chem* **2012**, *4* (5), 418–423.

101. Duan, L.; Wang, L.; Li, F.; Li, F.; Sun, L. Highly Efficient Bioinspired Molecular Ru Water Oxidation Catalysts with Negatively Charged Backbone Ligands. *Acc. Chem. Res.* **2015**, *48* (7), 2084–2096.

102. Gersten, S. W.; Samuels, G. J.; Meyer, T. J. Catalytic Oxidation of Water by an Oxo-Bridged Ruthenium Dimer. *J. Am. Chem. Soc.* **1982**, *104* (14), 4029–4030.

103. Elizarova, G. L.; Matvienko, L. G.; Lozhkina, N. V.; Parmon, V. N. Kinetic Study of Dioxygen Formation in Slightly Acidic Ru(bpy) 3 3+ Solutions in the Presence of Monomeric and Dimeric Homogeneous Cobalt Catalysts. *React Kinet Catal Lett* **1984**, *26* (1-2), 67–72.

104. Ellis, W. C.; McDaniel, N. D.; Bernhard, S.; Collins, T. J. Fast Water Oxidation Using Iron. *J. Am. Chem. Soc.* **2010**, *132* (32), 10990–10991.

105. Demeter, E. L.; Hilburg, S. L.; Washburn, N. R.; Collins, T. J.; Kitchin, J. R. Electrocatalytic Oxygen Evolution with an Immobilized TAML Activator. *J. Am. Chem. Soc.* **2014**, *136* (15), 5603–5606.

106. Fillol, J. L.; Codolà, Z.; Garcia-Bosch, I.; Gómez, L.; Pla, J. J.; Costas, M. Efficient Water Oxidation Catalysts Based on Readily Available Iron Coordination Complexes. *Nat Chem* **2011**, *3* (10), 807–813.

107. Fukuzumi, S.; Hong, D. Homogeneous versus Heterogeneous Catalysts in Water Oxidation. *Eur. J. Inorg. Chem.* **2014**, *2014* (4), 645–659.

108. Kohl, S. W.; Weiner, L.; Schwartsburd, L.; Konstantinovski, L.; Shimon, L. J. W.; Ben-David, Y.; Iron, M. A.; Milstein, D. Consecutive Thermal H2 and Light-Induced O_2 Evolution from Water Promoted by a Metal Complex. *Science* **2009**, *324* (5923), 74–77.

109. Li, G.; Ward, W. M.; Meyer, G. J. Visible Light Driven Nanosecond Bromide Oxidation by a Ru Complex with Subsequent Br–Br Bond Formation. *J. Am. Chem. Soc.* **2015**, *137* (26), 8321–8323.

110. Carrera, E. I.; McCormick, T. M.; Kapp, M. J.; Lough, A. J.; Seferos, D. S. Thermal and Photoreductive Elimination from the Tellurium Center of π-Conjugated Tellurophenes. *Inorg. Chem.* **2013**, *52* (23), 13779–13790.

111. Carrera, E. I.; Seferos, D. S. Efficient Halogen Photoelimination from Dibromo, Dichloro and Difluoro Tellurophenes. *Dalton Trans.* **2015**, *44* (5), 2092–2096.

112. Carrera, E. I.; Lanterna, A. E.; Lough, A. J.; Scaiano, J. C.; Seferos, D. S. A Mechanistic Study of Halogen Addition and Photoelimination from π-Conjugated Tellurophenes. *J. Am. Chem. Soc.* **2016**, *138* (8), 2678–2689.

113. Yang, H.; Gabbaï, F. P. Solution and Solid-State Photoreductive Elimination of Chlorine by Irradiation of a [PtSb]VII Complex. *J. Am. Chem. Soc.* **2014**, *136* (31), 10866–10869.

114. Raphael Karikachery, A.; Lee, H. B.; Masjedi, M.; Ross, A.; Moody, M. A.; Cai, X.; Chui, M.; Hoff, C. D.; Sharp, P. R. High Quantum Yield Molecular Bromine Photoelimination from Mononuclear Platinum(IV) Complexes. *Inorg. Chem.* **2013**, *52* (7), 4113–4119.

115. Perera, T. A.; Masjedi, M.; Sharp, P. R. Photoreduction of Pt(IV) Chloro Complexes: Substrate Chlorination by a Triplet Excited State. *Inorg. Chem.* **2014**, *53* (14), 7608–7621.

116. Wickramasinghe, L. A.; Sharp, P. R. Photoreduction of Pt(IV) Halo-Hydroxo Complexes: Possible Hypohalous Acid Elimination. *Inorg. Chem.* **2014**, *53* (3), 1430–1442.

117. Cook, T. R.; McCarthy, B. D.; Lutterman, D. A.; Nocera, D. G. Halogen Oxidation and Halogen Photoelimination Chemistry of a Platinum–Rhodium Heterobimetallic Core. *Inorg. Chem.* **2012**, *51* (9), 5152–5163.

118. Bragg, W. L. The Structure of Some Crystals as Indicated by Their Diffraction of X-Rays. *Proceedings of the Royal Society of London A: Mathematical, Physical and Engineering Sciences* **1913**, *89* (610), 248–277.

119. Ewald, P. P. Methods and Problems of Crystal Structure Analysis. In *Fifty Years of X-Ray Diffraction*; Ewald, P. P., Ed.; Springer US, 1962; pp 102–118.

120. Kuhn, P.; Wilson, K.; Patch, M. G.; Stevens, R. C. The Genesis of High-Throughput Structure-Based Drug Discovery Using Protein Crystallography. *Current Opinion in Chemical Biology* **2002**, *6* (5), 704–710.

121. Rüdlinger, M.; Schefer, J.; Chevrier, G.; Furer, N.; Güdel, H. U.; Haussühl, S.; Heger, G.; Schweiss, P.; Vogt, T.; Woike, T.; Zöllner, H. Light-Induced Structural Changes in Sodiumnitroprusside (Na2(Fe(CN)5NO)·2D2O) at 80 K. *Z. Physik B - Condensed Matter* **1991**, *83* (1), 125–130.

122. Rüdlinger, M.; Schefer, J.; Vogt, T.; Woike, T.; Haussühl, S.; Zöllner, H. Ground- and Light-Induced Metastable States of Sodiumnitroprusside. *Physica B: Condensed Matter* **1992**, *180–181, Part 1*, 293–298.

123. Pressprich, M. R.; White, M. A.; Vekhter, Y.; Coppens, P. Analysis of a Metastable Electronic Excited State of Sodium Nitroprusside by X-Ray Crystallography. *J. Am. Chem. Soc.* **1994**, *116* (12), 5233–5238.

124. Carducci, M. D.; Pressprich, M. R.; Coppens, P. Diffraction Studies of Photoexcited Crystals: Metastable Nitrosyl-Linkage Isomers of Sodium Nitroprusside. *J. Am. Chem. Soc.* **1997**, *119* (11), 2669–2678.

125. Guérin, L.; Collet, E.; Lemée-Cailleau, M.-H.; Buron-Le Cointe, M.; Cailleau, H.; Plech, A.; Wulff, M.; Koshihara, S.-Y.; Luty, T. Probing Photoinduced Phase Transition in a Charge-Transfer Molecular Crystal by 100 Picosecond X-Ray Diffraction. *Chemical Physics* **2004**, *299* (2–3), 163–170.

126. Makal, A.; Benedict, J.; Trzop, E.; Sokolow, J.; Fournier, B.; Chen, Y.; Kalinowski, J. A.; Graber, T.; Henning, R.; Coppens, P. Restricted Photochemistry in the Molecular Solid State: Structural Changes on Photoexcitation of Cu(I) Phenanthroline Metal-to-Ligand Charge Transfer (MLCT) Complexes by Time-Resolved Diffraction. *J. Phys. Chem. A* **2012**, *116* (13), 3359–3365.

127. Collet, E.; Moisan, N.; Baldé, C.; Bertoni, R.; Trzop, E.; Laulhé, C.; Lorenc, M.; Servol, M.; Cailleau, H.; Tissot, A.; Boillot, M.-L.; Graber, T.; Henning, R.; Coppens, P.; Cointe, M. B.-L. Ultrafast Spin-State Photoswitching in a Crystal and Slower Consecutive Processes Investigated by Femtosecond Optical Spectroscopy and Picosecond X-Ray Diffraction. *Phys. Chem. Chem. Phys.* **2012**, *14* (18), 6192–6199.

128. Cole, J. M. Photocrystallography. *Acta. Cryst. A.* **2008**, (A64), 259–271.

Chapter 2: Spectroscopic Observation of Intermediates in an HCl to H_2 Photocycle Promoted by Ni(II) Polypyridyl Halide Complexes

Portions of this chapter have been published:

2.1 Introduction

The photodriven splitting of hydrohalic acids (HX) into H_2 and X_2 is a promising approach to storing solar energy in the form of a redox flow battery[1] or chemical fuel.[2] The conversion of HX to H_2 and X_2 stores a considerable amount of energy: HCl splitting stores approximately the same amount of energy per electron as the conversion of H_2O to H_2 and ½ O_2 and requires the management of two less electrons and protons than water splitting.[3]

Whereas long-lived MLCT excited states are frequently encountered in the photochemistry of second- and third-row transition metal complexes, first-row transition metal complexes typically possess extremely short-lived charge transfer excited states[4–6] exacerbating the challenge of converting the absorbed photon to energy stored in chemical bonds. This phenomenon results from the compression of the crystal field splitting when moving from a second- to first- row metal. This results in the d–d ligand-field states being at lower energy than charge-separated states, serving as efficient relaxation pathways.[7,8] The consequence of this energetic reordering of excited states can be seen by comparing the lifetimes of charge-separated states of Ru and Fe polypyridyl complexes: Ru^{2+} polypyridyl complexes display charge-separated state lifetimes of 600–850 ns,[9–11] whereas the related Fe^{2+} polypyridyl complexes display charge separated lifetimes on the order of ~100 fs.[4,8]

In order to overcome the inherently short excited state lifetimes of nickel complexes, we proposed to couple the favorable redox characteristics of nickel complexes with the robust photophysics of photoredox mediators. Due to the ability of pyridinyl radicals to facilitate complex PCET reactions[12–14] and propensity of excited pyridinyl species to engage

in H-atom abstraction (HAA) reactions,[15–18] we turned our attention to bipyridine derivatives to fulfill the role of photoredox mediator.

This Chapter is concerned with a HX-to-H_2 photocycle promoted by a Ni(II)/Ni(0) couple and the use of transient spectroscopy to reveal critical photointermediates. Reduction of a Ni(II) dihalide complex by a polypyridyl photoredox mediator provides either Ni(I) or Ni(0) complexes dependent on the particular reaction conditions employed. The photogenerated Ni(0) species reacts with HCl to generate H_2 and regenerate the Ni(II) dihalide, demonstrating a photocycle for the evolution of H_2 from HCl mediated by an earth-abundant transition metal complex.

2.2 Results

2.2.1 Steady-State Photochemistry

Ni(II)Cl_2bc (complex **1**) is pseudo-tetrahedral in the solid state and in solution. THF solutions of **1** exhibit a UV–Vis absorption spectrum that features d–d absorptions at 500, 852, and 1005 nm (ε = 200, 70, and 100 M^{-1} cm^{-1}, respectively). Referenced to T_d symmetry, the d–d transitions arise from $^3T_1$ to $^3A_2$ and $^3T_2$ excitations;[19,20] the deviation of **1** from T_d symmetry gives rise to multiple transitions for each of these absorption manifolds.[21] The room-temperature magnetic moment, measured by the Evans method, was determined to be μ_{eff} = 3.6.[22] Photolysis (λ > 305 nm) of **1** in THF in the presence of both 2.0 equiv of 2,6-lutidine and 2.0 equiv of exogenous bathocuproine (bc) caused the pale pink reaction solution to turn dark purple (Figure 2.1a). The dark purple product was identified as the Ni(0) complex **2** by comparison of the UV–Vis and ^{1}H NMR spectra of the

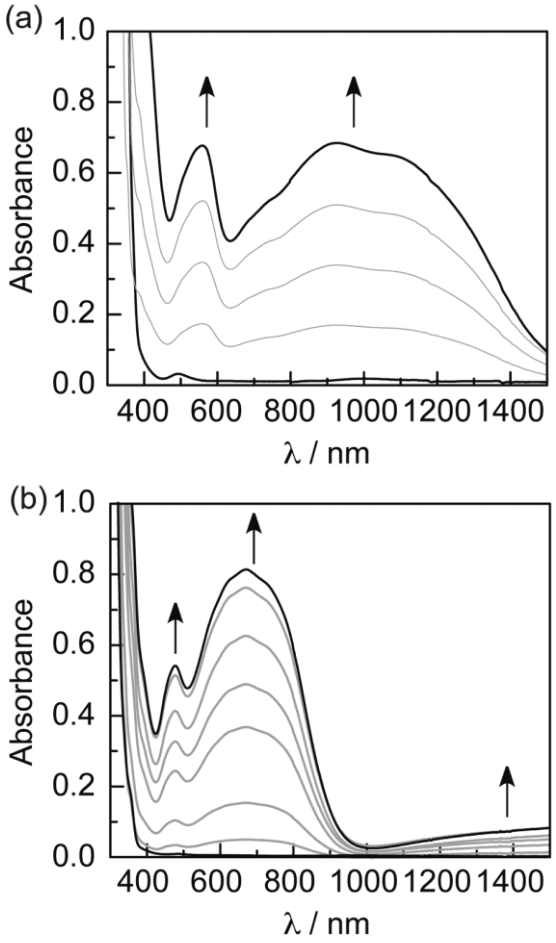

Figure 2.1. Spectral evolution during photolysis of (a) Ni(II) complex **1** to Ni(0) complex **2** in THF and (b) Ni(II) complex **1** to Ni(I) complex [**3**]Cl in 1:1 CH_3CN:1,4–cyclohexadiene.

photochemical reaction mixture to a spectrum obtained from a chemically prepared sample of **2**. Both the dark purple color and the C–C bond contraction[23] in the crystal structure of **2** are consistent with substantial redox noninnocence of the bathocuproine ligands in **2**, suggesting **2** is best described as a Ni(II) complex with two ligand-based radicals.

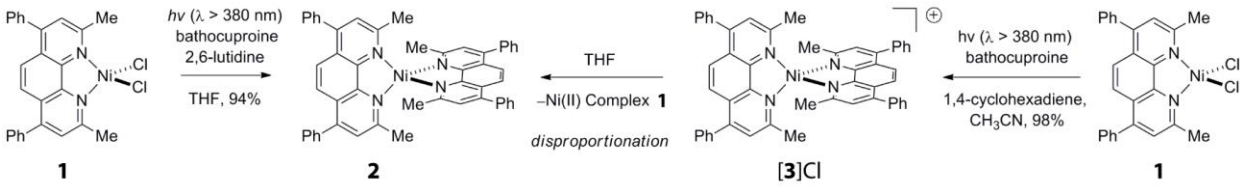

Figure 2.2. Photolysis of Ni(II) complex **1** in THF afforded Ni(0) complex **2**, while photolysis of **1** in CH_3CN/1,4-cyclohexadiene afforded Ni(I) complex [**3**]Cl.

In contrast to the photolysis of **1** in THF, steady-state photolysis of **1** in either CH_3CN or hexanes (poor H-atom donors) does not result in photoreduction. When Ni(II) complex **1** is photolyzed in CH_3CN in the presence of exogenous bathocuproine and 1,4-cyclohexadiene added as an H-atom donor (*vide infra*), a dark blue solution is obtained (Figure 2.1b). The identity of the blue photoproduct was established to be Ni(I) complex [**3**]Cl by comparison of the photochemical reaction mixture with the spectral data of independently prepared [**3**]OTf. ^{1}H NMR, EPR, and electronic absorption spectroscopies were used to assign the structure of [**3**]OTf. X-ray crystallographic analysis of a single crystal established the structure of [**3**]OTf to be a homoleptic Ni(I) structure.

The solvent-dependent photoreactivity of **1**, which undergoes either one- or two-electron photoreduction depending on the reaction solvent, was probed by examining the

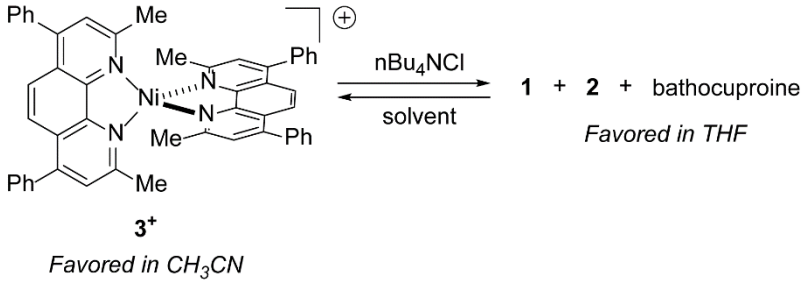

Figure 2.3. Solvent–dependent equilibrium favors Ni(I) complex **3**$^+$ in CH_3CN while Ni(II) and Ni(0) complexes **1** and **2** are favored in THF.

solvent-dependent behavior of the isolated Ni(I) complexes. The results of these experiments are summarized in Figure 2.3. Treatment of Ni(0) complex **2** with AgOTf affords Ni(I) complex [**3**]OTf, which is stable in both THF and CH_3CN. Treatment of a THF solution of [**3**]OTf with 1.0 equiv of *n*-Bu_4NCl prompted immediate disproportionation of $\mathbf{3}^+$ to Ni(II) complex **1** and Ni(0) complex **2**, with concurrent liberation of 0.5 equiv of bathocuproine. In contrast, [**3**]Cl is stable with respect to disproportionation in CH_3CN; treatment of [**3**]OTf with 1.0 equiv of *n*-BuN_4Cl in CH_3CN did not result in the observation of either **1** or **2**. Photochemical reactions also display solvent-dependent, chloride-induced disproportionation; concentration of the blue photoreaction mixture of Ni(I) complex [**3**]Cl produced by photolysis in CH_3CN and 1,4-cyclohexadiene and redissolving in THF affords a purple solution of **1** and **2**.

The effect of bis-imine ligand on the efficiency of photoreduction was probed using $NiCl_2$dmphen (**4**) (dmphen = 2,9-dimethyl-1,10-phenanthroline), $NiCl_2$dmbpy (**5**) (dmbpy = 6,6′-dimethyl-2,2′-bipyridine), and $NiCl_2$biq (biq = 2,2′-biquinoline) (**6**) (Figure 2.4). Both

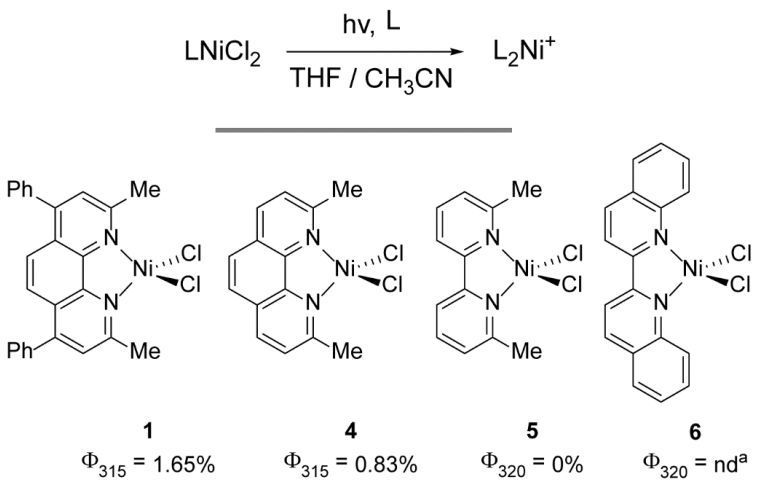

Figure 2.4. Quantum yield for photoreduction of Ni(II) complexes is correlated with reduction potential of the *bis*–imine ligand. Insolubility of **6** prevented determination of quantum yield.

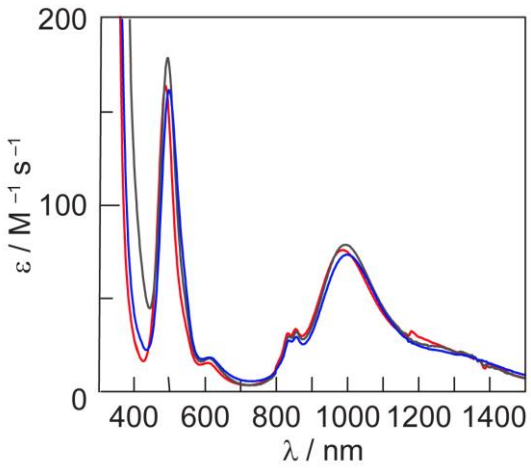

Figure 2.5. Electronic absorption spectra for **1** (—, black), **4** (—, blue), and **5** (—, red). The similarity of the d-d transitions in these complexes establishes similar solution-phase geometries.

$NiCl_2$dmphen (**4**) and $NiCl_2$biq (**6**) participate in photoreduction chemistry in analogy to complex **1** (Figure 2.14). In addition, isolated mononuclear Ni(I) complexes $Ni(dmphen)_2PF_6$ ([**7**]PF_6) and $Ni(biq)_2PF_6$ ([**8**]PF_6) exhibit chloride-induced disproportionation in THF to afford $Ni(dmphen)_2$ (**9**) and **4** or $Ni(biq)_2$ (**10**) and **6**, respectively. In contrast to complexes **1** and **4**, regardless of the wavelength of irradiation employed, $NiCl_2$(dmbpy) (**5**) is not photoreduced. The effect of ligand structure on photoreduction efficiency was probed by comparison of the quantum yields for one-electron photoreduction of complexes **1**, **4**, and **5**. Whereas complexes **1**, **4**, and **5** are isostructural in solution, established by both solution magnetic moment (**1**, μ_{eff} = 3.6; **4**, μ_{eff} = 3.5; **5**, μ_{eff} = 3.6) and similarity of d–d transitions (Figure 2.5), their photochemical quantum yields are 2.14% (**1**), 0.92% (**4**), and 0% (**5**). This trend follows the expected ease of reduction of the ancillary polypyridyl ligand.[24,25] The quantum yield for photoreduction of biquinoline-supported Ni(II) complex **6** could not be determined because of insolubility of **6** under photoreduction conditions.

2.2.2 Thermal Proton Reduction Reactions

With conditions in hand to achieve the two-electron photoreduction of Ni(II) chlorides, we examined the viability of proton reduction by the reduced Ni complexes. Treatment of Ni(0) complexes **2** and **9** with HCl in MeOH generates H_2 in 60 and 85% yield, respectively, along with Ni(II) complex **1** and **4**; the results of these experiments are summarized in Figure 2.6. Formation of **1** and **4** following H_2 evolving reactions of **2** and **9**, respectively, establishes a closed H_2-evolving photocycle using an earth-abundant transition metal

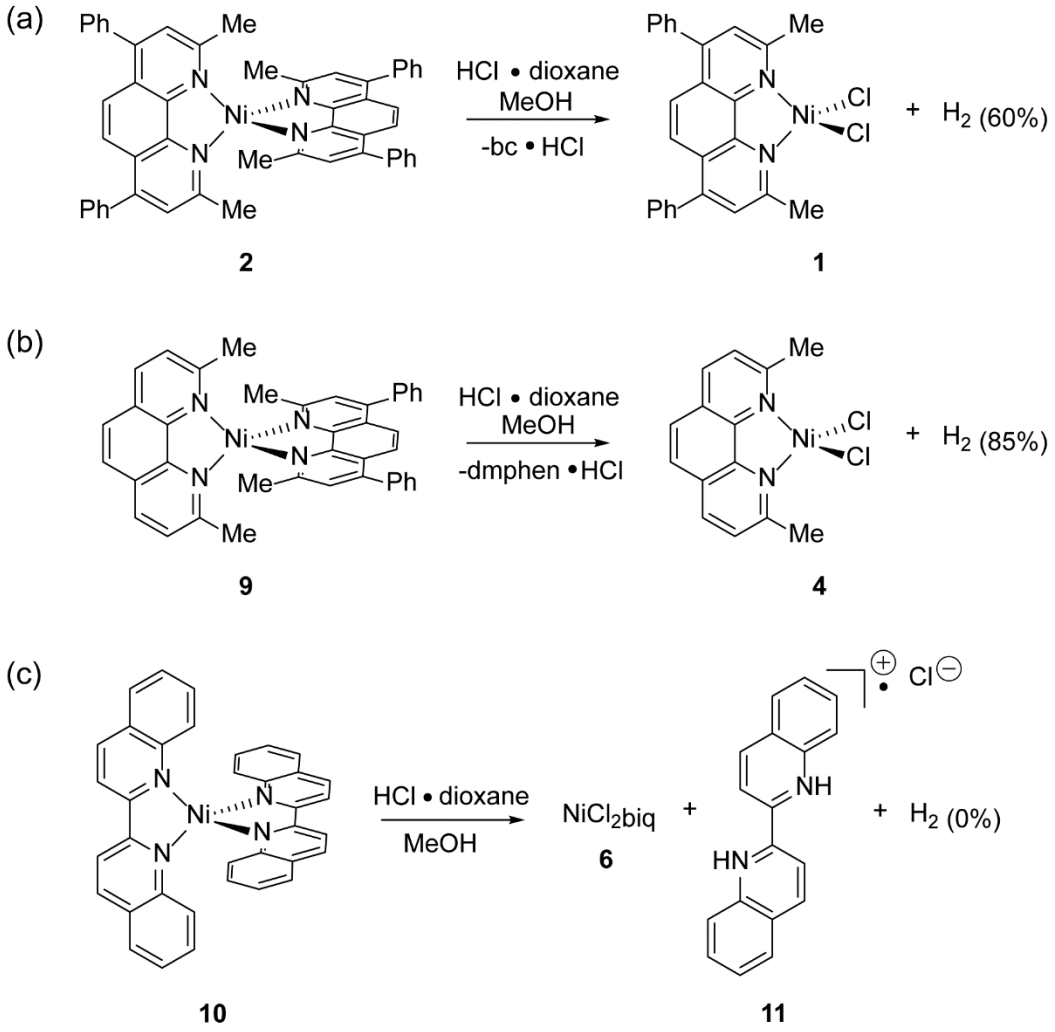

Figure 2.6. (a) Protonation of Ni(0) complex **2** affords Ni(II) chloride **1**, as well as H_2. (b) Protonation of Ni(0) complex **8** affords Ni(II) chloride **5**, together with pyridinyl radical **11**, but no H_2.

complex. While **1** is thermally stable to HCl, photolysis of **1** in the presence of protons leads to the loss of bathocuproine and <0.2 turnover of H_2 production.

The delicate thermodynamic balance required to achieve hydrogen production is manifest in the failure of complex **6** to generate detectable amounts of H_2. Whereas protonation of Ni(biq)$_2$ (**10**) generated Ni(II) complex **6**, no H_2 was observed. Instead of generating H_2, the reducing equivalents incipient in Ni(0) complex **10** promote the reduction of biq to afford pyridinyl radical **11**. Radical **11** could be directly prepared by sequential treatment of biq with K^0 and HCl. Neither thermolysis nor photolysis of **11** results in the generation of H_2. Attempts to isolate the product of one-electron reduction of phenanthroline derivatives, bathocuproine and dmphen, did not afford isolable products. In THF **6** undergoes reduction by the ligand radical K·biq to afforded Ni(0) complex **10** (Figure 2.7), demonstrating the ability of ligand radicals to directly reduce the Ni(II) complex.

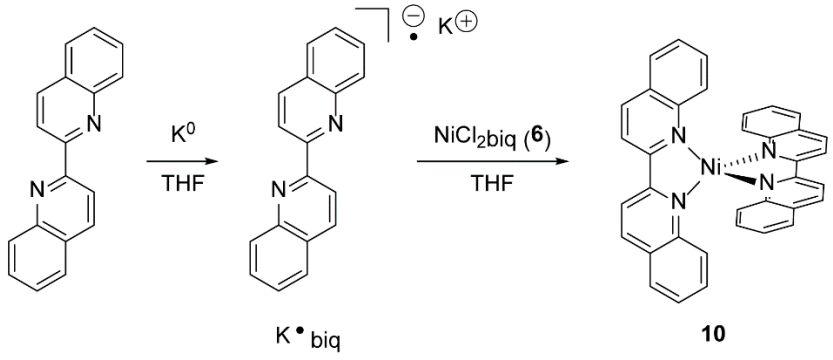

Figure 2.7. Treatment of Ni(II) complex **6** with stable ligand–radical K·biq affords Ni(0) complex **10**.

2.2.3 Time-Resolved Photochemical Experiments

In order to probe our contention that photogenerated pyridinyl radicals could mediate the requisite photoreduction chemistry, a nanosecond transient absorption (TA) spectrum of a solution of bathocuproine was recorded. The TA spectrum featured a growth centered at 526 nm (Figure 2.8a). We assign the transient species as ligand radical **12**, based on the TA spectra obtained upon flash photolysis of bipyridines, which also are ascribed to pyridinyl radicals generated by hydrogen-atom abstraction (HAA) reactions from solvent by electronically excited bipyridines.[15–18] The intensity of the TA signal at 526 nm is stronger in THF than in CH_3CN, and no TA signal is observed in hexane, consistent with the relative H-atom donor capacities of these solvents. Monitoring the decay of **12** at 526 nm provided a lifetime of 21.66 ± 0.43 μs (Figure 2.8b). The lifetime of **12** was diminished in the presence of Ni(II) complex **1**; a plot of τ_o/τ vs [**1**] is linear, consistent with Stern–Volmer kinetics and with a reaction between transient radical **12** and **1** (Figure 2.8b, inset). The calculated bimolecular rate constant of 3.0×10^9 M^{-1} s^{-1} is near the diffusion limit.[26]

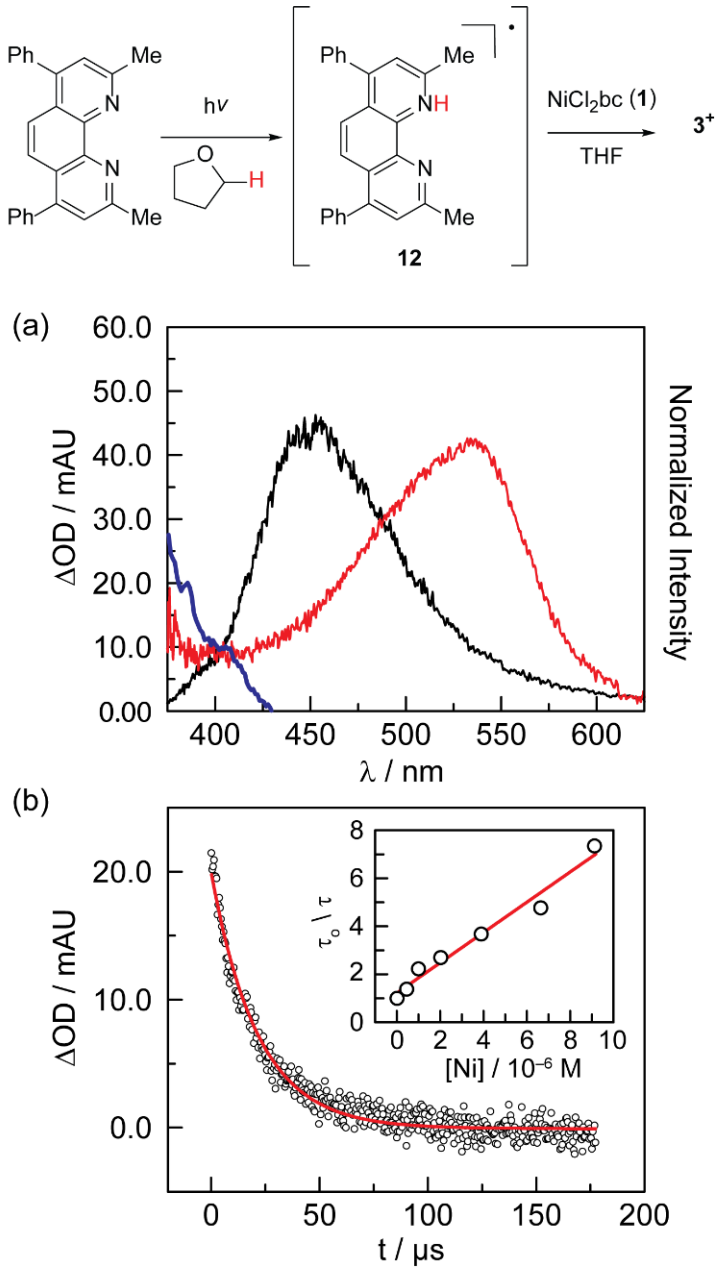

Figure 2.8. (a) Transient absorption spectrum (—, red) obtained by laser flash photolysis (355 nm pump) of a 1:1 THF/CH_3CN solution of bathocuproine, recorded at 40 ns delay: normalized absorption (—, blue) and emission (—, black) spectra of bathocuproine. (b) Single wavelength (526 nm) kinetic decay of transient intermediate. Inset: plot of τ_0/τ vs [**1**].

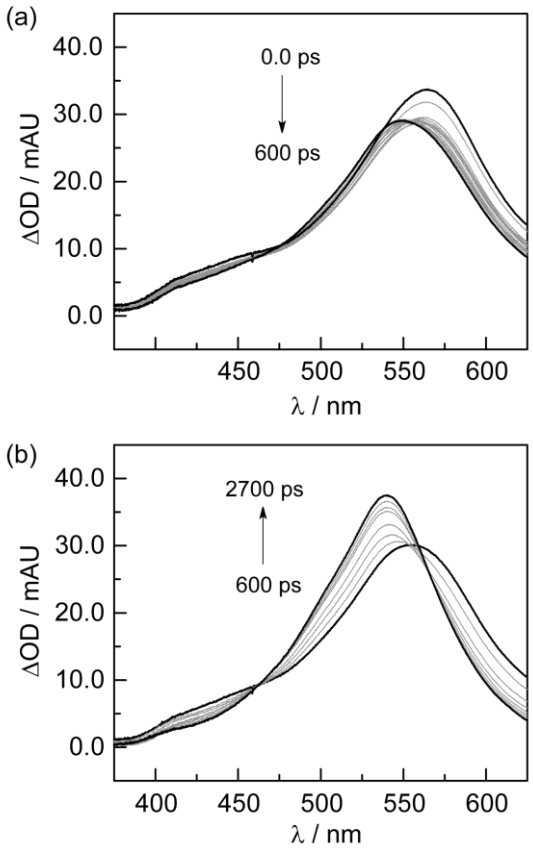

Figure 2.9. (a) Transient absorption spectra at early time points (0–600 ps) obtained by flash laser photolysis (315 nm pump) of bathocuproine (bc) in 1:1 THF:CH_3CN. Early time points show the conversion of ^{1}bc* to both ^{3}bc* and radical **12**. (b) Transient absorption spectra at later time points (600 – 2700 ps) obtained by flash laser photolysis (315 nm pump) of bathocuproine in 1:1 THF:CH_3CN. Late time points show the conversion of ^{3}bc* to radical **12**.

The dynamics of the photochemistry of bathocuproine (bc) were probed with ultrafast TA spectroscopy, which revealed two kinetic domains in the evolution of **12**. An initially formed signal, assigned as ^{1}bc* (λ_{max} = 565 nm), evolves without well-defined isosbestic points during the first 600 ps following the laser pulse. On the basis of analogy to ultrafast studies of 4,4′-bipyridine, we propose that this initial period involves both HAA by ^{1}bc* to

afford **12** and intersystem crossing to generate ^{3}bc* (Figure 2.9a).[15] Between 600 ps and 3 ns after the laser pulse, the observed TA spectrum evolves with tightly anchored isosbestic points consistent with the generation of **12** from ^{3}bc* (Figure 2.9b). In contrast to the relatively slow excited-state dynamics observed for bathocuproine, ultrafast TA spectra obtained by flash laser photolysis of Ni(II) complex **1** confirm the expectation of fast excited-state dynamics for first-row transition metal polypyridyls. A TA feature as 560 nm is observed for complex **1** and decays nearly to baseline within 15 ps of the laser pulse (Figure 2.10). Similar behavior was also observed for complexes **6** and **7**.

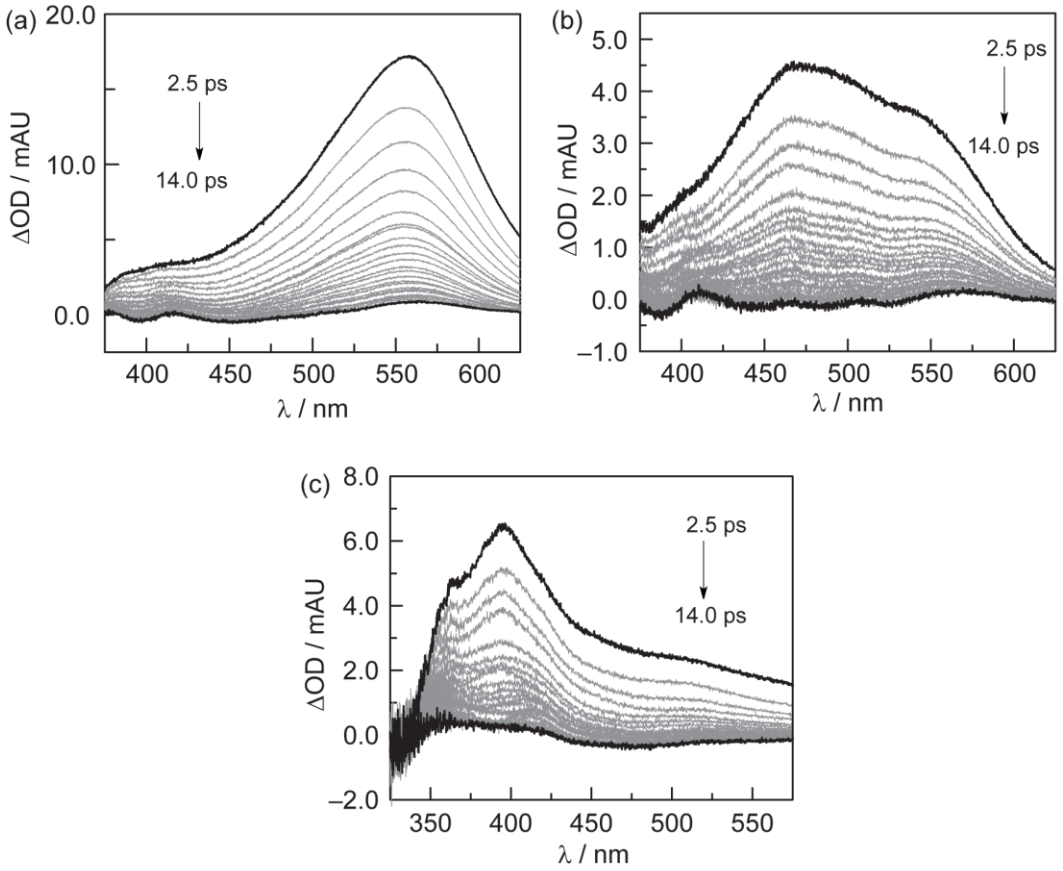

Figure 2.10. Ultrafast dynamics of laser flash photolysis of Ni(II) complexes (a) $NiCl_2$(bc) (**1**), (b) $NiCl_2$(dmphen) (**6**), (c) $NiCl_2$(dmbpy) (**7**). Samples were excited with 315 nm pulses in 1:1 THF:CH_3CN solution.

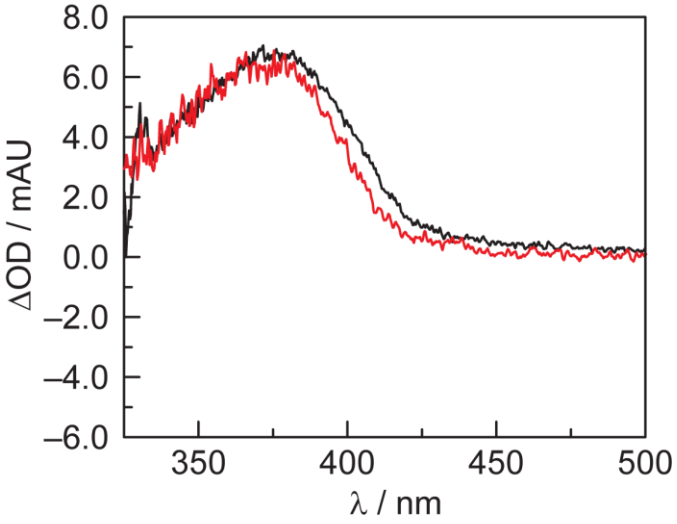

Figure 2.11. Transient absorption spectrum obtained by flash laser photolysis (310 nm pump) of dmbpy in THF (—, black) and hexanes (—, red). A TA spectrum, similar to the pictured spectrum in THF, was obtained for a 1:1 THF:CH_3CN solution of dmbpy.

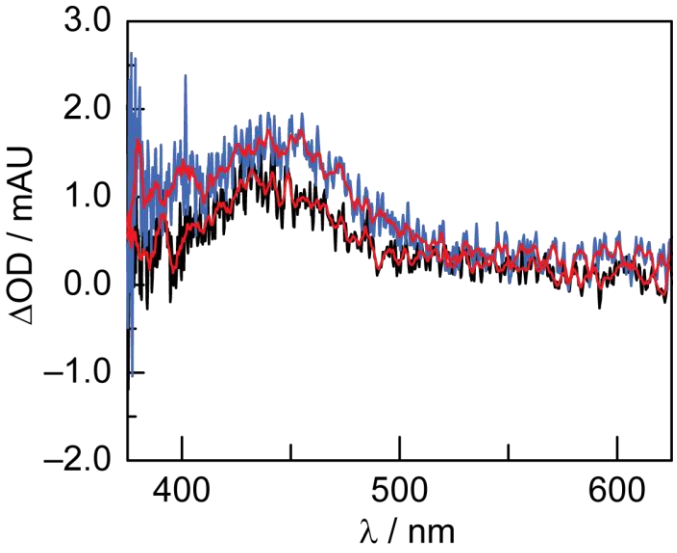

Figure 2.12. Transient absorption spectrum obtained by flash laser photolysis (310 nm pump) of dmphen in THF (—, black) and hexanes (—, blue). A TA spectrum, similar to the pictured spectrum in THF, was obtained for a 1:1 THF:CH_3CN solution of dmphen.

Nanosecond TA spectra were also obtained for dmphen and dmbpy. Flash laser photolysis of dmbpy revealed a feature centered at 370 nm (Figure 2.11). Unlike the TA spectrum of bathocuproine, the intensity of the observed feature in the TA spectrum of dmbpy did not display significant solvent dependence between THF and hexane. The lifetime of the transient species was quenched in the presence of Ni(II) complex **5**, but photoreduction was not observed. The TA spectrum of dmphen displays a feature centered at 440 nm (Figure 2.12), which correlates well to a reported spectrum of ^{3}phen*.[27] As in the case of bathocuproine and unlike dmbpy, the intensity of the dmphen TA feature at 440 nm does display solvent dependent intensity; the intensity in hexane is ~75% the intensity in THF.

2.3 Discussion

Thermal proton reduction by Ni(0) complexes sheds light on the ligand requirements of a HX photocycle. The thermal decomposition of **10** to **6** and **11** in the presence of HCl is non-productive owing the stability of the reduced biq radical. In contrast to **10**, protonation of **2** results in the generation of H_2 at 60% yield. Similar ligand reduction chemistry to **10** was not directly observed but may account for the non-quantitative generation of hydrogen by deleterious ligand radical processes as suggested by our inability to isolate reduced phenanthroline derivatives. This underscores the delicate balance that must be struck where sufficient driving force is necessary to reduce protons to H_2, yet excessive driving forces results in wasted energy and parasitic side phenomena.

Time resolved spectroscopy was employed to elucidate the underlying mechanism in the HX photocycle. Picosecond TA was used to confirm that the excited states of the Ni complexes are short lived and unlikely to be relevant to an HX photocycle. In contrast, the

picosecond TA of exogenous bathocuproine exhibits dynamics on both the picosecond and nanosecond timescales consistent with its known HAA photochemistry. Nanosecond TA was utilized to identify the intermediate photoproducts of the exogenous polypyridyl ligands and show that the excited states of bathocuproine and dimethyl-phenanthroline both display a solvent dependent ability to extract hydrogen atoms. Unlike in the case of bathocuproine and dimethyl-phenanthroline, the intensity of the observed feature in the TA spectrum of dmbpy does not display significant solvent dependence between THF and hexane. This observation, coupled with the similarity of the observed TA signal to a reported TA spectrum of the long-lived triplet excited state of 2,2′-bipyridine,[16] suggests that the observed TA spectrum arises from ^{3}dmbpy*, not a pyridinyl radical. The quenching of the lifetime of ^{3}dmbpy* by Ni(II) complex **5** without an observable reduction of Ni complex and our inability to detect H_2 in photolysis experiments suggest the method of quenching may be triplet–triplet annihilation to generate a fast relaxing Ni excited state.

H_2 generation of in steady state photolysis experiments showed a strong dependence on the ability of the exogenous photoredox mediator to obtain reducing equivalents from solvent: only the complexes composed of the H-atom abstracting ligands dimethyl-phenanthroline and bathocuproine were productive and only in the presence of weak C–H bonds. The combined observations of the radical nature of the ground state Ni(0) complexes, TA observation of HAA photoproducts, and solvent dependent photolysis show that pyridinyl radicals are key intermediates in the generation of H_2 in the complexes studied in this work. This underscores the critical role of the ligand to serve as both a multi-electron redox sink in the Ni complexes and as a photoredox mediator.

2.4 Conclusion

Photocycles for H_2 evolution from HCl require management of multiproton coupled electron transfer reaction (multi-PCET) events. HX-splitting photocatalysis has been achieved by taking advantage of the propensity of second- and third-row transition metals to participate in two-electron reactions. Similar HX-splitting photocycles have not been developed with first-row transition metal complexes. In addition to the facility of one-electron processes at first-row transition metal complexes, extremely short charge-separated state lifetimes are a challenge that needs to be addressed in order to achieve controlled multi-PCET photoreduction reactions. To address the problem of short charge-separated state lifetimes, we have utilized photoredox mediators such that the excited state properties can be independently tuned. Reduction of protons was achieved using a series of Ni complexes with a propensity for disproportionation to enforce the requisite multi-electron redox chemistry necessary for H_2 evolution.

We targeted bipyridines as photoredox mediators for the reduction of Ni(II) complexes on the expectation that bipyridine excited states could participate in HAA reactions to generate the requisite reducing pyridinyl radicals. Following this strategy, we have defined the photocycle shown in Figure 2.13 for photogeneration of H_2 mediated by earth-abundant Ni complexes. Ni(II) complex **1**, supported by a bathocuproine ligand, undergoes solvent-dependent photoreduction to either Ni(I) complexes (**3**$^+$) or Ni(0) complexes (**2**). Selectivity between one- and two- electron photoreduction was determined to arise from solvent-dependent chloride-ion-induced disproportionation. The proposed role of bipyridine as a photoredox mediator was probed via a series of TA experiments. The excited state lifetimes of Ni(II) complexes **1**, **6**, and **7** were found to be extremely short;

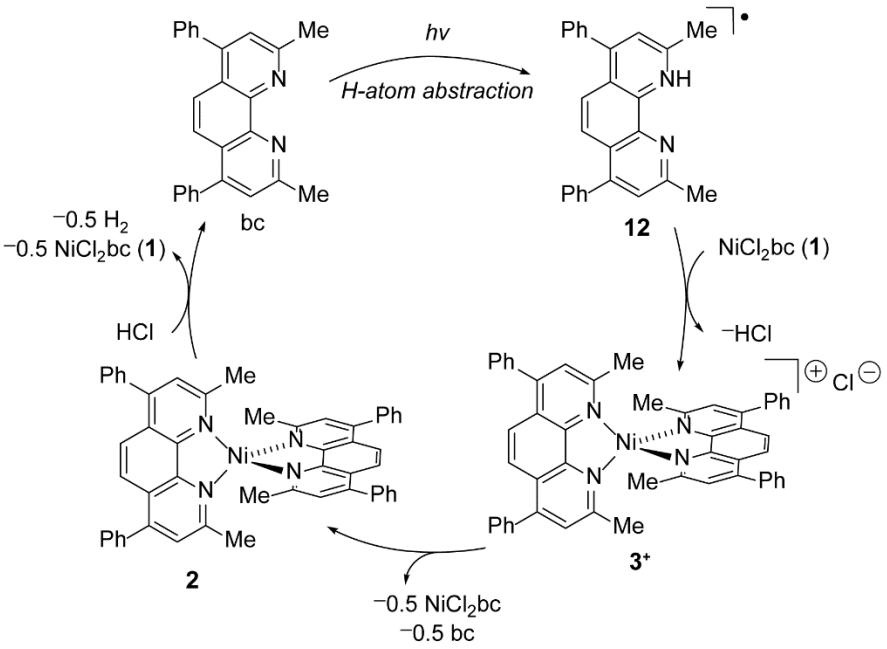

Figure 2.13. H_2-evolution cycle based on bipyridine photoredox chemistry.

ultrafast measurements revealed excited states that decay to baseline in 15 ps. Laser flash photolysis of free bathocuproine revealed the presence of a long-lived photogenerated intermediate, assigned to pyridinyl radical **12** based on solvent-dependent yields of **12** as well as on comparison of the TA spectrum of bathocuproine to previously reported TA spectra of similar bipyridines. Monitoring the lifetime of pyridinyl radical **12** as a function of [**1**] revealed that the lifetime of radical **12** is quenched by Ni(II) complex **1**. We have directly verified the viability of free ligand radicals to mediate Ni-centered reduction by treatment of Ni(II) complex **6** with K·biq, which results in the observation of Ni(0) complex **10**. A closed photocycle for H_2 evolution is thus established by protonation of photogenerated Ni(0) complex **2** with HCl, which generates **1** and H_2. These results presented herein thus demonstrate the feasibility of utilizing first-row transition metal complexes to couple multiple photoreduction reactions with H_2-evolving proton reduction.

Further work is needed to address the halide oxidizing half reaction in order to form a complete photo-catalytic H–X splitting cycle.

2.5 Experimental

Synthesis, characterization, thermally promoted reactions, and steady state photochemistry was performed by Prof. David C. Powers.

General Considerations

All reactions were carried out in an N_2- filled glovebox. Anhydrous solvents were obtained by filtration through drying columns.[28] $NiCl_2$dme (dme = 1,2-dimethoxyethane) and $Ni(cod)_2$ (cod = 1,5-cyclooctadiene) were obtained from Strem Chemicals, while 2,9-dimethyl-4,7-diphenyl-1,10-phenanthroline (bathocuproine), 2,9-dimethyl-1,10-phenanthroline (dmphen), 6,6′-dimethyl-2,2′-bipyridine (dmbpy), and 2,2′-biquinoline were obtained from Sigma Aldrich. All chemicals were used without purification. $NiCl_2$dmphen (**4**),[29] $NiCl_2$biq (**6**),[29] and $Ni(dmphen)_2$ (**9**) [30] were prepared according to literature procedures.

Physical Methods

NMR spectra were recorded at the Harvard University Department of Chemistry and Chemical Biology NMR facility on a Varian Unity/Inova 500 spectrometer operating at 500 MHz for ^1H acquisitions. NMR chemical shifts are reported in ppm with the residual solvent resonance as internal standard. UV–vis spectra were recorded at 293 K in quartz cuvettes on a Spectral Instruments 400 series diode array and were blanked against the appropriate solvent. Solution magnetic moments were determined using the Evans method[31] in 1:1 THF/CH_3CN and measured using ^{19}F NMR (hexafluorobenzene added); diamagnetic

corrections were estimated from Pascal constants.[32] Perpendicular mode X-band EPR spectra were recorded on Bruker ElexSys E500 EPR equipped with an N_2 dewer for measurements at 77 K. EPR spectra were referenced to diphenylpicrylhydrazyl, DPPH (g = 2.0037). Spectra were simulated using EasySpin 4.5.0 implemented with MATLAB to obtain g-values. EPR spectra of [**3**]OTf were collected in both 2-methyltetrahydrofuran (2-MeTHF) and 9:1 EtOH/MeOH, and the observed features showed no solvent dependence. Steady-state emission spectra were recorded on an automated Photon Technology International (PTI) QM 4 fluorimeter equipped with a 150 W Xe arc lamp and a Hamamatsu R928 photomultiplier tube. H_2 yields were determined by GC analysis and confirmed by independent Toepler pump combustion analysis.

Photolysis of Ni Complexes

Steady-state photochemical reactions were performed using a 1000 W high-pressure Hg/Xe arc lamp (Oriel), and the beam was passed through a water-jacketed filter holder containing the appropriate long- pass filter, an iris, and a collimating lens.

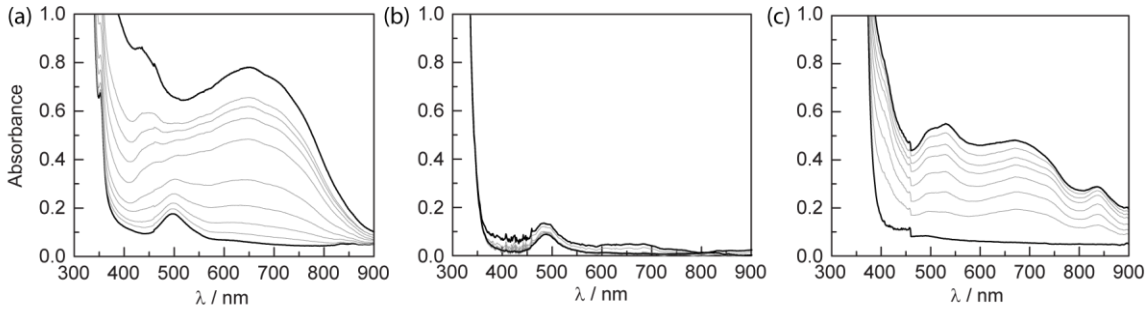

Figure 2.14. (a) Spectral evolution from photolysis of $NiCl_2$dmphen (**4**) in over 53 min of photolysis; the time interval between spectra was not constant. (b) Spectral evolution from photolysis of $NiCl_2$dmbpy (**5**) obtained at 10 min intervals over 60 min of photolysis. In addition, no photoreduction was observed when photolysis of **5** was carried out without a long-pass filter. (c) Spectral evolution from photolysis of $NiCl_2$biq (**6**) obtained at 2 min intervals over 14 min of photolysis. Conditions: 1:1 THF:CH_3CN with a 305 nm long-pass filter.

Nanosecond Transient Absorption

Nanosecond transient absorption (TA) measurements were made at 10 Hz with the pump light provided by the third harmonic (355 nm) of a Quanta-Ray Nd:YAG laser (Spectra-Physics) or with 310 nm light generated from the frequency doubled 620 nm signal of a Spectra-Physics Quanta-Ray MOPO-700 with FDO-970 option pumped with the 355 nm light from the aforementioned laser. The signal light passed through a Triax 320 spectrometer, where it was dispersed by a 300 groove/mm × 250 nm blazed grating and collected with either an intensified gated CCD camera (ICCD, CCD 30-11, Andor Technology, 1024 × 256 pixels, 26 μm^2) for TA spectra or a photomultiplier tube (PMT) for TA single-wavelength kinetics. PMT outputs were collected and averaged with a 1 GHz oscilloscope (LeCroy 9384CM). A TTL pulse synchronized with the Q-switch of the Infinity laser was delayed 99 ms before triggering the shutter for the probe light. Electronic delays were created with SRS DG535 delay generators (Stanford Research Systems). These delay boxes,

in combination with electronic shutters (Uniblitz), were used to create the necessary pulse sequence. Samples were prepared in 50 mL Schlenk flasks in an N_2-filled glovebox. Solutions were flowed through a 3 mm diameter, 1 cm path length flow cell (Starna, type 585.2) using a peristaltic pump and positive argon pressure.

Picosecond Transient Spectroscopy

Picosecond transient spectroscopy was performed on a home-built system built around a Coherent Libra HE Ti: Sapphire Amplifier System. The Libra HE incorporates a Coherent Vitesse oscillator that serves as the seed laser for the system. The Vitesse includes the mode-locked Ti:Sapphire oscillator cavity pumped by a Coherent Verdi, a continuous-wave diode-pumped green laser. The Libra system also includes a Coherent Evolution diode pump second harmonic Q-switched laser. The Evolution operates at a 1 kHz rate and provides the pump power to the amplifier module. The Libra-HE has an average output power of 3.5 W and a pulse width of 50 fs. 99.5% of the 800 nm output wavelength is directed into a Coherent OPerA SOLO optical parametric amplifier (OPA) with the remainder being focused into a calcium fluoride (CaF_2) substrate for continuum generation. The majority of the 800 nm beam is used to generate the pump beam in the OPA. Time resolution was achieved by propagating the excitation beam along a computer-controlled 1.70 m optical delay line with 1 μm precision (Aerotech ATS 62150). The pump and probe beams were focused collinearly at the continuously stirred sample with beam diameters of ~500 μm and ~250 μm respectively. The power of λ_{exc} was kept between 1-2μJ/pulse at the sample. Laser power was measured using either a Coherent J-25MB-HE meter coupled to a Coherent Labmax Top or an Ophir Laser Measurement Group ORION/PD Power Meter (PD300-UV-SIR-ROITS) fitted with an ORION head (#572775). Transient absorption (TA)

spectra were recorded at discrete times after excitation with 315 nm pump pulses. The spectrum was then resolved in the monochromator (ISA Instruments, TRIAX 320). For both full spectrum and single wavelength kinetic measurements, signal light entering the spectrometer was dispersed by a 300 × 500 blazed grating onto a Princeton Instruments PIXIS 100B CCD camera calibrated using a mercury argon pen lamp. Resulting spectra were averages of three replicates of 2000 sequences consisting of the four combinations of pump and probe used to correct for ambient and emissive signals for each time point, averaged together. Single wavelength kinetics where obtained by averaging 20 nm spectral windows about the wavelength of interest for each time point. In house developed software written in Python was used for acquisition control.

Preparation of Ni(II) Complexes ($LNiCl_2$)

Complex **1**. To a suspension of $NiCl_2$(dme) (181 mg, 8.23×10^{-4} mol, 1.00 equiv) in THF was added bathocuproine (297 mg, 8.23×10^{-4} mol, 1.00 equiv) as a solid. The mixture was stirred at 23 °C for 10 h, during which time a pink precipitate was observed. The mixture was concentrated to dryness and the residue was washed with THF and dried in vacuo to afford 403 mg of the title complex as a pink solid (96% yield). ^{1}H NMR (500 MHz, THF-d_8) δ (ppm): 80.05 (s, 2H), 28.12 (s, 2H), 18.5 (br s, 6H), 9.61(d,J=7.3Hz,4H),8.81(t,J=7.3Hz,2H),7.19(dd,J=7.3Hz, J = 7.3 Hz, 4H). μ_{eff} = 3.59 μB. Crystals suitable for single-crystal diffraction analysis were obtained by slow evaporation of a concentrated MeOH solution of the complex.

Complex **5** was prepared analogously: 97% yield. ^{1}H NMR (500 MHz, THF-d_8) δ (ppm): 77.3 (br s, 2H), 63.41 (s, 2H), 27.7 (br s, 6H), 23.07 (s, 2H). μ_{eff} = 3.57 μB. Crystals suitable

for single-crystal diffraction analysis were obtained by slow evaporation of a MeOH solution of the complex.

Preparation of Ni(0) Complexes (L_2Ni).

Complex **2**. To a suspension of $Ni(cod)_2$ (70.0 mg, 2.54×10^{-4} mol, 1.00 equiv) in THF was added bathocuproine (93.8 mg, 5.09×10^{-4} mol, 2.00 equiv) as a solid. The reaction mixture was warmed to 60 °C, at which temperature it was stirred for 12 h. The reaction mixture turned from a pale yellow suspension to an inky purple solution during the course of heating. The reaction mixture was filtered through Celite. The Celite was washed with THF, the filtrate was combined, and solvent was removed in vacuo to afford 184 mg of 6 as an air-sensitive dark purple solid (93% yield). ^{1}H NMR (500 MHz, C_6D_6) δ (ppm): 7.95 (s, 4H), 7.85 (s,4H),7.65(d,J=7.3Hz,8H),7.36(t,J=7.3Hz,4H),7.18(dd,J= 7.8 Hz, J = 7.8 Hz, 8H), 2.48 (s, 12H). Crystals suitable for single- crystal diffraction analysis were obtained from a THF solution of the complex layered with $PhCH_3$.

Complex **10** was prepared analogously: 81% yield. ^{1}H NMR (500 MHz, benzene-d6) δ (ppm): 10.22 (d, J = 8.3 Hz, 4H), 9.19 (d, J = 8.8 Hz, 4H), 7.56 (d, J = 7.8 Hz, 4H), 7.29 (t, J = 7.3 Hz, 4H), 7.15 (overlap with solvent signal, 4H), 6.80 (d, J = 8.8 Hz, 4H). Crystals suitable for single-crystal diffraction analysis were obtained from a THF solution of the complex layered with $PhCH_3$.

Preparation of Ni(I) Complexes ($L2Ni^+X^-$)

Complex [**3**]OTf. To a solution of $Ni(bathocuproine)_2$ (**6**) (59.0 mg, 7.57×10^{-5} mol, 1.00 equiv) in THF was added AgOTf (19.5 mg, 7.57×10^{-5} mol, 1.00 equiv) as a suspension in THF. The reaction solution immediately turned from dark purple to blue. The reaction

mixture was stirred at 23 °C for 30 min before being filtered through Celite. The filtrate was concentrated in vacuo and the residue was taken up in 1:1 THF/pentane. Complex [**3**]OTf was isolated by filtration to afford 55.1 mg of an air-sensitive dark blue solid (80% yield). ^{1}H NMR (500 MHz, THF-d_8) δ (ppm): 33.8 (br s, 4H), 12.51 (s, 4H), 8.00−7.96 (m, 12H), 7.07 (s, 8H), 0.8 (br s, 12H). EPR (9:1 EtOH/MeOH) g-value: g_1 = 2.4524; g_2 = 2.2039; g_3 = 2.1655. μ_{eff} = 2.46 μB.

Complexes [**7**]PF_6 and [**8**]ClO_4 were prepared analogously to complex **3**. Complex [**7**]PF_6: 82% yield. ^{1}H NMR (500 MHz, CD_3CN) δ (ppm): 33.0 (br s, 4H), 13.3 (s, 4H), 11.6 (br s, 4H), 0.4 (br s, 12H). μ_{eff} = 2.53 μB. EPR (9:1 EtOH:MeOH) g-value: g_1 = 2.4616; g_2 = 2.2004; g_3 = 2.1626. Crystals suitable for single-crystal diffraction analysis were obtained from a MeOH solution of the complex. Complex [**8**]ClO_4: 74% yield. ^{1}H NMR (500 MHz, CD_3CN) δ (ppm): 20.4 (br s, 4H), 19.7−19.4 (m, 12H), 10.7 (br s, 4H), 8.0 (s, 4H). Crystals suitable for single-crystal diffraction analysis were obtained from a MeOH solution of the complex.

Preparation of K·biq. To a solution of biq (250 mg, 9.72 × 10^{-4} mol, 1.00 equiv) in THF was added potassium (38.0 mg, 9.72 × 10^{-4} mol, 1.00 equiv) as a solid. The reaction mixture was stirred at 23 °C for 4 h, during which time the reaction mixture assumed a dark red- brown color. The reaction mixture was filtered through Celite and the filtrate was concentrated in vacuo to afford 55.1 mg of the title complex as an air-sensitive dark red-brown solid (94% yield). Treatment of K·biq with HCl·dioxane in THF results in immediate color change of the reaction solutions from red-brown to green. Removal of solvent in vacuo affords **11** as a green solid (71%). Crystals suitable for single-crystal diffraction analysis were obtained from a THF solution of the compound.

X-ray Crystallographic Details

All structures were collected on a Bruker three-circle platform goniometer equipped with an Apex II CCD and an Oxford cryostream cooling device at 100 K. Radiation was generated from a graphite fine focus sealed tube Mo Kα (0.710 73 Å) source. Crystals were mounted on a cryoloop or glass fiber pin using Paratone N oil. Data were integrated using SAINT and scaled with either a numerical or multiscan absorption correction using SADABS. The structures were solved by direct methods using SHELXS-97 and refined against F^2 on all data by full matrix least- squares with SHELXL-97. All non-hydrogen atoms were refined anisotropically. Hydrogen atoms were placed at idealized positions and refined using a riding model. Crystal data and refinement statistics are summarized in Table 2.1.

Table 2.1. Crystal data and structure refinement.

	1	**2**•THF	[**3**]OTf •3THF	[**7**]PF_6	[8]ClO_4•bc	**10**•0.5 PhH	**11**•THF
formula	$C_{26}H_{20}Cl_2N_2Ni$	$C_{56}H_{48}N_4NiO$	$C_{65}H_{64}F_3N_4NiO_6S$	$C_{28}H_{24}F_6N_4NiP$	$C_{54}H_{36}ClN_6NiO_4$	$C_{39}H_{27}N_4Ni$	$C_{22}H_{21}ClN_2O$
fw, g/mol	490.06	851.70	1144.98	620.19	927.04	610.35	364.86
temperature, K	100(2)	110(2)	110(2)	100(2)	100(2)	100(2)	100(2)
cryst system	monoclinic	monoclinic	monoclinic	triclinic	monoclinic	triclinic	triclinic
space group	*P2₁/c*	*P2₁/n*	*P2₁/c*	*P–1*	*P₂/n*	*P–1*	*P–1*
color	pink	purple	blue	red-black	purple	blue-green	green
a, Å	13.0496(9)	18.007(3)	17.4078(4)	10.590(3)	13.6604(9)	13.4506(6)	8.6703(15)
b, Å	21.9451(15)	11.3520(17)	11.0915(2)	10.945(3)	11.1003(7)	14.7269(6)	13.872(2)
c, Å	7.8238 (6)	21.176(3)	29.2364(6)	11.849(3)	13.7705(9)	15.8071(7)	15.823(3)
α, deg	90	90	90	76.804(4)	90	88.800(1)	77.753(3)
β, deg	104.450(1)	96.196(3)	90.371(1)	77.027(4)	98.787(1)	67.020(1)	81.643(3)
γ, deg	90	90	90	77.385(4)	90	88.659(1)	75.191(3)
V, A^3	2169.7(3)	4303.3(11)	5644.8(2)	1282.6(6)	2063.4(2)	2881.6(2)	1789.7(5)
Z	4	4	6	2	4	6	2
R1[a]	0.039	0.057	0.052	0.085	0.033	0.039	0.071
wR2[b]	0.098	0.170	0.127	0.277	0.084	0.084	0.187
GOF (F^2)	0.87	1.07	1.05	1.05	1.05	1.02	1.05

[a] $R1 = \Sigma||F_o| - |F_c||/\Sigma|F_o|$. [b] $wR2 = (\Sigma(w(F_o^2 - F_c^2)^2)/\Sigma(w(F_o^2)^2))^{1/2}$. [c] GOF $= (\Sigma w(F_o^2 - F_c^2)^2/(n - p))^{1/2}$ where n is the number of data and p is the number of parameters refined.

2.6 References

1. Yang, Z.; Zhang, J.; Kintner-Meyer, M. C. W.; Lu, X.; Choi, D.; Lemmon, J. P.; Liu, J. Electrochemical Energy Storage for Green Grid. *Chem. Rev.* **2011**, *111* (5), 3577–3613.

2. Esswein, A. J.; Nocera, D. G. Hydrogen Production by Molecular Photocatalysis. *Chem. Rev.* **2007**, *107* (10), 4022–4047.

3. Nocera, D. G. Chemistry of Personalized Solar Energy. *Inorg. Chem.* **2009**, *48* (21), 10001–10017.

4. McCusker, J. K. Femtosecond Absorption Spectroscopy of Transition Metal Charge-Transfer Complexes. *Acc. Chem. Res.* **2003**, *36* (12), 876–887.

5. Juban, E. A.; Smeigh, A. L.; Monat, J. E.; McCusker, J. K. Ultrafast Dynamics of Ligand-Field Excited States. *Coordination Chemistry Reviews* **2006**, *250* (13–14), 1783–1791.

6. Creutz, C.; Chou, M.; Netzel, T. L.; Okumura, M.; Sutin, N. Lifetimes, Spectra, and Quenching of the Excited States of Polypyridine Complexes of iron(II), ruthenium(II), and osmium(II). *J. Am. Chem. Soc.* **1980**, *102* (4), 1309–1319.

7. Monat, J. E.; McCusker, J. K. Femtosecond Excited-State Dynamics of an Iron(II) Polypyridyl Solar Cell Sensitizer Model. *J. Am. Chem. Soc.* **2000**, *122* (17), 4092–4097.

8. Ferrere, S.; Gregg, B. A. Photosensitization of TiO_2 by [FeII(2,2'-Bipyridine-4,4'-Dicarboxylic acid)$_2$(CN)$_2$]: Band Selective Electron Injection from Ultra-Short-Lived Excited States. *J. Am. Chem. Soc.* **1998**, *120* (4), 843–844.

9. Caspar, J. V.; Meyer, T. J. Photochemistry of tris(2,2'-bipyridine)ruthenium(2+) Ion ($Ru(bpy)_3^{2+}$). Solvent Effects. *J. Am. Chem. Soc.* **1983**, *105* (17), 5583–5590.

10. Kavarnos, G. J.; Turro, N. J. Photosensitization by Reversible Electron Transfer: Theories, Experimental Evidence, and Examples. *Chem. Rev.* **1986**, *86* (2), 401–449.

11. Damrauer, N. H.; Weldon, B. T.; McCusker, J. K. Theoretical Studies of Steric Effects on Intraligand Electron Delocalization: Implications for the Temporal Evolution of MLCT Excited States. *J. Phys. Chem. A* **1998**, *102* (19), 3382–3397.

12. Seshadri, G.; Lin, C.; Bocarsly, A. B. A New Homogeneous Electrocatalyst for the Reduction of Carbon Dioxide to Methanol at Low Overpotential. *Journal of Electroanalytical Chemistry* **1994**, *372* (1–2), 145–150.

13. Barton, E. E.; Rampulla, D. M.; Bocarsly, A. B. Selective Solar-Driven Reduction of CO2 to Methanol Using a Catalyzed P-GaP Based Photoelectrochemical Cell. *J. Am. Chem. Soc.* **2008**, *130* (20), 6342–6344.

14. Barton Cole, E.; Lakkaraju, P. S.; Rampulla, D. M.; Morris, A. J.; Abelev, E.; Bocarsly, A. B. Using a One-Electron Shuttle for the Multielectron Reduction of CO_2 to Methanol: Kinetic, Mechanistic, and Structural Insights. *J. Am. Chem. Soc.* **2010**, *132* (33), 11539–11551.

15. Buntinx, G.; Naskrecki, R.; Poizat, O. Subpicosecond Transient Absorption Analysis of the Photophysics of 2,2‘-Bipyridine and 4,4‘-Bipyridine in Solution. *J. Phys. Chem.* **1996**, *100* (50), 19380–19388.

16. Poizat, O.; Buntinx, G.; Valat, P.; Wintgens, V.; Bridoux, M. Photochemistry of 4,4’-Bipyridine: Nanosecond Absorption and Raman Study of the Hydrogen Atom Abstraction from Methanol and 2-Propanol. *J. Phys. Chem.* **1993**, *97* (22), 5905–5910.

17. Castellà-Ventura, M.; Kassab, E.; Buntinx, G.; Poizat, O. Structure of the Anion Radical of 2,2′-Bipyridine in Solution. *Phys. Chem. Chem. Phys.* **2000**, *2* (20), 4682–4689.

18. Enomoto, K.; LaVerne, J. A. Reactions of Hydrated Electrons with Pyridinium Salts in Aqueous Solutions. *J. Phys. Chem. A* **2008**, *112* (48), 12430–12436.

19. Benson, E. E.; Rheingold, A. L.; Kubiak, C. P. Synthesis and Characterization of 6,6′-(2,4,6-Triisopropylphenyl)-2,2′-Bipyridine (tripbipy) and Its Complexes of the Late First Row Transition Metals. *Inorg. Chem.* **2010**, *49* (4), 1458–1464.

20. Donoghue, J. T.; Drago, R. S. Non-Aqueous Coordination Phenomena-Complexes of Hexamethylphosphoramide. I. Preparation and Properties of Tetrahedral $[Zn\{PO[N(CH_3)_2]_3\}_4]^{+2}$, $[Co\{PO[N(CH_3)_2]_3\}_4]^{+2}$,and $[Ni\{PO[N(CH_3)_2]_3\}_4]^{+2}$ Compounds. *Inorg. Chem.* **1962**, *1* (4), 866–872.

21. Drago, R. S. *Phyiscal Methods for Chemists*, 2nd ed.; Surfside Scientific Publishers: Gainesville, FL, 1992; p 422.

22. Cotton, F. A.; Wilkinson, G.; Murillo, C. A.; Bochmann, M. *Advanced Inorganic Chemistry*, 6th ed.; Wiley: New York, 1999; p 840.

23. Scarborough, C. C.; Sproules, S.; Weyhermüller, T.; DeBeer, S.; Wieghardt, K. Electronic and Molecular Structures of the Members of the Electron Transfer Series $[Cr(^t bpy)_3]^n$ (n = 3+, 2+, 1+, 0): An X-Ray Absorption Spectroscopic and Density Functional Theoretical Study. *Inorg. Chem.* **2011**, *50* (24), 12446–12462.

24. Tokel-Takvoryan, N. E.; Hemingway, R. E.; Bard, A. J. Electrogenerated Chemiluminescence. XIII. Electrochemical and Electrogenerated Chemiluminescence Studies of Ruthenium Chelates. *J. Am. Chem. Soc.* **1973**, *95* (20), 6582–6589.

25. Krishnan, C. V.; Creutz, C.; Schwarz, H. A.; Sutin, N. Reduction Potentials for 2,2'-Bipyridine and 1,10-Phenanthroline Couples in Aqueous Solutions. *J. Am. Chem. Soc.* **1983**, *105* (17), 5617–5623.

26. Turro, N. J. *Modern Molecular Photochemistry*; University Science Books: Sausalito, CA, 1991; p 314.

27. Bandyopadhyay, B. N.; Harriman, A. Photoreduction of 1,10-phenanthroline. *J. Chem. Soc. Faraday Trans.* **1976**, *73*, 663–674.

28. Pangborn, A. B.; Giardello, M. A.; Grubbs, R. H.; Rosen, R. K.; Timmers, F. J. Safe and Convenient Procedure for Solvent Purification. *Organometallics* **1996**, *15* (5), 1518–1520.

29. Butcher, R. J.; Sinn, E. Synthesis and Relation between Magnetic and Structural Properties of a Series of Monomeric and Dimeric nickel(II) Complexes. Crystal and Molecular Structures of $[Ni(biq)Cl_2]_2$, $Ni(biq)Br_2$, $[Ni(dmp)Cl_2]_2$, $[Ni(dmp)Br_2]_2$ and $Ni(bc)I_2$. *Inorg. Chem.* **1977**, *16* (9), 2334–2343.

30. Fischer, R.; Langer, J.; Malassa, A.; Walther, D.; Görls, H.; Vaughan, G. A Key Step in the Formation of Acrylic Acid from CO_2 and Ethylene: The Transformation of a Nickelalactone into a Nickel-Acrylate Complex. *Chem. Commun.* **2006**, No. 23, 2510–2512.

31. Evans, D. F. 400. The Determination of the Paramagnetic Susceptibility of Substances in Solution by Nuclear Magnetic Resonance. *J. Chem. Soc.* **1959**, No. 0, 2003–2005.

32. Bain, G. A.; Berry, J. F. Diamagnetic Corrections and Pascal's Constants. *J. Chem. Educ.* **2008**, *85* (4), 532.

Chapter 3: Spectroscopic Observation of Secondary Coordination Sphere Effects in Halogen Photoelimination

Portions of this chapter have been published:

3.1 Introduction

Energy storage and conversion hinges upon efficient activation of small molecules. Multi-electron/multi-proton transformations such as H_2 and H_2O oxidations and H^+, O_2, and CO_2 reductions, are all examples of small molecule activation. The development of catalysts to effectively mediate these energy conversion transformations relies on the ability of the secondary coordination sphere to carefully choreograph proton and electron delivery.[1,2] For example, biological H_2 oxidation in Fe-only hydrogenase is accomplished via cooperation of second-coordination sphere bases, which enforce selective heterolytic cleavage of H_2 (Figure 3.1a).[3–5] Similarly, installation of biomimetic proton relays in the secondary-coordination sphere of transition metal complexes has emerged as a powerfully enabling design element for the development of selective catalysts based on earth-

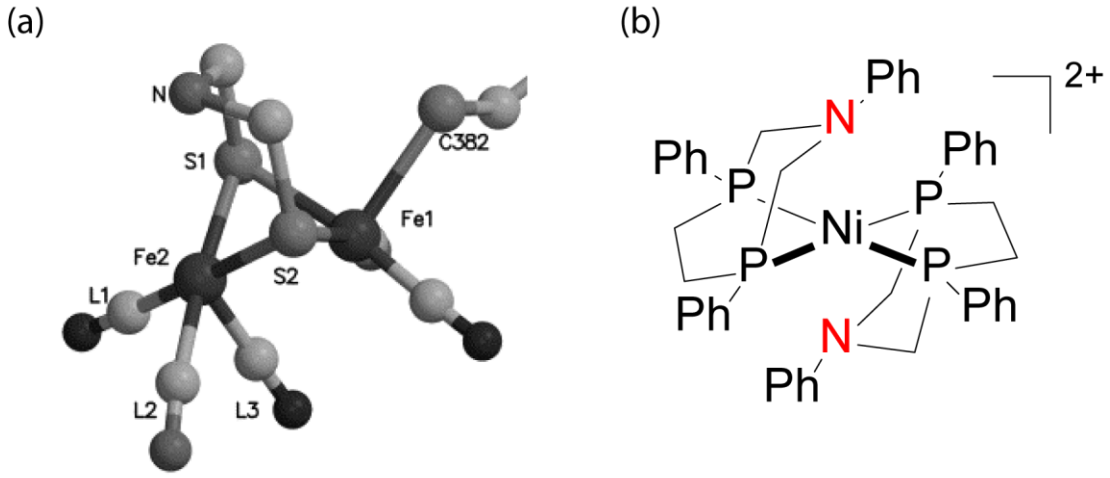

Figure 3.1. The active site of DdHase (a) exhibits a pendant base to facilitate the heterolytic cleavage of H_2. Synthetic catalysts (b) mimic the secondary coordination sphere of hydrogenase for H_2 activation.[6,7] Part (a) Reprinted from Journal of Inorganic Biochemistry, 91, Nicolet, Y.; Cavazza, C.; Fontecilla-Camps, J. C., Fe-only hydrogenases: structure, function and evolution, 1–8, Copyright 2002, with permission from Elsevier.

abundant first-row transition elements.[8] Introduction of basic functionality, as either pendant carboxylates (i.e. hangman porphyrin Figure 3.2a)[9–11] or tertiary amines (i.e. hydrogenase mimic Figure 3.1b),[6,7] in the secondary coordination sphere of electrocatalysts allows controllable coupling of proton and electron delivery to substrates during electrocatalysis. H-bonding from basic groups in the secondary coordination sphere has also been used in stoichiometric small molecule reactions to generate isolable metal oxido complexes (Figure 3.2b).[12,13]

HX-splitting photochemistry (X = Cl, Br) has been advanced as an approach to solar-to-fuels conversion in which proton reduction is coupled to halide oxidation to provide carbon-neutral, closed energy conversion cycles.[14–16] During an H–X splitting cycle two electrons must be simultaneously managed in the formation of X–X bonds which comprises the energy-storing step of the cycle. While selective two-electron halogen elimination reactions have been realized for 4d and 5d metal complexes,[17–26] the inherently shorter

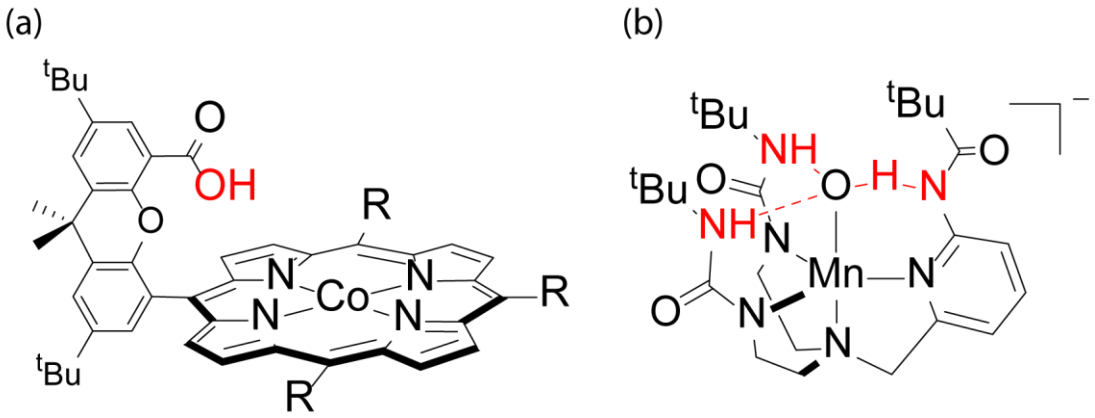

Figure 3.2. Functionality in the secondary coordination sphere that has been useful for promoting multielectron catalysis and stabilization of energetic intermediates.

excited state lifetimes and proclivity to participate in one-electron photoredox reactions contribute to the challenges that must be overcome to achieve energy storage via halogen elimination from 1st-row complexes.[27–29]

This Chapter is focused on a suite of Ni(III) trihalide complexes supported by bidentate phosphine ligands, $NiX_3(LL)$ (LL = bidentate phosphine), that engage in halogen elimination photoreactions both in solution and in the solid state with high quantum yield. The mechanism of halogen photoelimination is probed using a combined computational and spectroscopic approach. Computations show that the excited states responsible for the observed halogen elimination reactions are ligand-to-metal in character and are dissociative. Time-resolved photochemical studies have identified halogen atom adducts of ligand-based aromatic groups to be intermediates in the elimination reactions. As will be shown in this Chapter, the ability of these complexes to promote efficient halogen elimination is attributed to the ability of the secondary coordination sphere to guide the photoeliminating halogen from the primary coordination sphere via an aromatic-halogen interaction (Figure 3.3), resulting in suppression of the exothermic back reaction.

Figure 3.3. The photoeliminated chlorine atom (*vide infra*) is guided away from the primary coordination sphere due to stabilization by the ligand substituents.

3.2 Results

3.2.1 Characterization of Mononuclear Ni(III) Complexes

The Ni(III) complexes shown in (Figure 3.4) display no ^{1}H NMR or ^{31}P NMR spectra. Evans method and variable-temperature EPR indicated the complexes are S = ½, as expected for mononuclear d^7 complexes. The EPR spectrum of compounds **1** are shown in Figure 3.5 through Figure 3.7. The EPR spectra display pseudo-axial doublet signal with g_x, $g_y > 2$ and $g_z \sim 2.000$ and a four-line superhyperfine coupling pattern in the g_z direction (Table 3.1). The superhyperfine coupling is a direct probe of the coupling of the d_z^2 unpaired electron with the nuclear magnetic moment of the apical halide ligand (I = 3/2 for both Br and Cl) and is a measure of the degree of electron delocalization of the unpaired electron along the apical Ni(III)–X bond.[30] The superhyperfine coupling ($|A_z|$) varies depending on the bidentate phosphine backbones and the arene substituents of the phosphine groups.

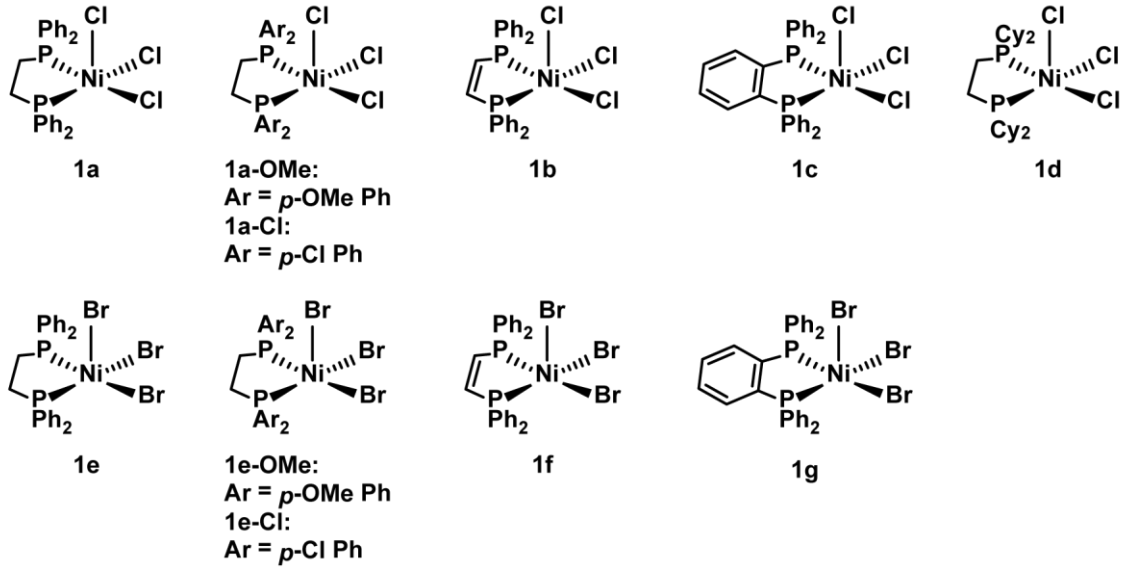

Figure 3.4. Ni(III) trihalide complexes supported by bidentate phosphine ligands.

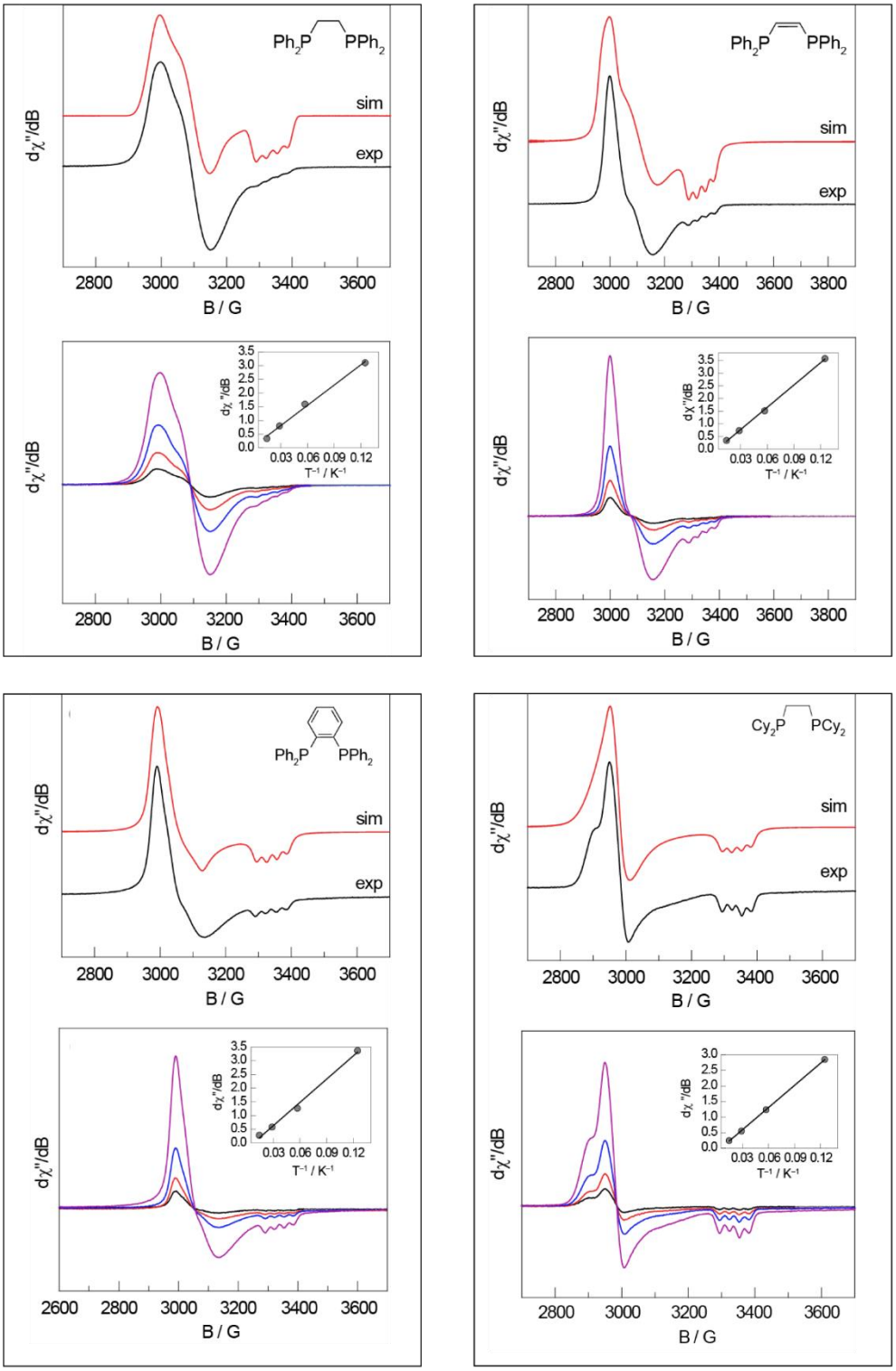

Figure 3.5. EPR spectrum of $NiCl_3$ complexes. Upper: 8 K EPR (—, black) and simulation (—, red). Lower: Temperature dependence of EPR intensity.

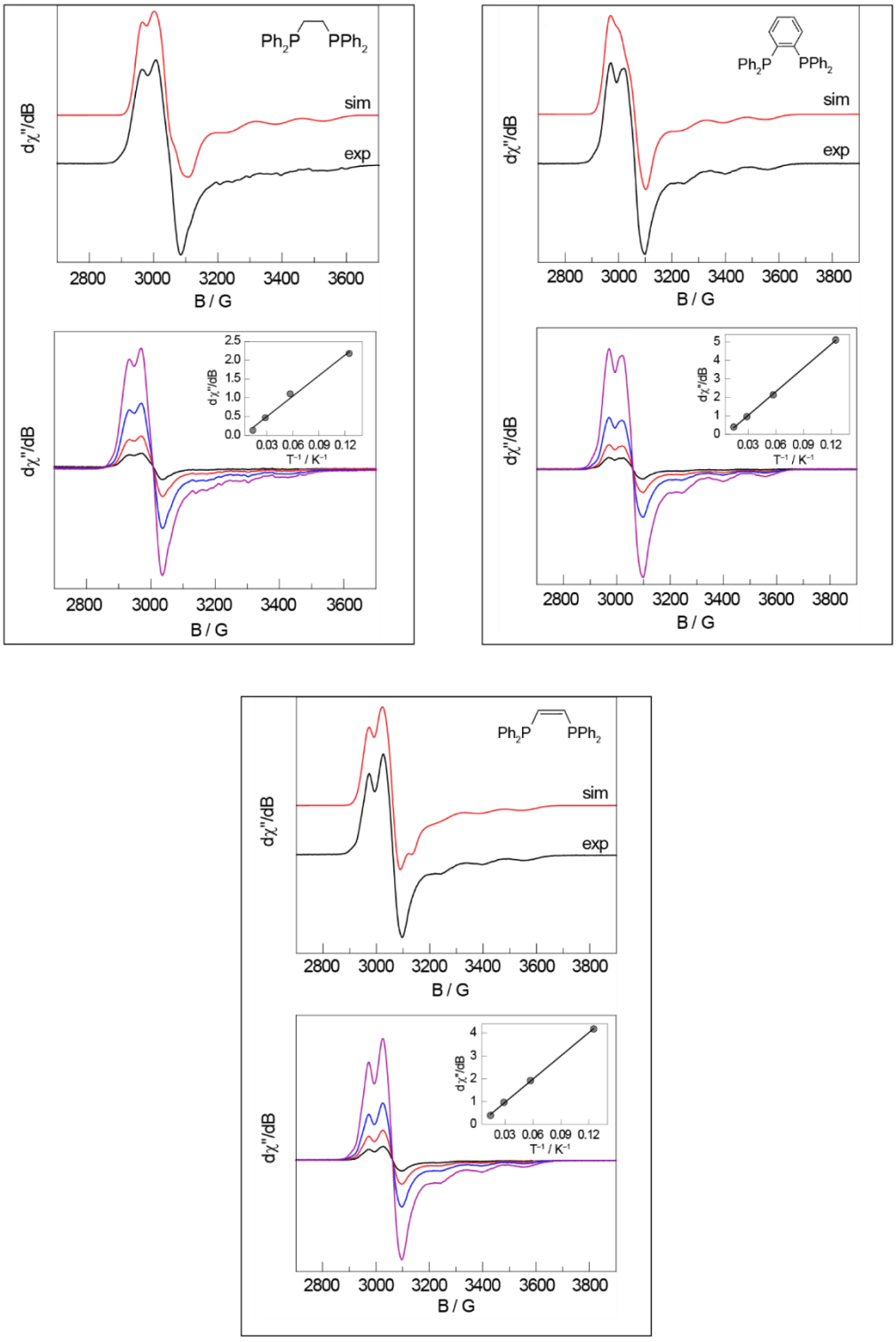

Figure 3.6. EPR spectrum of $NiBr_3$ complexes. Upper: 8 K EPR (—, black) and simulation (—, red). Lower: Temperature dependence of EPR intensity.

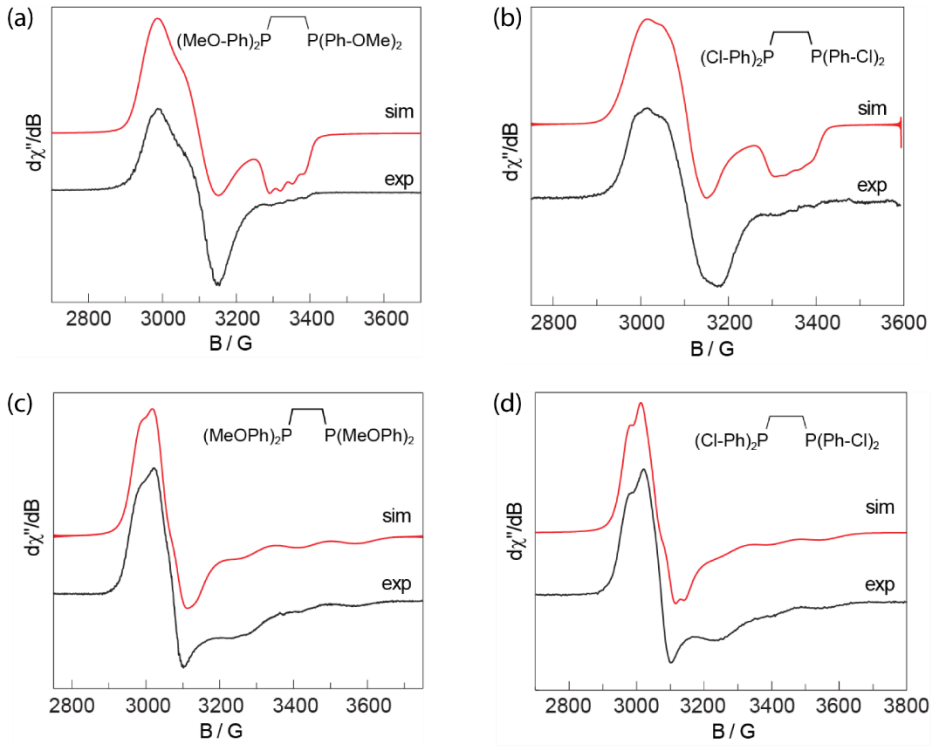

Figure 3.7. EPR spectrum of (a) $NiCl_3$(dppe-OMe) (**1a-OMe**), (b) $NiCl_3$(dppe-Cl) (**1a-Cl**), for the simulation of the axial hyperfine, $|A_z|$, was fixed to 90 MHz and not optimized. (c) $NiBr_3$(dppe-Cl) (**1e-Cl**), (d) $NiBr_3$(dppe-Cl) (**1e-Cl**) recorded at 77 K, (—, black) and simulated (—, red).

Table 3.1. EPR parameters derived from fitting of NiX_3(LL) (**1**) spectra.

Compound	g_x	g_y	g_z	$\|A_z\|$/MHz
1a: $NiCl_3$(dppe)	2.245	2.164	2.012	95
1a-OMe: $NiCl_3$(dppe-OMe)	2.258	2.169	2.017	95
1a-Cl: $NiCl_3$(dppe-Cl)	2.241	2.165	2.01	–
1b: $NiCl_3$(dppey)	2.241	2.155	2.013	92
1c: $NiCl_3$(dppb)	2.232	2.196	2.010	92
1d: $NiCl_3$(dcpe)	2.280	2.260	2.010	81
1e: $NiBr_3$(dppe)	2.203	2.203	2.025	400
1e-OMe: $NiBr_3$(dppe-OMe)	2.208	2.208	2.025	420
1e-Cl: $NiBr_3$(dppe-Cl)	2.201	2.191	2.025	410
1f: $NiBr_3$(dppey)	2.192	2.187	2.024	430
1g: $NiBr_3$(dppb)	2.226	2.176	2.020	420

The electronic absorption spectra spectrum of Ni(II) complex **3c** is representative of the Ni(II) complexes discussed herein and is dominated by an intense band at ~285 nm that is flanked by a shoulder at ~335 nm and a much weaker band at 463 nm. Oxidation of complexes **3c** to complex **1c** results in a bathochromic shift of the 335 nm absorption feature to 348 nm and a slight hypsochromic shift of the 463 nm absorption feature to 440 nm. In addition, a pronounced absorption at 657nm for complex **3c** is notably absent in Ni(II) complex. The profiles of the bromide and chloride Ni(III) complexes are similar, but the latter is red-shifted indicating that the electronic absorption characteristics of the nickel halide complexes reported here are largely determined by X→Ni(III) charge transfer.

3.2.2 Halogen Photoelimination Chemistry

Irradiation of CH_2Cl_2 solutions of $NiX_3(LL)$ (**1**) with visible light ($\lambda > 400$ nm) leads to clean conversion to the corresponding reduced $NiX_2(LL)$ (**3**) as determined by both UV-vis

Table 3.2. Quantum yields of $NiX_3(LL)$ halogen elimination photochemistry.[a]

LL	$NiCl_3(LL)$	Φ_p		$NiBr_3(LL)$	Φ_p
dppe	**1a**	0.764		**1e**	0.169
dppe-OMe	**1a-OMe**	0.230		**1e-OMe**	0.352
dppe-Cl	**1a-Cl**	0.128		**1e-Cl**	0.056
dppey	**1b**	0.960		**1f**	0.401
dppb	**1c**	0.077		**1g**	0.047
dcpe [b]	**1d**	0.201			
	w/5% C_6H_6	0.330			
	w/10% C_6H_6	0.410			
	w/20% C_6H_6	0.490			
	w/30% C_6H_6	0.591			
	w/40% C_6H_6	0.622			

[a] in CH_2Cl_2, λ_{exc} = 370 nm bandpass filter. [b] in CH_3CN solution with percent addition of benzene.

and $^{31}P\{^{1}H\}$ NMR. All observed isosbestic points are well-anchored (Figure 3.8), and no P-containing side-products were observed by $^{31}P\{^{1}H\}$ NMR (Figure 3.9–Figure 3.11). Halogen photoelimination quantum yields (Φ_p) from each of the Ni(III) complexes were measured actinometrically (against potassium ferrioxalate) and are summarized in Table **3.2**.

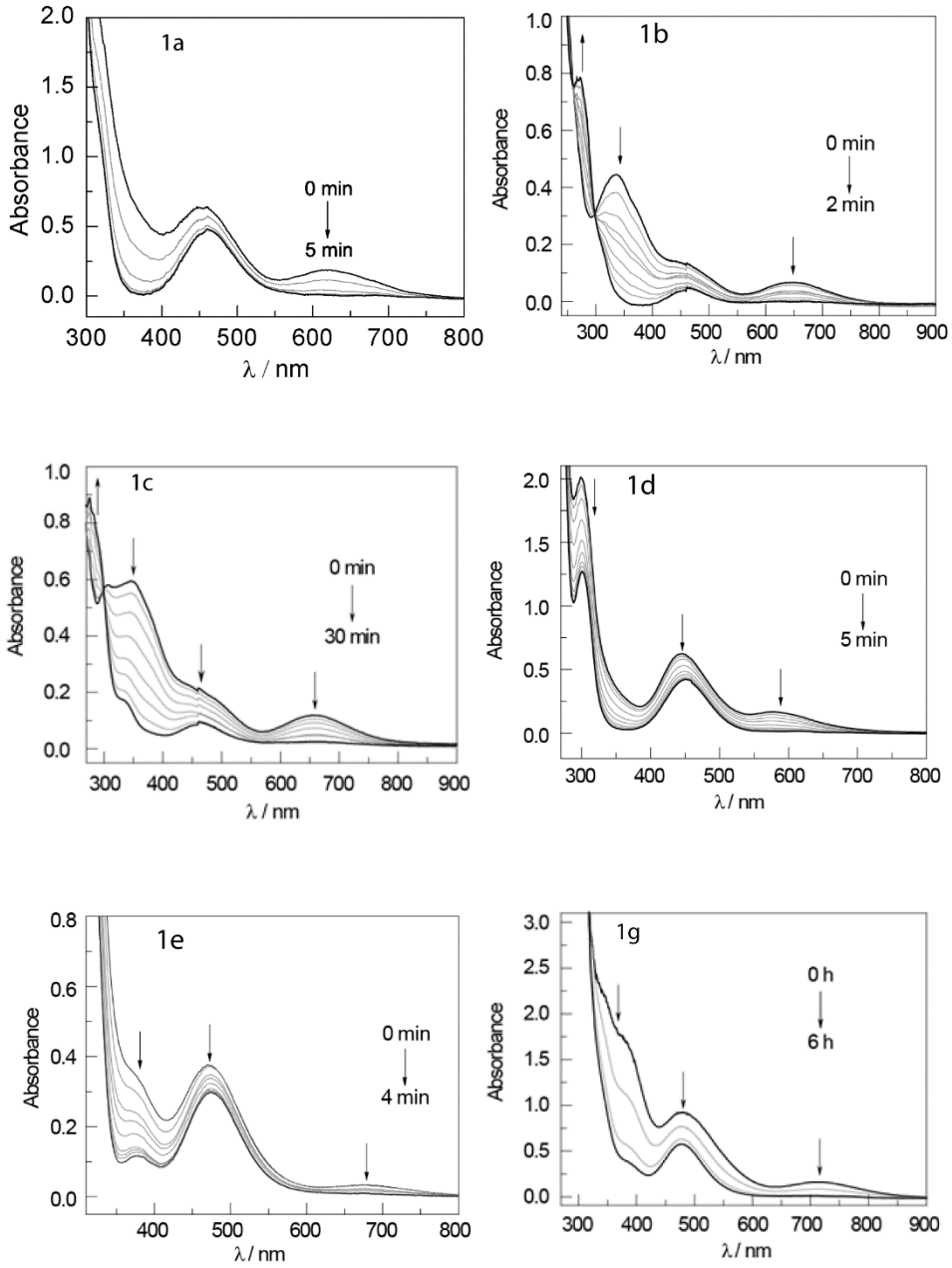

Figure 3.8. Photolysis of species **1** to **3** under irradiation with λ_{exc} > 400 nm light. Arrows indicate the direction of evolution during the photolysis.

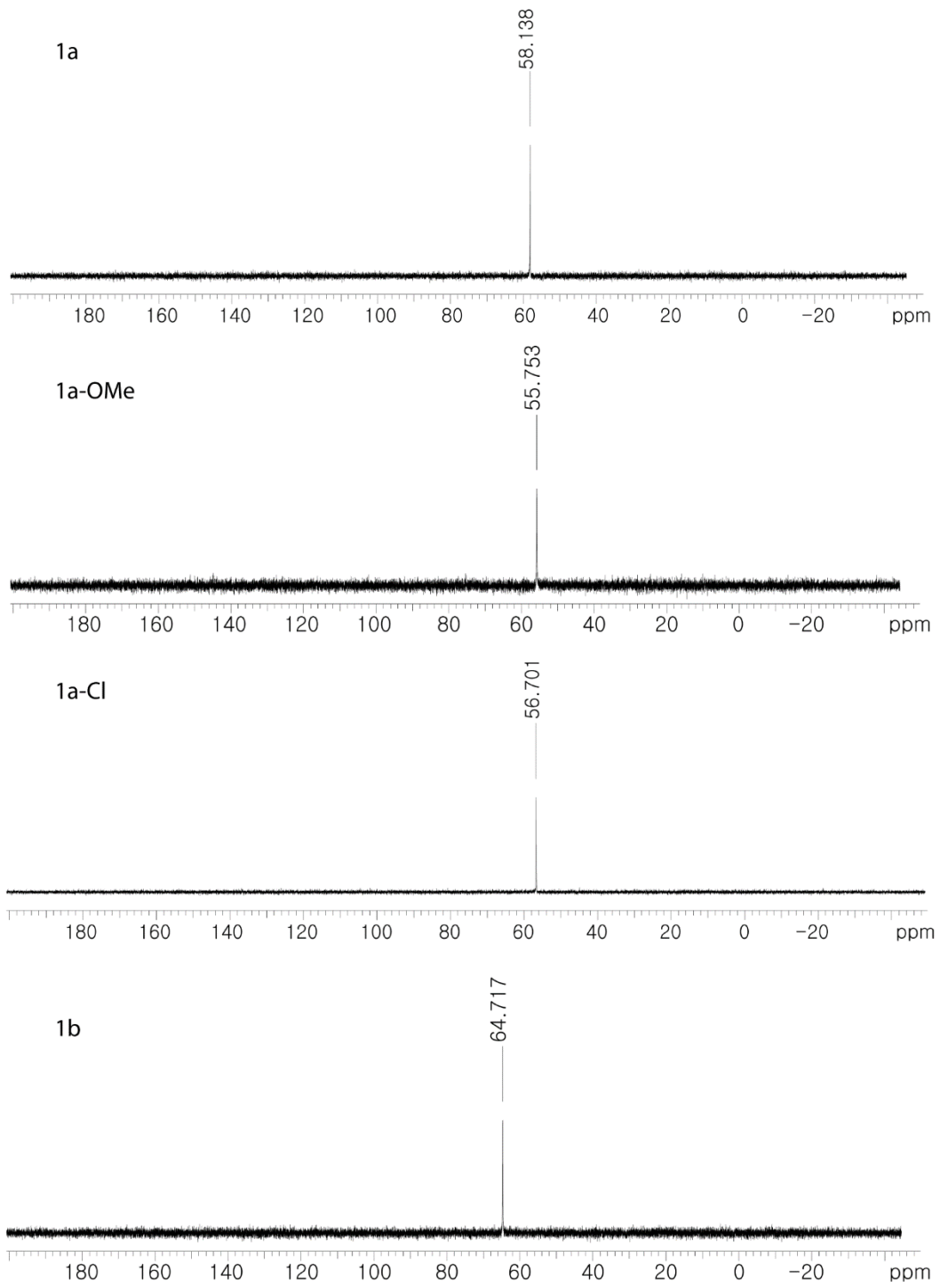

Figure 3.9. $^{31}P\{^{1}H\}$ NMR spectrum of the reaction solution obtained by photolysis of **1a–1b** with visible light (λ > 400 nm) recorded in CD_2Cl_2 at 23 °C.

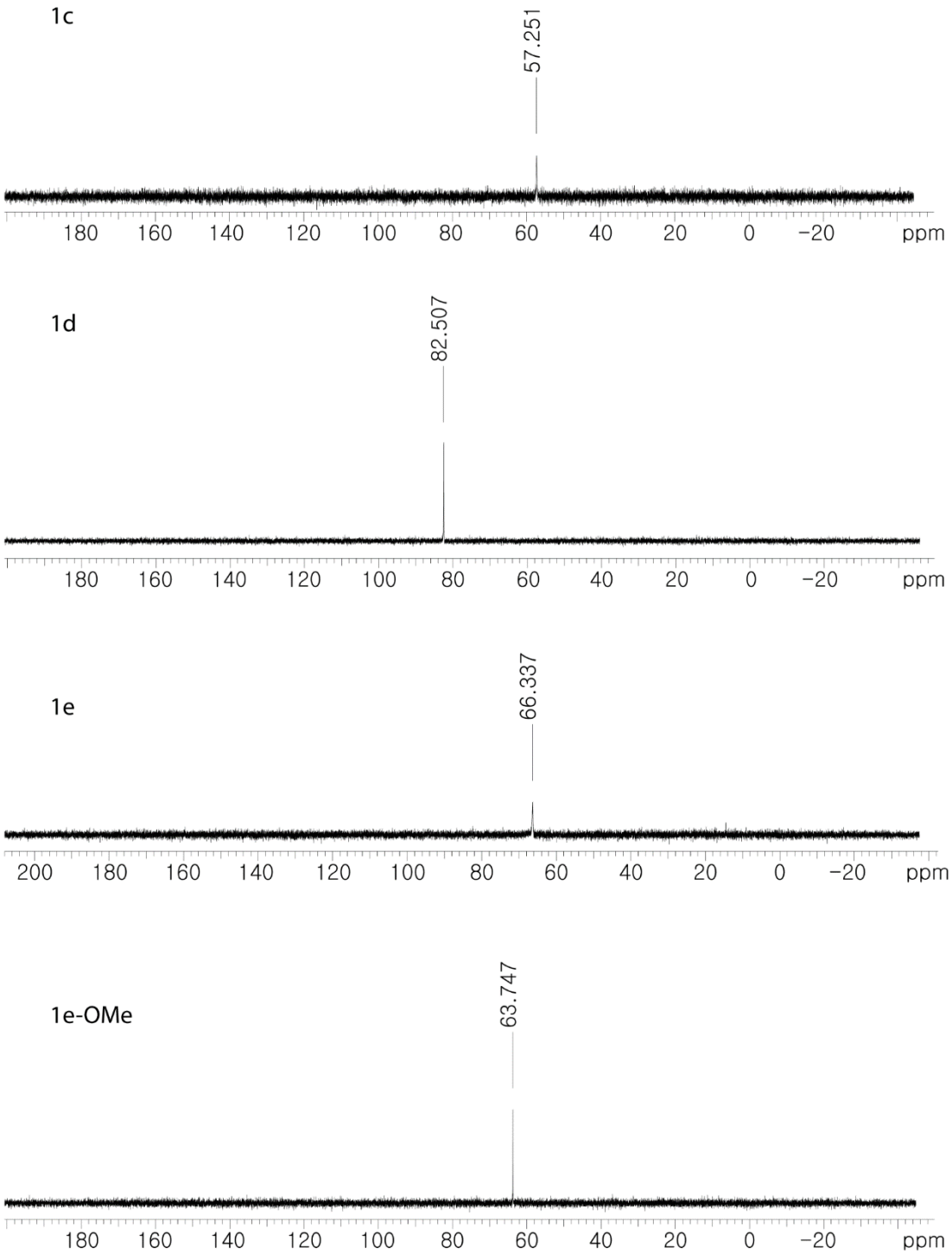

Figure 3.10. $^{31}P\{^{1}H\}$ NMR spectrum of the reaction solution obtained by photolysis of **1c–1e-OMe** with visible light (λ > 400 nm) recorded in CD_2Cl_2 at 23 °C.

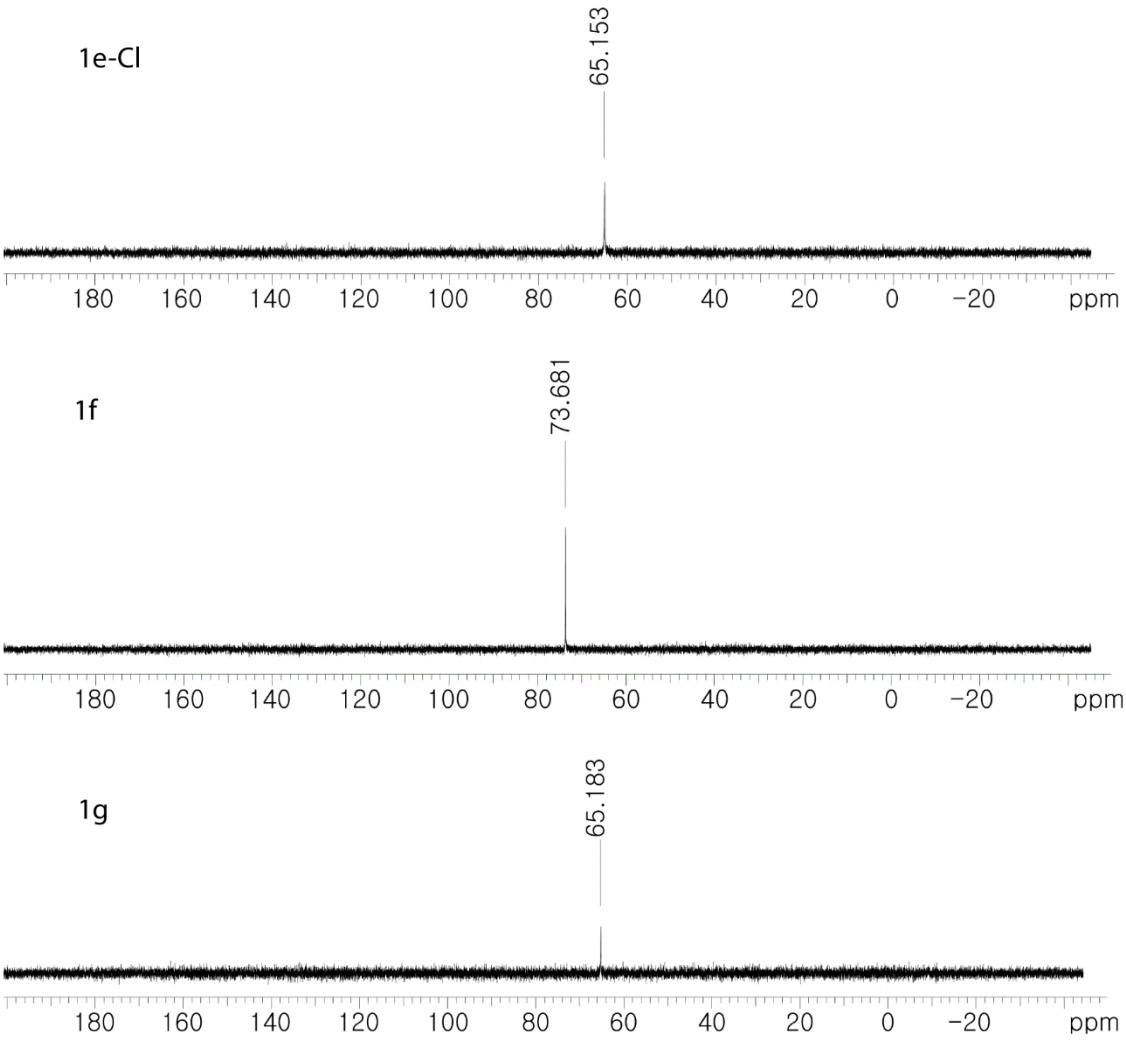

Figure 3.11. $^{31}P\{^{1}H\}$ NMR spectrum of the reaction solution obtained by photolysis of **1e-Cl–1g** with visible light (λ > 400 nm) recorded in CD_2Cl_2 at 23 °C.

The presence of an aromatic group in the second coordination sphere significantly enhances Φ_p. The photochemical quantum yield, Φ_p, for cyclohexyl phosphine complex $NiCl_3$(dcpe) is Φ_p(**1d**) = 20.1% whereas that for the dppe complex is Φ_p(**1a**) = 76.4% and near unity for the dppey complex **1b**. We note that the presence of an aromatic solvent increases the Φ_p of **1d.** The addition of benzene to CH_3CN solutions causes Φ_p to increase monotonically to an asymptotic Φ_p of ~60% at mixtures higher than 30%. Addition of 30% CCl_4 showed negligible improvement in the photoefficiency (Φ_p = 20.8%), demonstrating that the change in solvent dielectric ($\varepsilon(C_6H_6)$ = 2.27 and $\varepsilon(CCl_4)$ = 2.24) is not the source of increased quantum yield for CH_3CN/benzene mixtures. A similar change in Φ_p was also observed for the addition of benzene to solutions of $NiCl_3$(dppb) (**1c**) (Φ_p = 8% in CH_3CN vs Φ_p = 35% with 30% benzene). Halogen photoelimination from substituted dppe-supported NiX_3(LL) complexes was also examined to probe the effects of the electronic properties of the phosphine without modifying the steric environment about the metal center. The quantum yields for para-OMe and para-Cl substituted dppe derivatives were determined to be 35.0% and 5.6% for **1a-OMe** and **1a-Cl**, respectively.

3.2.3 Time-Resolved Photochemistry

Nanosecond TA was utilized to search for intermediates in the photolysis process of the $NiCl_3$(LL) complexes. For all Ni(III)Cl_3(LL) complexes the spectrum was found to evolve on the microsecond timescale suggestive of an intermediate species. The prompt TA spectrum is a superposition of the bleach signal of the starting complex **1**, the absorption of the final product **3**, and any transient species generated in the instrument response time. Subtraction of the spectrum obtained after the system has fully evolved to the final photoproduct from that of the prompt spectrum yields the spectrum of the transient

species. Figure 3.12 shows the absorption spectrum of the transient species obtained 40 ns after laser excitation of $NiCl_3$(dppe) (**1a**) which displays an absorption maximum at 366 nm as well as a broad band with a maximum at 530 nm. As highlighted in Figure 3.12, the transient possesses spectral features are similar to the chlorine-atom charge transfer adduct of benzene, generated by either laser flash photolysis or pulse radiolysis.[31–34] A similar result is obtained for all of the Ni(III)Cl_3(LL) complexes described herein (Figure 3.13 through Figure 3.20). In every case we observe a transient intermediate that is consistent with Cl-atom adduct formed with the ligand aryl group. Single-wavelength kinetics were monitored for each of the observed transient intermediates and lifetimes of the transient were observed to vary between 100 ns and 10 μs.

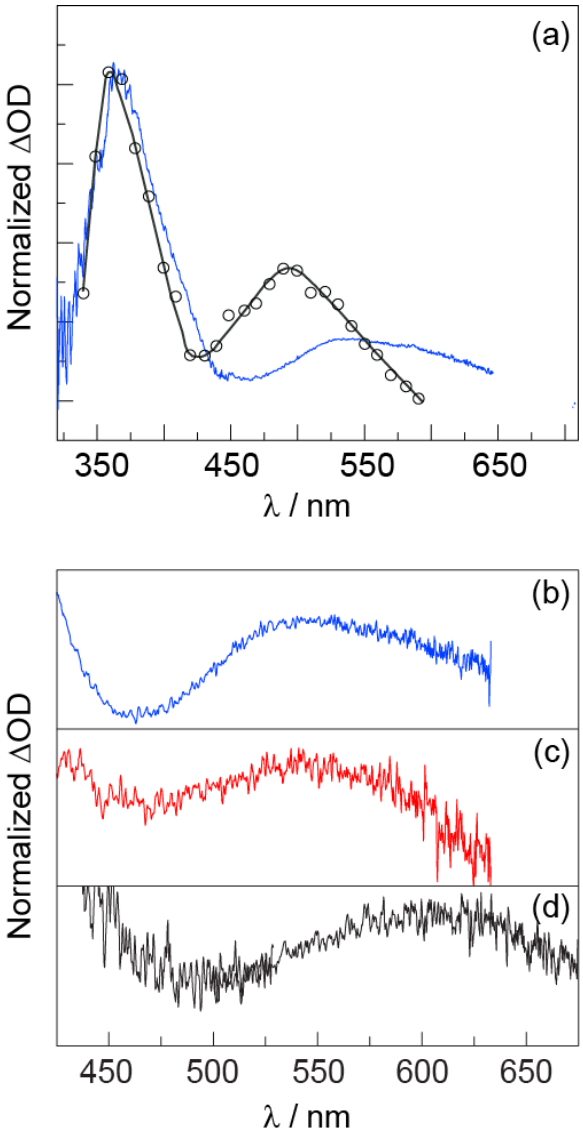

Figure 3.12. (a) Comparison between transient absorption spectrum generated by subtracting the difference spectrum of a 0.44 mM solution of **1a,** $NiCl_3(dppe)$, in CH_3CN acquired at a 50 μs time delay from that acquired at a 40 ns time delay (λ_{exc} = 355 nm). The low energy transient feature shifts to lower energy with the introduction of electron donating substituents of the phenyl ring of dppe along the series (b) **1a**, (c) **1a-Cl** and (d) **1a-OMe**.

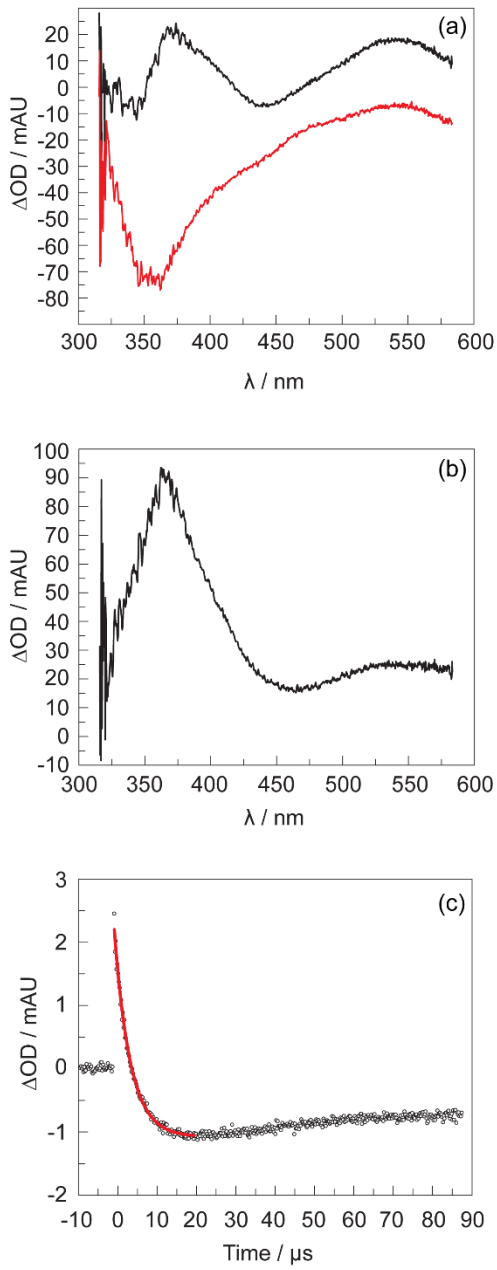

Figure 3.13. Transient absorption spectra obtained by laser flash photolysis (355 nm pump) of $NiCl_3$(dppe) (**1a**) (0.44 mM solution in CH_3CN). (a) Transient absorption spectra recorded at 50 ns (—, black), and 50 μs (—, red) after laser pulse. (b) Absorption spectrum of the intermediate species (**2a**) calculated from the difference of TA spectra recorded at 50 ns and 50 μs. (c) Single wavelength kinetic trace of a CH_3CN solution of $NiCl_3$(dppe) (**1a**) pumped at 355 nm and recorded at 560 nm. Initial component lifetime: $\tau = 4.0 \pm 0.1$ μs.

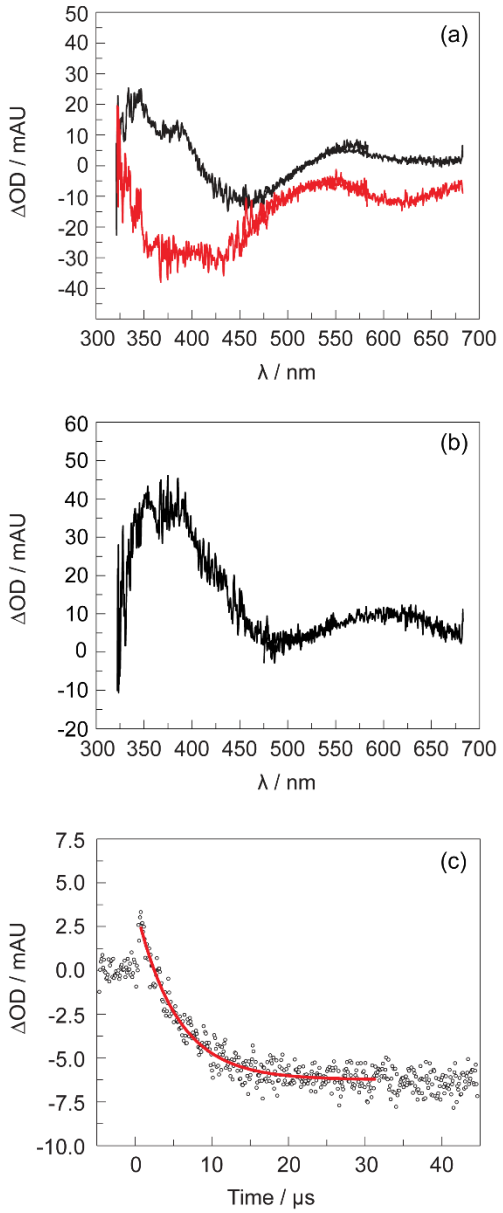

Figure 3.14. Transient absorption spectra obtained by laser flash photolysis (355 nm pump) of $NiCl_3$(dppe-OMe) (**1a-OMe**) (0.44 mM solution in CH_3CN). TA spectra are composites of spectra acquired with windows centered at 450 and 550 nm. (a) Transient absorption spectra recorded at 70 ns (—, black), and 50 μs (—, red) after laser pulse. (b) Absorption spectrum of the intermediate species (**1a-OMe**) calculated from the difference of TA spectra recorded at 70 ns and 50 μs. (c) Single wavelength kinetic trace of a CH_3CN solution of $NiCl_3$(dppe-OMe) (**1a-OMe**) pumped at 355 nm and recorded at 600 nm. Initial component lifetime: $\tau = 5.3 \pm 0.2$ μs.

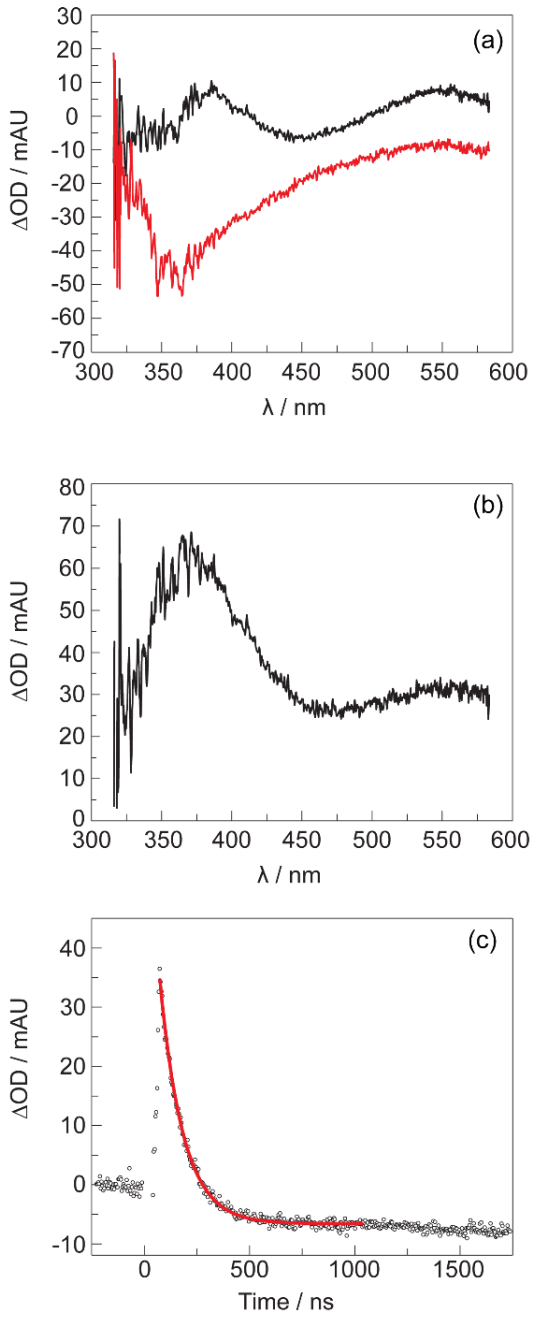

Figure 3.15. Transient absorption spectra obtained by laser flash photolysis (355 nm pump) of $NiCl_3$(dppe-Cl) (**1a-Cl**) (0.44 mM solution in CH_3CN). (a) Transient absorption spectra recorded at 70 ns (**—**, black) and 50 μs (**—**, red) after laser pulse. (b) Absorption spectrum of the intermediate species (**2a-Cl**) calculated from the difference of TA spectra recorded at 70 ns and 50 μs. (c) Single wavelength kinetic trace of a CH_3CN solution of $NiCl_3$(dppe-Cl) (**1a-Cl**) pumped at 355 nm and recorded at 550 nm. Initial component lifetime: $\tau = 100 \pm 1$ ns.

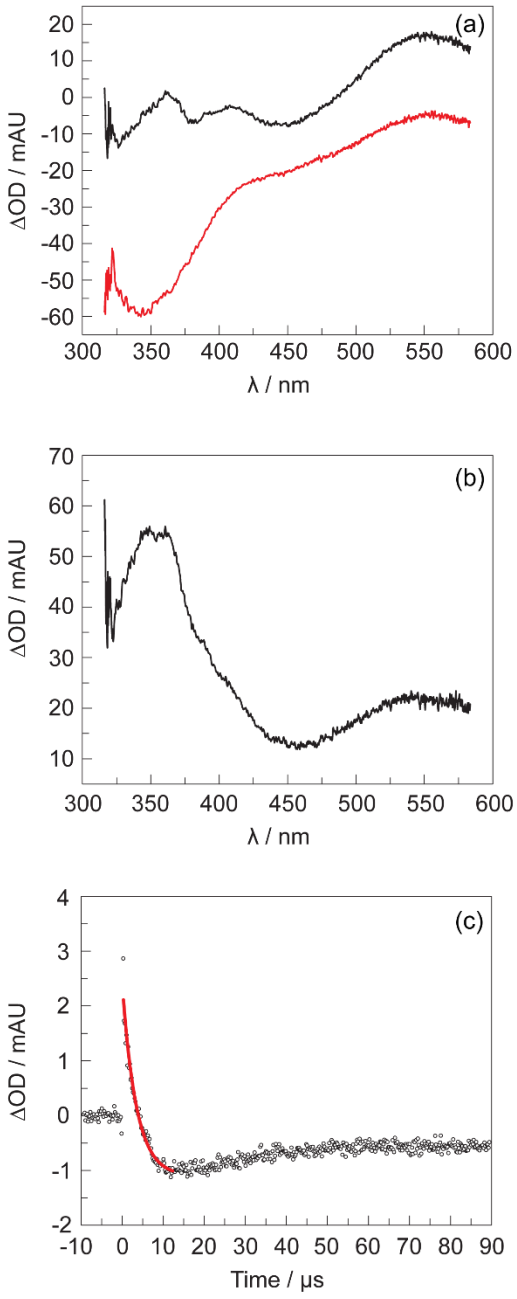

Figure 3.16. Transient absorption spectra obtained by laser flash photolysis (355 nm pump) of $NiCl_3$(dppey) (**1b**) (0.44 mM solution in CH_3CN). (a) Transient absorption spectra recorded at 50 ns (—, black), and 50 μs (—, red) after laser pulse. (b) Absorption spectrum of the intermediate species (**2b**) calculated from the difference of TA spectra recorded at 50 ns and 50 μs. (c) Single wavelength kinetic trace of a CH_3CN solution of $NiCl_3$(dppey) (**1b**) pumped at 355 nm and recorded at 550 nm. Initial component lifetime: $\tau = 3.4 \pm 0.2$ μs.

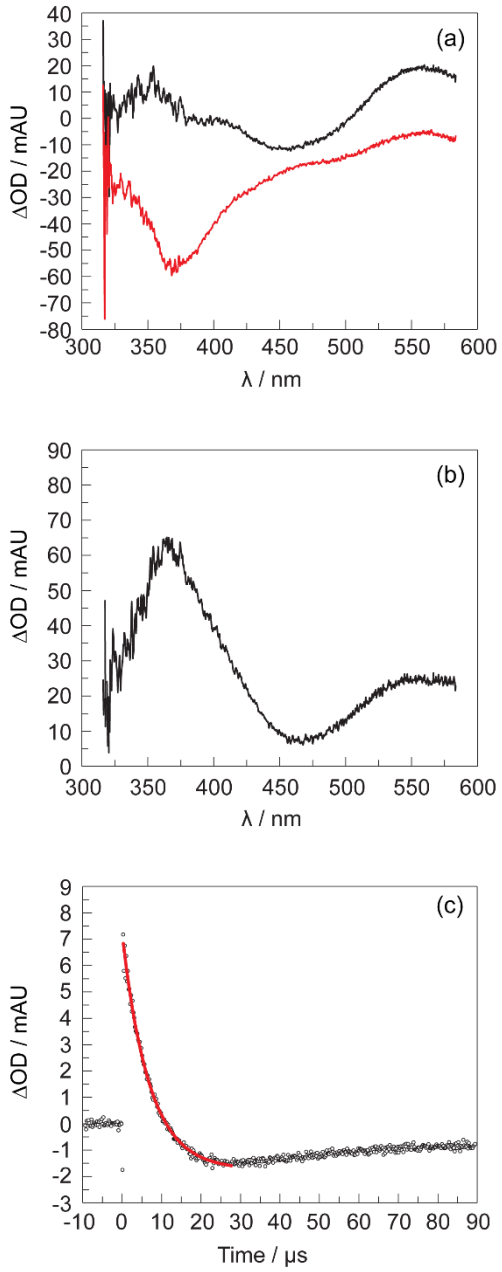

Figure 3.17. Transient absorption spectra obtained by laser flash photolysis (355 nm pump) of $NiCl_3$(dppb) (**1c**) (0.44 mM solution in CH_3CN). (a) Transient absorption spectra recorded at 300 ns (—, black), and 50 μs (—, red) after laser pulse. (b) Absorption spectrum of the intermediate species (**2c**) calculated from the difference of TA spectra recorded at 300 ns and 50 μs. (c) Single wavelength kinetic trace of a CH_3CN solution of $NiCl_3$(dppb) (**1c**) pumped at 355 nm and recorded at 550 nm. Initial component lifetime: $\tau = 6.8 \pm 0.1$ μs.

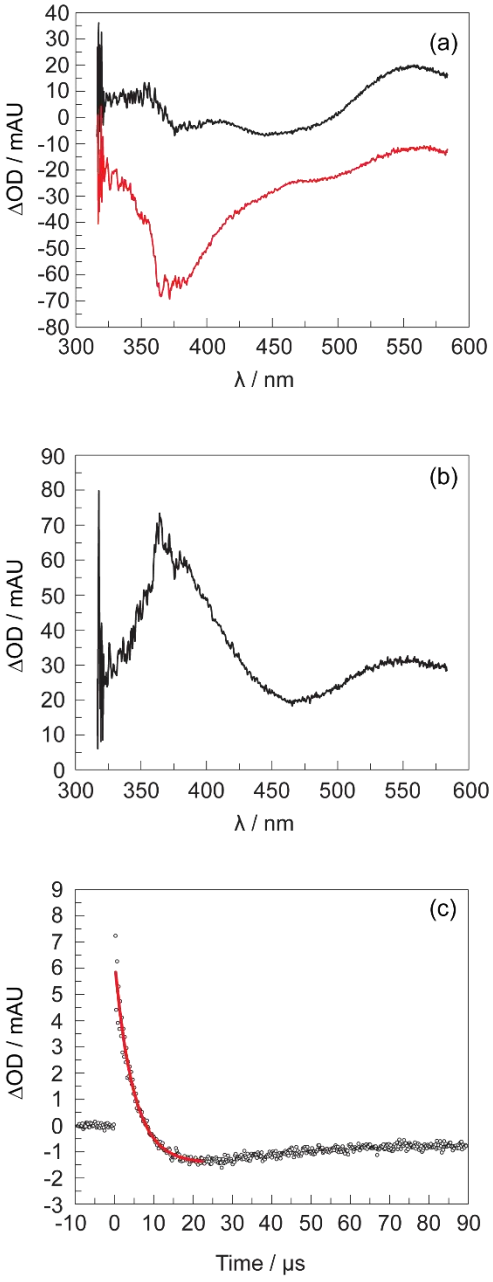

Figure 3.18. Transient absorption spectra obtained by laser flash photolysis (355 nm pump) of $NiCl_3$(dppb) (**1c**) (0.44 mM solution in 30/70 benzene/CH_3CN). (a) Transient absorption spectra recorded at 300 ns (—, black), and 50 μs (—, red) after laser pulse. (b) Absorption spectrum of the intermediate species (**2c**) calculated from the difference of TA spectra recorded at 300 ns and 50 μs. (c) Single wavelength kinetic trace of a solution (0.44 mM in 30:70 benzene:CH_3CN) of $NiCl_3$(dppb) (**1c**) pumped at 355 nm and recorded at 550 nm. Initial component lifetime: $\tau = 4.7 \pm 0.2$ μs.

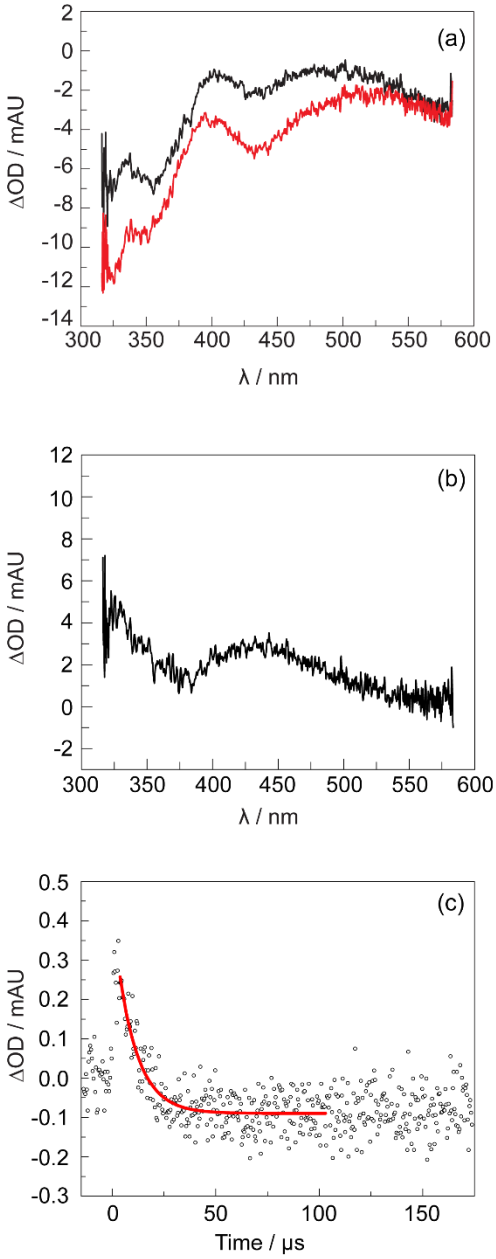

Figure 3.19. Transient absorption spectra obtained by laser flash photolysis (355 nm pump) of $NiCl_3$(dcpe) (**1d**) (0.44 mM solution in CH_3CN). (a) Transient absorption spectra recorded at 80 ns (—, black), and 50 μs (—, red) after laser pulse. (b) Absorption spectrum of the intermediate species (**2d**) calculated from the difference of TA spectra recorded at 80 ns and 50 μs. (c) Single wavelength kinetic trace of a solution of $NiCl_3$(dcpe) (**1d**) pumped at 355 nm and recorded at 440 nm. Initial component lifetime: $\tau = 9.8 \pm 0.8$ μs.

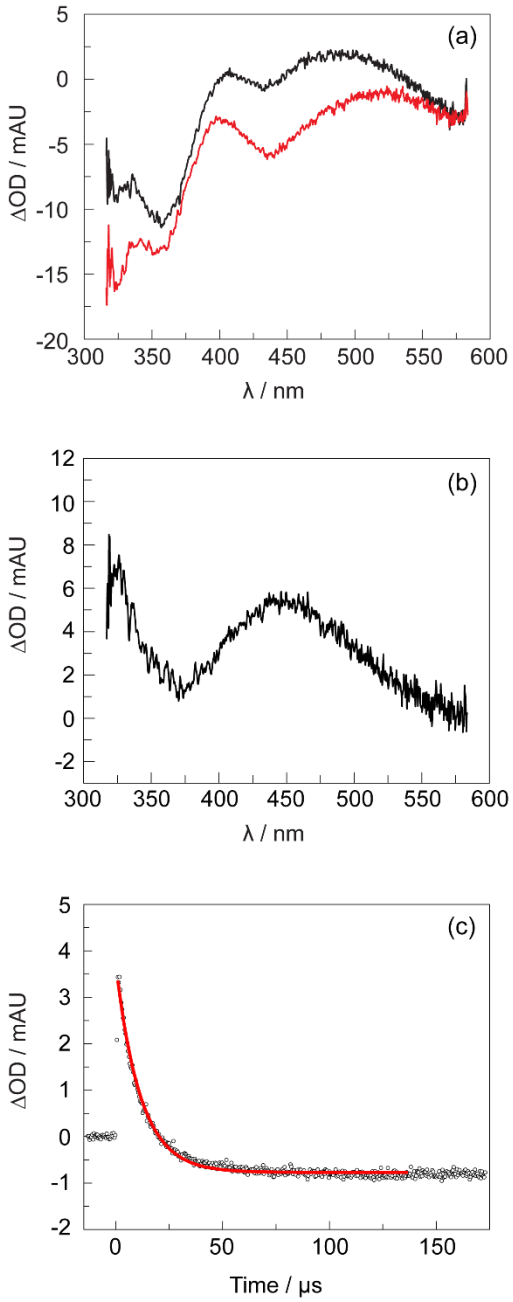

Figure 3.20. Transient absorption spectra obtained by laser flash photolysis (355 nm pump) of $NiCl_3$(dcpe) (**1d**) (0.44 mM solution in 30:70 benzene:CH_3CN). (a) Transient absorption spectra recorded at 380 ns (—, black), and 50 μs (—, red) after laser pulse. (b) Absorption spectrum of the intermediate species (**2d**) calculated from the difference of TA spectra recorded at 380 ns and 50 μs. (c) Single wavelength kinetic trace of a solution (0.44 mM in 30:70 benzene:CH_3CN) $NiCl_3$(dcpe) (**1d**) pumped at 355 nm and recorded at 550 nm. Initial component lifetime: $\tau = 11.5 \pm 0.1$ μs.

Further support for an intermediate Cl-atom|aromatic adduct formed along the pathway of the halogen elimination photochemistry of the $NiX_3(LL)$ complexes was obtained by investigating substituted dppe-supported Ni(III) complexes. The λ_{max} of the transient intermediate is perturbed by the presence of substituents on the dppe ligand. As shown in Figure 3.12b–d, the λ_{max} of the transient spectrum red shifts with donor substituent on the aryl (**1a**, λ_{max} = 530 nm; **1a-Cl**, λ_{max} = 540 nm; **1a-OMe**, λ_{max} = 610 nm). This observed red shift in the energy of the Cl-atom|aromatic adduct with increasing donor properties of the substituent group is consistent with the spectral trend previously reported for Cl-atom|aromatic adducts as observed by pulse radiolysis experiments.[31]

Given that Φ_p for halogen photoelimination increases with the addition of benzene (Table 3.2), we examined the TA spectrum of complex **1d** in the presence of 30% benzene. The nanosecond-resolved TA spectrum of cyclohexyl phosphine Ni(III) complex **1d** exhibits a weak feature with a maximum at 430 nm (Figure 3.19). The signal intensity of the observed transient intermediate at 430 nm increases substantially with that addition of benzene to the solution and it slightly red shifts; the time evolution of the transient decay remains essentially unchanged (Figure 3.20).

3.2.4 Solution-Phase Calorimetry

The chlorine photoeliminaiton enthalpies were determined by solution calorimetric measurements of the addition of $PhICl_2$ to of $Ni(II)Cl_2(LL)$ complexes (**3**) as detailed in the experimental section. The heat of reaction was calculated using Equations 3.1 through 3.3. The known heat of reaction of chlorine release from solid $PhICl_2$ was corrected for the enthalpy of solution of the solid $PhICl_2$, which was measured separately. The enthalpies of

Cl_2 addition to compounds of **3**, listed in Table 3.3, were obtained from Equation 3.3 and are the average of three independent measurements. All complexes confront endothermic barriers to halogen elimination with complex **1a** possessing significant energy storage capacity for the Cl_2 photoelimination reaction (Figure 3.21).

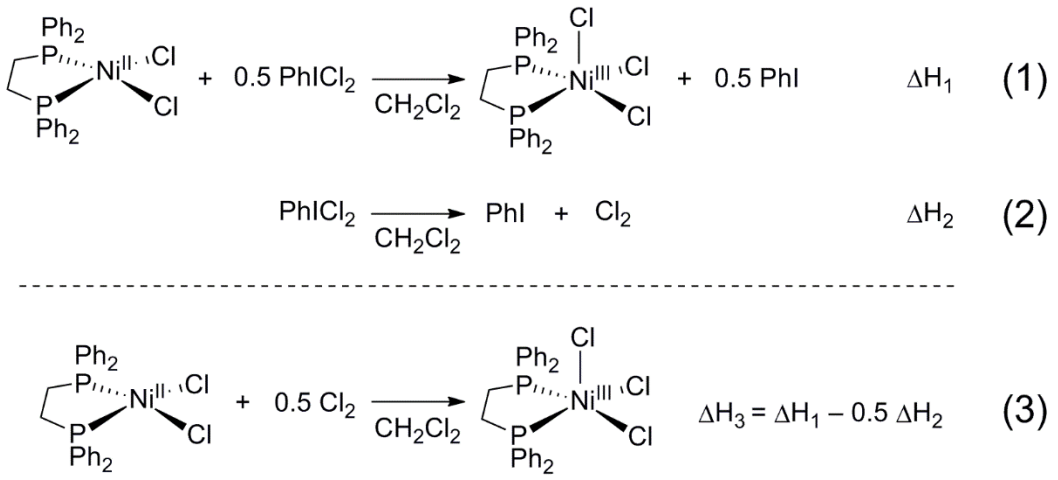

Table 3.3. Reaction enthalpy for chlorination of Ni(II) complexes.

$$NiCl_2(LL) + 0.5\ Cl_2 \longrightarrow NiCl_3(LL)$$

LL	ΔH (kcal mol^{-1})
dppe	–23.7
dppey	–20.8
dppb	–16.7
dcpe	–7.0

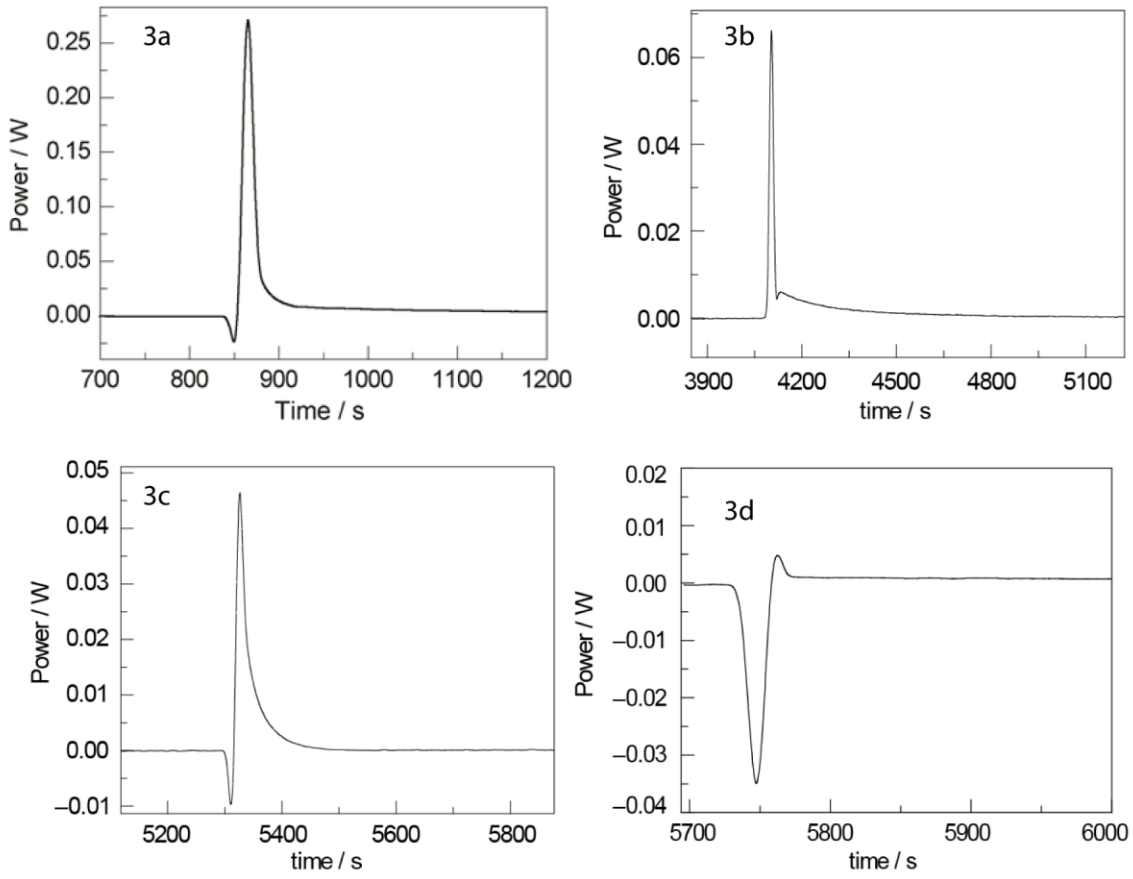

Figure 3.21. Thermograms for the reaction of compounds (**3a–d**) and $PhICl_2$ in CH_2Cl_2.

3.2.5 Computational Results

DFT geometry optimization of **1f** was performed as described in the Experimental section. The DFT-based ground state wavefunction is consistent with a Ni(III) center and an unpaired electron/hole residing in an antibonding Ni d_{z^2}/halide p_z orbital, which results in a delocalized metal-to-apical-ligand bonding description consistent with EPR spectroscopy (e.g., DFT-based spin densities of ~0.81 and ~0.23 for Ni(III) and the apical halide, respectively, for **1f**).

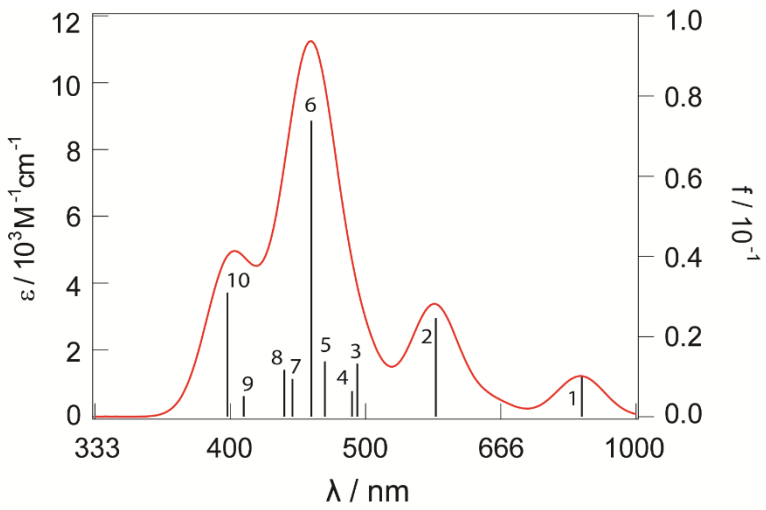

Figure 3.22. Relevant oscillators (oscillator strength > 0.02; solid blue bars) from TD–DFT calculations for complex **1f** with simulated absorption spectrum overlaid (solid red line).

To gain insight into the nature of the excited states of the Ni(III) compounds, TD-DFT calculations were performed using the optimized geometry of **1f**. The calculated absorption spectrum largely reproduces the spectral features observed in the experimental data (Figure 3.22 and Table 3.4). On the basis of the TD-DFT results, the lower energy absorption feature (~575 nm) arises from an apical Br(p(π))→ Ni(d_{x2-y2}) LMCT, while the

Table 3.4. TD-DFT calculated transitions (PCM = CH_2Cl_2).[a]

State	λ (nm)	Energy (eV)	*f*[a]	Contributions	Assignment
1	833	1.48	0.0099	170A → 172A (78%) 168A → 172A (10%)	α(pσ(ap)) → α(d(x^2-y^2))
2	575	2.16	0.0246	169B → 172B (29%) 166A → 172A (17%) 168A → 172A (14%)	β(pπ(ap)) → β(d(x^2-y^2))
3	493	2.51	0.0132	165A → 172A (48%) 170B → 172B (15%)	α(Phπ) → α(d(x^2-y^2))
4	488	2.55	0.0064	157A → 172A (26%) 169B → 172B (21%)	α(pπ (dis)) → α(d(x^2-y^2))
5	465	2.67	0.0138	164A → 172A (29%) 164B → 171B (19%) 157A → 172A (12%)	α(Phπ) → α(d(x^2-y^2))
6	455	2.73	0.0738	164A → 172A (46%) 164B → 171B (23%)	α(Phπ) → α(d(x^2-y^2))
7	440	2.82	0.0096	156B → 171B (30%) 152B → 171B (12%) 165B → 171B (12%)	β(pσ(ap)) → β(d(z^2))
8	435	2.85	0.0117	157A → 172A (18%) 159A → 172A (14%) 160A → 172B (13%) 165B → 172B (11%)	α(pπ (dis)) → α(d(x^2-y^2)) + α(Phπ) → α(d(x^2-y^2))
9	408	3.04	0.0055	158A → 172A (45%) 164B → 172B (12%)	α(Phπ) → α(d(x^2-y^2))
10	398	3.11	0.0316	158A → 172A (16%) 164B → 172B (10%)	α(Phπ) → α(d(x^2-y^2))

a Calculated transitions with oscillator strengths greater than 0.0050 are listed.

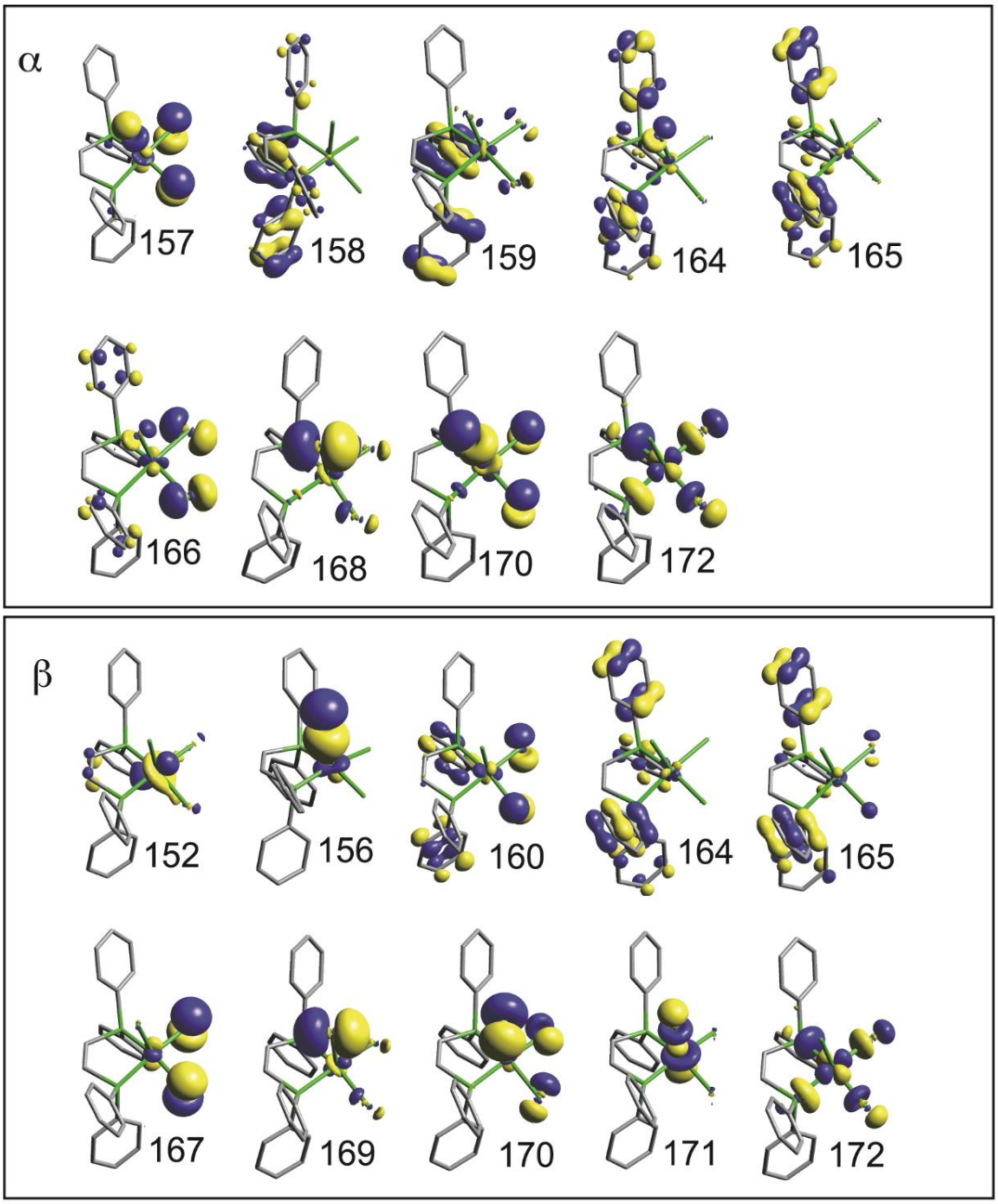

Figure 3.23. Representative molecular orbitals of complex **1f**.

higher energy absorption feature (~400–500 nm) largely consists of intense phenyl ring π → Ni($d_{x^2-y^2}$) charge transfer (CT) transitions and weak basal Br(p(π)) → Ni($d_{x^2-y^2}$) LMCTs. These assignments are consistent with the photochemical results in that the lower energy CT feature decays upon irradiation while the higher energy feature persists. An apical Br(p(σ)) → Ni(d_{z^2}) LMCT absorption is predicted within the higher energy absorption envelope (~440 nm, state 7, Figure 3.22 and Table 3.4). Transitions to the unoccupied Ni(d_{z^2}) orbital (i.e., the β-LUMO) eliminate any formal Ni-apical halide bond order and would be expected to result in significant destabilization of the apical nickel halide bond.

We explored the nature of the ground and excited state potential energy surface (PES) for elongation of the Ni–apical halide bond for **1f** using TD-DFT techniques. The CH_2Cl_2 corrected PESs for Ni–Br bond loss are given in Figure 3.24a, in which the TD-DFT calculated σ → σ* excited state energy is plotted as a function of ligand-metal bond distance. Note that this transition involves excitation of a β p_z/d_{z^2} bonding electron to the β p_z/d_{z^2} anti-bonding MO, β156 and β171 in Figure 3.23. This LMCT state is clearly dissociative,[35] as can be seen from the TD-DFT ground and excited state surfaces, resulting in the formation of a one-electron reduced Ni(II) S=0 metal center and a Br radical.

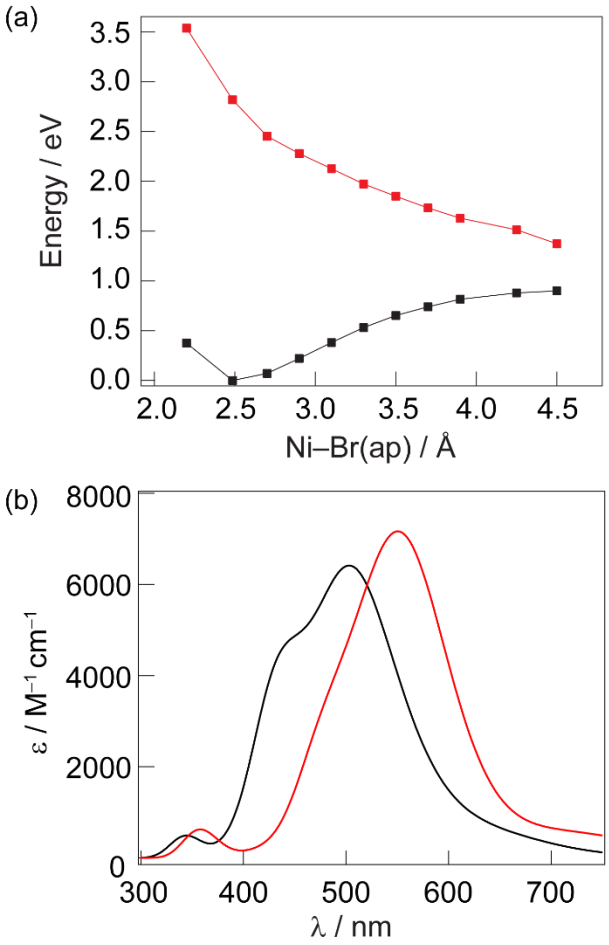

Figure 3.24. (a) CH_2Cl_2 corrected PESs (S = ½) of **1f** as a function of Ni–Br(ap) bond cleavage. Ground state energies are given as black squares, and the energies of the β(pσ(Br(ap))) → β(Ni(d(z^2))) LMCT excited state (7 in Table 3.4) are given as red squares. Note that the PES of this σ → σ* excited state is repulsive and can, upon excitation, result in homolytic cleavage of the Ni(III)–Br bond to a Br radical and a low-spin, S = 0 Ni(II) metal center. (b) Computational results of the charge transfer transitions of NiX_3(dppey) complexes. Gas phase TD-DFT calculated absorption spectra for **2b**, (—, black line) and **2f**, (—, red line).

In addition to the PES, we have geometry optimized the resulting Cl-atom|aromatic charge-transfer intermediates for both **1b** and 1**f**. DFT frequency calculations indicate local energetic minima for both complexes, which is consistent with the TA spectroscopic results and previous reports of the energetics of halogen|arene complexes.[36] The preferred halogen atom|arene interaction is roughly η_1 (C–X distances of ~2.6 and 2.9 Å for the Cl and Br radicals, respectively). Mulliken spin densities are consistent with significant charge transfer, i.e., a closed-shell Ni(II) ion associated to a halide atom (e.g., spin densities of 0.00, 0.66, and 0.75 for Ni(II), Cl and Br, respectively). The TD-DFT calculated absorption spectra are given in Figure 3.24b and predict relatively intense charge transfer features at ~475 and ~550 nm for the Cl and Br adducts, respectively, consistent with the measured absorption spectra. The parentage of these transitions arises from a filled, bonding halide(p)|arene(p(π)) donor orbitals and the β-LUMO, which is an anti-bonding halide(p)|arene(p(π)) molecular orbital (Fig. S55 illustrates representative orbital contours).

The amount of total electron donation from the phosphine ligand to Ni(III) has been explored using Charge decomposition analyses (CDA).[37] The values have been computed for all $NiCl_3$(LL) and $NiBr_3$(LL) complexes and are compared to the quantum yields in Figure 3.25. A positive correlation between quantum yield and electron donation of the phosphine backbone to Ni(III) is observed for both $NiCl_3$(LL) and $NiBr_3$(LL) complexes.

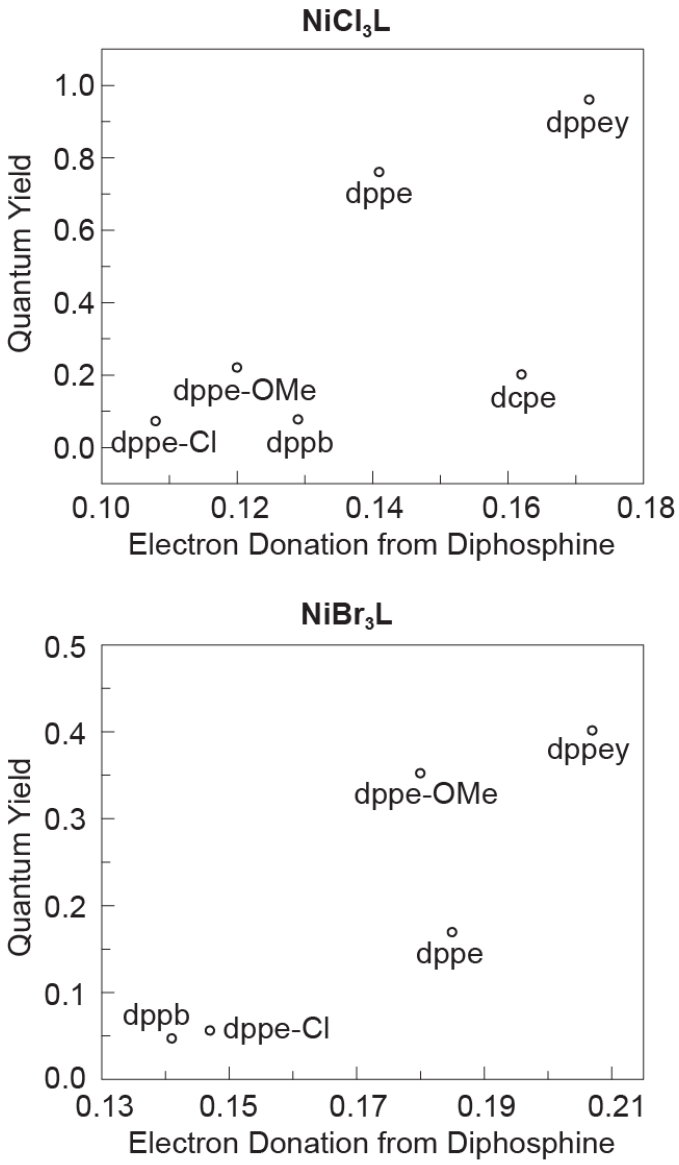

Figure 3.25. Plot of experimental quantum yield versus computed electron donation from the diphosphine backbone to the NiX_3 core.

3.3 Discussion

The significant oxidizing power of Ni(III) suggested the possibility of developing a halogen elimination photochemistry based on Ni(III) complexes and thus the possibility of developing HX-splitting energy storing cycles. To this end, we targeted $NiX_3(LL)$ complexes (X = Cl, Br; LL = bidentate phosphine) (**1**), which are synthesized by the oxidation of corresponding Ni(II) square planar $NiX_2(LL)$ complexes (**3**) with halogen sources. All of the Ni(III) compounds are paramagnetic and possess a square pyramidal primary coordination sphere.

Steady-state photolysis of Ni(III) complexes **1** results in their clean conversion to Ni(II) complexes **3**. The solution photochemistry is characterized by tightly anchored isosbestic points, and both UV-vis and ^{31}P NMR indicate that the photoelimination proceeds cleanly. All of the complexes demonstrate an efficient halogen elimination photochemistry with quantum yields reaching as high as 96%. In general, Cl_2 photoelimination proceeds at higher quantum efficiencies than Br_2 elimination from homologous complexes (Table 3.2). In solution, halogen is trapped by H-atom abstraction from solvent and consequently the photoevolved halogen equivalents are not observed.[38,39] The need to trap the eliminated halogen is circumvented when the photochemistry is carried out in the solid state. Solid-state photolysis of thin-films of Ni(III) complexes **1** affords the Ni(II) complexes **3** and molecular halogen, which has been isolated, characterized, and quantified. Solution-phase calorimetry indicates that halogen addition to Ni(II) is substantially exothermic (Table 3.3), and thus photoelimination from $NiX_3(LL)$ compounds represents an energy-storing transformation.

TA spectra of intermediate generated by $NiCl_3$(LL) photoexcitation display two distinct spectral features: an absorption in the UV region and a broad absorption in the visible region. The photointermediate observed in the TA spectrum of complexes with unsubstituted aryl phosphines exhibits a UV feature at ~350 nm and a band in the visible region at λ_{max} ~ 550 nm. As shown in Figure 3.12, the spectrum of the intermediates is consistent with that of halogen|aryl CT complexes, though it is red-shifted as compared to simple CT adducts owing to electron donation from the phosphine group. The CT absorption band further red-shifts with the introduction of donor groups on the phenyl phosphine. The TA intermediate of **1a-Cl** and **1a-OMe** (Figure 3.12b–c) shifts to 540 nm and 600 nm respectively, consistent with the observed shift of CT bands in arene|Br complexes resulting from aryl substitution with electron donors.[40]

To probe the influence of aromatic residues on the halogen elimination photochemistry, the phenyl groups of the dppe were replaced with cyclohexyl group. Complex **1d** participates in solution-phase halogen elimination but with considerably attenuated quantum yield. A transient intermediate of **1d** is observed but it is weak and considerably blue-shifted from **1a**. Halogen atom adducts of cyclohexane are known and as observed here, the signal is weak and the charge transfer band is blue shifted (λ_{max} = 435 nm) due to an increase in ionization energy of cyclohexane as compared to an aromatic group.[41] Due to the predicted blue shift coupled with the clean conversion to starting material upon photolysis, we believe that the intermediate observed in the TA spectrum of **1d** is also a Cl-radical complex, **2d**. Upon the addition of increasing concentrations of benzene, the quantum yield approaches an asymptotic value of ~65%. We believe that the enhancement in quantum yield is due to specific radical-π interactions, because addition of CCl_4 (similar

dielectric to benzene) did not have a measurable influence on Φ_p. When the TA spectrum of complex **1d** is measured in the presence of 30% benzene, the spectral feature exhibits a 15 nm bathochromic shift (λ_{max} = 450 nm) and the rate of decay of the intermediate is essentially unchanged (Figure 3.19 and Figure 3.20). The enhancement in Φ_p upon the addition of benzene without a change in the time evolution of the intermediate suggests that benzene is enhancing the initial dissociation of the chlorine radical from the nickel center, but does not react at a competitive rate with generated intermediate. The observed decay rate of the intermediate ($\sim 10^5$ s^{-1}) is considerably slower than the dissociation rates observed for Cl-benzene adducts ($\sim 10^6$ s^{-1}).[34] Therefore, only a small and undetectable concentration of Cl-benzene complex would be formed during the experiment.

The computed excited state PES of **1f** (Figure 3.24a) provides further support for rapid halide radical elimination. The excited state PESs are dissociative in both gas phase and dielectric corrected (CH_2Cl_2) calculations suggesting a rapid dissociation of the halide radical from the photoreduced Ni center.[42,43] The fate of the halide radical is then dictated by its subsequent back reaction or sequestration by solvent. Utilization of secondary coordination interactions with arene ligands appears to provide an effective pathway to guide the halogen atom out of the primary coordination sphere, thereby preventing the energetically favored back reaction. For the resulting charge transfer intermediate, the nature of the dominant transitions observed in the TA spectra are predicted by TD-DFT calculations as arene to halide charge transfer, consistent with the spectral shift of the absorptions upon perturbation of the arene ring by the addition of methoxy groups.

Examination of the relationship of Φ_p with both reaction enthalpy and super hyperfine coupling does not reveal a strong correlation of Φ_p with either M–L covalency or reaction thermodynamics (Table 3.1 and Table 3.3, respectively); however, a positive correlation between ligand donor properties (as determined using CDA analyses) and Φ_p was observed. The positive correlation of Φ_p with electron donation from the phosphine ligand to the metal center suggests that the electronic structure has a significant influence on the photolysis reaction. An important factor governing Φ_p will be the relative rates of the various decay pathways of the dissociative electronic excited state. Nonradiative decay pathways have been shown to be sensitive to changes in ligand donor ability[44,45] and electron rich ligands may play a role in suppressing these pathways in the excited $NiX_3(LL)$ complexes studied.

3.4 Conclusion

Photochemical, transient spectroscopic and computational results of the $NiX_3(LL)$ complexes point to the formation of a relatively long-lived (3 μs) transient species derived from a dissociative ligand-to-metal charge transfer (LMCT) excited state. The photodissociative Ni(III)–halogen intermediate is stabilized by interaction of the photoeliminating halogen atom with an aryl ring of the secondary coordination sphere. The efficiency of the photoelimination can be directly traced to the stability of the charge transfer halogen|aryl adduct. Interactions with aromatic groups of a coordinating ligand offers a means to suppress rapid back reactions and increase the quantum yield for halogen elimination, which is the critical step in designing photocatalytic HX splitting cycles.

These results reveal two design principles for enhancing the efficiency of photochemical processes. First, high photoefficiency can be obtained from first row

transition metal complexes by leveraging barrierless dissociative excited states. Such processes are expected to be very fast, mitigating the intrinsically short excited state lifetimes of first row transition metal complexes. Second, enhancements in efficiency can be obtained for photochemical transformations by leveraging the secondary coordination sphere to suppress the generally exothermic back reaction.

3.5 Experimental

Synthesis, steady state photochemistry, and calorimetry experiments were performed by Seung Jun Hwang. TA was done in collaboration with Andrew G. Maher. Calculations were performed by Dr. Ryan G. Hadt.

General Considerations

All reactions were carried out in an N_2-filled glovebox. Anhydrous solvents were obtained from drying columns and stored over activated molecular sieves.[46] $NiCl_2$(dme) (dme = 1,2-dimethoxyethane), $NiBr_2$(dme), dppb (dppb = bis(diphenylphosphino)benzene), dppey (dppey = *cis*-bis(diphenylphos-phino)ethylene), and $NiCl_2$(dppe) (dppe = 1,2-bis(diphenylphosphino)ethane) were obtained from Strem Chemicals. Bromine, dppe, and dcpe (dcpe = 1,2-bis(dicylohexylphosphino)ethane) were obtained from Sigma Aldrich. $PhICl_2$,[47] dppe-MeO (dppe-MeO = 1,2-*bis*(di-4-methoxyphenyl)phosphine)ethane), and dppe-Cl (dppe-Cl = 1,2-*bis*(di-4-chlorophenyl)phosphine)ethane) were prepared according to literature procedures.[48] Ni(III) complexes (**1**) and Ni(II)complexes (**3**) that are discussed herein are enumerated based on the halide (X) and supporting phosphine (LL) ligand: X = Cl, LL = dppe, **1a**, **3a**; X = Cl, LL = dppe-OMe: **1a-OMe**, **3a-OMe**; X = Cl, LL = dppe-Cl: **1a-Cl**, **3a-Cl**; X = Cl, LL = dppey: **1b**, **3b**; X = Cl, LL = dppb: **1c**, **3c**; X = Cl, LL = dcpe: **1d**, **3d**; X = Br, LL = dppe: **1e**, **3e**; X = Br,

LL = dppe-Cl: **1e-Cl**, **3e-Cl**; X = Br, LL = dppe-OMe: **1e-OMe**, **3e-OMe**; X = Br, LL = dppey: **1f**, **3f**; X = Br, LL = dppb: **1g**, **3g**. Complexes **1a**,[49] **1b**,[49] **1c**,[49], **1e**,[49] **1f**,[49] **1g**,[49] **3a**,[50] **3a-OMe**,[48] **3b**,[51] **3c**,[52] **3d**,[53] **3e**,[40] **3e-OMe**,[54] and **3f**[55] were prepared by according to literature procedures. NMR spectra were recorded at the Harvard University Department of Chemistry and Chemical Biology NMR facility on a Varian Unity / Inova 600 spectrometer operating at 600 MHz for ^{1}H acquisitions and 162 MHz for $^{31}P\{^{1}H\}$ acquisitions. NMR chemical shifts are reported in ppm with the residual solvent resonance as internal standard. $^{31}P\{^{1}H\}$ NMR chemical shifts were referenced to an external 85% H_3PO_4 standard. Solution magnetic moments were determined using the Evans method in CH_3CN or CH_2Cl_2 and measured using ^{19}F NMR (hexafluorobenzene added); diamagnetic corrections were estimated from Pascal constants.[56] UV-vis spectra were recorded at 293 K in quartz cuvettes on a Spectral Instruments 400 series diode array blanked against the appropriate solvent. EPR spectra were recorded on a Bruker ELEXIS E-500 or E-580 spectrometer equipped with a Bruker ER4122 SHQE-W1 resonator and an Oxford Instruments ESR 900 cryostat. EPR spectra were simulated using EasySpin 4.5.5 to obtain g-values and hyperfine constants.[57]

Preparation of Ni(II) Dihalide Complexes (NiX_3(LL))

Ni(II) complexes $NiCl_2$(dppe-Cl) (**3a-Cl**), $NiBr_2$(dppe-Cl) (**3e-Cl**), and $NiBr_2$(dppb) (**3g**) were prepared by sequential treatment of NiX_2(dme) (X = Cl and Br) with an equimolar amount of the appropriate phosphine in THF, precipitation with pentane, and isolation by vacuum filtration.

Preparation of Ni(III) Trichloride Complexes ($NiCl_3$(LL))

The following preparation of complex **1a-OMe** is representative of other members of this family. In a scintillation vial was added 60 mg (0.093 mmol) of $NiCl_2$(dppe-OMe) (**3a-OMe**) followed by 2 mL CH_3CN. In a separate vial was added 15.3 mg (0.055 mmol, 0.6 equiv) of $PhICl_2$ and 2 mL CH_3CN. $PhICl_2$ was added dropwise to the solution of **3a-OMe** during which time a color change from orange to green was observed. The solution was stirred with the exclusion of light for 5 min at 23 °C at which time the solvent was removed in vacuo to yield a green solid. The residue was washed with pentane and dried in vacuo to afford 55 mg of the tile complex as a green solid (86% yield). EPR (1:1 $CH_3CN/PhCH_3$) g-value: g_1 = 2.258; g_2 = 2.169; g_3 = 2.017. μ_{eff} = 2.17 μB. EPR (1:1 $CH_3CN/PhCH_3$) g-value: g_1 = 2.241; g_2 = 2.165; g_3 = 2.01. μ_{eff} = 2.13 μB. Complex $NiCl_3$(dcpe) (**1d**) was prepared analogously except CH_2Cl_2 was used as solvent and Et_2O was used to wash: green solid; 60% yield. EPR (1:1 $CH_3CN/PhCH_3$) g-value: g_1 = 2.26; g_2 = 2.28; g_3 = 2.01. μ_{eff} = 2.10 μB.

Preparation of Ni(III) Tribromide Complexes ($NiBr_3$(LL))

The following preparation of complex **1e-OMe** is representative of other members of this family. A sample of $NiBr_2$(dppe-OMe) (**3e-OMe**) (60 mg, 0.081 mmol) was dissolved in 2 mL of CCl_4. A solution of 0.194 M Br_2 (206 μL, 0.041 mmol, 0.5 equiv) in CH_2Cl_2 was added dropwise to give a black solution, which was stirred at 23 °C for 30 min in the dark. The volatiles were removed in vacuo to give the product as a dark brown powder. The residue was washed with pentane and dried in vacuo (80% Yield). EPR (1:1 $CH_2Cl_2/PhCH_3$) g-value: g_1 = 2.208; g_2 = 2.208; g_3 = 2.025. μ_{eff} = 1.95 μB. Complex **1e-Cl** was prepared analogously: dark brown solid; 77% yield. EPR (1:1 $CH_3CN/PhCH_3$) g-value: g_1 = 2.201; g_2 = 2.191; g_3 = 2.025. μ_{eff} = 1.90 μB.

Photochemistry

Steady-state photochemical reactions were performed using a 1000 W high-pressure Hg/Xe arc lamp (Oriel) and the beam was passed through a water-jacketed filter holder containing the appropriate long-pass filter, an iris and a collimating lens. Samples were photolyzed in a constant-temperature circulating water bath. Photochemical quantum yields (Φ_p) were determined using 370 nm monochromatic light, which was generated with a 370 nm Hg line filter on a 1000 W Hg/Xe arc lamp. Potassium ferrioxalate solution (0.006M) was used as a chemical actinometer.[58] The photo flux was determined from the average of actinometric measurements before and after irradiation of the reaction samples. Each Φ_p determination was carried out in triplicate on solutions of the complex in CH_2Cl_2 or CH_3CN with benzene. Nanosecond resolved transient absorption (TA) spectroscopy experiments were performed using a system described previously,[59] but with an iHR320 spectrometer. The 355 nm laser pulses (8-10 ns at FWHM) used for excitation were generated using the third harmonic of a 10 Hz Nd:YAG pulsed laser. The white-light continuum was provided by a Xe-arc lamp set to 2.0 ms pulses with 30 A current. A 250 nm or 1000 nm blaze grating (300 grooves/mm) was used for spectral acquisitions centered below 500 nm and above 500 nm, respectively. For full spectrum TA acquisitions, the entrance slit was set to 0.16 mm (3.0 nm resolution) and the gate time for the CCD was 100 ns to 200 ns. For single-wavelength kinetics experiments, the entrance and exit slits were set to 3 nm resolution, and 1.0 kV bias was used for the photomultiplier tube (PMT). PMT outputs were collected and averaged with a 1 GHz oscilloscope (LeCroy 9384CM). The full spectra are averages of 50-200 four-spectrum sequences and the single-wavelength kinetics traces are averages of 500-1000 acquisitions. CH_3CN solutions of complexes **1a**–**1d**

were prepared in 100 mL Schlenk flasks in an N_2-filled glovebox. During TA acquisitions the solutions were flowed without recirculation through a 3-mm diameter, 1-cm path length flow cell (Starna, type 585.2) using a peristaltic pump and positive N_2 pressure.

X-Ray Crystallographic Details

Single crystals of **1c** were obtained from a CH_2Cl_2 solution layered with toluene. Crystals of **1g** were obtained from a CH_2Cl_2/$PhCH_3$ solution of the complex layered with a small amount of Br_2 in CH_2Cl_2 solution. Diffraction data were collected either on a Bruker three-circle platform goniometer equipped with an Apex II CCD and an Oxford cryostream cooling device (100 K) with radiation from a graphite fine focus sealed tube Mo Kα (0.71073 Å) source or on a vertically mounted Bruker D8 three-circle platform goniometer equipped with an Apex II CCD and an Oxford Diffraction Helijet cooling device (15 K) with synchrotron radiation (0.41328 Å) supplied to ChemMatCARS located at Advances Photon Source (APS), Argonne National Laboratory (ANL). Crystals were mounted on a glass fiber pin using Paratone N oil. Data was collected as a series of φ and/or ω scans. Data was integrated using SAINT and scaled with multi-scan absorption correction using SADABS.[60] The structures were solved by intrinsic phasing using SHELXT (Apex2 program suite v2014.1) and refined against F^2 on all data by full matrix least squares with SHELXL-97.[61] All non-H atoms were refined anisotropically. H atoms were placed at idealized positions and refined using a riding model. Crystal data and refinement statistics are summarized in Table 3.5 and thermal ellipsoid plots are collected in Fig. 4. X-ray crystal structures of **1c**, **1g**, **3c** and **3e** are available from the Cambridge Crystal Structure Database (1040260, 1040259, 1401868, and 1401864, respectively).

Table 3.5. Crystal data and structure refinement for **1c** and **1g**.

	$NiCl_3$(dppb) (1c)	**$NiBr_3$(dppb) (1g)**
formula	$C_{30}H_{24}Cl_3NiP_2$	$C_{16.5}H_{15}Br_{1.5}Cl_3Ni_{0.5}P$
CCDC #	1040260	1040259
fw, g/mol	611.49	499.83
temp, K	100 (2)	15 (2)
cryst system	Monoclinic	Monoclinic
space group	*P2(1)*	*P2(1)/m*
color		
a, Å	9.7441 (9)	8.7809 (4)
b, Å	14.730 (1)	21.401 (1)
c, Å	10.2714 (9)	10.6362 (5)
α, deg	90	90
β, deg	113.297 (2)	113.3720 (7)
γ, deg	90	90
V, A^3	1354.1 (2)	1834.8 (2)
Z	2	4
R1[a]	0.0525	0.0187
wR2[b]	0.0861	0.0439
GOF[c] (F^2)	0.983	1.039
R_{int}	0.0678	0.0210

[a] $R1 = \Sigma||F_o| - |F_c||/\Sigma|F_o|$. [b] $wR2 = (\Sigma(w(F_o^2 - F_c^2)^2)/\Sigma(w(F_o^2)^2))^{1/2}$. [c] $GOF = (\Sigma w(F_o^2 - F_c^2)^2/(n - p))^{1/2}$ where n is the number of data and p is the number of parameters refined.

Solution-Phase Calorimetry

Solution-phase calorimetry measurements were carried out using a Thermometric 2225 Precision Solution calorimeter. In the glove box, a CH_2Cl_2 solution of Ni(II) dichloride was prepared. This solution was transferred to the glass cell of the calorimeter, which was equipped with an ampule-breaking rod. A small glass ampule containing $PhICl_2$ was added, sealed, and loaded into the calorimeter. Following temperature equilibration (achieved standard deviation of 2 μK after 2 h), the reaction was initiated by breaking the ampoule and rotating the calorimeter to ensure complete mixing. Electrical calibrations were run before and after breaking the ampoule. The enthalpy of chlorination of Ni(II) was determined by subtracting half the enthalpy of chlorination of PhI from the experimentally measured reaction enthalpy. Measured data was corrected for the enthalpy of solution of the solid $PhICl_2$, which was measured separately. Reported data is the average of three independent measurements.

Computational Details

All DFT calculations were performed using the Gaussian 09, Revision D.01 software suite.[62] For all calculations, the B3LYP[63–65] hybrid exchange-correlation functional was used in combination with a split basis set (TZVP66 for Ni, P, and Br; TZV67 for C and H). Starting geometries for gas-phase optimization were obtained from crystallographic coordinates; frequency calculations were carried out to ensure structures represented energetic minima. Geometries used for DFT calculations are available free of charge on the ACS Publications website at DOI: 10.1021/acs.organomet.5b00568. Time-dependent DFT (TD-DFT) single point calculations were carried out on the gas-phase geometry optimized models using the same combination of functional and basis sets. Where used, solvation

effects were included using the polarized continuum model (PCM). Ground and excited state potential energy surfaces (PESs) for metal-apical halide bond loss were constructed using constrained geometry optimizations coupled to subsequent TD-DFT calculations. Charge decomposition analyses (CDA) were carried out using the AOMix program (revision 6.82).[68] The degree of phosphine ligand donation was calculated using NiX_3 and phosphine ligands as fragments; the degree of phosphine ligand donation was calculated as the difference in total electron donation (sum of all occupied α and β molecular orbitals) from the phosphine ligand to NiX_3 and back-donation between NiX_3 and the phosphine ligand. Wavefunction contours were generated using the β-LUMO program.[69]

3.6 References

1. Rosenthal, J.; Nocera, D. G. Role of Proton-Coupled Electron Transfer in O–O Bond Activation. Acc. Chem. Res. 2007, 40 (7), 543–553.

2. Rosenthal, J.; Nocera, D. G. Oxygen Activation Chemistry of Pacman and Hangman Porphyrin Architectures Based on Xanthene and Dibenzofuran Spacers. In *Progress in Inorganic Chemistry*; Karlin, K. D., Ed.; John Wiley & Sons, Inc., 2007; pp 483–544.

3. Nicolet, Y.; Cavazza, C.; Fontecilla-Camps, J. C. Fe-Only Hydrogenases: Structure, Function and Evolution. *Journal of Inorganic Biochemistry* **2002**, *91* (1), 1–8.

4. Nicolet, Y.; Lemon, B. J.; Fontecilla-Camps, J. C.; Peters, J. W. A Novel FeS Cluster in Fe-Only Hydrogenases. *Trends in Biochemical Sciences* **2000**, *25* (3), 138–143.

5. Peters, J. W. Structure and Mechanism of Iron-Only Hydrogenases. *Current Opinion in Structural Biology* **1999**, *9* (6), 670–676.

6. DuBois, M. R.; DuBois, D. L. The Roles of the First and Second Coordination Spheres in the Design of Molecular Catalysts for H2 Production and Oxidation. *Chem. Soc. Rev.* **2008**, *38* (1), 62–72.

7. Rakowski Dubois, M.; Dubois, D. L. Development of Molecular Electrocatalysts for CO_2 Reduction and H_2 Production/Oxidation. *Acc. Chem. Res.* **2009**, *42* (12), 1974–1982.

8. Bediako, D. K.; Solis, B. H.; Dogutan, D. K.; Roubelakis, M. M.; Maher, A. G.; Lee, C. H.; Chambers, M. B.; Hammes-Schiffer, S.; Nocera, D. G. Role of Pendant Proton Relays and Proton-Coupled Electron Transfer on the Hydrogen Evolution Reaction by Nickel Hangman Porphyrins. *PNAS* **2014**, *111* (42), 15001–15006.

9. McGuire, R. Jr.; Dogutan, D. K.; Teets, T. S.; Suntivich, J.; Shao-Horn, Y.; Nocera, D. G. Oxygen Reduction Reactivity of cobalt(II) Hangman Porphyrins. *Chem. Sci.* **2010**, *1* (3), 411–414.

10. Dogutan, D. K.; McGuire, R. Jr.; Nocera, D. G. Electocatalytic Water Oxidation by Cobalt(III) Hangman β-Octafluoro Corroles. *J. Am. Chem. Soc.* **2011**, *133* (24), 9178–9180.

11. Lee, C. H.; Dogutan, D. K.; Nocera, D. G. Hydrogen Generation by Hangman Metalloporphyrins. *J. Am. Chem. Soc.* **2011**, *133* (23), 8775–8777.

12. Borovik, A. S. Bioinspired Hydrogen Bond Motifs in Ligand Design: The Role of Noncovalent Interactions in Metal Ion Mediated Activation of Dioxygen. *Acc. Chem. Res.* **2005**, *38* (1), 54–61.

13. Park, Y. J.; Matson, E. M.; Nilges, M. J.; Fout, A. R. Exploring Mn–O Bonding in the Context of an Electronically Flexible Secondary Coordination Sphere: Synthesis of a Mn(III)–oxo. *Chem. Commun.* **2015**, *51* (25), 5310–5313.

14. Esswein, A. J.; Nocera, D. G. Hydrogen Production by Molecular Photocatalysis. *Chem. Rev.* **2007**, *107* (10), 4022–4047.

15. Nocera, D. G. Chemistry of Personalized Solar Energy. *Inorg. Chem.* **2009**, *48* (21), 10001–10017.

16. Teets, T. S.; Nocera, D. G. Photocatalytic Hydrogen Production. *Chem. Commun.* **2011**, *47* (33), 9268–9274.

17. Cook, T. R.; Surendranath, Y.; Nocera, D. G. Chlorine Photoelimination from a Diplatinum Core: Circumventing the Back Reaction. *J. Am. Chem. Soc.* **2009**, *131* (1), 28–29.

18. Lin, T.-P.; Gabbaï, F. P. Two-Electron Redox Chemistry at the Dinuclear Core of a TePt Platform: Chlorine Photoreductive Elimination and Isolation of a TeVPtI Complex. *J. Am. Chem. Soc.* **2012**, *134* (29), 12230–12238.

19. Yang, H.; Gabbaï, F. P. Solution and Solid-State Photoreductive Elimination of Chlorine by Irradiation of a [PtSb]VII Complex. *J. Am. Chem. Soc.* **2014**, *136* (31), 10866–10869.

20. Raphael Karikachery, A.; Lee, H. B.; Masjedi, M.; Ross, A.; Moody, M. A.; Cai, X.; Chui, M.; Hoff, C. D.; Sharp, P. R. High Quantum Yield Molecular Bromine Photoelimination from Mononuclear Platinum(IV) Complexes. *Inorg. Chem.* **2013**, *52* (7), 4113–4119.

21. Perera, T. A.; Masjedi, M.; Sharp, P. R. Photoreduction of Pt(IV) Chloro Complexes: Substrate Chlorination by a Triplet Excited State. *Inorg. Chem.* **2014**, *53* (14), 7608–7621.

22. Teets, T. S.; Nocera, D. G. Halogen Photoreductive Elimination from Gold(III) Centers. *J. Am. Chem. Soc.* **2009**, *131* (21), 7411–7420.

23. Powers, D. C.; Chambers, M. B.; Teets, T. S.; Elgrishi, N.; Anderson, B. L.; Nocera, D. G. Halogen Photoelimination from Dirhodium Phosphazane Complexes via Chloride-Bridged Intermediates. *Chem. Sci.* **2013**, *4* (7), 2880–2885.

24. Cook, T. R.; Esswein, A. J.; Nocera, D. G. Metal–Halide Bond Photoactivation from a PtIII–AuII Complex. *J. Am. Chem. Soc.* **2007**, *129* (33), 10094–10095.

25. Cook, T. R.; McCarthy, B. D.; Lutterman, D. A.; Nocera, D. G. Halogen Oxidation and Halogen Photoelimination Chemistry of a Platinum–Rhodium Heterobimetallic Core. *Inorg. Chem.* **2012**, *51* (9), 5152–5163.

26. Teets, T. S.; Lutterman, D. A.; Nocera, D. G. Halogen Photoreductive Elimination from Metal–Metal Bonded Iridium(II)–Gold(II) Heterobimetallic Complexes. *Inorg. Chem.* **2010**, *49* (6), 3035–3043.

27. Creutz, C.; Chou, M.; Netzel, T. L.; Okumura, M.; Sutin, N. Lifetimes, Spectra, and Quenching of the Excited States of Polypyridine Complexes of iron(II), ruthenium(II), and osmium(II). *J. Am. Chem. Soc.* **1980**, *102* (4), 1309–1319.

28. McCusker, J. K. Femtosecond Absorption Spectroscopy of Transition Metal Charge-Transfer Complexes. *Acc. Chem. Res.* **2003**, *36* (12), 876–887.

29. Juban, E. A.; Smeigh, A. L.; Monat, J. E.; McCusker, J. K. Ultrafast Dynamics of Ligand-Field Excited States. *Coordination Chemistry Reviews* **2006**, *250* (13–14), 1783–1791.

30. Bruin, B. D.; Hetterscheid, D. G. H.; Koekkoek, A. J. J.; Grützmacher, H. In Progress in Inorganic Chemistry; Karlin, K. D., Ed.; J. Wiley and Sons: New York, 2007; Vol. 55, p 247.

31. Bühler, R. E.; Ebert, M. Transient Charge-Transfer Complexes with Chlorine Atoms by Pulse Radiolysis of Carbon Tetrachloride Solutions. *Nature* **1967**, *214* (5094), 1220–1221.

32. Strong, R. L.; Rand, S. J.; Britt, J. A. Charge-Transfer Spectra of Iodine Atom-Aromatic Hydrocarbon Complexes1. *J. Am. Chem. Soc.* **1960**, *82* (19), 5053–5057.

33. Bossy, J. M.; Buehler, R. E.; Ebert, M. Pulse Radiolysis of Organic Halogen Compounds. II. Transient Bromine-Atom Charge-Transfer Complexes Observed by Pulse Radiolysis. *J. Am. Chem. Soc.* **1970**, *92* (4), 1099–1101.

34. Förgeteg, S.; Bérces, T. Laser Flash Photolysis Study of Chlorine Atom/simple Arene π-Complexes in Carbon Tetrachloride and Acetonitrile. *Journal of Photochemistry and Photobiology A: Chemistry* **1993**, *73* (3), 187–195.

35. Sokolov, A. Y.; Schaefer III, H. F. Ground and excited state properties of photoactive platinum(iv) diazido complexes: Theoretical considerations. *Dalton Trans*. **2011**, *40*, 7571.

36. Tsao, M.-L.; Hadad, C. M.; Platz, M. S. Computational Study of the Halogen Atom–Benzene Complexes. *J. Am. Chem. Soc.* **2003**, *125* (27), 8390–8399.

37. Dapprich, S.; Frenking, G. Investigation of Donor-Acceptor Interactions: A Charge Decomposition Analysis Using Fragment Molecular Orbitals. *J. Phys. Chem.* **1995**, *99* (23), 9352–9362.

38. Hendry, D. G.; Mill, T.; Piszkiewicz, L.; Howard, J. A.; Eigenmann, H. K. A Critical Review of H-Atom Transfer in the Liquid Phase: Chlorine Atom, Alkyl, Trichloromethyl, Alkoxy, and Alkylperoxy Radicals. *Journal of Physical and Chemical Reference Data* **1974**, *3* (4), 937–978.

39. Olbregts, J.; Brasseur, G.; Arijs, E. Reaction of Acetonitrile and Chlorine Atoms. *Journal of Photochemistry* **1984**, *24* (4), 315–322.

40. Raner, K. D.; Lusztyk, J.; Ingold, K. U. Ultraviolet/visible Spectra of Halogen Molecule/arene and Halogen Atom/arene .pi.-Molecular Complexes. *J. Phys. Chem.* **1989**, *93* (2), 564–570.

41. Alfassi, Z. B.; Huie, R. E.; Mittal, J. P.; Neta, P.; Shoute, L. C. T. Charge-Transfer Complexes of Bromine Atoms with Haloalkanes and Alkanes. *J. Phys. Chem.* **1993**, *97* (36), 9120–9123

42. Rosker, M. J.; Dantus, M.; Zewail, A. H. Femtosecond Real-time Probing of Reactions. I. The Technique. *The Journal of Chemical Physics* **1988**, *89* (10), 6113–6127.

43. Roberts, G.; Zewail, A. H. Femtosecond Real-Time Probing of Reactions. 7. A Quantum- and Classical-Mechanical Study of the Cyanogen Iodide Dissociation Experiment. *J. Phys. Chem.* **1991**, *95* (21), 7973–7993.

44. Della Ciana, L.; Dressick, W. J.; Sandrini, D.; Maestri, M.; Ciano, M. Synthesis and Characterization of a New Family of Luminescent Cis-(4,4'-X2-5,5'-Y2-2,2'-bipyridine)$_2$Os(CO)Cl(PF_6) Complexes (X = NEt_2, OMe, Me, H, Cl, Y = H; X = H, Y = Me; X = Y = Me): Control of Excited-State Properties by Bipyridyl Substituents. *Inorg. Chem.* **1990**, *29* (15), 2792–2798.

45. Takizawa, S.; Shimada, K.; Sato, Y.; Murata, S. Controlling the Excited State and Photosensitizing Property of a 2-(2-Pyridyl)benzo[b]thiophene-Based Cationic Iridium Complex through Simple Chemical Modification. *Inorg. Chem.* **2014**, *53* (6), 2983–2995.

46. Pangborn, A. B.; Giardello, M. A.; Grubbs, R. H.; Rosen, R. K.; Timmers, F. J. Safe and Convenient Procedure for Solvent Purification. *Organometallics* **1996**, *15* (5), 1518–1520.

47. Zielinska, A.; Skulski, L. A Solvent-Free Synthesis of (dichloroiodo)arenes from Iodoarenes. *Tetrahedron Letters* **2004**, *45* (5), 1087–1089.

48. Fawcett, J.; Hope, E. G.; Stuart, A. M.; Sherrington, J. Coordination Chemistry of 1,2-Bis{di-(4-Methoxyphenyl)phosphino}ethane (L-L) to Nickel, Palladium and Platinum: Single Crystal Structures of [MCl2(L-L)] (M = Ni, Pd). *Inorganica Chimica Acta* **2006**, *359* (11), 3535–3539.

49. Gray, L. R.; Higgins, S. J.; Levason, W.; Webster, M. Co-Ordination Chemistry of Higher Oxidation States. Part 8. Nickel(III) Complexes of Bi- and Multi-Dentate Phosphorus and Arsenic Ligands; Crystal and Molecular Structure of [Ni(Ph2PCH2CH2PPh2)Br3]·C6H5Me. *J. Chem. Soc., Dalton Trans.* **1984**, No. 3, 459–467.

50. Zarkesh, R. A.; Hopkins, M. D.; Jordan, R. F. Halogenolysis of a Nickelalactone Complex Produces β-Halo-Anhydrides. *Eur. J. Inorg. Chem.* **2014**, *2014* (32), 5491–5494.

51. Bomfim, J. A. S.; de Souza, F. P.; Filgueiras, C. A. L.; de Sousa, A. G.; Gambardella, M. T. P. Diphosphine Complexes of Nickel: Analogies in Molecular Structures and Variety in Crystalline Arrangement. *Polyhedron* **2003**, *22* (12), 1567–1573.

52. Smeets, B. J. J.; Meijer, R. H.; Meuldijk, J.; Vekemans, J. A. J. M.; Hulshof, L. A. Process Design and Scale-Up of the Synthesis of 2,2‘:5‘,2‘ ‘-Terthienyl. *Org. Process Res. Dev.* **2003**, *7* (1), 10–16.

53. Carroll, M. E.; Barton, B. E.; Gray, D. L.; Mack, A. E.; Rauchfuss, T. B. Active-Site Models for the Nickel–Iron Hydrogenases: Effects of Ligands on Reactivity and Catalytic Properties. *Inorg. Chem.* **2011**, *50* (19), 9554–9563.

54. Angulo, I. M.; Bouwman, E.; Lutz, M.; Mul, W. P.; Spek, A. L. Autoionization of Homogeneous Nickel(II) Diphosphane Hydrogenation Catalysts. An NMR Study and Crystal Structures of [Ni(o-MeO-dppe)I2] and [Ni(o-MeO-dppe)2](PF6)2. *Inorg. Chem.* **2001**, *40* (9), 2073–2082.

55. Jarrett, P. S.; Sadler, P. J. Nickel(II) Bis(phosphine) Complexes. *Inorg. Chem.* **1991**, *30* (9), 2098–2104.

56. Bain, G. A.; Berry, J. F. Diamagnetic Corrections and Pascal’s Constants. *J. Chem. Educ.* **2008**, *85* (4), 532.

57. Stoll, S.; Schweiger, A. EasySpin, a Comprehensive Software Package for Spectral Simulation and Analysis in EPR. *Journal of Magnetic Resonance* **2006**, *178* (1), 42–55.

58. Montalti, M.; Credi, A.; Prodi, L.; Gandolfi, M. T. *Handbook of Photochemistry*, 3rd ed.; Taylor and Francis: Boca Raton, 2006.

59. Holder, P. G.; Pizano, A. A.; Anderson, B. L.; Stubbe, J.; Nocera, D. G. Deciphering Radical Transport in the Large Subunit of Class I Ribonucleotide Reductase. *J. Am. Chem. Soc.* **2011**, *134* (2), 1172–1180.

60. Bruker AXS (2009). Apex II. Bruker AXS, Madison, Wisconsin.

61. Sheldrick, G. M. Experimental phasing with *SHELXC*/*D*/*E*: combining chain tracing with density modification. *Acta Cryst.* **2010**, *D66*, 479.

62. Frisch, M. J.; Trucks, G. W.; Schlegel, H. B.; Scuseria, G. E.; Robb, M. A.; Cheeseman, J. R.; Scalmani, G.; Barone, V.; Mennucci, B.; Petersson, G. A.; Nakatsuji, H.; Caricato, M.; Li, X.; Hratchian, H. P.; Izmaylov, A. F.; Bloino, J.; Zheng, G.; Sonnenberg, J. L.; Hada, M.; Ehara, M.; Toyota, K.; Fukuda, R.; Hasegawa, J.; Ishida, M.; Nakajima, T.; Honda, Y.; Kitao, O.; Nakai, H.; Vreven, T.; Montgomery, J. A., Jr.; Peralta, J. E.; Ogliaro, F.; Bearpark, M.; Heyd, J. J.; Brothers, E.; Kudin, K. N.; Staroverov, V. N.; Keith, T.; Kobayashi, R.; Normand, J.; Raghavachari, K.; Rendell, A.; Burant, J. C.; Iyengar, S. S.; Tomasi, J.; Cossi, M.; Rega, N.; Millam, J. M.; Klene, M.; Knox, J. E.; Cross, J. B.; Bakken, V.; Adamo, C.; Jaramillo, J.; Gomperts, R.; Stratmann, R. E.; Yazyev, O.; Austin, A. J.; Cammi, R.; Pomelli, C.; Ochterski, J. W.; Martin, R. L.; Morokuma, K.; Zakrzewski, V. G.; Voth, G. A.; Salvador, P.; Dannenberg, J. J.; Dapprich, S.; Daniels, A. D.; Farkas, O.; Foresman, J. B.; Ortiz, J. V.; Cioslowski, J.; Fox, D. J. *Gaussian 09*, revision D.01; Gaussian, Inc.: Wallingford, CT, 2009.

63. Stephens, P. J.; Devlin, F. J.; Chabalowski, C. F.; Frisch, M. J. Ab Initio Calculation of Vibrational Absorption and Circular Dichroism Spectra Using Density Functional Force Fields. *J. Phys. Chem.* **1994**, *98* (45), 11623–11627.

64. Lee, C.; Yang, W.; Parr, R. G. Development of the Colle-Salvetti Correlation-Energy Formula into a Functional of the Electron Density. *Phys. Rev. B* **1988**, *37* (2), 785–789.

65. Becke, A. D. Density-functional Thermochemistry. III. The Role of Exact Exchange. *The Journal of Chemical Physics* **1993**, *98* (7), 5648–5652.

66. Schäfer, A.; Huber, C.; Ahlrichs, R. Fully Optimized Contracted Gaussian Basis Sets of Triple Zeta Valence Quality for Atoms Li to Kr. *The Journal of Chemical Physics* **1994**, *100* (8), 5829–5835.

67. Schäfer, A.; Horn, H.; Ahlrichs, R. Fully Optimized Contracted Gaussian Basis Sets for Atoms Li to Kr. *The Journal of Chemical Physics* **1992**, *97* (4), 2571–2577.

68. (a) Gorelsky, S. I.; Lever, A. B. P. Electronic structure and spectra of ruthenium diimine complexes by density functional theory and INDO/S. Comparison of the two methods. *J. Organomet. Chem*. **2001**, *635*, 187. (b) Gorelsky, S. I. *AOMix: Program for Molecular Orbital Analysis*, revision 6.82; http://www.sg-chem.net, Ottawa, ON, 2013.

69. Kieber-Emmons, M. T. *Lumo*, Version 0.9b; Burlingame, CA, 2011.

Chapter 4: Observation of Chloride-Bridged Photointermediates in Valence-Isomeric Rh_2 Complexes

Portions of this chapter have been published:

Reproduced in part with permission from Powers, D. C.; Anderson, B. L.; Hwang, S. J.; Powers, T. M.; Pérez, L. M.; Hall, M. B.; Zheng, S.-L.; Chen, Y.-S.; Nocera, D. G. *J. Am. Chem. Soc.* **2014**, *136* (43), 15346–15355. Copyright 2014 American Chemical Society.

Reproduce in part from Powers, D. C.; Chambers, M. B.; Teets, T. S.; Elgrishi, N.; Anderson, B. L.; Nocera, D. G. Halogen Photoelimination from Dirhodium Phosphazane Complexes via Chloride-Bridged Intermediates. *Chem. Sci.* **2013**, *4* (7), 2880–2885 with permission from the Royal Society of Chemistry.

4.1 Introduction

Polynuclear transition metal complexes are revered for their ability to perform multielectron transformations. Polynuclear transition metal sites commonly comprise redox catalysts in biological and chemical settings. Examples of multielectron redox transformations facilitated by polynuclear metal cofactors abound in nature with notable examples such as O_2 and H^+ reduction,[1,2] H_2O oxidation,[3] and N_2 fixation.[4,5] In heterogeneous catalysis, high-nuclearity surface features, such as step edges and defects that are capable of interacting with substrates via multipoint binding, are often proposed as catalyst active sites.[6–9]

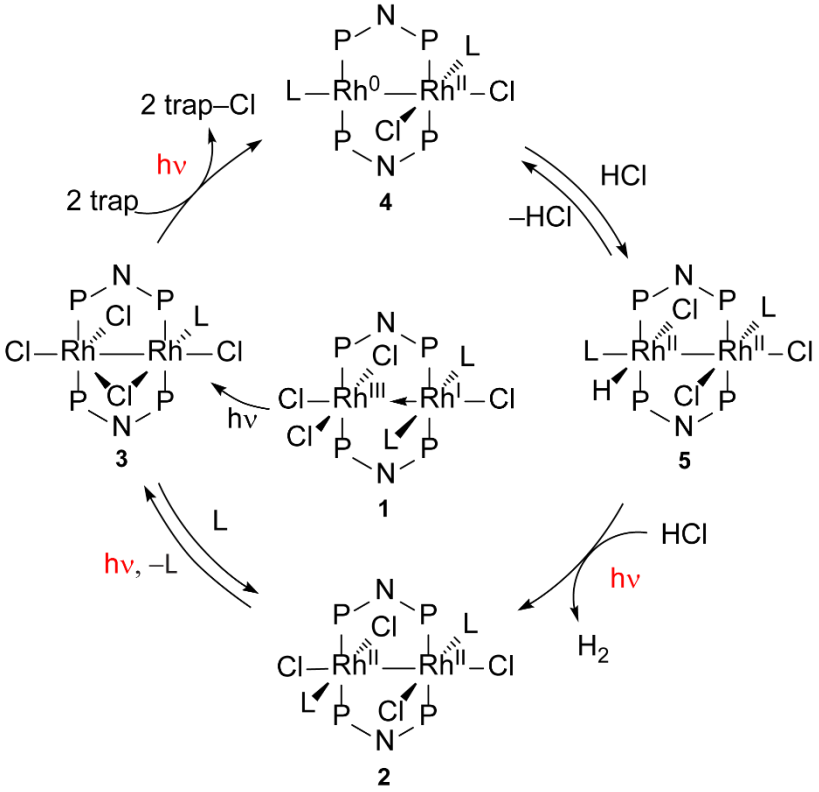

Figure 4.1. HX-splitting photocycle catalyzed by Rh_2[I,III] complex **1** or Rh_2[II,II] complex **2** involves both proton reduction and halide oxidation. The critical halide oxidation step is proposed to proceed from halide-bridged intermediate **3**.

HX-splitting, like H_2O-splitting schemes, stores substantial energy but necessitates the management of only two proton/electron equivalents in contrast to the four implicit in H_2O splitting.[3,10,11] We have developed a family of two-electron mixed-valent dirhodium HX-splitting photocatalysts (i.e., Rh_2[I,III] complex **1** and Rh_2[II,II] complex **2**, Figure 4.1) predicated on the hypothesis that two-electron mixed valency can engender molecular excited states with the proclivity to engage in two-electron redox transformations.[12,13] These complexes have proven to be adept at multielectron photoreactions; H_2-evolving photocatalysis has been realized in which formal halogen elimination reactions close the catalytic cycle.[14,15]

This Chapter explores the mechanism of photoreduction of two dirhodium valence isomers: a two-electron, mixed-valence Rh_2[I,III] complex **1** and a valence-symmetric Rh_2[II,II] complex **2**. Transient spectroscopy experiments suggest that two complexes proceed through a common photochemical intermediate, complex **3**, which we propose to be a chloride-bridged complex. Photocrystallography provided direct information regarding structural changes associated with intermediates of consequence to halogen elimination. Together with solution-phase and solid-state transient absorption (TA) and density functional theory (DFT) modeling, we establish that halide-bridged intermediates are the critical intermediates of halogen elimination from two-electron bimetallic cores. These insights lead to the synthesis of a new suite of dirhodium complexes which allowed isolation and independent evaluation of the chemistry of the halide-bridged bimetallic complexes and the positive identification of the proposed photo-intermediate, complex **3**. These results implicate binuclear reductive elimination as the operative mechanism for halogen photoelimination in this class of complexes.

4.2 Results

4.2.1 Steady State Photochemistry of Dirhodium Isocyanides

While developing the new structural class of HCl-splitting dirhodium photocatalysts,[16] we isolated two dirhodium valence isomers: two-electron mixed-valent Rh_2[I,III] complex **1** and valence-symmetric Rh_2[II,II] complex **2**. Complexes **1** and **2** undergo photoreduction under identical conditions (Figure 4.2). Photolysis of a THF solution of **1** (λ >295 nm), which displays absorbance features at 329 and 379 nm, resulted in the consumption of **1** and formation of the valence-symmetric isomer **2** and the chlorine elimination product complex **4** (Figure 4.3a). Photolysis of the lower energy feature (λ >380 nm) leads exclusively to complex **2**, maintaining isosbestic points through the process (Figure 4.3b). Complex **2** exhibits a single prominent band in the 300 nm region at λ ~350 nm. Photolysis of **2** leads directly to the elimination product, complex **4** (Figure 4.3c).

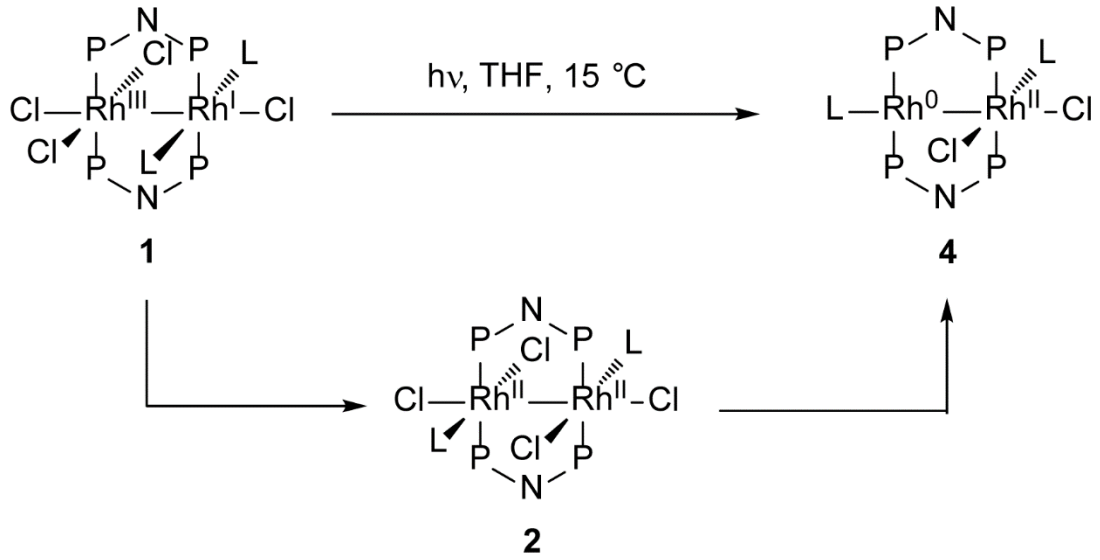

Figure 4.2. Photolysis of two-electron mixed-valent Rh_2[I,III] complex **1** affords Rh_2[0,II] complex **4** via both direct halogen elimination, as well as isomerization to valence-symmetric Rh_2[II,II] **2**, which undergoes halogen elimination; L = 1-adamantylisocyanide, P–N–P = (bis(trifluoroethoxy)phosphinyl)methylamine (tfepma).

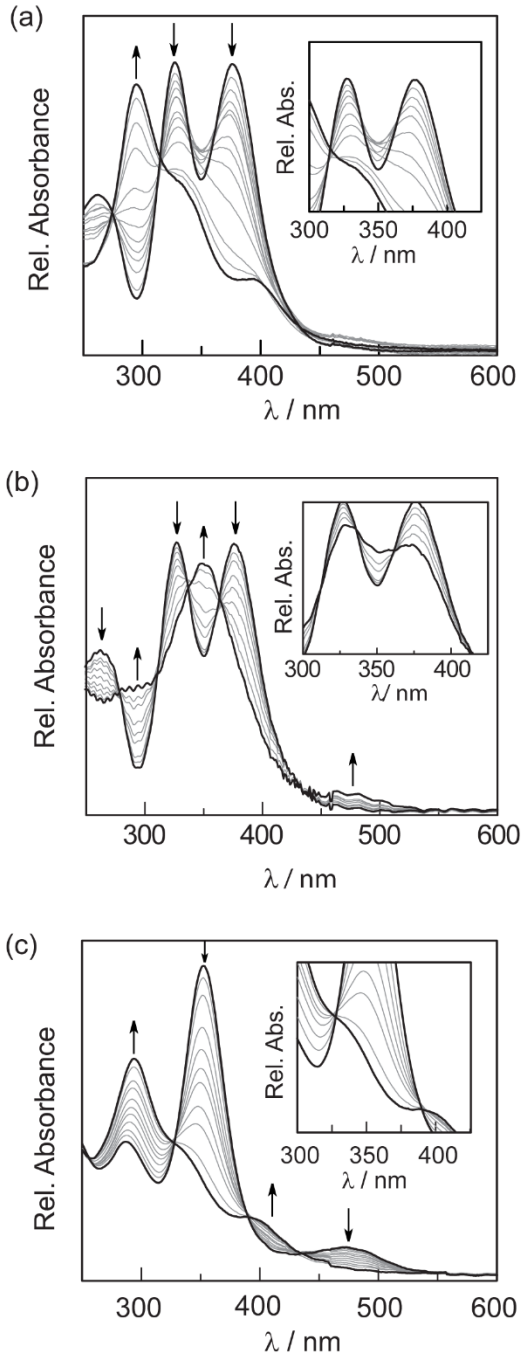

Figure 4.3. (a) Photolysis of complex **1** (λ >295 nm) results in production of both **2** and **4**. (b) Photolysis of complex **1** (λ >380 nm) leads to the exclusive production of **2**. (c) Photolysis of complex **2** (λ >295 nm) proceeds directly to complex **4**.

4.2.2 Transient Absorption Spectroscopy of Dirhodium Isocyanides

Based on the similarity photochemistry of complexes **1** and **2**, we posited that a common intermediate may be accessed in photolysis of these complexes. To evaluate this contention, laser flash photolysis (λ_{exc} > 355 nm) of complexes **1** and **2** in THF was carried out and the transient absorption (TA) difference spectra shown in Figure 4.4 (— black) were obtained. The TA spectrum of **1** exhibits ground-state bleaches at 329 and 379 nm

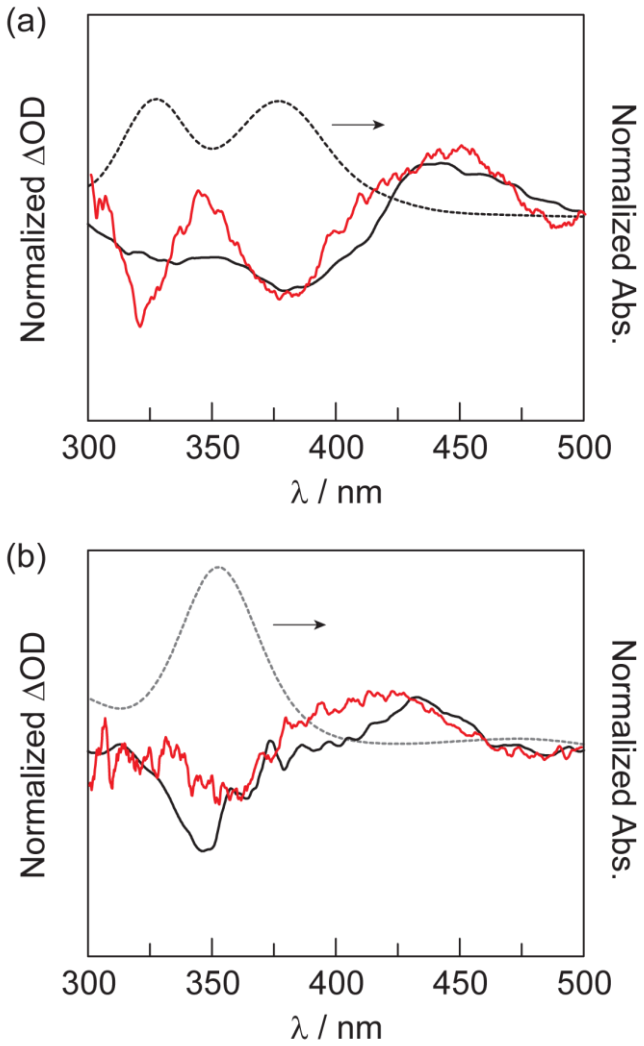

Figure 4.4. UV–vis spectra (dotted black), solution-phase TA spectra (solid black), and thin-film TA spectra (red) of (a) Rh_2[I,III] complex **1** and (b) Rh_2[II,II] complex **2**. TA spectra were obtained by flash laser photolysis (355 nm) and recorded at a 1 μs delay.

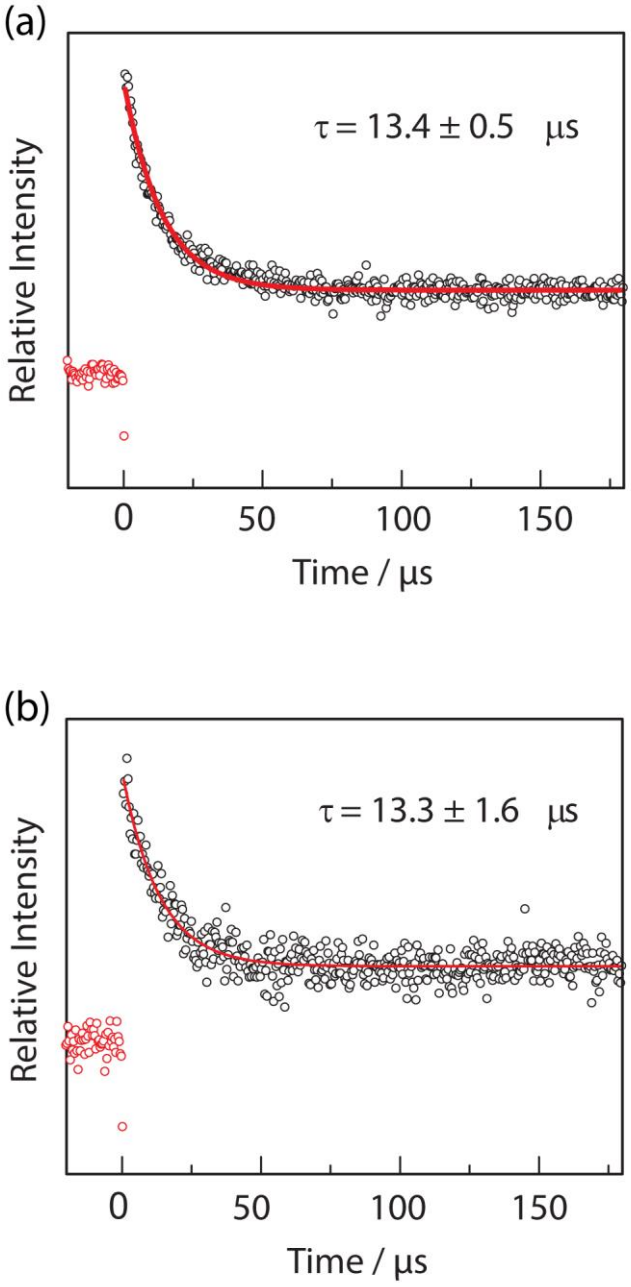

Figure 4.5. (a) Single wavelength kinetic trace of a THF solution of complex **1** pumped at 355 nm and recorded at 437 nm. (b) Single wavelength kinetic trace of a THF solution of complex **2** pumped at 355 nm and recorded at 437 nm.

and a spectral growth at ~440 nm. The new spectral feature at ~440 nm is not an absorption feature of either **2** or **3** and thus represents a species that is not observed in the steady-state photolysis experiment. Laser flash photolysis of complex **2** revealed a TA spectrum with a ground-state bleach at ~350 nm and also a spectral growth at ~440 nm. Excepting a narrower line-shape for the absorbance feature of **1**, the transient absorption spectra of **1** and **2** are very similar for λ_{exc} > 400 nm. This narrowing of the 440 nm TA signal of **1** is consistent with a superposition of a ground state bleach centered at ~460 nm with the spectral growth at ~440 nm. Owing to the similarities of the transient profiles of **1** and **2** at λ > 400 nm, we propose that photolysis of **1** and **2** affords a common intermediate. Thin-film TA spectroscopy was used to establish the homology of solution-phase and solid state photoreactions. Thin films of complexes **1** and **2**, drop cast from either THF or CH_2Cl_2 solutions, showed UV−vis absorption spectra with the same spectral features as observed in solution spectra of **1** and **2** (Figure 4.6). TA spectra (λ_{exc} = 355 nm) of these films were

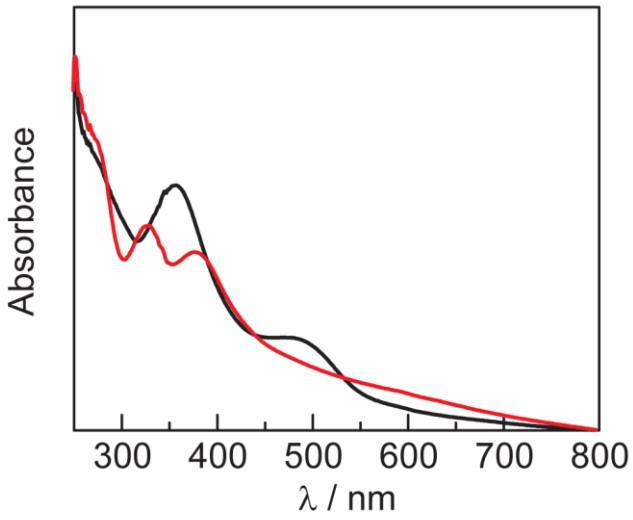

Figure 4.6. Solid-state absorption spectra of Rh_2[I,III] complex **1** (red) and Rh_2[II,II] complex **2** (black) obtained by measuring the wavelength-dependent absorbance of thin films drop cast on glass slides. The same sample preparation was used in measuring TA spectra of thin films.

recorded at 1 μs delay and show similar features to those observed in solution-phase TA spectra of these complexes, confirming the formation of the same photointermediate in both solution and solid state (Figure 4.4).

4.2.3 Photocrystallography

Steady-state photocrystallography experiments were performed at the Advanced Photon Source (APS) housed at Argonne National Laboratory (ANL) using synchrotron radiation (0.41328 Å) and a 365 nm LED light source (5 mW power measured at the crystal). A photodifference map was generated by comparing diffraction data obtained for a

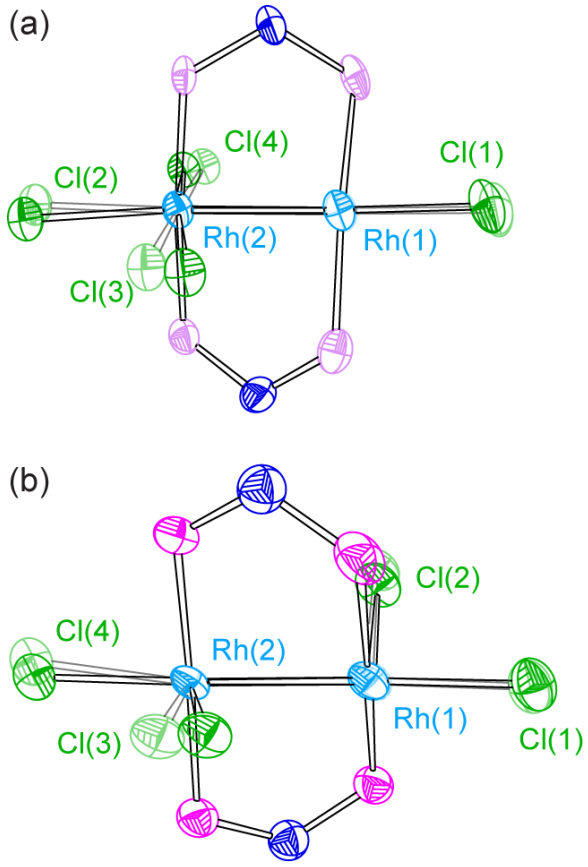

Figure 4.7. Thermal ellipsoid plots of photocrystallography results with photoinduced structures (solid) superimposed on dark structures (faded). (a) Rh_2[I,III] (complex **1**) plot; Rh^1–Rh^2–Cl^3 91.05(5)° (dark), 83.2(2)° (photoinduced). (b) Rh_2[II,II] (complex **2**) plot; Rh^1–Rh^2–Cl^3 91.15(5)° (dark), 78(2)° (photoinduced).

single crystal of Rh_2[I,III] complex **1** in the dark with diffraction data obtained for the same crystal during irradiation (Figure 4.7a). The crystal was not moved between the acquisitions of the two data sets and thus the orientation matrix was unchanged during the experiment. The difference map showed the presence of a photoinduced structure populated at 5.7(9)% of the crystal. Examination of the structural perturbations in the photoinduced structure shows ligand reorganization that would be anticipated during a migration of one of the chloride ligands to a bridging position; key metrics include the Rh^1–Rh^2–Cl^3 bond angle, which contracts from 91.05(5) to 83.2(2)° in the photoinduced structure. Concurrent with this, Rh^1–Rh^2–Cl^4 expands from 90.97(5) to 92(2)°. Additionally, Rh^2–Cl^3, which is the bond vector participating in partial migration from terminal to bridging coordination mode, elongates from 2.362(2) to 2.66(4) Å.

The extent of laser heating of the sample during data acquisition was examined by comparing the size of thermal ellipsoids of atoms not involved in the primary photoreaction (i.e., N-atoms in the phosphazane ligand) with the size of thermal ellipsoids for the same atoms as a function of temperature.[17] On the basis of this analysis, laser heating warmed the single crystal of **1** from 15 to ~250 K (Figure 4.8). The metrical parameters of **1** do not show significant temperature-dependent variation (Table 4.1), confirming that the difference map arises from photochemical, not thermal effects.

The photoinduced structure derived from complex **1** was accessed rapidly during irradiation. Comparison of specific reflections from the structures obtained in the dark and under illumination revealed a set of reflections that showed substantial intensity changes upon irradiation. Examination of these particular reflections as the light was turned on

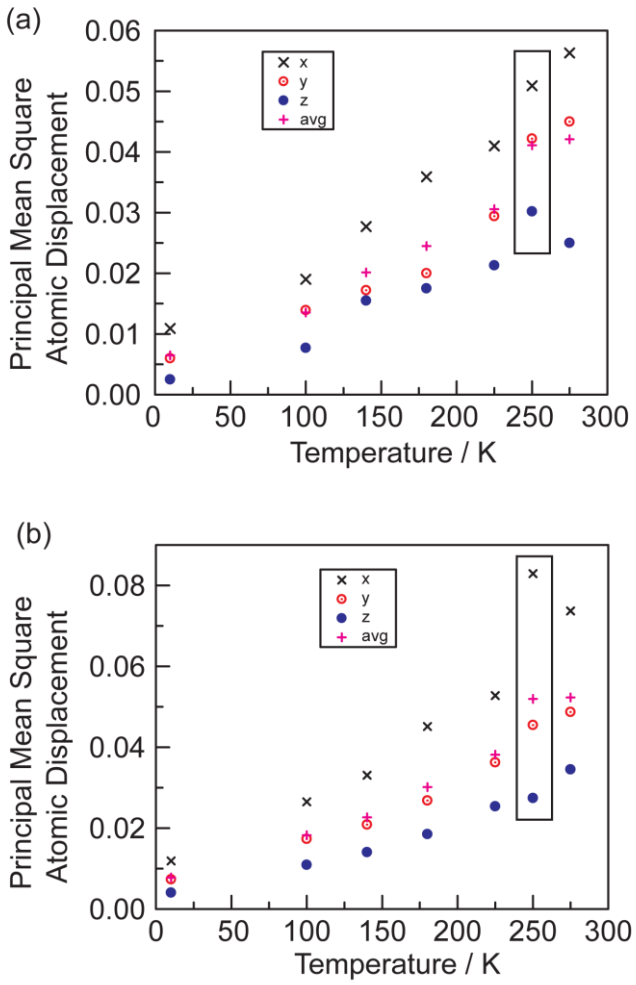

Figure 4.8. Principal mean square atomic displacements (U) for Rh_2[I,III] complex **1** as a function of temperature plotted for (a) nitrogen atoms in the bridged phosphazane ligands (b) oxygen atoms of the OCH_2CF_3 groups. Thermal parameters obtained during photocrystallography are highlighted in a box.

Table 4.1. Selected metrical parameters for Rh_2[I,III] complex **1** as a function of temperature.

Complex **1**	15 K	100 K	150 K	200 K	250 K
Rh–Rh (Å)	2.7153 (7)	2.7154 (9)	2.7166 (7)	2.7159 (7)	2.7188 (8)
Rh^1–Cl^1 (Å)	2.458 (2)	2.4619 (2)	2.473 (2)	2.470 (2)	2.473 (2)
Rh^1–Cl^2 (Å)	2.382 (2)	2.373 (2)	2.387 (2)	2.383 (2)	2.385 (2)
Rh^2–Cl^3 (Å)	2.379 (2)	2.381 (2)	2.378 (2)	2.379 (2)	2.379 (2)
Rh^2–Cl^4 (Å)	2.472 (2)	2.470 (2)	2.463 (2)	2.462 (2)	2.467 (2)
Rh^1–Rh^2–Cl^3 (°)	92.12 (5)	90.54 (6)	91.15 (5)	90.98 (4)	90.77 (5)
Rh^1–Rh^2–Cl^4 (°)	90.87 (4)	90.77 (6)	91.11 (5)	90.97 (5)	90.63 (6)

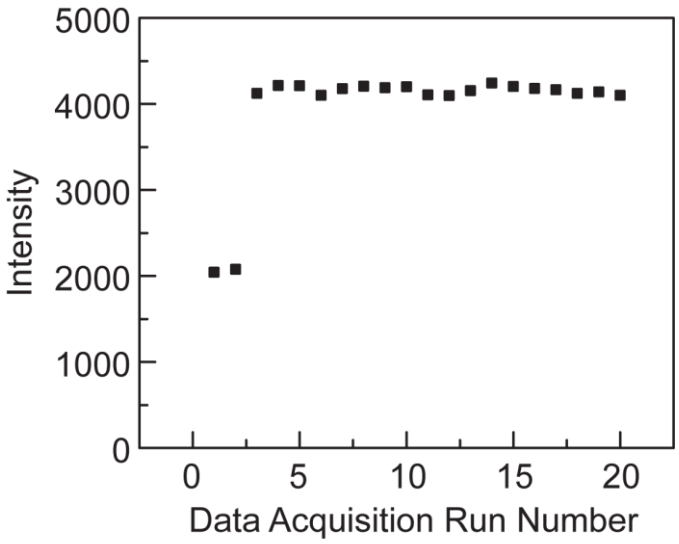

Figure 4.9. Plot of the intensity of reflection [9,–1,3] of **1** as a function of time. The laser was turned on after the second data point in the above plot.

showed that the intensity changes as a step function: the intensity increased rapidly relative to data collection and then reaches a steady-state value during irradiation (Figure 4.9).

A steady-state photocrystallography experiment was also performed using a single crystal of Rh_2[II,II] complex **2** under identical conditions as those of the aforementioned experiment with **1** (15 K, 5 mW 365 nm irradiation, 0.41328 Å synchrotron radiation). A photoinduced structure was identified in the photodifference map in which the Rh^1–Rh^2–Cl^3 angle contracts from 91.15(5) to 78(2)° upon irradiation (Figure 4.7a). Partial migration of Cl^3 toward the bridging position is accompanied by substantial elongation of the Rh–Cl bond (2.378(2) to 2.57(8) Å). The photoinduced geometry could be identified in the photodifference map generated from **2**, but full-molecule disorder in the available single crystals of **2** precluded determination of the population of the photoinduced structure. Variable-temperature crystallography experiments performed on a single crystal of **2** confirm that the observed structural effects are photoinduced, not thermally promoted. Similar to experiments carried out with complex **1**, the photoinduced structure is accessed rapidly relative to data acquisition. Upon cessation of irradiation, the photoinduced structure is no longer observed in the photodifference map, indicating that the photoinduced state is accessed only during steady-state irradiation.

4.2.4 Electronic Structure Calculations

Natural bond order (NBO) calculations were undertaken to evaluate the electronic structure of the dirhodium complexes investigated in this study. Herein, computed structures are referred to by letter, not compound numbers (i.e., **A** is the computed structure of **1**). In each of **A**, **B**, and **C** (i.e., computed structures of **1**, **2**, and **3**, respectively),

the highest-occupied NBO is Rh−Rh bonding. The Rh−Rh bond in **A** is polarized, as would be expected of a dative bond between a d^6 and a d^8 metal (Rh_a/Rh_b = 38.5:61.5). For valence symmetric Rh_2[II,II] structure **B**, the Rh−Rh bond is symmetrically shared by the two Rh atoms (Rh_a/Rh_b = 51.3:48.7). Consistent with a two-electron mixed-valent formulation, the M−M bond of structure **C** is polarized to a similar extent as that of the M−M bond in **A** (Rh_a/Rh_b = 42.6:57.4), consistent with the bonding predictions of the covalent bond classification for a dative covalent bond between the Rh centers.[18,19]

Density functional theory (DFT) calculations, summarized in Figure 4.10, address the structural manifestations of complete dissociation of one isocyanide ligand, as would be anticipated in the solution phase where free diffusion of the dissociated ligand is expected. Removal of one isocyanide ligand from either Rh_2[I,III] structure **A** or Rh_2[II,II] structure **B** results in site vacant structures $\mathbf{A}_{vac}$ and $\mathbf{B}_{vac}$, respectively. Structures $\mathbf{A}_{vac}$ and $\mathbf{B}_{vac}$ were evaluated with single-point calculations because neither could be located as a stationary point: both $\mathbf{A}_{vac}$ and $\mathbf{B}_{vac}$ evolved to structure **C** without a barrier. Reaction of photoextruded isocyanide ligand with chloride-bridged structure **C** could proceed at Rh_b to regenerate Rh_2[I,III] complex **A** or at Rh_a to accomplish photoisomerization to Rh_2[II,II] complex **B**. The computed relative transition state energies for conversion of **C** to **A** and **C** to **B** are 10.8 and 11.7 kcal/mol, respectively.

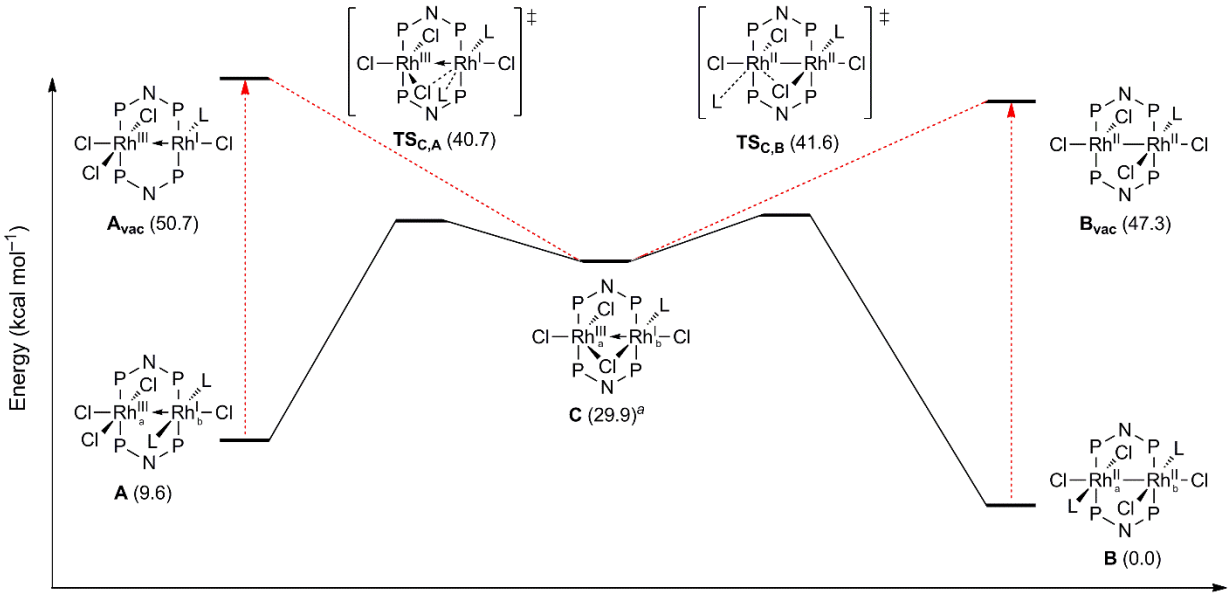

Figure 4.10. Calculated gas-phase stationary points in the interconversions of Rh_2 structures **A**–**C**. Site-vacant complexes $\mathbf{A}_{vac}$ and $\mathbf{B}_{vac}$ were evaluated by single-point calculations. Energies are solvent-corrected electronic energies at 0 K. [a]Sum of E_0(**C**) and $E_0(CH_3CN)$.

Table 4.2. Computed bond metrics as a function of M–L distance.

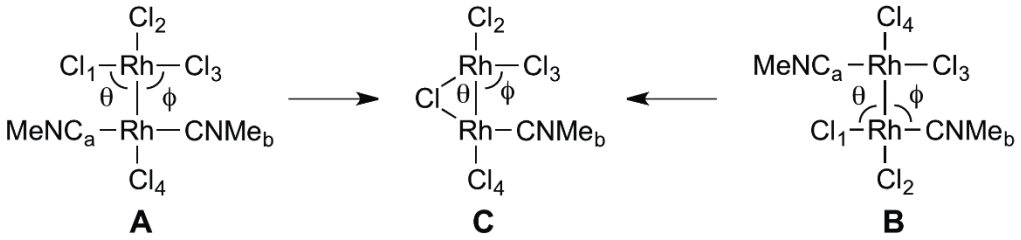

Rh–L$_a$(Å)	θ (°)	ϕ (°)	Rh–L$_a$(Å)	θ (°)	ϕ (°)
1.99 (**A**)	89.99	94.05	1.93 (**B**)	90.80	91.97
2.20	89.25	94.60	2.20	90.39	82.81
2.46	88.10	95.40	2.46	84.49	93.61
2.70	86.62	96.40	2.70	88.43	94.12
2.90	84.12	97.94	2.90	86.51	95.21
3.15	78.91	100.85	3.15	81.25	97.17
∞ (**C**)	58.16	101.13	∞ (**C**)	58.16	101.13

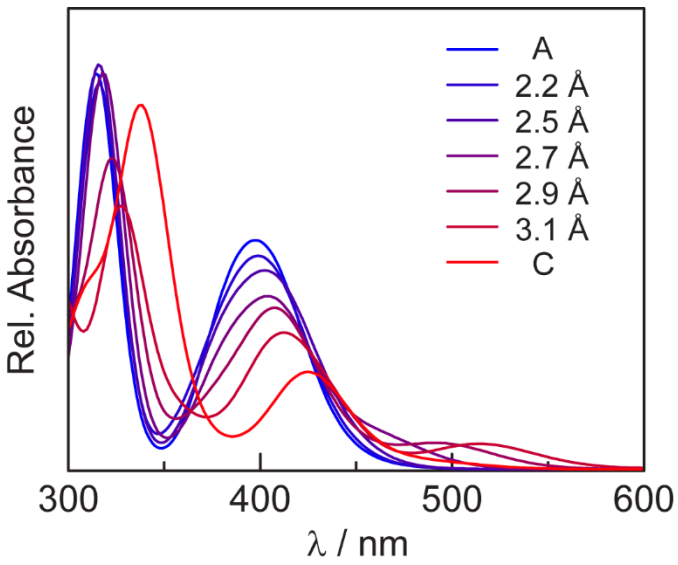

Figure 4.11. Simulated absorption spectra for TD-DFT calculations of **A** as a function of M–L bond length shows a systematic red shift of absorption features as the CH_3CN is gradually removed.

As opposed to solution photochemistry, free ligand dissociation during photocrystallography experiments is not possible because ligand motions are constrained by the crystal matrix.[20] To probe the impact of restricted isocyanide ligand dissociation, the geometry of Rh_2[I,III] structure **A** was evaluated as a function of M–L bond length. The results are tabulated in Table 4.2 and show that small perturbations of the M–L bond length are sufficient to induce nascent migration of a proximal Cl ligand toward a bridging position. Similar M–L bond-length-dependent migrations were computed starting with Rh_2[II,II] structure **B**. TD-DFT calculations of both **A** and **B** as a function of M–L bond length show that even partial migration of a Cl ligand toward a bridging site begins to give rise to the spectral features observed in thin-film TA measurements of both **1** and **2** (**Figure 4.11**).

4.2.5 Photochemistry of Dirhodium Carbonyls

To evaluate the hypothesis that complete ligand rearrangement to a Cl-bridged intermediate is impeded in the solid state, a new suite of complexes in which the bulky AdNC ligands of **1** and **2** are replaced with small volatile CO ligands was prepared. The synthetic chemistry and X-ray characterization of these complexes is summarized in Figure 4.12. Our contention that complexes supported by volatile ligands would participate in solid-state photochemistry was probed by irradiation of a thin film of trans-**7** under vacuum (20 mTorr). Trans-**7** is an analogue of Rh_2[II,II] complex **2** in which the AdNC ligands of **2** have been replaced by CO ligands. Solution-phase (Figure 4.13a) and solid-state photolysis of trans-**7** led to the expulsion of a CO ligand and the formation of Cl-bridged monocarbonyl complex **8** confirmed by single-crystal X-ray diffraction of the photoproduct. Photolysis of monocarbonyl Rh_2 complex **8** in THF results in the disappearance of the UV–vis features of **8** and the evolution of features attributable to

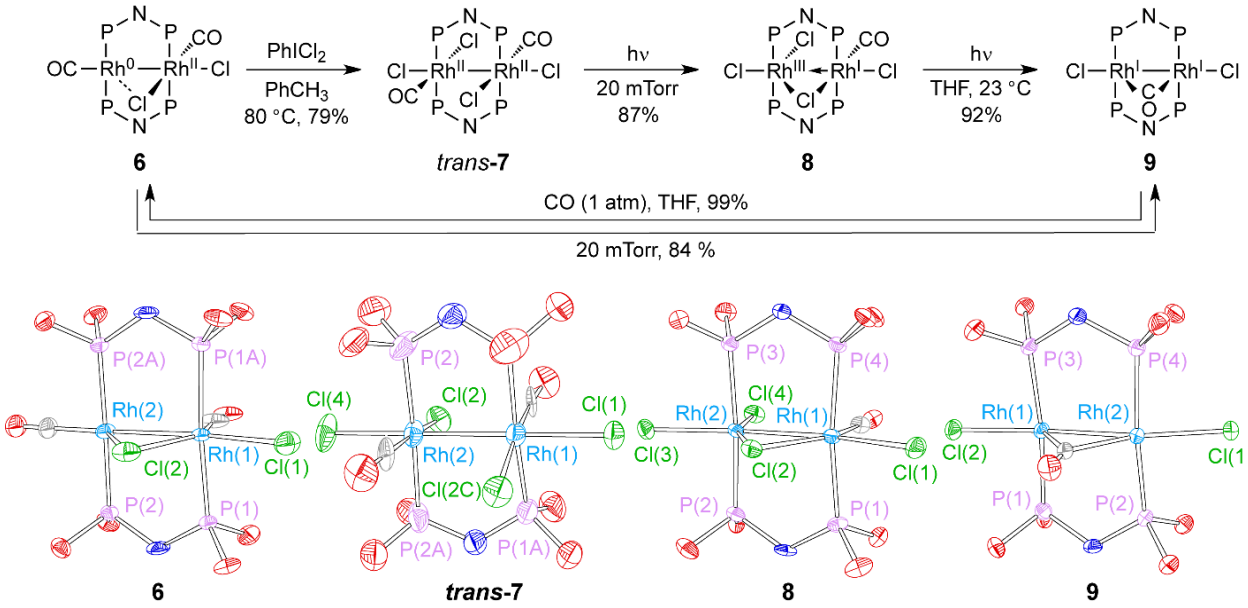

Figure 4.12. Synthesis of a suite of Rh_2 carbonyl complexes. Thermal ellipsoid plots of **6**–**9** in which solvent molecules, H atoms, and $-CH_2CF_3$ groups have been removed for clarity. Ellipsoids are drawn at 50% probability.

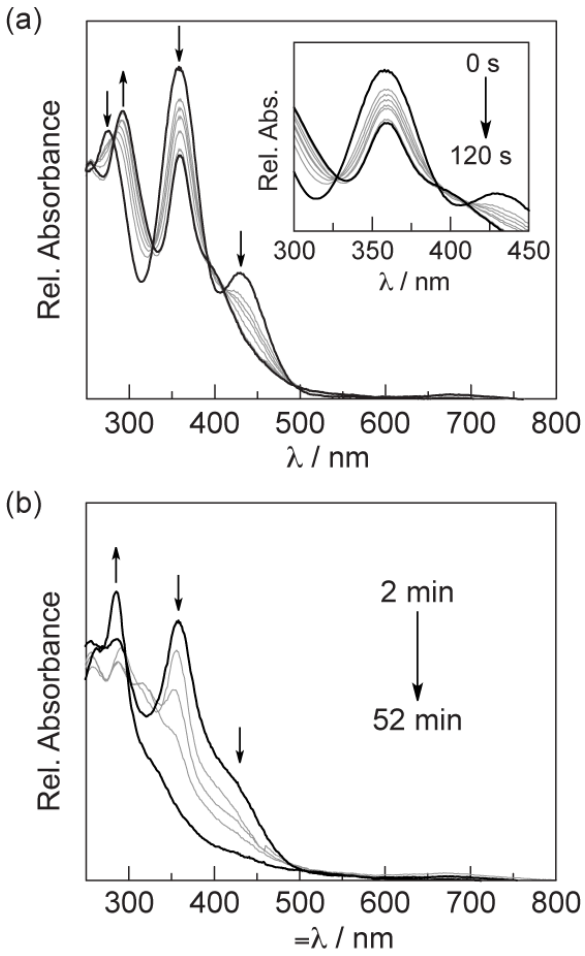

Figure 4.13. Spectral evolution for the photolysis of trans-**7** in THF (λ_{exc} > 305 nm). (a) During the first 120 s, trans-**7** is converted to Cl-bridged Rh_2 complex **8**. (b) Subsequently, **8** is converted to Rh_2[I,I] complex **9**, the product of halogen photoelimination.

complex **9**, the product of two-electron photoreduction (Figure 4.13b). Complex **9** produced by photolysis of **8** displayed identical spectral features to those of an authentic sample prepared by removal of a CO ligand from complex **6** under vacuum. Monocarbonyl complex **9** is converted to dicarbonyl Rh_2 complex **6** by exposure to 1 atm of CO in 99% yield.

Access to Rh_2 monocarbonyl complex **9** provided an avenue toward synthesis of AdNC-supported μ-Cl-Rh_2 intermediate **3**. Treatment of monocarbonyl complex **9** with 1 equiv of

AdNC, followed by oxidation with $PhICl_2$ led to Rh_2[II,II] complex **10**, supported by one AdNC and one CO ligand (Figure 4.14). Solid state photolysis of **10** under vacuum led to the expulsion of the CO ligand and isolation of μ-Cl-Rh_2 complex **3**. Prepared from **10**, complex **3** was indefinitely stable and could be independently characterized. Subtraction of the extinction spectra of complexes **1** and **2** from the extinction spectrum measured for **3** confirmed that the photointermediate observed in the TA spectra of **1** and **2** is indeed Cl-bridged complex **3** (Figure 4.15).

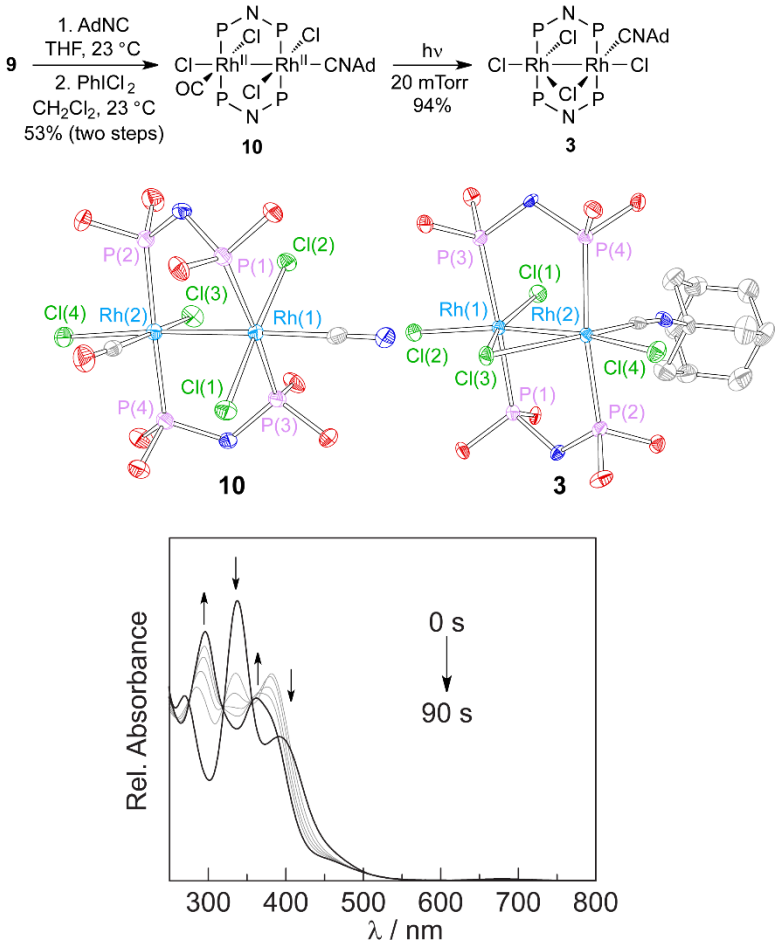

Figure 4.14. Synthesis of Cl-bridged complex **3** by CO photoextrusion from complex 10. Thermal ellipsoid plots of **3** and **10** in which H atoms, $-CH_2CF_3$ groups, and adamantyl group from **10** have been omitted for clarity. Ellipsoids are drawn at 50% probability. Spectral evolution for the photolysis of **10** in THF (λ_{exc} > 305 nm) shows conversion to **3** from CO extrusion.

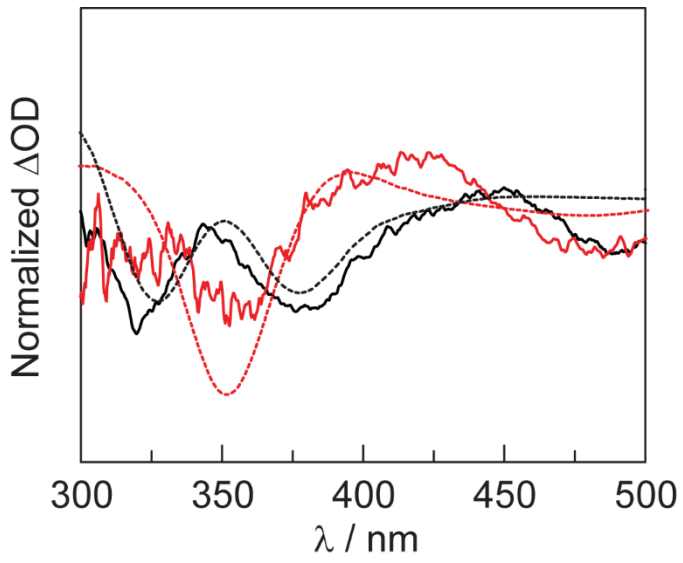

Figure 4.15. TA spectra (solid) obtained by laser flash photolysis of **1** (—, black) and **2** (—, red) thin films (355 nm pump, 1 μs delay). Simulated TA spectra (dotted) obtained by taking the difference of the extinction spectra of **3** with **1** and **2**, respectively.

4.3 Discussion

Our group has developed dirhodium complexes on the hypothesis that mixed-valent complexes will give rise to the requisite multielectron photoreactions necessary for HX splitting. Families of phosphazane-bridged complexes have been developed, and they display the targeted multielectron chemistry, but catalysts that accomplish authentic HX splitting to afford both H_2 and X_2 in the absence of chemical traps have proven to be elusive. Rational development of new HX-splitting platforms has been limited by a dearth of information regarding the mechanism of halogen elimination, thus establishing an imperative for an understanding of the critical steps preceding halogen elimination.

In analogy to the hydride-bridged transition states, which have been proposed for H_2 evolving reactions from diiridium complexes, [13,21] we postulated that the photointermediate in the TA spectrum is chloride-bridged structure **3** (Figure 4.1 and

Figure 4.14). TA spectroscopy has provided evidence for a photointermediate, but it cannot establish a structure. We have employed photocrystallography to directly probe photoinduced structural changes associated with halogen photoelimination.[22–24] To use photocrystallography reliably to gain insight into the structures of reaction intermediates in solution, the same photointermediates must be accessed in the solid state. The thin-film, nanosecond-resolved TA measurements shown in Figure 4.4 establish the homology of solution-phase and solid-state intermediates; the same TA line shape is generated in solution-phase and solid-state experiments. The nature of this photoreduction intermediate that is common to complexes **1** and **2** is unveiled by the steady-state photocrystallography experiments summarized in Figure 4.7. Both Rh_2[I,III] complex **1** and Rh_2[II,II] complex **2** display photoinduced structures characteristic of partial halide migration to a bridging position.

DFT calculations lend support to the structural changes observed by photocrystallography. Specifically, in solution-phase experiments, photodissociated ligands can diffuse away from the transition metal fragment, whereas in the solid state, free diffusion is not possible. Our calculations support the contention that in solution complete dissociation of photoextruded ligands will lead to the formation of chloride-bridged structure **3** (Figure 4.10). In the solid state, ligand diffusion is constrained and thus, while M–L bond elongation is achievable, complete dissociation is not possible. We modeled this scenario by evaluating the effect of M–L bond elongation of the geometry of the binuclear core and found that at small elongations of the M–L bond partial migration of a chloride ligand toward a bridging configuration was observed (Table 4.2).

The observation of incomplete ligand migration by photocrystallography emphasizes the rigorous demand of solid-state photoreactions, in which dissociation and diffusion of ligands are not typically possible; the presence of AdNC ligands prevents access to a complete rearrangement to a halide-bridged structure. Management of solid state ligand inventory was achieved by replacing AdNC ligands with small, volatile CO ligands (Figure 4.12). Photolysis of trans-**7**, an analogue of **2** in which the AdNC ligands are replaced by CO ligands, initially affords chloride-bridged complex **8**, which confirms that photoextrusion of an L-type ligand initially generates a halide-bridged complex (Figure 4.13a). The halide-bridged complex appears as an intermediate in an interrupted halogen elimination reaction, as further irradiation of **8** led to the isolation of Rh[I,I] complex **9**, which arises from two-electron photoreduction of **8** (Figure 4.13b).

The two-step reaction sequence, ligand loss to generate a ligand-bridged intermediate followed by two-electron photoreduction, represents an intramolecular example of the two steps of canonical binuclear elimination mechanisms. Binuclear reductive elimination reactions are proposed to proceed via (1) generation of an open coordination site on the metal alkyl complex by either ligand dissociation or migratory insertion, (2) intermolecular reaction of the unsaturated fragment with a metal hydride to generate a hydride-bridged intermediate, and (3) migration of the alkyl or acyl group onto the bridging hydride to generate the observed organic products as well as binuclear transition metal complexes (Equation 4.1).[25–27] Such binuclear elimination has been proposed for complexes based on

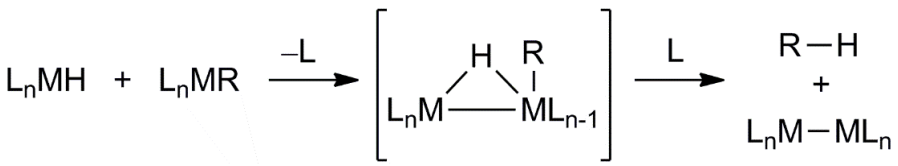

(1)

most of the transition metal series,[28–31] and it is proposed to be operative during both Co- and Rh-catalyzed hydroformylation reactions under some conditions.[32–35] We have previously proposed a binuclear reductive elimination mechanism for the H_2 evolution step of HX-splitting catalysis with phosphazane-bridged Ir_2 complexes.[21] On the basis of the results shown in Figure 4.4, Figure 4.7, and Figure 4.12, we now observe that a similar mechanism may be operative for halogen photoelimination.

To firmly establish a binuclear elimination pathway for halogen photoelimination from AdNC-supported complexes **1** and **2**, we sought to directly prepare and characterize the proposed AdNC-supported chloride-bridged intermediate. While preparation by ligand extrusion from either **1** or **2** was judged to be implausible given the short lifetime measured for **3** under these conditions (~15 μs, Figure 4.5), we anticipated that the complex may be isolable if recombination of the photoextruded ligand with the Rh_2 fragment could be avoided. Taking advantage of the solid-state ligand management enabled with CO ligands, we have prepared and isolated complex **3**, which is the exact transient intermediate that would be generated during halogen elimination from complexes **1** and **2**. We note that chloride-bridged complex **3** is furnished directly by the extrusion of one equivalent of CO upon the solid-state photolysis of **10**, an analogue of **2** in which the Rh_2 core is supported by one AdNC and one CO ligand (Figure 4.14). With the absorption spectrum of **3** in hand, Figure 4.15 shows that the TA spectra obtained by laser flash photolysis of **1** or **2** is closely replicated by computing the difference spectra expected based on the experimentally measured ground-state absorption spectra of **1**–**3**.

The confirmed intermediacy of **3** in halogen elimination from **1** and **2** demonstrates that halogen elimination proceeds by a canonical binuclear elimination pathway in which

both steps, ligand dissociation to afford a ligand-bridged intermediate and subsequent M–X bond activation, can be directly observed. To our knowledge, the chemistry reported herein is the first instance in which these two steps of binuclear elimination have been directly observed.

4.4 Conclusion

The results reported herein offer evidence that X_2 elimination from Rh_2 complexes proceeds via ligand-bridged intermediates, and, accordingly, they inform next-generation catalyst design. Phosphazane-bridged binuclear complexes have been proposed to facilitate ligand rearrangements to ligand-bridged intermediates owing to the ligand's ability to accommodate two-electron changes at the metal core with minimal reorganization energy.[21] The photocrystallography experiments described here support this contention by showing the prevalence of halide-bridged intermediates that preceded M–X bond activation. Although the solid state imposes constraints on the requisite ligand-bridged intermediates, we have leveraged the volatility of carbonyl ligands to allow for the isolation of halide-bridged structures during an interrupted binuclear elimination. This strategy has been exploited to characterize the absorption spectrum of the exact halide-bridged intermediate that is observed transiently (<15 μs) during photocatalysis. Because the solid state offers a mechanism to prevent the back reaction of reactive volatile photoproducts such as X_2, these results suggest that by clever design of the ligand coordination sphere obstacles imposed on photochemical transformations in the solid state might be overcome.

Identification of binuclear elimination as the mechanism of halogen photoelimination in this class of HX splitting catalysts provides direct mechanistic insight for improving the photocycle depicted in Figure 4.1. The photocycle requires three photons, two of which are

necessary for halogen photoelimination. Stabilization of the bridged complex would obviate the need for the first photochemical process required to prepare the bridged dirhodium complex for binuclear halogen elimination. Aryl isocyanides are known to stabilize the bridged structures and due to the mechanistic information obtained from of this work, our group has now show that stabilized bridged complexes result in enhanced catalytic activity with respect to the photocycle studied in this work.[36] These results reinforce the notion that polynuclear transition metal sites provide a favorable platform for performing multielectron redox transformations.

4.5 Experimental

Synthesis, characterization, steady state photolysis, and thermally promoted reaction chemistry was performed by Prof. David C. Powers. Photocrystallography was performed in collaboration with Prof. David C. Powers, Seung Jun Hwang, Tamara M. Powers, Dr. Shao-Liang Zheng, and Dr. Yu-Sheng Chen. Computations were performed by Prof. David C. Powers and Dr. Lisa M. Pérez.

General Considerations

All reactions were carried out in an N_2-filled glovebox. Anhydrous solvents were obtained from drying columns.[37] $[Rh(cod)Cl]_2$ and $[Rh(CO)_2Cl]_2$ were obtained from Strem Chemicals and used without purification. Ligand tfepma,[38] Rh_2[II,II] complex **2**,[16] and Rh2[0,II] complex **4**[16] were prepared as previously described.

Physical Methods

NMR spectra were recorded at the Harvard University Department of Chemistry and Chemical Biology NMR facility on a Varian Mercury 400 spectrometer operating at 400

MHz for ^{1}H acquisitions, 162 MHz for ^{31}P acquisitions, and 375 MHz for ^{19}F acquisitions. NMR chemical shifts are reported in ppm, with the residual solvent resonance as internal standard. UV–vis spectra were recorded at 293 K in quartz cuvettes on a Spectral Instruments 400 series diode array blanked against the appropriate solvent. IR spectra were recorded with powdered samples on a PerkinElmer Spectrum 400 FT-IR/FT-FIR spectrometer outfitted with a Pike Technologies GladiATR attenuated total reflectance accessory with a monolithic diamond stage and pressure clamp.

Photochemistry

Steady-state photochemical reactions were performed using a 1000 W high-pressure Hg/Xe arc lamp (Oriel), and the beam was passed through a water-jacketed filter holder containing the appropriate long-pass filter, an iris, and a collimating lens. Samples were photolyzed in a constant-temperature circulating water bath (23 °C). Nanosecond transient absorption measurements were made with the pump light provided by the third harmonic (355 nm) of a Quanta-Ray Nd:YAG laser (Spectra-Physics) running at 10 Hz. Probe white light was provided by a 75 W Xe-arc lamp (Photon Technologies Inc.). The signal light passed through a Triax 320 spectrometer, where it was dispersed by a 300 nm × 250 nm blazed grating and collected with either an intensified gated CCD camera (ICCD, CCD 30-11, Andor Technology, 1024 × 256 pixels, 26 μm^2) for TA spectra or a photomultiplier tube (PMT) for TA single-wavelength kinetics. PMT outputs were collected and averaged with a 1GHz oscilloscope (LeCroy 9384CM). A TTL pulse synchronized with the Q-switch of the Infinity laser was delayed 99 ms before triggering the shutter for the probe light. Electronic delays were created with SRS DG535 delay generators (Stanford Research Systems). These

delay boxes, in combination with electronic shutters (Uniblitz), were used to create the necessary pulse sequence. Solution-phase TA measurements were performed on THF solutions of **1** and **2**, and solid-state TA measurements were performed on samples prepared by drop-casting solutions of **1** and **2** (from either CH_2Cl_2 or THF) on glass slides and allowing them to dry under ambient conditions for 1 h. All TA measurements were carried out at 23 °C.

X-ray Crystallographic Details

X-ray structures of complexes **3** and **6**–**10** and variable-temperature (VT) X-ray data were collected on a Bruker three-circle platform goniometer equipped with an Apex II CCD and an Oxford cryostream cooling device operating between 100 and 275 K. Radiation was from a graphite fine focus sealed tube Mo Kα (0.71073 Å) source. Crystals were mounted on a glass fiber pin using Paratone N oil. Data was collected as a series of φ and/or ω scans. Data was integrated using SAINT and scaled with multiscan absorption correction using SADABS.[39] The structures were solved by intrinsic phasing using SHELXT (Apex2 program suite, v2014.1) and refined against F^2 on all data by full matrix least-squares with SHELXL-97.[40] All non-hydrogen atoms were refined anisotropically. H atoms were placed at idealized positions and refined using a riding model. Crystal data and refinement statistics are summarized in

and

Table **4.4** and thermal ellipsoid plots are collected in Figure 4.12, Figure 4.14, and Figure 4.16. Powder diffraction experiments were carried out with a Bruker D2 Phaser using a Cu anode.

Table 4.3. Crystal Data and Structure Refinement.

	3	**6**·THF	*trans*-**7**	**8**
formula	$C_{29}H_{37}Cl_4F_{24}N_3O_8P_4Rh_2$	$C_{24}H_{28}Cl_2F_{24}N_2O_{11}P_4Rh_2$	$C_{20}H_{22}Cl_4F_{24}N_2O_{10}P_4Rh_2$	$C_{19}H_{22}Cl_4F_{24}N_2O_9P_4Rh_2$
CCDC #	1008080	1006061	1006063	1006064
fw, g/mol	1483.12	1377.51	1377.90	1349.07
temp, K	100 (2)	100 (2)	100 (2)	100 (2)
cryst system	triclinic	monoclinic	monoclinic	triclinic
space group	*P-1*	*C2/m*	*C2/c*	*P-1*
color	yellow	orange	orange	orange
a, Å	10.2286 (8)	32.468 (6)	23.308 (1)	12.2293 (7)
b, Å	12.356 (1)	21.017 (4)	23.326 (1)	18.579 (1)
c, Å	20.409 (2)	14.625 (3)	16.9357 (7)	19.257 (1)
α, deg	94.387 (1)	90	90	89.993 (1)
β, deg	96.782 (1)	114.336 (2)	107.939 (1)	87.029 (1)
γ, deg	99.181 (1)	90	90	87.275 (1)
V, A^3	2516.5 (3)	9093 (3)	8760.2 (6)	4364.3 (5)
Z	4	12	8	6
R1[a]	0.059	0.087	0.070	0.061
wR2[b]	0.116	0.267	0.211	0.151
GOF[c] (F^2)	1.00	1.07	1.03	1.00
R_{int}	0.095	0.094	0.066	0.118

[a] $R1 = \Sigma||F_o| - |F_c||/\Sigma|F_o|$. [b] $wR2 = (\Sigma(w(F_o^2 - F_c^2)^2)/\Sigma(w(F_o^2)^2))^{1/2}$. [c] $GOF = (\Sigma w(F_o^2 - F_c^2)^2/(n - p))^{1/2}$ where n is the number of data and p is the number of parameters refined.

Table 4.4. Crystal Data and Structure Refinement.

	cis-**7**	**9**·Et_3NHCl	**10** · CH_2Cl_2
formula	$C_{20}H_{22}Cl_4F_{24}N_2O_{10}P_4Rh_2$	$C_{25}H_{17}Cl_3F_{24}N_3O_9P_4Rh_2$	$C_{30.4}H_{37}Cl_{4.8}F_{24}N_3O_9P_4Rh_2$
CCDC #	1006062	1006060	1007461
fw, g/mol	1377.90	1415.05	1544.32
temp, K	100(2)	100 (2)	100(2)
cryst system	monoclinic	tetragonal	orthorhombic
space group	*C2/c*	$I4_1cd$	$P2_12_12_1$
color	orange	orange	red-orange
a, Å	24.42 (1)	23.271 (1)	12.5066 (9)
b, Å	8.739 (5)	23.271 (1)	16.302 (1)
c, Å	20.35 (1)	36.041 (2)	27.644 (2)
α, deg	90	90	90
β, deg	101.450 (9)	90	90
γ, deg	90	90	90
V, A^3	4255 (4)	19517 (2)	5636.3 (7)
Z	4	24	4
R1[a]	0.091	0.033	0.042
wR2[b]	0.241	0.072	0.095
GOF[c] (F^2)	1.05	1.04	1.02
R_{int}	0.071	0.100	0.102

[a] $R1 = \Sigma||F_o| - |F_c||/\Sigma|F_o|$. [b] $wR2 = (\Sigma(w(F_o^2 - F_c^2)^2)/\Sigma(w(F_o^2)^2))^{1/2}$. [c] $GOF = (\Sigma w(F_o^2 - F_c^2)^2/(n - p))^{1/2}$ where n is the number of data and p is the number of parameters refined.

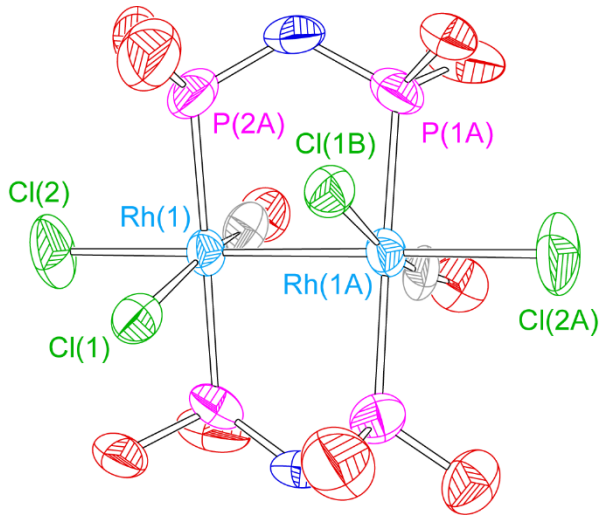

Figure 4.16. Thermal ellipsoid plot of *cis*-$Rh_2(CO)_2Cl_4(tfepma)_2$ (*cis*-**7**) in which H-atoms, *N*-methyl groups, and CH_2CF_3 groups have been removed for clarity. Ellipsoids are drawn at 50% probability.

Photocrystallography data was collected using 0.41328 Å radiation at temperature of 15 K (Oxford Diffraction Helijet) on a vertical mounted Bruker D8 three-circle platform

goniometer equipped with an Apex II CCD at ChemMatCARS located at the Advanced Photon Source (APS), Argonne National Laboratory (ANL). Illumination was provided by a Thorlabs 365 nm LED (M365L2) and was delivered to the sample via a 100 μm i.d. fiber optic. Dark structures were solved and refined as described above. For data sets obtained during irradiation, non-H atoms of the product were located in difference-Fourier maps, calculated with coefficients F_0(irradiated) − F_0(dark), and then refined with constraints on the product molecule's atomic displacement parameters to the corresponding values of the reactant molecule (EADP instructions of SHELXL97). The percentage of the reactant in the crystal was treated as a variable in the refinements.

Computational Details

B3LYP[41–43] calculations were performed using the Gaussian 09, revision D.01, suite of software.[44] Model complexes in which adamantyl isocyanide ligand was replaced with a methyl isocyanide and the bridging tfepma ligands were replaced with bis(fluoromethoxyphosphino)methylamine (fmpma) ligands were used in all computations. These model structures are less severe truncations than have previously been employed in computational investigations of phosphazane bridged dirhodium complexes.[10,11,45] Gas-phase geometry optimizations and TD-DFT calculations were carried out using an SDD basis set for Rh[46] and 6-31G* for all other atoms.[47,48] Stationary points were characterized with frequency calculations. Single-point solvent corrections (THF) were carried out using a polarizable continuum model using the integral equation formalism variant. B3LYP geometries well reproduced experimental metrical parameters, obtained by X-ray crystallography, and provided similar structural parameters as optimizations carried out with either the M06[49,50] or M06-L[51] functional. Geometries used

for DFT calculations are available free of charge via the ACS Publications website at DOI: 10.1021/ja508218v. Computed absorption spectra (line broadening 0.15 eV) reproduced experimental absorption spectra. NBO calculations[52–55] were carried out using Gaussian NBO, version 3.1[56] with results summarized in Table 4.5 and Table 4.6.

Table 4.5. NBO description of Rh–Rh bond in MeNC-supported structures.

	Rh_2[I,III] **A**		Rh_2[II,II] **B**		μ-Cl-Rh_2 **C**	
Rh center	Rh^{I}	Rh^{III}	Rh_a	Rh_b	Rh–L	Rh
Parentage (%)	61.53	38.47	51.28	48.72	57.40	42.60
Composition	s (13.90) p (44.95) d (41.15)	s (12.24) p (48.68) d (39.08)	s (13.35) p (46.34) d (40.31)	s (13.26) p (46.69) d (40.05)	s (14.20) p (44.53) d (41.27)	s (13.41) p (46.51) d (40.08)

Table 4.6. NBO description of Rh–Rh bond in CO-supported structures.

	Rh_2[I,III] **SD**		Rh_2[II,II] **SE**		μ-Cl-Rh_2 **SF**	
Rh center	Rh^{I}	Rh^{III}	Rh_a	Rh_b	Rh–L	Rh
Parentage (%)	64.89	35.11	51.51	48.49	57.09	42.91
Composition	s (14.12) p (45.81) d (40.07)	s (11.88) p (49.53) d (38.59)	s (13.40) p (46.64) d (39.97)	s (13.20) p (47.07) d (39.74)	s (13.67) p (46.10) d (40.22)	s (13.37) p (46.54) d (40.09)

Synthesis of $Rh_2(tfepma)_2(AdNC)_2Cl_4$ (1)

To a saturated solution of Rh_2[0,II] complex **4** (50.0 mg, 3.18 × 10–5 mol, 1.00 equiv) in $PhCH_3$ was added $PhICl_2$ (17.5 mg, 6.36 × 10^{-5} mol, 2.00 equiv) as a solid. The reaction solution was heated to 80 °C for 10 h, during which time a green solid precipitated. The reaction mixture was cooled to –20 °C for 20 min, at which time the green solid was

collected, washed with pentane, and dried in vacuo to afford 46 mg of the title complex (88% yield). ^{1}H NMR (300 MHz, THF-d8) δ (ppm): 5.21–4.73 (m, 16H), 3.10 (pseudoquintet, J = 4.1 Hz, 6H), 2.11 (s, 18H), 1.71 (s, 12H). ^{31}P{^{1}H NMR (121.5 MHz, THF-d_8) δ (ppm): 113.8 (m, 4P). IR: νCN = 2211 cm^{-1}. Combustion Anal. Calc. C, 29.22; H, 3.19; N, 3.42; Found: C, 29.08; H, 3.21; N, 3.12.

Synthesis of Rh_2(tfepma)$_2$(CO)$_2Cl_2$ (6)

To a solution of $[Rh(CO)_2Cl]_2$ (38.0 mg, 9.77 × 10^{-5} mol, 1.00 equiv) in THF (3 mL) at 23 °C was added tfepma (95.2 mg, 1.95 × 10^{-4} mol, 2.00 equiv) dropwise as a THF (2 mL) solution. The reaction mixture was stirred at 23 °C for 1 h, during which time evolution of bubbles was observed and the color of the reaction mixture turned from orange to dark red. Complex **6** was not isolated as a solid because removal of solvent led to a mixture of Rh_2(tfepma)$_2$(CO)$_2Cl_2$ (6) and Rh_2(tfepma)$_2$(μ-CO)Cl_2 (**9**) and thus solution characterization (^{1}H NMR, ^{19}F NMR, ^{31}P NMR, and UV−vis) was carried out using the reaction solution without further purification. On the basis of integration of the ^{1}H NMR spectrum against hexamethylbenzene (internal standard), the yield of 6 was 98%. ^{1}H NMR (THF-d_8, 23 °C): δ 4.96–4.88 (m, 4H), 4.84–4.74 (m, 12H), 2.99 (pseudoquintet, J = 3.6 Hz, 6H). ^{31}P NMR (THF-d8, 23 °C): δ 131.2–130.2 (m, 4P). ^{19}F NMR (THF-d8, 23 °C): δ −75.5 (dt, J = 19.7 Hz, J = 9.2 Hz, 24F). IR: νCN = 2002 cm^{-1}. Crystals suitable for single-crystal diffraction analysis were obtained from a THF solution layered with pentane at −30 °C. Satisfactory combustion analysis could not be obtained because **6** was not stable to evacuation of solvent.

Synthesis of $Rh_2(tfepma)_2(CO)_2Cl_4$ (7)

To a solution of $[Rh(CO)_2Cl]_2$ (44.0 mg, 1.13×10^{-4} mol, 1.00 equiv) in $PhCH_3$ (5 mL) at 23 °C was added tfepma (110 mg, 2.26×10^{-4} mol, 2.00 equiv) dropwise as a $PhCH_3$ (1 mL) solution. The reaction mixture was stirred at 23 °C for 1 h, during which time evolution of bubbles was observed and the color of the reaction mixture turned from orange to dark red. $PhICl_2$ (46.6 mg, 1.70×10^{-4} mol, 1.50 equiv) was added as a solid. ^{31}P NMR analysis of an aliquot of the reaction mixture showed the presence of two ^{31}P NMR signals (multiplets at 105.3–104.5 and 102.2–101.5 ppm) in a 2:1 ratio, assigned as trans-**7** and cis-**7**, respectively (Figure 4.17). Heating the reaction mixture at 70 °C for 2 h resulted in the

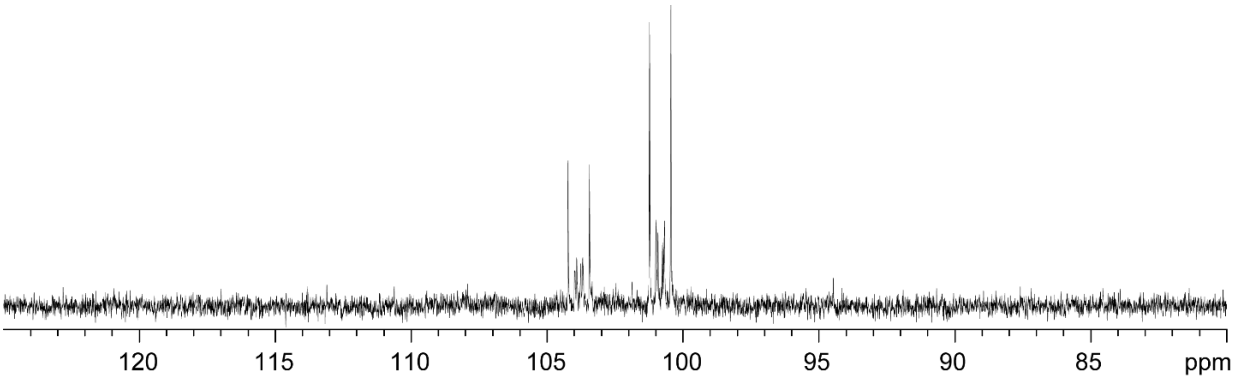

Figure 4.17. ^{31}P NMR spectrum of the reaction mixtures of **6** with $PhICl_2$ in $PhCH_3$ at 23 °C; the spectrum displays signals attributed to cis-**7** and trans-**7**.

conversion of trans-**7** to cis-**7**. The reaction mixture was cooled to −30 °C for 1 h, at which time a precipitate was observed. The solvent was decanted, and the residue washed with pentane and dried in vacuo to afford 123 mg of the title complex as a yellow solid in 79% yield. trans-**7**: 1H NMR (C_6D_6, 23 °C): δ 4.86–4.83 (m, 8H), 4.51–4.46 (m, 4H), 4.36–4.31 (m, 4H), 2.58 (pseudoquintet, J = 3.9 Hz, 6H). 31P NMR (C_6D_6, 23 °C): δ 105.3–104.5 (m, 4P). ^{19}F NMR (C6D6, 23 °C): δ −74.68 (t, J = 7.9 Hz, 12F), −75.09 (t, J = 7.9 Hz, 12F). IR: νCN = 2082 cm^{-1}. Crystals of cis-**7** suitable for single-crystal diffraction analysis were obtained from a

THF solution layered with pentane at −30 °C, and crystals of trans-**7** suitable for single-crystal diffraction analysis were obtained from a CH_2Cl_2 solution layered with hexane at −30 °C.

Synthesis of Rh_2(tfepma)$_2$(CO)(μ-Cl)Cl_3 (8)

A thin film of trans-**7** (47.0 mg, 3.41 × 10^{-4} mol, 1.00 equiv) was deposited on the wall of a two chamber photoreaction vessel and dried in vacuo for 12 h. Broad-band photolysis of the thin film with a 1000 W Hg lamp was carried out for 4 h under dynamic vacuum (20 mTorr). The residue was taken up in CH_2Cl_2, layered with pentane, and cooled to −30 °C for 1 h, at which time the solvent was decanted. The residue was dried in vacuo to afford 40.1 mg of the title complex as a yellow solid in 87% yield. ^{1}H NMR (C6D6, 23 °C): δ 5.02–4.92 (m, 2H), 4.72–4.64 (m, 2H), 4.56–4.46 (m, 4H), 4.45–4.39 (m, 2H), 4.29–4.15 (m, 6H), 2.61 (pseudoquintet, J = 3.9 Hz, 6H). 31P NMR (C6D6, 23 °C): δ 106.8–104.2 (m, 4P). ^{19}F NMR (C_6D_6, 23 °C): δ −74.49 (t, J = 7.9 Hz, 6F), −74.90 (t, J = 7.9 Hz, 6F), −74.92 (t, J = 7.9 Hz, 6F), −75.08 (t, J = 7.9 Hz, 6F). IR: νCN = 2086 cm^{-1}. Crystals of **8** suitable for single-crystal diffraction analysis were obtained from a THF solution layered with pentane at −30 °C.

Synthesis of Rh_2(tfepma)$_2$(μ-CO)Cl_2 (9)

To a solution of $[Rh(CO)_2Cl]_2$ (63.7 mg, 1.64 × 10^{-4} mol, 1.00 equiv) in THF (5 mL) at 23 °C was added tfepma (160 mg, 3.28 × 10−4 mol, 2.00 equiv) dropwise as a THF (5 mL) solution. The reaction mixture was stirred at 23 °C for 1 h, during which time evolution of bubbles was observed and the color of the reaction mixture turned from orange to dark red. The solvent was removed in vacuo. The residue was dissolved in CH_2Cl_2 (5 mL), and the solvent was removed in vacuo. The redissolution/evaporation sequence was repeated four times, and the residue was triturated in pentane to afford 176 mg of complex **9** as an

orange solid (84% yield). ^{1}H NMR (CD_2Cl_2, 23 °C): δ 4.70–4.60 (m, 8H), 4.59–4.47 (m, 8H), 2.75 (pseudoquintet, J = 3.5 Hz, 6H). ^{31}P NMR (CD_2Cl_2, 23 °C): δ 130.1–129.1 (m, 4P). ^{19}F NMR (CD_2Cl_2, 23 °C): δ −75.3 (br s, 24F). IR: ν CN = 1812 cm^{-1}. Combustion analysis, found (calcd): C, 17.95 (17.84); H, 1.96 (1.73); N, 2.17 (2.19). Crystals suitable for single-crystal diffraction analysis were obtained from a THF solution **9** and Et_3NHCl layered with pentane at −30 °C.

Synthesis of Rh_2(tfepma)$_2$(CO)(AdNC)Cl_4 (10)

To a solution of Rh_2(tfepma)$_2$(μ-CO)Cl_2 (**9**) (120 mg, 9.40 × 10^{-5} mol, 1.00 equiv) in THF (2 mL) at 23 °C was added AdNC (15.2 mg, 9.40 × 10−5 mol, 1.00 equiv) dropwise as a THF (1 mL) solution. The reaction mixture was stirred at 23 °C for 30 min, and the solvent was removed in vacuo. The residue was taken up in CH_2Cl_2 (2 mL), and $PhICl_2$ (28.4 mg, 1.03 × 10^{-}4 mol, 1.10 equiv) was added. Hexanes (15 mL) were added, and the reaction mixture was cooled to −30 °C for 12 h, at which time 75.3 mg of complex **10** was isolated as an orange crystalline solid (53% yield). ^{1}H NMR (CD_2Cl_2, 23 °C): δ 5.22–5.14 (m, 4H), 4.83–4.68 (m, 8H), 4.65–4.55 (m, 4H), 3.02 (pseudoquintet, J = 3.9 Hz, 6H), 2.25 (br s, 3H), 2.18 (br s, 6H), 1.80 = 1.71 (m, 6H). ^{31}P NMR (CD_2Cl_2, 23 °C): δ 113.6–111.1 (m, 2P), 108.4–106.7 (m, 2P). ^{19}F NMR (CD_2Cl_2, 23 °C): δ −75.3 (t, J = 7.9 Hz, 6F), −75.4 (t, J = 7.9 Hz, 6F), −75.5 (t, J = 7.9 Hz, 6F), −75.8 (t, J = 7.8 Hz, 6F). IR: νCN = 2193 cm^{-1}, 2093 cm^{-1}. Crystals suitable for single-crystal diffraction analysis were obtained from a CH_2Cl_2 solution of **10** layered with hexanes at −30 °C.

Synthesis of Rh_2(tfepma)$_2$AdNC(μ-Cl)Cl_3 (3)

A thin film of trans-**7** (52.0 mg, 3.44 × 10−4 mol, 1.00 equiv) was deposited on the wall of a two-chamber photoreaction vessel and dried in vacuo for 12 h. Broad-band photolysis

of the thin film with a 1000 W Hg lamp was carried out for 4 h under dynamic vacuum (20 mTorr). The residue was taken up in CH_2Cl_2, layered with pentane, and cooled to −30 °C for 1 h, at which time the solvent was decanted. The residue was dried in vacuo to afford 48.0 mg of complex **3** as a yellow solid (94% yield). ^{1}H NMR (CD2Cl2, 23 °C): δ 4.93−4.83 (m, 4H), 4.82−4.67 (m, 6H), 4.62−4.54 (m, 2H), 4.51−4.45 (m, 2H), 4.36−4.27 (m, 2H), 3.02 (pseudoquintet, J = 3.9 Hz, 6H), 2.13 (br s, 3H), 2.09 (s, 6H), 1.72−1.64 (m, 6H). ^{31}P NMR (CD2Cl2, 23 °C): δ 116.5−114.4 (m, 2P), 113.2−111.1 (m, 2P). ^{19}F NMR (C6D6, 23 °C): δ −74.64 (t, J = 7.9 Hz, 6F), −75.30 to −75.4 (m, 18F). IR: νCN = 2199 cm^{-1}. Crystals of **3** suitable for single-crystal diffraction analysis were obtained by cooling a saturated CH2Cl2/hexanes solution of **3** to −30 °C.

4.6 References

1. Ferguson-Miller, S.; Babcock, G. T. Heme/Copper Terminal Oxidases. *Chem. Rev.* **1996**, *96* (7), 2889–2908.

2. Fontecilla-Camps, J. C.; Volbeda, A.; Cavazza, C.; Nicolet, Y. Structure/Function Relationships of [NiFe]- and [FeFe]-Hydrogenases. *Chem. Rev.* **2007**, *107* (10), 4273–4303.

3. McEvoy, J. P.; Brudvig, G. W. Water-Splitting Chemistry of Photosystem II. *Chem. Rev.* **2006**, *106* (11), 4455–4483.

4. Hoffman, B. M.; Lukoyanov, D.; Yang, Z.-Y.; Dean, D. R.; Seefeldt, L. C. Mechanism of Nitrogen Fixation by Nitrogenase: The Next Stage. *Chem. Rev.* **2014**, *114* (8), 4041–4062.

5. Holm, R. H.; Kennepohl, P.; Solomon, E. I. Structural and Functional Aspects of Metal Sites in Biology. *Chem. Rev.* **1996**, *96* (7), 2239–2314.

6. Dahl, S.; Logadottir, A.; Egeberg, R. C.; Larsen, J. H.; Chorkendorff, I.; Törnqvist, E.; Nørskov, J. K. Role of Steps in N_2 Activation on Ru(0001). *Phys. Rev. Lett.* **1999**, *83* (9), 1814–1817.

7. Zambelli, T.; Wintterlin, J.; Trost, J.; Ertl, G. Identification of the "Active Sites" of a Surface-Catalyzed Reaction. *Science* **1996**, *273* (5282), 1688–1690.

8. Kratzer, P.; Pehlke, E.; Scheffler, M.; Raschke, M. B.; Höfer, U. Highly Site-Specific H2 Adsorption on Vicinal Si Surfaces. *Phys. Rev. Lett.* **1998**, *81* (25), 5596–5599.

9. Jaramillo, T. F.; Jørgensen, K. P.; Bonde, J.; Nielsen, J. H.; Horch, S.; Chorkendorff, I. Identification of Active Edge Sites for Electrochemical H2 Evolution from MoS2 Nanocatalysts. *Science* **2007**, *317* (5834), 100–102.

10. Cook, T. R.; Dogutan, D. K.; Reece, S. Y.; Surendranath, Y.; Teets, T. S.; Nocera, D. G. Solar Energy Supply and Storage for the Legacy and Nonlegacy Worlds. *Chem. Rev.* **2010**, *110* (11), 6474–6502.

11. Esswein, A. J.; Nocera, D. G. Hydrogen Production by Molecular Photocatalysis. *Chem. Rev.* **2007**, *107* (10), 4022–4047.

12. Cotton, F. A.; Nocera, D. G. The Whole Story of the Two-Electron Bond, with the δ Bond as a Paradigm. *Acc. Chem. Res.* **2000**, *33* (7), 483–490.

13. Nocera, D. G. Chemistry of Personalized Solar Energy. *Inorg. Chem.* **2009**, *48* (21), 10001–10017.

14. Heyduk, A. F.; Nocera, D. G. Hydrogen Produced from Hydrohalic Acid Solutions by a Two-Electron Mixed-Valence Photocatalyst. *Science* **2001**, *293* (5535), 1639–1641.

15. Esswein, A. J.; Veige, A. S.; Nocera, D. G. A Photocycle for Hydrogen Production from Two-Electron Mixed-Valence Complexes. *J. Am. Chem. Soc.* **2005**, *127* (47), 16641–16651.

16. Elgrishi, N.; Teets, T. S.; Chambers, M. B.; Nocera, D. G. Stability-Enhanced Hydrogen-Evolving Dirhodium Photocatalysts through Ligand Modification. *Chem. Commun.* **2012**, *48* (76), 9474–9476.

17. Schmøkel, M. S.; Kamiński, R.; Benedict, J. B.; Coppens, P. Data Scaling and Temperature Calibration in Time-Resolved Photocrystallographic Experiments. *Acta Crystallogr., A, Found. Crystallogr.* **2010**, *66* (Pt 6), 632–636.

18. Parkin, G. *Metal–Metal Bonding in Bridging Hydride and Alkyl Compounds*. In *Metal-Metal Bonding*; Parkin, G., Ed.; Structure and Bonding; Springer Berlin Heidelberg, **2010**; pp 113–145.

19. Green, M. L. H.; Parkin, G. Application of the Covalent Bond Classification Method for the Teaching of Inorganic Chemistry. *J. Chem. Educ.* **2014**, *91* (6), 807–816.

20. Makal, A.; Benedict, J.; Trzop, E.; Sokolow, J.; Fournier, B.; Chen, Y.; Kalinowski, J. A.; Graber, T.; Henning, R.; Coppens, P. Restricted Photochemistry in the Molecular Solid State: Structural Changes on Photoexcitation of Cu(I) Phenanthroline Metal-to-Ligand Charge Transfer (MLCT) Complexes by Time-Resolved Diffraction. *J. Phys. Chem. A* **2012**, *116* (13), 3359–3365.

21. Gray, T. G.; Veige, A. S.; Nocera, D. G. Cooperative Bimetallic Reactivity: Hydrogen Activation in Two-Electron Mixed-Valence Compounds. *J. Am. Chem. Soc.* **2004**, *126* (31), 9760–9768.

22. Coppens, P.; Sokolow, J.; Trzop, E.; Makal, A.; Chen, Y. On the Biexponential Decay of the Photoluminescence of the Two Crystallographically-Independent Molecules in Crystals of $[Cu(I)(phen)(PPh_3)_2][BF_4]$. *J. Phys. Chem. Lett.* **2013**, *4* (4), 579–582.

23. Makal, A.; Trzop, E.; Sokolow, J.; Kalinowski, J.; Benedict, J.; Coppens, P. The development of Laue techniques for single-pulse diffraction of chemical complexes: time-resolved Laue diffraction on a binuclear rhodium metal-organic complex. *Acta Crystallogr., Sect. A* 2011, 67, 319–326

24. Benedict, J. B.; Makal, A.; Sokolow, J. D.; Trzop, E.; Scheins, S.; Henning, R.; Graber, T.; Coppens, P. Time-Resolved Laue Diffraction of Excited Species at Atomic Resolution: 100 Ps Single-Pulse Diffraction of the Excited State of the Organometallic Complex $Rh^2(\mu\text{-}PNP)_2(PNP)_2{\cdot}BPh_4$. *Chem. Commun.* **2011**, *47* (6), 1704–1706.

25. Evans, J.; Okrasinski, S. J.; Pribula, A. J.; Norton, J. R. Mechanism of Reductive Elimination. 3. Methyl Radical Elimination from Cis-Dimethyltetracarbonylosmium. *J. Am. Chem. Soc.* **1977**, *99* (17), 5835–5836.

26. Carter, W. J.; Okrasinski, S. J.; Norton, J. R. Mechanisms of the Elimination Reactions of $Os(CO)_4(H)R$ and $Os(CO)_4R_2$. *Organometallics* **1985**, *4* (8), 1376–1386.

27. Carter, W. J.; Kelland, J. W.; Okrasinski, S. J.; Warner, K. E.; Norton, J. R. Mononuclear Hydrido Alkyl Carbonyl Complexes of Osmium and Their Polynuclear Derivatives. *Inorg. Chem.* **1982**, *21* (11), 3955–3960.

28. Wolczanski, P. T.; Threlkel, R. S.; Bercaw, J. E. Reduction of Coordinated Carbon Monoxide to "Zirconoxy" Carbenes with Permethylzirconocene Dihydride. *J. Am. Chem. Soc.* **1979**, *101* (1), 218–220.

29. Janowicz, A. H.; Bergman, R. G. Methane-Producing Hydrogenolysis of (.eta.5-cyclopentadienyl)(triphenylphosphine)dimethylcobalt(III). An Autocatalytic Mechanism Involving a Binuclear Metal Dihydride/metal Dialkyl Reaction as a Critical Step. *J. Am. Chem. Soc.* **1981**, *103* (9), 2488–2489.

30. Jones, W. D.; Huggins, J. M.; Bergman, R. G. Comparative Reactivities of Two Isoelectronic Transition-Metal Hydrides with Transition-Metal Carbonyls and Alkyls. *J. Am. Chem. Soc.* **1981**, *103* (15), 4415–4423.

31. Nappa, M. J.; Santi, R.; Halpern, J. Mechanisms of the Carbon-Hydrogen Bond-Forming Binuclear Reductive Elimination Reactions of Benzyl- and Hydridomanganese Carbonyls. *Organometallics* **1985**, *4* (1), 34–41.

32. Alemdaroğlu, N. H.; Penninger, J. L. M.; Oltay, P. D. E. Study of the Mechanism of Hydroformylation at Industrial Reaction Conditions. *Monatshefte für Chemie* **1976**, *107* (5), 1153–1165.

33. Norton, J. R. Organometallic Elimination Mechanisms: Studies on Osmium Alkyls and Hydrides. *Acc. Chem. Res.* **1979**, *12* (4), 139–145.

34. Hebrard, F.; Kalck, P. Cobalt-Catalyzed Hydroformylation of Alkenes: Generation and Recycling of the Carbonyl Species, and Catalytic Cycle. *Chem. Rev.* **2009**, *109* (9), 4272–4282.

35. Liu, G.; Li, C.; Guo, L.; Garland, M. Experimental Evidence for a Significant Homometallic Catalytic Binuclear Elimination Reaction: Linear-Quadratic Kinetics in the Rhodium Catalyzed Hydroformylation of Cyclooctene. *Journal of Catalysis* **2006**, *237* (1), 67–78.

36. Powers, D. C.; Hwang, S. J.; Zheng, S.-L.; Nocera, D. G. *Inorg. Chem.* **2014**, *53* (17), 9122–9128.

37. Pangborn, A. B.; Giardello, M. A.; Grubbs, R. H.; Rosen, R. K.; Timmers, F. J. Safe and Convenient Procedure for Solvent Purification. *Organometallics* **1996**, *15* (5), 1518–1520.

38. Iridium Complexes. In *Inorganic Syntheses*; Rauchfuss, T. B., Ed.; John Wiley & Sons, Inc., 2010; pp 164–178.

39. Apex II; Bruker AXS: Madison, WI, 2009.

40. Sheldrick, G. M. Experimental phasing with SHELXC/D/E: combining chain tracing with density modification. Acta Crystallogr. **2010**, *D66*, 479–485

41. Stephens, P. J.; Devlin, F. J.; Chabalowski, C. F.; Frisch, M. J. Ab Initio Calculation of Vibrational Absorption and Circular Dichroism Spectra Using Density Functional Force Fields. *J. Phys. Chem.* **1994**, *98* (45), 11623–11627.

42. Lee, C.; Yang, W.; Parr, R. G. Development of the Colle-Salvetti Correlation-Energy Formula into a Functional of the Electron Density. *Phys. Rev. B* **1988**, *37* (2), 785–789.

43. Becke, A. D. Density-functional Thermochemistry. III. The Role of Exact Exchange. *The Journal of Chemical Physics* **1993**, *98* (7), 5648–5652.

44. Frisch, M. J.; Trucks, G. W.; Schlegel, H. B.; Scuseria, G. E.; Robb, M. A.; Cheeseman, J. R.; Scalmani, G.; Barone, V.; Mennucci, B.; Petersson, G. A.; Nakatsuji, H.; Caricato, M.; Li, X.; Hratchian, H. P.; Izmaylov, A. F.; Bloino, J.; Zheng, G.; Sonnenberg, J. L.; Hada, M.; Ehara, M.; Toyota, K.; Fukuda, R.; Hasegawa, J.; Ishida, M.; Nakajima, T.; Honda, Y.; Kitao, O.; Nakai, H.; Vreven, T.; Montgomery, J. A., Jr.; Peralta, J. E.; Ogliaro, F.; Bearpark, M.; Heyd, J. J.; Brothers, E.; Kudin, K. N.; Staroverov, V. N.; Keith, T.; Kobayashi, R.; Normand, J.; Raghavachari, K.; Rendell, A.; Burant, J. C.; Iyengar, S. S.; Tomasi, J.; Cossi, M.; Rega, N.; Millam, J. M.; Klene, M.; Knox, J. E.; Cross, J. B.; Bakken, V.; Adamo, C.; Jaramillo, J.; Gomperts, R.; Stratmann, R. E.; Yazyev, O.; Austin, A. J.; Cammi, R.; Pomelli, C.; Ochterski, J. W.; Martin, R. L.; Morokuma, K.; Zakrzewski, V. G.; Voth, G. A.; Salvador, P.; Dannenberg, J. J.; Dapprich, S.; Daniels, A. D.; Farkas, O.; Foresman, J. B.; Ortiz, J. V.; Cioslowski, J.; Fox, D. J. *Gaussian 09*, revision D.01; Gaussian, Inc.: Wallingford, CT, 2009.

45. Teets, T. S.; Lutterman, D. A.; Nocera, D. G. Halogen Photoreductive Elimination from Metal–Metal Bonded Iridium(II)–Gold(II) Heterobimetallic Complexes. *Inorg. Chem.* **2010**, *49* (6), 3035–3043.

46. Andrae, D.; Häußermann, U.; Dolg, M.; Stoll, H.; Preuß, H. Energy-Adjustedab Initio Pseudopotentials for the Second and Third Row Transition Elements. *Theoret. Chim. Acta* **1990**, *77* (2), 123–141.

47. Ditchfield, R.; Hehre, W. J.; Pople, J. A. Self-Consistent Molecular-Orbital Methods. IX. An Extended Gaussian-Type Basis for Molecular-Orbital Studies of Organic Molecules. *The Journal of Chemical Physics* **1971**, *54* (2), 724–728.

48. Rassolov, V. A.; Ratner, M. A.; Pople, J. A.; Redfern, P. C.; Curtiss, L. A. 6-31G* Basis Set for Third-Row Atoms. *J. Comput. Chem.* **2001**, *22* (9), 976–984.

49. Zhao, Y.; Truhlar, D. G. Density Functionals with Broad Applicability in Chemistry. *Acc. Chem. Res.* **2008**, *41* (2), 157–167.

50. Zhao, Y.; Truhlar, D. G. The M06 Suite of Density Functionals for Main Group Thermochemistry, Thermochemical Kinetics, Noncovalent Interactions, Excited States, and Transition Elements: Two New Functionals and Systematic Testing of Four M06-Class Functionals and 12 Other Functionals. *Theor Chem Account* **2007**, *120* (1-3), 215–241.

51. Zhao, Y.; Truhlar, D. G. A New Local Density Functional for Main-Group Thermochemistry, Transition Metal Bonding, Thermochemical Kinetics, and Noncovalent Interactions. *The Journal of Chemical Physics* **2006**, *125* (19), 194101.

52. Reed, A. E.; Curtiss, L. A.; Weinhold, F. Intermolecular Interactions from a Natural Bond Orbital, Donor-Acceptor Viewpoint. *Chem. Rev.* **1988**, *88* (6), 899–926.

53. Weinhold, F.; Landis, C. R. Valency and Bonding: *A Natural Bond Orbital Donor–Acceptor Perspective*; Cambridge University Press: New York, **2005**.

54. Foster, J. P.; Weinhold, F. Natural Hybrid Orbitals. *J. Am. Chem. Soc.* **1980**, *102* (24), 7211–7218.

55. Reed, A. E.; Weinstock, R. B.; Weinhold, F. Natural Population Analysis. *The Journal of Chemical Physics* **1985**, *83* (2), 735–746.

56. Glendening, E.D.; Reed, A. E.; Carpenter, J. E.; Weinhold, F. NBO, version 3.1: University of Wisconsin: Madison, WI.

Chapter 5: Charge Transfer Studies of Peroxide Dianion

Portions of this chapter have been published:

5.1 Introduction

In the context of small molecule activation, the chemistry of the reduced oxygen species superoxide and peroxide is important to both industrial and biological processes. In biological systems oxygen is vital to aerobic respiration,[1] yet oxygen is also a source of toxic free radicals.[2] In industry superoxide and peroxide serve as environmentally friendly oxidizing agents for a variety of important chemical transformations. The chemistry of oxygen and reduced oxygen species are important to lithium air batteries which is a hot area of research due to their potential for high gravimetric energy density.[3]

While the superoxide anion has been studied extensively,[4–7] peroxide dianion has remained largely unprobed. Due to its highly concentrated negative charge, peroxide anions are commonly found as multidentate ligands in metal complexes[8] or in a hydrogen bonding environment provided by an inclusion complex.[9] For example, crystallographic studies of class Ib ribonucleotide reductase (Figure 5.1) have provided evidence for the

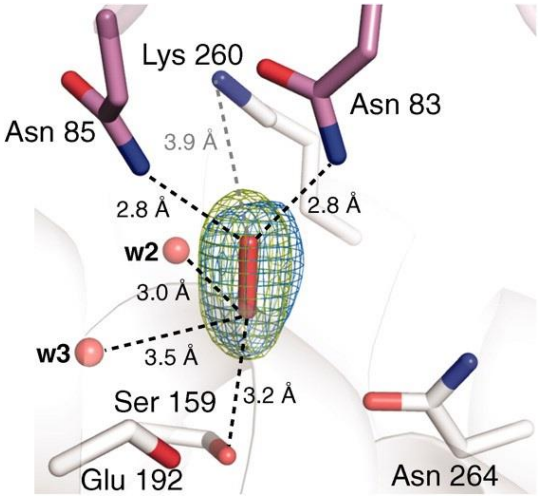

Figure 5.1. Peroxide bound in the hydrogen bonding pocket of class Ib ribonucleotide reductase. From Boal, A. K.; Cotruvo, J. A.; Stubbe, J.; Rosenzweig, A. C. Structural Basis for Activation of Class Ib Ribonucleotide Reductase. *Science* **2010**, *329* (5998), 1526–1530. Reprinted with permission from AAAS.

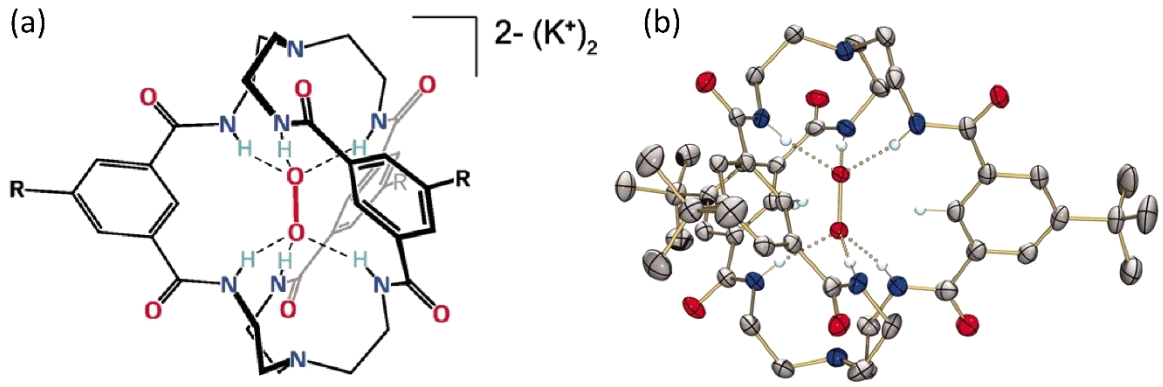

Figure 5.2. Connectivity (a) and crystallographic structure (b) of $[O_2 \subset m\text{BDCA-5t-H}_6]^{2-}$. From Lopez, N.; Graham, D. J.; McGuire, R.; Alliger, G. E.; Shao-Horn, Y.; Cummins, C. C.; Nocera, D. G. Reversible Reduction of Oxygen to Peroxide Facilitated by Molecular Recognition. *Science* **2012**, *335* (6067), 450–453. Reprinted with permission from AAAS.

inclusion of peroxide anion (HO_2^-) in the hydrogen bonding channel of class Ib ribonucleotide reductase.[10] In work leveraging advances in anion recognition chemistry,[11] Cummins, Nocera, and coworkers have provided the first example of solubilized peroxide dianion which has been isolated by encapsulation inside the hydrogen bonding cleft of the hexacarboxamide cryptand ligand, *m*BDCA-5t-H_6 (Figure 5.2).[12] Encapsulated peroxide dianion offer the unique opportunity to study the redox properties of molecular peroxide without the complications of bond transformations inherent to hydrogen peroxide or metal bound peroxide adducts.

Our initial investigations of the charge transfer properties of peroxide dianion utilized electrochemical techniques.[12] Under electrochemical conditions oxidation of $[O_2 \subset m\text{BDCA-5t-H}_6]^{2-}$ appears to be a two electron process, bypassing the superoxide species. Later studies utilized stopped-flow techniques with a series of quinones and suggested a large reorganization energy associated with the encapsulated peroxide dianion.[13]

In this Chapter, we probe the fundamental phenomena governing electron transfer from peroxide dianion. To achieve this, we utilize laser flash photolysis to probe the kinetics of electron transfer from peroxide dianion beyond the limits of diffusion. By the judicious choice of *tris*(bipyridyl) ruthenium(II) complexes ($Ru(bpy)_3^{2+}$) as photo-oxidants due to their complementary charge with $[O_2 \subset m\text{BDCA-5t-H}_6]^{2-}$, and the phenomena of ion pairing allows for the measurement of first order oxidation of peroxide dianion. The measured electron transfer rates are evaluated in the framework of classical Marcus theory to gain insight into the properties governing charge transfer within the encapsulated peroxide moiety. Density functional theory (DFT) calculations are used analyze the extent to which the encapsulating ligand, *m*BDCA-5t-H_6, perturbs the ET properties of its guest peroxide dianion. These results show that the peroxide moiety dominates the internal reorganization energy of the system, suggesting that management of the O–O bond is critical for minimizing the activation barrier for electron transfer in dioxygen species.

5.2 Results

5.2.1 Ion Pair Formation

The complementary charges of $[O_2 \subset m\text{BDCA-5t-H}_6]^{2-}$ and $Ru(bpy)_3^{2+}$ makes them susceptible to the phenomena of ion pairing at elevated concentrations, facilitating the circumvention of the diffusion limit. The salt $[Ru(bpy)_3][O_2 \subset m\text{BDCA-5t-H}_6]$ was prepared by salt metathesis as described in the experimental section. Single crystal X-ray diffraction of the prepared $[Ru(bpy)_3][O_2 \subset m\text{BDCA-5t-H}_6]$ was acquired to probe the level of interaction between the $[Ru(bpy)_3]^{2+}$ and $[O_2 \subset m\text{BDCA-5t-H}_6]^{2-}$ moieties. In the crystal lattice the ruthenium(II) polypyridyl complex can be found in close proximity of the cryptand (Figure 5.3). The crystallographically characterized peroxide O–O bond distance

is measured to be 1.479 Å, a typical value for known forms of anionic peroxide,[9,10,14] signaling that the encapsulated peroxide dianion is not significantly perturbed in the ion pair.

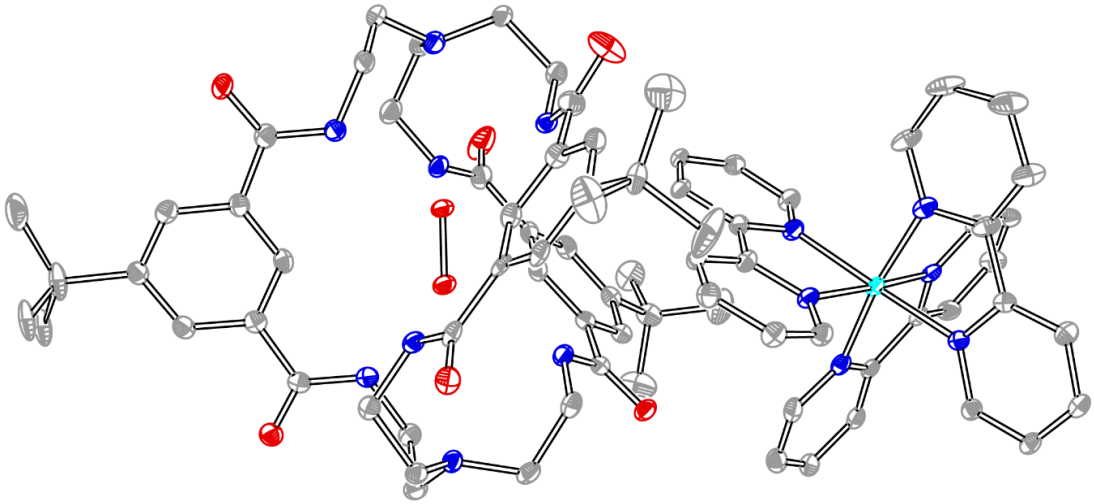

Figure 5.3. Crystal structure of $[Ru(bpy)_3][O_2 \subset m\text{BDCA-5t-H}_6]$. The peroxide bond distance is measured to be 1.479 Å, typical of known forms of anionic peroxide. Hydrogen atoms and solvent molecules omitted for clarity.

5.2.2 Stern-Volmer Emission Quenching

Initial spectroscopic experiments utilized the emissive triplet excited state of $Ru(bpy)_3^{2+}$ to probe bimolecular electron transfer by means of a Stern-Volmer quenching analysis (Equations 5.1 and 5. 2). In order to manipulate the concentration of $[O_2 \subset m\text{BDCA-5t-H}_6]^{2-}$ independent of the concentration of $Ru(bpy)_3^{2+}$, excess $[K(18\text{-crown-6})]_2[O_2 \subset m\text{BDCA-5t-H}_6]$ was used as the quenching agent. With increasing concentration of

$$\frac{I_0}{I} = (1 + k_q \tau_0 [Q]) \quad (1)$$

$$\frac{\tau_0}{\tau} = (1 + k_q \tau_0 [Q]) \quad (2)$$

$[K(18\text{-crown-}6)]_2[O_2 \subset m\text{BDCA-5t-H}_6]$ both the emission intensity and lifetime decrease monotonically, indicative of bimolecular quenching of the $Ru(bpy)_3^{2+*}$ excited state. Fitting the emission data to the Stern-Volmer relationships, Equations 5.1 and 5.2, steady state emission and the time resolved and quenching experiments yield quenching rate constants of 1.7×10^{10} $M^{-1}s^{-1}$ and 1.3×10^{10} $M^{-1}s^{-1}$, respectively. Both rates are in relatively good agreement and consistent with near diffusion limited quenching (Figure 5.4).

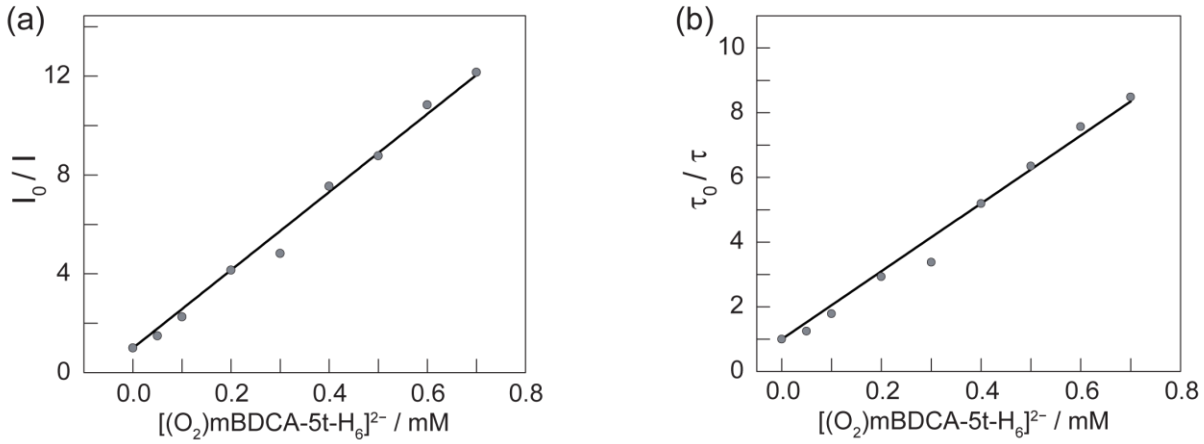

Figure 5.4. (a) Steady state and (b) time resolved emission quenching of $Ru(bpy)_3^{2+*}$ as a function of $[K(18\text{-crown-}6)]_2[O_2 \subset m\text{BDCA-5t-H}_6]$ concentration.

In principle, ion pairing should manifest itself in the steady state Stern-Volmer analysis. For a system in which both dynamic and static quenching mechanisms operate, the steady-state emission intensity quenching is expressed by Equation 5.3.[15] The quadratic nature of Equation 5.3 implies a deviation from linearity in the Stern-Volmer plots when static quenching is present. The ion pairing constant, K_{IP}, may be estimated using Debye-Huckel

$$\frac{I_0}{I} = (1 + k_q\tau_0[Q])(1 + K_{IP}[Q]) \qquad (3)$$

theory as detailed in the experimental section. Under the conditions of our emission quenching experiments K_{IP} is estimated to be small (~60 – 90 M^{-1} depending on the ionic strength). At the submillimolar concentrations of $[(O_2)\subset m\text{BDCA-5t-H}_6]^{2-}$ used for quenching experiments $K_{IP}[Q]$ is << 1, and thus the emission intensity quenching is dominated by dynamic quenching, resulting in the observed linear steady state Stern-Volmer curve.

5.2.3 Nanosecond Transient Absorption

In order to determine the nature of the $Ru(bpy)_3^{2+*}$ quenching, nanosecond transient absorption (TA) experiments were performed under a nitrogen atmosphere on $[Ru(bpy)_3][O_2\subset m\text{BDCA-5t-H}_6]$ obtained from salt metathesis. At short durations following laser excitation (~500 ns) a growth centered at 505 nm is observed which is indicative of the reduced photosensitizer (Figure 5.5a).[16,17] TA spectra of $[Ru(bpy)_3]Cl_2$ and free *m*BDCA-5t-H_6 (no encapsulated peroxide) shows negligible growth at 505 nm indicating that the encapsulated peroxide dianion is the primary electron donor (Figure 5.5b). Single wavelength kinetics recorded with different concentrations of $[Ru(bpy)_3][O_2\subset m\text{BDCA-5t-H}_6]$ show a positive correlation between concentration with both the rate of formation and total yield of $Ru(bpy)_3^{+}$ (Figure 5.5c), consistent with bimolecular reductive quenching of the $Ru(bpy)_3^{2+*}$ excited state by $[O_2\subset m\text{BDCA-5t-H}_6]^{2-}$. Pseudo first order rate constants were obtained from monoexponential fits of the kinetic traces to yield a bimolecular rate constant of 2.0×10^{10} $M^{-1}s^{-1}$, in good agreement with the emission quenching results. On longer timescales $Ru(bpy)_3^{+}$ begins to decay back to baseline with non-exponential kinetics. This can be attributed to the back reaction of the strongly reducing $Ru(bpy)_3^{+}$ with

the generated $[O_2 \subset m\text{BDCA-5t-H}_6]^-$ as well as the reaction of $Ru(bpy)_3^{+}$ with O_2 generated from the potential disproportionation of the superoxide adduct, $[O_2 \subset m\text{BDCA-5t-H}_6]^{-}$.[12]

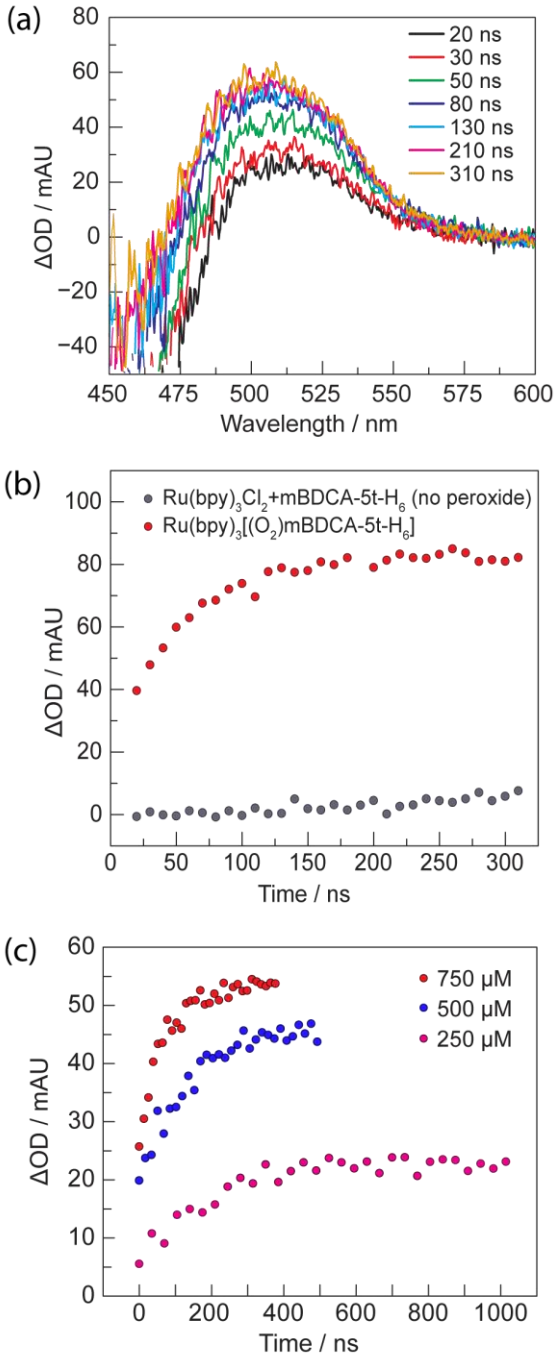

Figure 5.5. (a) Spectral evolution of the TA signal from a 750 μM $[Ru(bpy)_3][O_2 \subset m\text{BDCA-5t-H}_6]$ sample showing a 505 nm growth over evolve over 300 ns. (b) Comparison of the 505 nm TA signal between 750 μM $[Ru(bpy)_3][O_2 \subset m\text{BDCA-5t-H}_6]$ and 900 μM $Ru(bpy)_3Cl_2$ + mBDCA-5t-H_6 (no peroxide). (c) Concentration dependence of the TA of $[Ru(bpy)_3][O_2 \subset m\text{BDCA-5t-H}_6]$ observed at 505 nm.

5.2.4 Picosecond Transient Absorption

Picosecond TA experiments were performed to probe electron transfer at rates faster than diffusion. TA of solutions of $[Ru(bpy)_3][O_2 \subset m\text{BDCA-5t-H}_6]$ at concentrations approaching 1 mM show the formation of a peak at 525 nm on the picosecond timescale

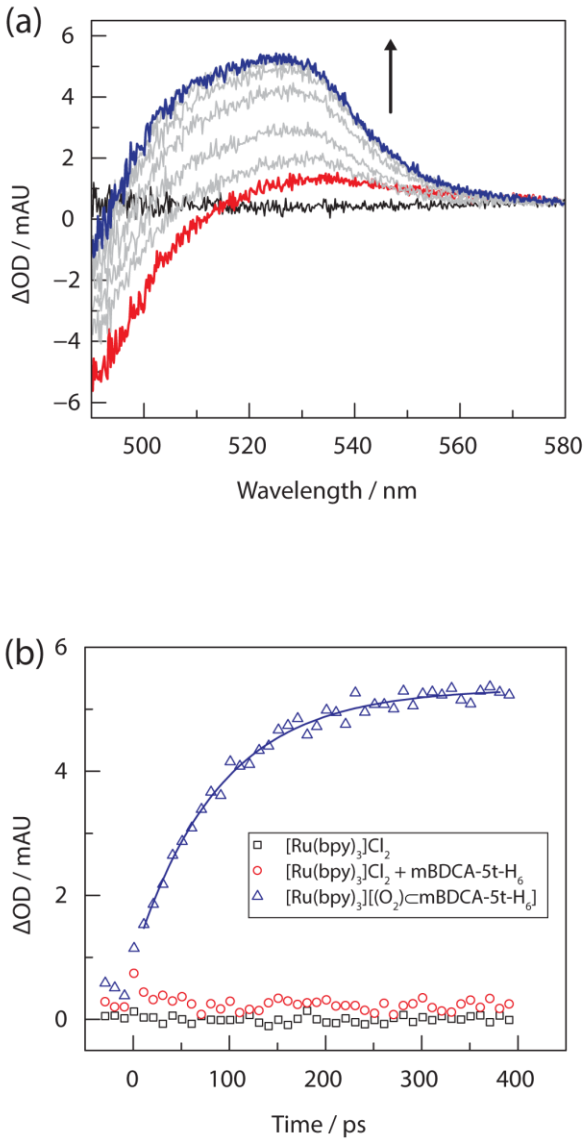

Figure 5.6. (a) 525 nm growth observed in the picosecond TA experiments over the time window of 1 ps (—, red) to 400 ps (—, blue). (b) Time evolution of the 525 nm TA signal for samples of $[Ru(bpy)_3]Cl_2$ (black squares), $[Ru(bpy)_3]Cl_2$ + *m*BDCA-5t-H_6 (red circules), and $[Ru(bpy)_3][O_2 \subset m\text{BDCA-5t-H}_6]$ (blue triangles). The growth curve of $Ru(bpy)_3^{+}$ fits to a monoexponential function with a time constant of 90±8 ps.

(Figure 5.6a). The 20 nm red shift of the TA growth is the result of the superposition of the bleach feature of the $Ru(bpy)_3^{2+*}$ excited state, which has a maximum at 450 nm that tails into the red regions, with the weaker growth of the reduced species $Ru(bpy)_3^{+}$ centered at 505 nm. The growth of the 525 nm feature exhibits monoexponential kinetics with a time constant of 90±8 ps, faster than the limit of diffusion at these concentrations by approximately three orders of magnitude. When the concentration of $[Ru(bpy)_3][O_2 \subset m\text{BDCA-5t-H}_6]$ is decreased the intensity of the 525 nm growth also decreases but the time constant remains unchanged (Figure 5.7). The concentration dependence and fast kinetics are consistent with charge transfer between ion pairs of $[Ru(bpy)_3]^{2+}$ and $[O_2 \subset m\text{BDCA-5t-H}_6]^{2-}$ which form a detectable population at concentrations approaching 1 mM.

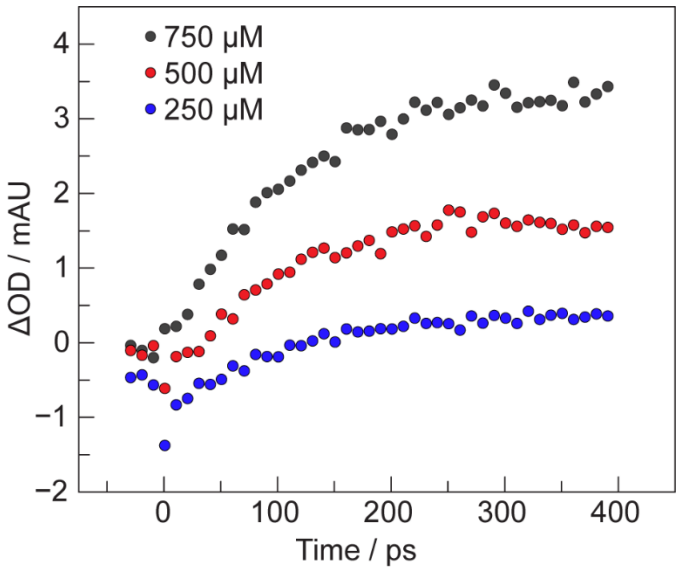

Figure 5.7. Single-wavelength kinetic traces from picosecond TA monitored at 525 nm for $[Ru(bpy)_3][O_2 \subset m\text{BDCA-5t-H}_6]$ with concentrations of 250 µM (blue), 500 uM (red), and 750 µM (black).

In order to confirm ion pairing between $[Ru(bpy)_3]^{2+}$ and $[O_2 \subset m\text{BDCA-5t-H}_6]^{2-}$, the TA experiments were repeated in DMF solutions at elevated ionic strength supplied by 0.1 M tetrabutylammonium hexafluorophosphate (TBA-PF_6) in an effort to disrupt the pairing interaction. Nanosecond TA shows that the 505 nm growth is preserved, albeit with a decrease in the rate of formation, a phenomenon commonly known as the kinetic salt effect (Figure 5.8).[18] In contrast, the 525 nm signal observed in picosecond transient absorption is completely absent (Figure 5.9). The observation that ET is maintained on the diffusional

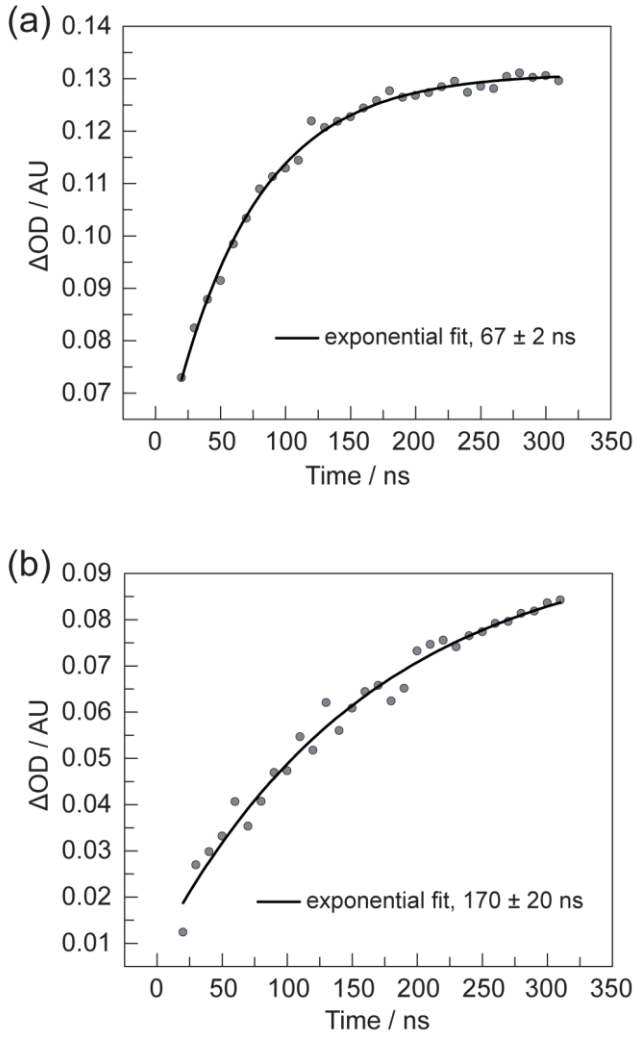

Figure 5.8. Nanosecond TA $[Ru(bpy)_3][O_2 \subset m\text{BDCA-5t-H}_6]$ (a) without TBA-PF_6, and (b) with 0.1 M TBA-PF_6. The decrease in the bimolecular quenching rate constant is attributed to the kinetic salt effect.

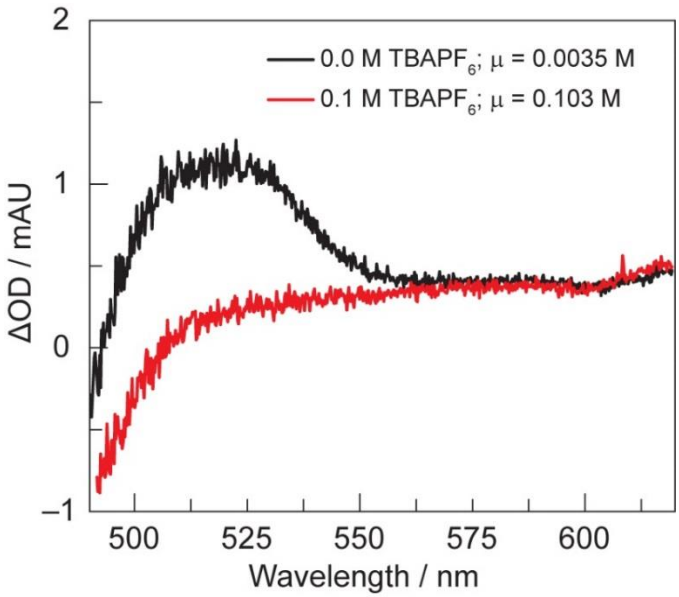

Figure 5.9. Picosecond TA of $[Ru(bpy)_3][O_2 \subset m\text{BDCA-5t-H}_6]$ without (—, black) and with (—, red) 0.1 M TBA-PF_6 at a 400 ps delay.

timescale scale of the nanosecond TA experiments implies that the lack of signal on the picosecond timescale is due to the disruption of ion pair formation and not deleterious reactivity between the electrolyte and the components of the $[Ru(bpy)_3][O_2 \subset m\text{BDCA-5t-H}_6]$ salt.

In order to probe the effect of driving force on the rate of electron transfer, a series of ruthenium(II) polypyridyl complexes, $Ru(L)(L')_2^{2+}$ where L and L' are bipyridyl ligands decorated with electron donating or withdrawing groups on the 4 and 4' positions, were prepared (Table 5.1). Salt metathesis reactions to form their respective $[Ru(L)(L')_2][O_2 \subset m\text{BDCA-5t-H}_6]$ salt complexes were unsuccessful for ruthenium(II) complexes with bipyridyl ligands containing electron withdrawing groups such as tris(4,4'-dichloro-2,2'-bipyridyl) and tris(bis(4,4'-trifluoromethyl)-2,2'-bipyridyl), instead

generating chloride and fluoride adducts of *m*BDCA-5t-H_6, respectively as determined by NMR.

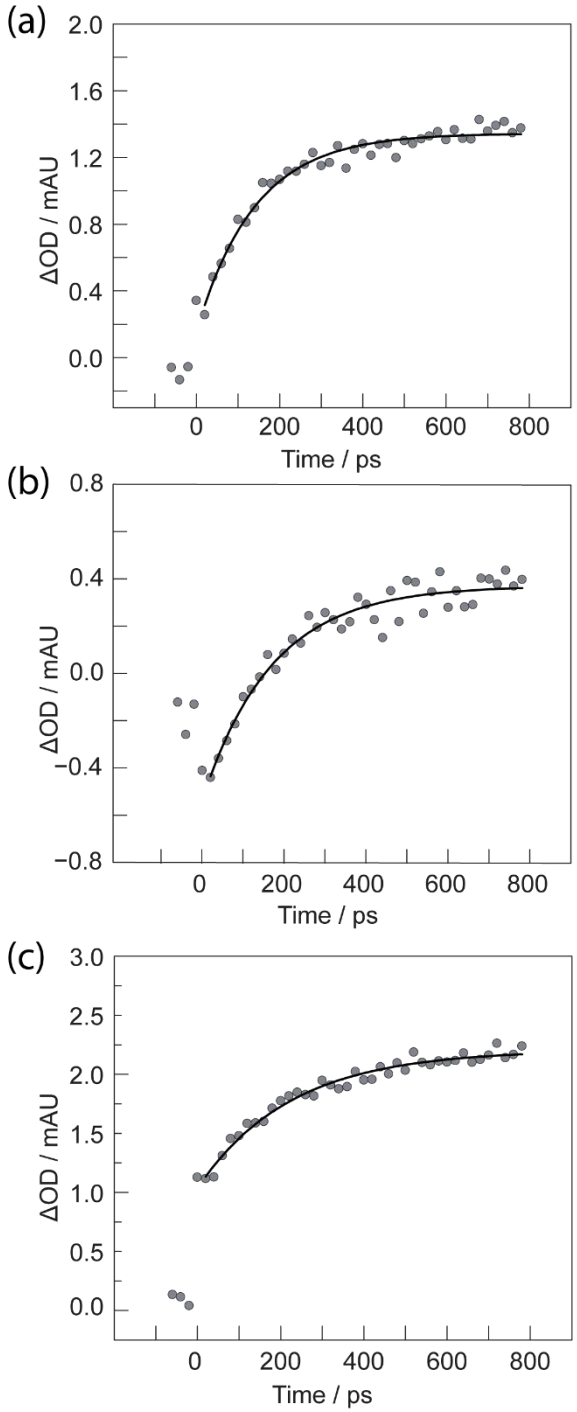

Figure 5.10. 525 nm trace of picosecond TA for 1 mM samples of $[O_2 \subset m\text{BDCA-5t-}H_6]^{2-}$ salts of (a) $Ru(bpy)_2(dmbpy)^{2+}$, (b) $Ru(bpy)_2(dOMebpy)^{2+}$, (c) $Ru(dmbpy)_3^{2+}$.

Table 5.1. Electrochemical and Photophysical Data of Ruthenium Polypyridyl Complexes.

Ru^{II} complex	$E°^{a}$(II/I)/V	$E_{00}{}^{a}$/eV	E(II*/I)/V	$-\Delta G°'^{b}$/eV	k_{ET} / s^{-1}
$Ru(bpy)_3^{2+}$	−1.73	2.11	0.39	1.15	1.1×10^{10}
$Ru(bpy)_2(dmbpy)^{2+}$	−1.76[c]	2.08	0.33	1.09	6.3×10^{9}
$Ru(bpy)_2(dOMebpy)^{2+}$	−1.77	2.05	0.29	1.05	5.5×10^{9}
$Ru(dmbpy)_3^{2+}$	−1.84[c]	2.06	0.22	0.99	4.6×10^{9}

[a] E_{00} determined from fitting of 77 K emission spectra as detailed in the experimental section (Figure 5.17). [b] Driving forces were calculated as detailed in the experimental section using $E°([(O_2^{-})\subset m\text{BDCA-5t-H6}]/[(O_2^{2-})\subset m\text{BDCA-5t-H6}])$ = −0.85 V vs Fc+/Fc, ref 13. [c] Redox potential adjusted to Fc^{+}/Fc reference couple, ref 19.

Picosecond TA of salts of the encapsulated peroxide with the ruthenium(II) complexes in Table 5.1 were performed (Figure 5.10). Each species exhibits spectral features similar to those observed with the $Ru(bpy)_3^{2+}$ salt of $[O_2\subset m\text{BDCA-5t-H}_6]^{2-}$ and all obey first order kinetics with the rates of electron transfer increasing monotonically with driving force.

5.2.5 Marcus Analysis of Unimolecular ET Rate Constants

The series of electron transfer rates obtained from the picosecond TA data were evaluated using the Marcus theory of electron transfer. A least-squares fit of the data to Equation 5.4 provides an estimate for both the magnitude of the electronic coupling term, $|H_{ab}|$, and the total reorganization energy, λ, with values of 9 ± 3 cm^{-1} and 1.5 ± 0.1 eV for $|H_{ab}|$ and λ respectively (Figure 5.11).

$$k_{ET} = \frac{2\pi}{\hbar}|H_{ab}|^2 \frac{1}{\sqrt{4\pi\lambda k_B T}} e^{\frac{-(\Delta G°' + \lambda)^2}{4\lambda k_B T}} \qquad (4)$$

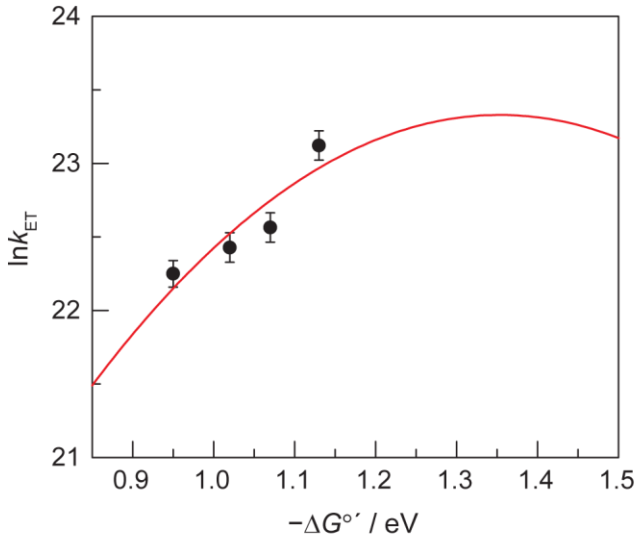

Figure 5.11. Semi-log plot of k_{ET} vs the free energy driving force for [Ru(II) complex][(O_2)⊂*m*BDCA-5t-H_6] salts in DMF. The calculated fit of Equation 5.4 is illustrated (▬, red line).

The semiclassical Marcus equation neglects nuclear tunneling effects that can become significant when high frequency vibrations ($\hbar\omega \geq 4k_BT$) contribute to the internal reorganization energy.[20,21] To address the validity of the classical limit the ET rates were also fit to a model that accounts for the quantum mechanical nature of the Frank-Condon term, Equations 5.5 through 5.9, where ω_{ox} and ω_{red} are the angular vibrational frequencies

$$k_{\mathrm{ET}} = \frac{2\pi}{\hbar}|H_{ab}|^2 \frac{e^S S^{\upsilon} e^{\frac{-(\Delta G^{\circ'}+\lambda_0+\upsilon\hbar\omega)^2}{4\lambda k_B T}}}{\Gamma(\upsilon+1)\hbar\omega} \tag{5}$$

$$\upsilon = \frac{-\Delta G^{\circ'}-\lambda_0}{\hbar\omega} - \frac{2\lambda_0 k_B T}{(\hbar\omega)^2}\ln\left(\frac{-\Delta G^{\circ'}-\lambda_0}{S\hbar\omega}\right) \tag{6}$$

$$\mathrm{S} = \frac{\lambda_i}{\hbar\omega} \tag{7}$$

$$\omega = \left(\frac{2\omega_{\mathrm{ox}}^2\omega_{red}^2}{\omega_{\mathrm{ox}}^2+\omega_{red}^2}\right)^{1/2} \tag{8}$$

$$\lambda = \lambda_i + \lambda_o \tag{9}$$

of the reduced and oxidized species, respectively and λ_i and λ_o are the inner and outer sphere contributions to the reorganization energy, respectively. Using known vibrational frequencies for the peroxide[22] and superoxide[23] and calculating λ_o to be 0.60 eV using the dielectric continuum model (*vide infra*) we calculate $|H_{ab}|$ and λ_i to be 16 ± 9 cm^{-1} and 1.2 ± 0.3 eV, respectively.

The classical and quantum models yield values that are within error of one another. However, the high uncertainty of $|H_{ab}|$ limits our ability to draw robust conclusions about the electronic coupling other than that it is likely to be small. In principal, UV-vis spectroscopy can be employed to detect optical charge transfer transitions in the ion pairs.[24] However, a charge transfer band was not observed above the detection limit (Figure 5.12) in the 500 to 800 nm region where it would be expected for a system with weak electronic coupling (Equation 5.10), which is unsurprising in light of the weak absorptivity expected for such bands ($\varepsilon \sim 10^2$ $M^{-1}cm^{-1}$)[25] and the limited concentrations achievable for ion pairs in DMF (~ 100 μM).

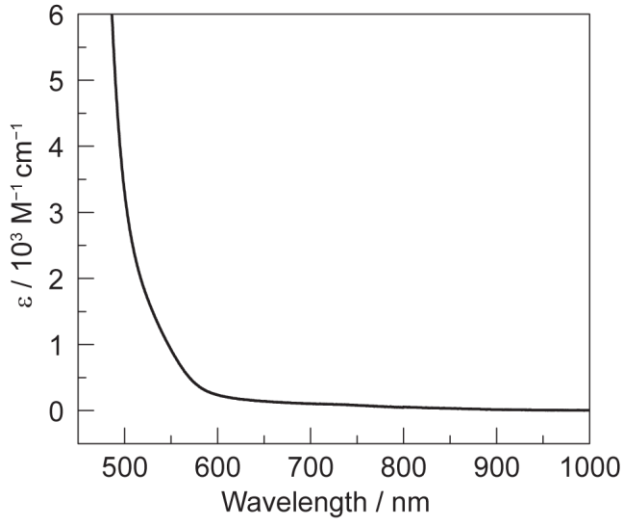

Figure 5.12. UV-Vis absorption spectrum of the 500 to 800 nm region where a charge transfer band would be expected to be observed for the $[Ru(bpy)_3][O_2 \subset m\text{BDCA-5t-H}_6]$ ion pair. All spectral features in the region can be attributed to the $Ru(bpy)_3^{2+}$ ion.

$$E_{\mathrm{op}} \approx \lambda + \Delta G^{\circ'} \tag{10}$$

5.2.6 Evaluation of the Internal Reorganization Energy

To gain insight into the contributions to the reorganization energy of the ET process, calculations using a harmonic oscillator model and DFT where performed. The harmonic oscillator model provides a simple method with which to estimate the internal reorganization energy of a single stretching mode.[20] In the harmonic oscillator approximation, Equation 5.11, where f_j^r and f_j^p are the force constants for the reduced and oxidized species, respectively, and Δq_j is the change in bond length, we presume that the peroxide moiety will dominate the internal reorganization energy due to its large change in bond length and large force constants. DFT will serve as a check for this approximation (*vide infra*). Using the known bond lengths and force constants for peroxide (1.497 Å, 2.8 N/cm force constant)[22] and superoxide (1.28 Å, 6.17 N/cm force constant)[23] we calculate the contribution to the reorganization energy from an *isolated* peroxide/superoxide moiety to be 0.90 eV.

$$\lambda_i = \sum_j \frac{f_j^r f_j^p}{f_j^r + f_j^p} \left(\Delta q_j\right)^2 \tag{11}$$

To incorporate the effect of the cryptand ligand on $\lambda_i(O_2^{2-}/O_2^{-})$ as well as conformational changes of the ligand itself upon ET, density functional theory (DFT) was applied to calculate λ_i in the classical limit for the complete $[(O_2)\subset m\text{BDCA-5t-H}_6]^{2-}$ ion. This technique has been used successfully to calculate the internal reorganization energy for

blue copper proteins.[26] This approximation assumes identical curvature of both diabatic states, a fundamental assumption of linear Marcus theory[20,27,28] that has been show to provide good results even in the case of highly asymmetric free energy surfaces.[29] Estimates for λ_i are obtained using DFT by computing the difference in energy of a species in its distorted and ground state geometries. The internal reorganization energy of the entire $[O_2 \subset m\text{BDCA-5t-H}_6]^{2-}$ moiety is calculated as $\lambda_i\ [(O_2^{2-}/O_2^{-}) \subset m\text{BDCA-5t-H}_6] = E[(O_2^{2-}) \subset m\text{BDCA-5t-H}_6]_{\text{supereroxide-equil-geom}} - E[(O_2^{2-}) \subset m\text{BDCA-5t-H}_6]_{\text{peroxide-equil-geom}}$ where E is single point energy as determined by DFT calculations. Geometry optimizations were performed for the peroxide-cryptand and superoxide-cryptand adducts using the crystal structure coordinates of the $[(O_2) \subset m\text{BDCA-5t-H}_6]^{2-}$ anion as a starting point for geometry optimization. The computed peroxide O–O bond distance (1.506 Å) and the average computed amide nitrogen to peroxide oxygen bond distances (2.728 Å) are in good agreement with distances measured in the crystal structure (1.497 Å and 2.685 Å respectively), supporting the validity of the computations. Although the superoxide adduct cannot be isolated, let alone crystalized owing to its proclivity to disproportionate in the presence of the cryptand,[13] the computed O–O bond distance (1.36 Å) is also in good agreement with that measured in crystalline potassium superoxide (1.28 Å).[30] The energies obtained from single point energy calculations of the peroxide-cryptand in its optimized geometry as well as in the optimized geometry the superoxide adduct are listed in Table 5.2. The energy difference between the peroxide-cryptand adduct in the superoxide and peroxide equilibrium geometries yields an internal reorganization energy of λ_i = 0.88 eV. In order to assess the agreement between the inner sphere reorganization energies calculated using the harmonic model (Equation 5.11) and those calculated with the DFT approach

Table 5.2. Single point energies determined from DFT calculations.

Structure	Energy/eV
$E[(O_2)\subset mBDCA\text{-}5t\text{-}H_6]^{2-}$ supereroxide-equil-geom	−79132.32
$E[(O_2)\subset mBDCA\text{-}5t\text{-}H_6]^{2-}$peroxide-equil-geom	−79133.20
$E[O_2]^{2-}$ supereroxide-equil-geom	−4081.68
$E[O_2]^{2-}$peroxide-equil-geom	−4082.41

described above, we also applied the DFT method to the free peroxide dianion. The difference of the calculated single point energies (Table 5.2) afforded an internal reorganization energy of λ_i = 0.73 eV for an isolated peroxide/superoxide moiety, consistent with a minor deviation from the harmonic oscillator approximation.

As the internal reorganization energy of the ruthenium(II) polypyridyl moiety has been shown to be negligible,[31] the final contribution to the Marcus reorganization energy is the rearrangement of outer sphere solvent dipoles which can be calculated using a dielectric continuum model, Equation 5.12, where D_{op} and D_s are the optical and static dielectric constants of the solvent and a_1 and a_2 are the radii of the two reactants and r is the separation distance.[20] The molecular radius of the $[(O_2)\subset m\text{BDCA-5t-H}_6]^{2-}$ anion (r_{avg} = 5.0 Å) was taken as the geometric mean of the radii along the three axes of the crystal structure (Figure 5.13); we prefer to use this metric versus closest distance of the ions from the crystal structure as the distance of closest approach is unlikely to be sampled on average in solution. Together with the r_{avg} = 6.5 Å for the ruthenium complex,[32] we calculate an outer

$$\lambda_o = (\Delta e)^2 \left[\frac{1}{2a_1} + \frac{1}{2a_2} - \frac{1}{r}\right]\left[\frac{1}{D_{op}} - \frac{1}{D_s}\right] \qquad (12)$$

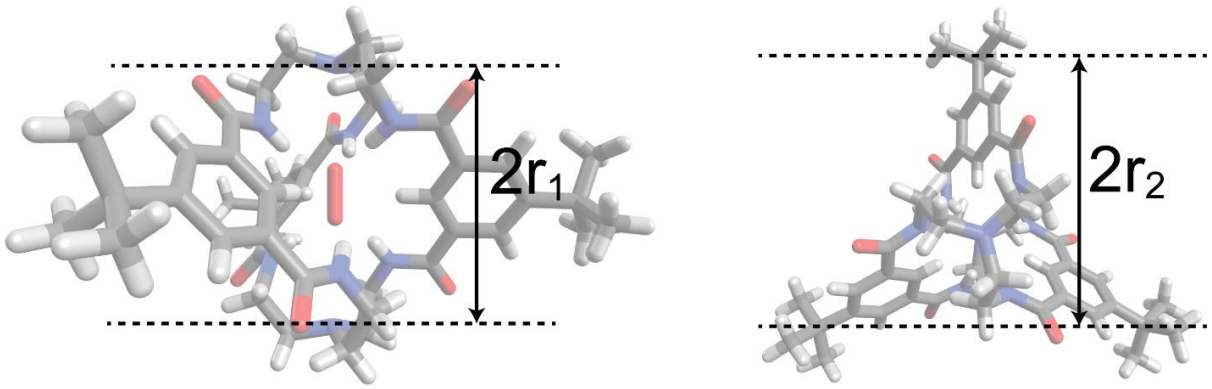

Figure 5.13. The distance r_1 is taken as half the distance between the apical nitrogen atoms of the cryptand from the crystal structure geometry and r_2 is taken as half the height of the equilateral triangle formed by the quaternary carbons of the three *tert*-butyl groups of the cryptand. Because the of the C_3 symmetry of the cryptand, two distances are taken to be r_2. The effective cryptand radius was calculated to be the geometric mean of three distances: r_1, r_2 and r_3 (= r_2),

$$r_{avg} \approx \sqrt[3]{r_1\, r_2\, r_2}.$$

sphere reorganization energy of 0.60 eV for the ET reaction in DMF (D_{op} = 2.05, D_s = 36.7) using the dielectric continuum model. Adding this value to the inner sphere contribution calculated for the $[(O_2) \subset m\text{BDCA-5t-H}_6]^{2-}$ moiety, a total reorganization energy of λ = 1.48 eV obtained from computation.

5.3 Discussion

Ion pairing at elevated concentration results in parallel pathways for oxidation of the peroxide species by the photosensitizer: diffusion limited charge transfer between unbound ions in solution and fast unimolecular charge transfer between the two components of the ion pair (Figure 5.14). Charge transfer between unbound pairs manifests itself as a concentration dependence, leading to the observed emission quenching (Figure 5.4). The lack of observable static quenching in the steady state emission

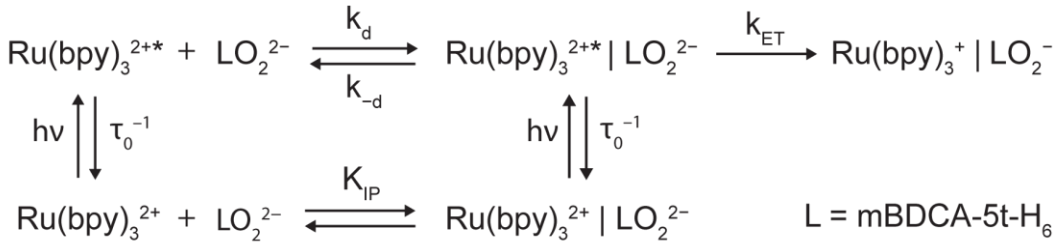

Figure 5.14. Depiction of the parallel pathways resulting in photo-oxidation of the encapsulated peroxide dianion.

data is consistent with the small ion pairing constant, K_{IP}, as predicted by Debye-Hückel theory for our experimental conditions.

Whereas a bimolecular ET reaction is diffusion-limited, photoinduced charge transfer within an ion-pair of the complex ion permits the intrinsic ET kinetics to be isolated. The range of ET driving forces we were able to probe was hampered by reactivity of the ground state species of the ion pair, precluding observation of ET in the Marcus inverted region. This deleterious chemistry is attributed to the strongly nucleophilic nature of the encapsulated peroxide dianion. Notwithstanding the limited range of driving forces we were able to probe, fitting the data of Table 5.1 to Equation 5.4 and 5.5 yields results that are consistent with the system at hand. The modest electronic coupling of $|H_{ab}| = 8 \pm 3$ cm^{-1} is consistent with other non-covalently bound donor-acceptor assemblies[33] and suggests nonadiabatic electron transfer, attributable to the sterically shielding environment of the cryptand ligand.

The calculations of the inner sphere reorganization energy, λ_i, provide further insight into the reorganization energy of the ion pair obtained from TA data. Investigation of the isolated λ_i (O_2^{2-}/O_2^-) obtained from both a harmonic oscillator approximation and DFT

methods produced similar results lending validity to the models. When comparing the values of λ_i (O_2^{2-}/O_2^-) = 0.73 eV with λ_i [(O_2^{2-}/O_2^-)⊂*m*BDCA-5t-H_6] = 0.88 eV obtained from DFT, we can conclude that the peroxide dianion itself dominates the inner sphere reorganization energy for the oxidation of [(O_2)⊂*m*BDCA-5t-H_6]$^{2-}$ and the cryptand contribution is minor. When accounting for the outer sphere solvent dipole reorganization contribution of 0.60 eV obtained from the dielectric continuum model, the calculations are in excellent agreement with the value of λ = 1.5 ± 0.1 eV obtained from the fit of the experimental data shown in Figure 5.11 to a semiclassical Marcus model.

5.4 Conclusion

The intrinsic reactivity of this diatomic dianion is difficult to establish because it does not typically exist in a soluble form. To this end, the cavity of hexacarboxamide cryptand (⊂*m*BDCA-5t-H_6) offers a platform from which to investigate the dianion's electron transfer chemistry. By forming complex salts of the [(O_2)⊂*m*BDCA-5t-H_6]$^{2-}$ with Ru(II) polypyridyl dications, a photoinduced ET reaction chemistry of peroxide may be established without the limits imposed by diffusion. Picosecond TA spectroscopy allows for the direct measurement of the activated electron transfer rate constant, k_{ET}, which is on the order of 10^{10} s^{-1}. The driving-force dependence of k_{ET}, obtain from a homologous series of Ru(II) polypryridyl cations, allows for the determination of the Marcus parameters of the system which are in good agreement with estimates from calculations. Evaluation of λ_i shows that the contraction of the peroxide O–O bond prior to ET dominates the reorganization energy of the system with little contribution from the cryptand ligand. This suggests that the encapsulated peroxide provides a faithful model system with which to study the ET kinetics of free peroxide dianion with limited structural influence from the cryptand. The

concentration of the internal reorganization energy in the O–O bond suggests that management of the O–O bond length is an important consideration in the design of water oxidation or oxygen reduction catalysts. This design principle could be evaluated through modification of the ligand scaffold to compress the equilibrium bond length of the encapsulated peroxide, reducing the internal reorganization energy associated with the oxidation of peroxide to superoxide.

5.5 Experimental

TA and emission experiments were performed in collaboration with Andrew G. Maher. $[(O_2)\subset m\text{BDCA-5t-H}_6]^{2-}$ salts were prepared and characterized by Matthew Nava and Dr. Nazario Lopez. X-ray crystal structure determination was performed by Prof. David C. Powers.

General Methods

All reagents, unless otherwise indicated, were purchased from Aldrich. Solvents were purified on a Glass Contour Solvent Purification System manufactured by SG Water USA, LLC. NMR solvents were obtained from Cambridge Isotope Laboratories. ^{1}H NMR spectra were obtained at the MIT Department of Chemistry Instrumentation Facility on a Bruker 400 MHz spectrometer. Elemental analysis was performed by Robertson Microlit Labratories. Microwave-assisted synthesis was accomplished using a CEM Discover microwave reactor. UV-vis spectra were recorded on a Varian Cary 5000 UV-vis-NIR spectrophotometer. Steady-state emission spectra were obtained on a PTI QM 4 Fluorometer, with a 150 W Xe-arc lamp for excitation and a Hamamatsu R928 photomultiplier tube for detection. All samples for the room temperature optical

spectroscopy experiments were prepared using DMF stored over activated 3 Å molecular sieves in a N_2-atmosphere glovebox. Samples were prepared in: 1.0 cm path length quartz cuvettes (Starna, Inc.) with Teflon screw-caps for room temperature emission spectroscopy; in 1.0 mm path length quartz cuvettes (Starna, Inc.) for UV vis spectroscopy; in custom 2.0 mm path length high-vacuum cells for nanosecond and picosecond transient absorption (TA) spectroscopy; and in quartz EPR tubes, which were brought to 77 K using liquid nitrogen for low temperature emission spectroscopy. Electrochemical measurements were made in an N_2-atmosphere glovebox using a CH Instruments 760D Electrochemical Workstation using CHI Version 10.03 software. Thin-layer UV-vis spectroelectrochemistry experiments were performed using a 0.5 mm path length quartz cell with an Ocean Optics USB4000 spectrophotometer and DT-Mini-2GS UV-vis-NIR light source in conjunction with the CH electrochemical workstation.

Synthesis of $[Ru(dmbpy)_3][PF_6]_2$

The previously reported synthesis[34] of $Ru(dmbpy)_3^{2+}$ was modified by isolating the PF_6^- salt. $RuCl_3 \cdot xH_2O$ (88 mg) and 4,4′-dimethyl-2,2′-bipyridine (324 mg) were loaded into a 100 mL round-bottom flask along with 11.4 mL of deionized H_2O. To the flask was added 3 mL of 0.1 M HCl and the mixture was brought to reflux. After 90 min, 1.7 mL of 30% neutralized hypophosphoric acid was added to the flask. The mixture continued to reflux for 1 h, at which point it was allowed to cool. After filtration, the solution was concentrated and excess sodium hexafluorophosphate was added, resulting in the formation of an orange precipitate. The precipitate was collected by vacuum filtration and washed ×3 with THF. The solid was dried at 80 °C under vacuum overnight. The ^1H NMR spectrum of the product was consistent with literature reports of the compound.[35]

Synthesis of $[Ru(bpy)_2(dmbpy)]Cl_2$

The previously reported synthesis[36] of $Ru(bpy)_2(dmbpy)^{2+}$ was adapted for the microwave technique. $Ru(bpy)_2Cl_2$ (104 mg) and 4,4′-dimethyl-2,2′-bipyridine (278 mg) were dissolved in 15 mL of ethanol contained within a 35-mL microwave reactor tube. The reaction mixture was subjected to microwave irradiation for 1.75 h at a reaction condition of 120 °C. Upon completion of the reaction, the solution was filtered while still warm and the filtrate was brought to dryness. H_2O (40 mL) was added to the remaining solid and the solution was washed ×4 with $CHCl_3$. The aqueous fraction was again brought to dryness to furnish the product. The product was dried at 80 °C under vacuum overnight. The ^1H NMR spectrum of the product was consistent with literature reports of the compound.[35]

Synthesis of $[Ru(bpy)_2(dOMebpy)]Cl_2$

The title compound was prepared as described above for $[Ru(bpy)_2(dmbpy)]Cl_2$ but a stoichiometric amount of 4,4′-dimethoxy-2,2′-bipyridine was used rather than an excess.

Preparation of Ru-bpy | Peroxide Salt

$[K_2(DMF)_5][(O_2)\subset m\text{BDCA-5t-H}_6]$, which was prepared by previously published procedures,[13] (1 equiv) and the corresponding ruthenium(II) bipyridyl chloride or hexafluorophosphate salt (1 equiv) were placed as solids into a 20 mL scintillation vial equipped with a Teflon stir bar. The solids were dissolved in DMF (2 mL). This dark red solution was allowed to stir at room temperature for ~5 min, after which it was passed through a 200-nm Teflon membrane syringe filter to remove KCl. To the filtrate, diethyl ether (15 mL) was added to induce solids precipitation. The resulting slurry was allowed to stir at room temperature for 10 min to ensure complete precipitation of the product. The

resulting dark red solid was collected on a medium sintered glass frit, washed with diethyl ether (3 × 5 mL) and dried under dynamic vacuum for 3 h. The ^{1}H NMR spectrum indicates a 1:1 integration of the Ru complex cation to peroxide adduct dianion.

[Ru(bpy)$_3$][(O$_2$)⊂*m*BDCA-5t-H$_6$]

[K$_2$(DMF)$_5$][(O$_2$)⊂*m*BDCA-5t-H$_6$] (260 mg, 0.196 mmol) and [Ru(bpy)$_3$]Cl$_2$ (126 mg, 0.196 mmol) were employed in the aforementioned procedure to furnish 270 mg (95%) of product. ^{1}H NMR (400 MHz, DMSO-*d*$_6$, δ): [(O$_2$)⊂*m*BDCA-5t-H$_6$]$^{2-}$: 14.62 (s, 6 H), 10.14 (s, 3 H), 8.13 (s, 6 H), 3.37 (br, 6 H), 2.59 (br d, 6 H), 2.34 (br d, 12 H), 1.29 (s, 27 H). Ru(bpy)$_3^{2+}$: 8.76 (d, 6 H), 8.06 (t, 6 H), 7.71 (d, 6 H), 7.50 (t, 6 H). ^{13}C NMR (100 MHz, DMSO-*d*$_6$, δ): [(O$_2$)⊂*m*BDCA-5t-H$_6$]$^{2-}$: 165.58, 148.99, 135.00, 126.74, 124.21, 59.93, 40.83, 34.38, 31.16. [Ru(bpy)$_3$]$^{2+}$: 156.44, 151.17, 137.81, 127.83, 124.37. Anal. Calcd (Found) for [Ru(bpy)$_3$][(O$_2$)⊂*m*BDCA-5t-H$_6$]·6DMF, C$_{96}$H$_{136}$N$_{20}$O$_{14}$Ru$_1$: C, 60.97 (60.44); H, 7.03 (7.01); N, 14.81 (14.44).

[Ru(bpy)$_2$(dmbpy)][(O$_2$)⊂*m*BDCA-5t-H$_6$]

[K$_2$(DMF)$_5$][(O$_2$)⊂*m*BDCA-5t-H$_6$] (164 mg, 0.124 mmol) and [Ru(bpy)$_2$(dmbpy)]Cl$_2$ (85 mg, 0.127 mmol) were employed in the aforementioned procedure to furnish 162 mg (89%) of product. ^{1}H NMR (400 MHz, DMSO-*d*$_6$, δ): [(O$_2$)⊂*m*BDCA-5t-H$_6$]$^{2-}$: 14.59 (s, 6 H), 10.10 (s, 3 H), 8.14 (s, 6 H), 3.37 (br, 6 H), 2.59 (br d, 6 H), 2.33 (br d, 12 H), 1.30 (s, 27 H). [Ru(bpy)$_2$(dmbpy)]$^{2+}$: 8.80 (d, 4 H), 8.71 (s, 2 H), 8.10 (t, 4 H), 7.73 (t, 4 H), 7.53 (q, 6 H), 7.36 (d, 2H), 2.52 (s, 6H).

[Ru(bpy)$_2$(dOMebpy)][(O_2)⊂*m*BDCA-5t-H_6]

[K_2(DMF)$_5$][(O_2)⊂*m*BDCA-5t-H_6] (112 mg, 0.084 mmol) and [Ru(bpy)$_2$(dOMebpy)]Cl_2 (60.6 mg, 0.086 mmol) were employed in the aforementioned procedure to furnish 110 mg (86%) of product. ^{1}H NMR (400 MHz, DMSO-d_6, δ): [(O_2)⊂*m*BDCA-5t-H_6]$^{2-}$: 14.59 (s, 6 H), 10.10 (s, 3 H), 8.15 (s, 6 H), 3.37 (br, 6 H), 2.59 (br d, 6 H), 2.33 (br d, 12 H), 1.30 (s, 27 H). Ru(bpy)$_2$(dmbpy)$^{2+}$: 8.78 (d, 4 H), 8.48 (s, 2 H), 8.10 (q, 4 H), 7.82 (d, 2 H), 7.72 (d, 2 H), 7.51 (m, 4H), 7.41 (d, 2H), 7.15 (d, 2H), 3.98 (s, 6H).

[Ru(dmbpy)$_3$][(O_2)⊂*m*BDCA-5t-H_6]

[K_2(DMF)$_5$][(O_2)⊂*m*BDCA-5t-H_6] (111 mg, 0.084 mmol) and [Ru(dmbpy)$_3$]PF_6 (79 mg, 0.084 mmol) were employed in the aforementioned procedure to furnish 123 mg (95%) of product. ^{1}H NMR (400 MHz, DMSO-d_6, δ): [(O_2)⊂*m*BDCA-5t-H_6]$^{2-}$: 14.60 (s, 6 H), 10.09 (s, 3 H), 8.14 (s, 6 H), 3.37 (br, 6 H), 2.59 (br d, 6 H), 2.31 (br d, 12 H), 1.29 (s, 27 H). [Ru(dmbpy)$_3$]$^{2+}$: 8.68 (s, 6 H), 7.49 (d, 6 H), 7.32 (d, 6 H), 2.49 (s, 18 H).

Crystallography

Structural data were collected as a series of φ scans using 0.41328 Å radiation at temperature of 15 K (Oxford Diffraction Helijet) on a vertical mounted Bruker D8 three-circle platform goniometer equipped with an Apex II CCD at ChemMatCARS located at Advances Photon Source (APS), Argonne National Laboratory (ANL). Crystals were mounted on a glass fibre using Paratone N oil. Data were integrated using SAINT[37] and scaled with a multi-scan absorption correction using SADABS. The structures were solved by direct methods using SHELXS-97 and refined against F^2 on all data by full matrix least

squares with SHELXL-97.[38] All non-hydrogen atoms were refined anisotropically. Hydrogen atoms were placed at idealized positions and refined using a riding model.

Table 5.3. Crystal data and structure refinement metrics.

	[Ru(bpy)$_3$][(O_2)⊂*m*BDCA-5t-H_6]
formula	$C_{194}H_{268}N_{41}O_{29}Ru_2$
CCDC #	1030626
fw, g/mol	3840.36
temp, K	15
cryst system	monoclinic
space group	C2/c
color	orange
a, Å	29.8268 (15)
b, Å	17.7117 (9)
c, Å	38.0786 (19)
α, deg	90
β, deg	96.7900 (7)
γ, deg	90
V, Å^3	19975.2 (17)
Z	4
R1[a]	0.068
wR2[b]	0.215
GOF[c] (F^2)	1.08
R_{int}	0.069

[a] $R1 = \Sigma||F_o| - |F_c||/\Sigma|F_o|$. [b] $wR2 = (\Sigma(w(F_o^2 - F_c^2)^2)/\Sigma(w(F_o^2)^2))^{1/2}$. [c] $GOF = (\Sigma w(F_o^2 - F_c^2)^2/(n - p))^{1/2}$ where n is the number of data and p is the number of parameters refined.

Spectroscopic Experiments

Nanosecond TA experiments were performed using a modified version of a previously-reported home-built Nd:YAG laser system.[39] In the modified setup, the previously-used Triax 320 spectrometer has been replaced by a Horiba iHR320 spectrometer. The output of the Xe-arc lamp was set to 2.0 ms pulses with 30 A current. The reported experiments used a 250 nm blaze grating (300 grooves/mm). The entrance slit for the monochromator was set to 5 nm resolution and the gate time for the CCD was 40 ns. The power of the pump beam (λ = 355 nm) was set to 2 mJ/pulse. The TA spectra reported are averages of 4 replicates of 5 four-spectrum sequences. Drift in the baseline of the transient absorption spectra was corrected by setting the ΔOD value for each spectrum equal to 0.00 mAU between 575-600 nm, where both $Ru(bpy)_3^{+}$ and $Ru(bpy)_3^{2+*}$ are optically silent. Single-wavelength kinetics traces were obtained by averaging 13 nm spectral windows about the wavelength of interest for each time point. Lifetime measurements were made using a least-squares fit using the OriginPro 8.5 data analysis software.

Picosecond TA experiments were performed using a previously-reported home-built Ti:sapphire laser system.[40] The excitation wavelength was set to 325 nm with a power kept between 10-20 μJ/pulse at the sample. The continuum for the probe pulses was generated by focusing an 800 nm beam through a CaF_2 substrate. The reported experiments used a 500 nm blaze grating (300 grooves/mm) and the entrance slit for the monochromator was set to 4 nm. The TA spectra reported are averages of 4-6 replicates of 500 four-spectrum sequences. Drift in the baseline of TA spectra was corrected by setting the ΔOD value for each spectrum equal to 0.00 mAU between 575-585 nm. The spectra were also corrected by subtracting an average of 3 spectra taken at negative delays, i.e. time points at which the

probe pulse arrives at the sample before the pump pulse. Single-wavelength kinetics traces were obtained by averaging 10 nm spectral windows about the wavelength of interest for each time point. The reported time constants and rate constants are the average of 3-5 samples. Lifetime measurements were made using a least-squares fit using the OriginPro 8.5 data analysis software. The uncertainty in the values is reported as a 95% confidence interval.

In steady-state emission quenching experiments samples were excited with 400 nm light. Each sample comprised 0.1 mM $[Ru(bpy)_3]Cl_2$ and a different concentration of $[K(18\text{-crown-6})]_2[(O_2)\subset m\text{BDCA-5t-H}_6]$ ranging from 0.0 mM to 0.7 mM. The emission spectrum of $[Ru(bpy)_3]Cl_2$ was recorded and integrated three times, and the average integrated emission intensity was used for Stern-Volmer analysis.

In time resolved emission quenching experiments the excitation source was the same Ti:sapphire laser system used for TA experiments. Emission data was collected using a Hamamatsu C4334 Streak Scope camera that has been described previously.[41] The laser excitation source was tuned to 400 nm, and the power was attenuated to 2.5 mW using a neutral density filter in front of the sample. A 1 μs or 5 μs time window was used, and 5000 exposures were captured for each sample. The same samples were used for both the steady-state and time-resolved emission quenching experiments. The emission decays traces were fit with monoexponential functions to afford the lifetime of excited $[Ru(bpy)_3]Cl_2$ in each sample. The lifetimes were then used for Stern-Volmer analysis.

Computational Methods

Density functional theory (DFT) calculations were performed using ORCA version 3.0.42 Structure optimizations were performed using the BP86 functional and polarized Ahlrichs TZV basis sets: H: TZV(p); main-group: TZV(2d)).[43,44] Single point energies were computed using the B3LYP hybrid functional and foregoing basis sets as implemented in ORCA 3.0.[45-47] Geometries used for DFT calculations are available free of charge via the ACS Publications website at DOI: 10.1021/jp5110505.

Estimation of K_{IP} from picosecond TA data

The ion-pair equilibrium constant K_{IP} for [Ru(bpy)$_3$][(O_2)⊂*m*BDCA-5t-H_6] in DMF may be estimated using the picosecond transient absorption data. This can be achieved by calculating the yield of $Ru(bpy)_3^{+}$ using the magnitude of the growth of the TA signal at 525 nm from its initial value in the prompt spectrum to its final value once the signal is fully formed at a 400 ps delay. We use a value of $\Delta\varepsilon$ = 13,200 $M^{-1}cm^{-1}$ at 525 nm for the $Ru(bpy)_3^{+}$ species based on spectroelectrochemical data (Figure 5.15). This analysis assumes that all excited ion-pairs undergo charge separation.

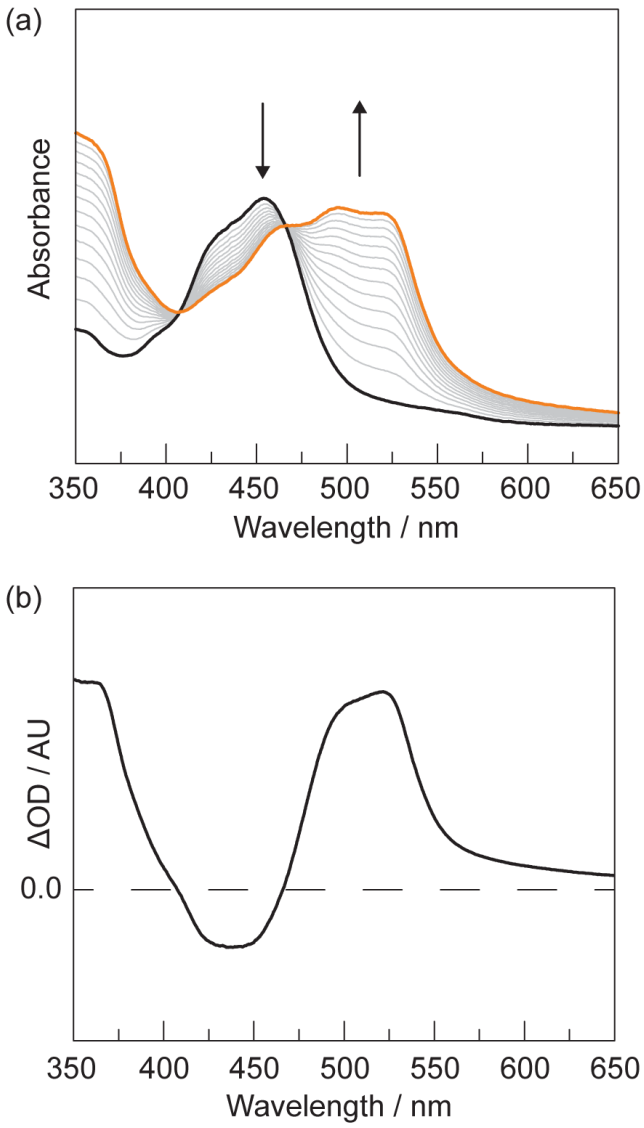

Figure 5.15. (a) Thin layer spectroelectrochemistry of $[Ru(bpy)_3]Cl_2$ in DMF with 0.1 M $TBAPF_6$ supporting electrolyte. Electrolysis was performed at –1.8 V vs Ag wire pseudo-reference electrode and using a platinum flag working electrode and platinum wire counter electrode. Spectra were acquired every 8 seconds during electrolysis. Black trace = initial, orange trace = final. (b) Difference spectrum for $Ru(bpy)_3^{+}$ | $Ru(bpy)_3^{2+}$ generated by subtracting the initial trace from the final trace of the spectroelectrochemical acquisition.

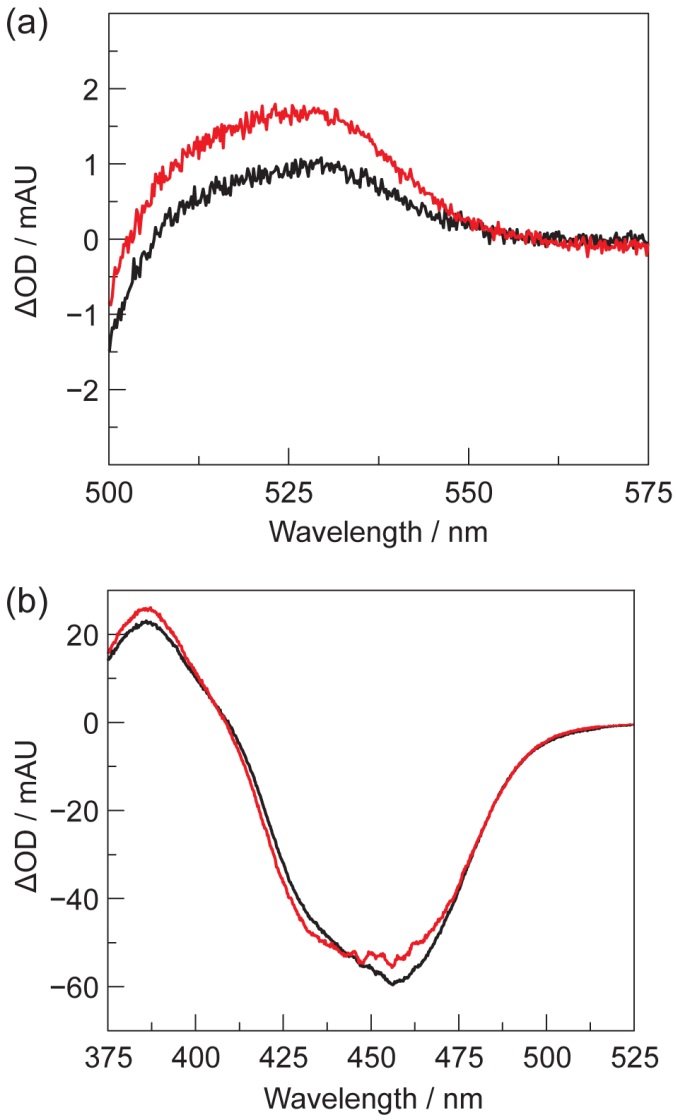

Figure 5.16. Picosecond transient absorption spectra of samples of $[Ru(bpy)_3][(O_2)\subset m\text{BDCA-5t-H}_6]$ at concentrations of 0.25 mM (—, black lines) and 0.5 mM (—, red lines) taken at delays of (a) 400 ps and (b) 1 ps.

The initial yield of excited $Ru(bpy)_3^{2+*}$ can be determined using the magnitude of the bleach in the TA spectrum at 448 nm at a prompt delay and a value of $\Delta\varepsilon = -11{,}300\ M^{-1}cm^{-1}$ at 448 nm.[48] Data used for the calculation is provided in Figure 5.16.

By taking the ratio of $[Ru(bpy)_3^{2+*}]_{initial}$:$[Ru(bpy)_3^{+}]_{400\ ps}$ from the picosecond TA data as being equal to the ratio of free $Ru(bpy)_3^{2+}$ to ion-paired $Ru(bpy)_3^{2+}$ in solution, K_{IP} can be

estimated using the definition of K_{IP} and conservation of mass, Equations 5.13 and 5.14, respectively.

For a sample containing 250 μM $[Ru(bpy)_3][(O_2)\subset m\text{BDCA-5t-H}_6]$ in DMF, the growth of the $Ru(bpy)_3^{+}$ TA signal at 525 at a delay of 400 ps had a magnitude of 1.6 mAU,

$$K_{IP} = \frac{\left[\text{Ru(bpy)}_3^{2+}\right]_{\text{ion-paired}}}{\left(\left[\text{Ru(bpy)}_3^{2+}\right]_{\text{free}}\right)^2} \tag{13}$$

$$\left[\text{Ru(bpy)}_3^{2+}\right]_{\text{free}} + \left[\text{Ru(bpy)}_3^{2+}\right]_{\text{ion-paired}} = [[\text{Ru(bpy)}_3][(O_2)\subset m\text{BDCA-5t-H}_6]] \tag{14}$$

corresponding to a concentration of $[Ru(bpy)_3^{+}]_{400\text{ ps}} = 6.1 \times 10^{-7}$ M. The prompt bleach at 448 nm had a magnitude of 55 mAU, corresponding to a concentration of $[Ru(bpy)_3^{2+*}]_{\text{initial}} = 2.5 \times 10^{-5}$ M. This affords a ratio of 41 for $[Ru(bpy)_3^{2+*}]_{\text{initial}}$:$[Ru(bpy)_3^{+}]_{400\text{ ps}}$ at this concentration. Using Equations 5.13 and 5.14, a K_{IP} of 1.0×10^2 M^{-1} is estimated.

For a sample containing 500 μM $[Ru(bpy)_3][(O_2)\subset m\text{BDCA-5t-H}_6]$ in DMF, the growth of the $Ru(bpy)_3^{+}$ TA signal at 525 at a delay of 400 ps had a magnitude of 2.2 mAU, corresponding to a concentration of $[Ru(bpy)_3^{+}]_{400\text{ ps}} = 8.3 \times 10^{-7}$ M. The prompt bleach at 448 nm had a magnitude of 54 mAU, corresponding to a concentration of $[Ru(bpy)_3^{2+*}]_{\text{initial}} = 2.5 \times 10^{-5}$ M. It should be noted that the magnitude of the bleach might be slightly suppressed in this experiment due to low transmittance of the white light probe pulse at 448 nm at this high concentration. The measured concentrations afford a ratio of 30 for $[Ru(bpy)_3^{2+*}]_{\text{initial}}$: $[Ru(bpy)_3^{+}]_{400\text{ ps}}$ at this concentration. Using Equations 5.13 and 5.14, a K_{IP} of 68 M^{-1} is estimated.

Debye-Huckel Treatment for Estimation of K_{IP}

The equilibrium constant for the formation of an ion pair between two spherical molecules due to coulombic attraction can be estimated using the Debye-Huckel theory (Equation 5.15) where δ_r is estimated to be 0.8 Å.

$$K_{\mathrm{IP}} = \frac{4\pi \mathrm{N_{Av}} r^2 \delta_r e^{\frac{-w(r)}{\mathrm{k_B}T}}}{D_s(1+\kappa r)} \tag{15}$$

Calculation of Driving Forces of Charge Transfer

In the high temperature semiclassical Marcus theory model (Equation 5.4) $|H_{ab}|$ is the magnitude of the electronic coupling matrix element, $\Delta G^{\circ\prime}$ is the work-corrected free energy of reaction, and λ the is reorganization energy of the cross reaction. The expression for $\Delta G^{\circ\prime}$ is exemplified for the case of $[Ru(bpy)_3][(O_2)\subset m\text{BDCA-5t-H}_6]$ as Equations 5.16 through 5.18. Note: $E_{(LO_2^-/LO_2^{2-})}$ = –0.85 V vs. Fc^+/Fc.[12]

$$\Delta G^{\circ\prime} = -\mathrm{e}\left(E_{(\mathrm{Ru(bpy)_3^{2+}/Ru(bpy)_3^{+}})} - E_{(\mathrm{LO_2^-/LO_2^{2-}})} + E^*_{\mathrm{Ru(bpy)_3^{2+}}}\right) + w^p - w^r \tag{16}$$

$$w^{ij}(r) = \frac{z_i z_j}{D_s(1+\kappa r)} \tag{17}$$

$$\kappa = \left(\frac{8\pi \mathrm{N_{Av}}\mu}{1000 D_s \mathrm{k_B}T}\right)^{1/2} \tag{18}$$

The work terms for bringing the reactants or products to their separation distance, r = 11.5 Å using the hard sphere model, can be approximated using Debye-Huckel theory[20,49] by Equation 5.17 where z_i and z_j are the charges of the species (+2/–2 for the reactants;

+1/−1 for the products), D_s is the dielectric constant of the medium (36.7 for DMF), and κ, for a solution of ionic strength μ, is given by Equation 5.18 where N_{AV} is *Avogadro's* number and k_B is Boltzmann's constant. In evaluating the work terms, a concentration of 1.0 millimolar was used for the [Ru(II) polypyridyl complex][$(O_2)\subset m$BDCA-5t-H_6], and the temperature, T, was 295 K.

Determination of E_{00} from Emission Data

The excited state energy, E_{00}, of the ruthenium polypyridyl complexes can be obtained, to a simple approximation, by fitting the 77 K emission spectra (Figure 5.17) using a Frank-Condon analysis, Equation 5.19 where S is the dimensionless Huang-Rhys factor, $\hbar\omega$ is the vibrational energy spacing, and $\Delta\bar{\nu}_{1/2}$ is the bandwidth,[50,51] and are tabulated in Table 5.4.

$$I(\bar{\nu}) = \sum_{n}^{5} \left(\frac{E_{00} - n\hbar\omega}{E_{00}}\right)^3 \left(\frac{S^n}{n!}\right) \exp\left[-4\ln 2 \left(\frac{\bar{\nu} - E_{00} + n\hbar\omega}{\Delta\bar{\nu}_{1/2}}\right)^2\right] \qquad (19)$$

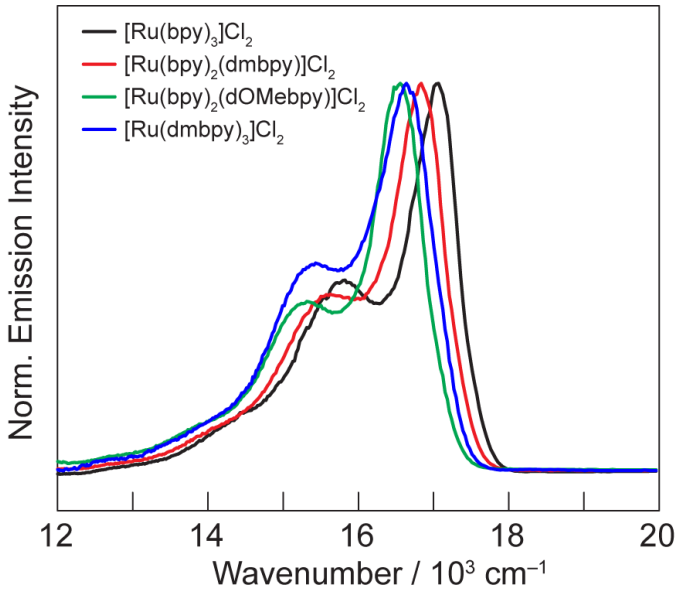

Figure 5.17. Normalized steady-state emission spectra (λ_{exc} = 455 nm) of $[Ru(bpy)_3]Cl_2$ (—, black line), $[Ru(bpy)_2(dmbpy)]Cl_2$ (—, red line), $[Ru(bpy)_2(dOMebpy)]Cl_2$ (—, green line) and $[Ru(dmbpy)_3]Cl_2$ (—, blue line) in DMF at 77 K. The E_{00} energy was taken to be equal to the (0–0) emission band observed in the vibrational progression.

Table 5.4. Emission spectra fitting parameters for ruthenium polypyridyl complexes.

Ru^{II} complex	**E_{00}/eV**	**S**	**$\hbar\omega$/cm^{-1}**	**$\Delta\bar{\nu}_{1/2}$/cm^{-1}**
$Ru(bpy)_3^{2+}$	2.11	0.7	1220	860
$Ru(bpy)_2(dmbpy)^{2+}$	2.08	0.6	1230	900
$Ru(bpy)_2(dOMebpy)^{2+}$	2.05	0.6	1250	890
$Ru(dmbpy)_3^{2+}$	2.06	0.7	1230	980

5.6 References

1. Kelly, D. J.; Hughes, N. J.; Poole, R. K. *Helicobacter pylori: Physiology and Genetics*; Mobley, H. L., Mendz, G. L., Hazell, S. L., Eds.; ASM Press: Washington (DC), 2001.

2. Kohen, R.; Nyska, A. Invited Review: Oxidation of Biological Systems: Oxidative Stress Phenomena, Antioxidants, Redox Reactions, and Methods for Their Quantification. *Toxicol Pathol* **2002**, *30* (6), 620–650.

3. Girishkumar, G.; McCloskey, B.; Luntz, A. C.; Swanson, S.; Wilcke, W. Lithium–Air Battery: Promise and Challenges. J. Phys. Chem. Lett. 2010, 1 (14), 2193–2203.

4. Stanbury, D. M.; Mulac, W. A.; Sullivan, J. C.; Taube, H. Superoxide Reactions with (isonicotinamide)pentaammineruthenium(II) and -(III). *Inorg. Chem.* **1980**, *19* (12), 3735–3740.

5. Sawyer, D. T.; Valentine, J. S. How Super Is Superoxide? *Acc. Chem. Res.* **1981**, *14* (12), 393–400.

6. Sawyer, D. T.; Chiericato, G.; Angelis, C. T.; Nanni, E. J.; Tsuchiya, T. Effects of Media and Electrode Materials on the Electrochemical Reduction of Dioxygen. *Anal. Chem.* **1982**, *54* (11), 1720–1724.

7. Wood, P. M. The Potential Diagram for Oxygen at pH 7. *Biochemical Journal* **1988**, *253* (1), 287–289.

8. B. Meunier, Ed., *Metal-Oxo and Metal-Peroxo Species in Catalytic Oxidations* (Springer, Berlin, 2000).

9. Kato, T.; Fujimoto, T.; Tsutsui, A.; Tashiro, M.; Mitsutsuka, Y.; Machinami, T. Identification of a Discrete Peroxide Dianion, O_2^{2-}, in a Two Sodium–(1,6-Anhydro-β-maltose)$_2$–Peroxide Complex. *Chemistry Letters* **2010**, *39* (2), 136–137.

10. Boal, A. K.; Cotruvo, J. A.; Stubbe, J.; Rosenzweig, A. C. Structural Basis for Activation of Class Ib Ribonucleotide Reductase. *Science* **2010**, *329* (5998), 1526–1530.

11. Kang, S. O.; Llinares, J. M.; Powell, D.; VanderVelde, D.; Bowman-James, K. New Polyamide Cryptand for Anion Binding. *J. Am. Chem. Soc.* **2003**, *125* (34), 10152–10153.

12. Lopez, N.; Graham, D. J.; McGuire, R.; Alliger, G. E.; Shao-Horn, Y.; Cummins, C. C.; Nocera, D. G. Reversible Reduction of Oxygen to Peroxide Facilitated by Molecular Recognition. *Science* **2012**, *335* (6067), 450–453.

13. Ullman, A. M.; Sun, X.; Graham, D. J.; Lopez, N.; Nava, M.; De Las Cuevas, R.; Müller, P.; Rybak-Akimova, E. V.; Cummins, C. C.; Nocera, D. G. Electron-Transfer Studies of a Peroxide Dianion. *Inorg. Chem.* **2014**, *53* (10), 5384–5391.

14. Tallman, R. L.; Margrave, J. L.; Bailey, S. W. The Crystal Structure of Sodium Peroxide. *J. Am. Chem. Soc.* **1957**, *79* (11), 2979–2980.

15. Lakowicz, J. R. *Principles of Fluorescence Spectroscopy*, 3rd ed.; Springer: New York, 2006.

16. Creutz, C.; Sutin, N. Electron-Transfer Reactions of Excited States: Direct Evidence for Reduction of the Charge-Transfer Excited State of tris(2,2'-bipyridine)ruthenium(II). *J. Am. Chem. Soc.* **1976**, *98* (20), 6384–6385.

17. Anderson, C. P.; Salmon, D. J.; Meyer, T. J.; Young, R. C. Photochemical Generation of $Ru(bpy)_3^+$ and 0_2^-. *J. Am. Chem. Soc.* **1977**, *99* (6), 1980–1982.

18. Atkins, P.; de Paula, J. *Physical Chemistry for the Life Sciences*; Macmillan: New York, 2011.

19. Mabrouk, P.; Wrighton, M. Resonance Raman Spectroscopy of the Lowest Excited State of Derivatives of Tris(2,2´-bipyridine)ruthenium(II): Substituent Effects on Electron Localization in Mixed-Ligand Complexes. *Inorg. Chem.* **1986**, *25*, 526–531.

20. Marcus, R. A.; Sutin, N. Electron Transfers in Chemistry and Biology. *Biochimica et Biophysica Acta (BBA) - Reviews on Bioenergetics* **1985**, *811* (3), 265–322.

21. Marcus, R. A. The Second R. A. Robinson Memorial Lecture. Electron, Proton and Related Transfers. *Faraday Discuss. Chem. Soc*. **1982**, *74*, 7–15.

22. Wiberg, E.; Wiberg, N.; Holleman, A. F. Inorganic Chemistry; Academic Press: San Diego, CA, 2001.

23. Creighton, J. A.; Lippincott, E. R. Vibrational Frequency and Dissociation Energy of the Superoxide Ion. J. Chem. Phys. 1964, 40, 1779–1780.

24. Hush, N. S. Intervalence-Transfer Absorption. Part 2. Theoretical Consideration and Spectroscopic Data. In *Progress in Inorganic Chemistry*; Cotton, F. A., Ed.; John Wiley & Sons, Inc.: Hoboken NJ, 1967; Vol. 8, pp 391–444.

25. Curtis, J. C.; Meyer, T. J. Outer-Sphere Charge Transfer in Mixed-Metal Ion Pairs. *Inorg. Chem*. **1982**, *21*, 1562–1571.

26. Olsson, M. H. M.; Ryde, U.; Roos, B. O. Quantum Chemical Calculations of the Reorganization Energy of Blue-Copper Proteins. *Protein Science* **1998**, *7* (12), 2659–2668.

27. Warshel, A. Dynamics of Reactions in Polar Solvents. Semiclassical Trajectory Studies of Electron-Transfer and Proton-Transfer Reactions. *J. Phys. Chem.* **1982**, *86* (12), 2218–2224.

28. King, G.; Warshel, A. Investigation of the Free Energy Functions for Electron Transfer Reactions. *The Journal of Chemical Physics* **1990**, *93* (12), 8682–8692.

29. Marcus, R. A. On the Theory of Electron-Transfer Reactions. VI. Unified Treatment for Homogeneous and Electrode Reactions. *The Journal of Chemical Physics* **1965**, *43* (2), 679–701.

30. Abrahams, S. C.; Kalnajs, J. The Crystal Structure of α-Potassium Superoxide. *Acta Crystallographica* **1955**, *8* (8), 503–506.

31. Creutz, C.; Keller, A. D.; Sutin, N.; Zipp, A. P. Poly(pyridine)ruthenium(II)-Photoinduced Redox Reactions of Bipyridinium Cations, Poly(pyridine)rhodium Complexes, and Osmium Ammines. *J. Am. Chem. Soc.* **1982**, *104* (13), 3618–3627.

32. Brown, G. M.; Sutin, N. A Comparison of the Rates of Electron Exchange Reactions of Ammine Complexes of Ruthenium(II) and –(III) with the Predictions of Adiabatic, Outer-sphere Electron Transfer Models. *J. Am. Chem. Soc.* **1979**, *101*, 883–892.

33. Young, E. R.; Rosenthal, J.; Hodgkiss, J. M.; Nocera, D. G. Comparative PCET Study of a Donor-Acceptor Pair Linked by Ionized and Nonoionized Asymmetric Hydrogen-Bonded Interfaces. *J. Am. Chem. Soc.* **2009**, *131*, 7678–7684.

34. Segers, D. P.; DeArmond, M. K. Emission Studies of Transition-Metal Complexes of 2,2´-dipyridylamine. 2. Tris Complexes of Ruthenium(II). *J. Phys. Chem.* **1982**, *86*, 3768–3776.

35. McClanahan, S. F.; Dallinger, R. F.; Holler, F. J.; Kincaid, J. R. Mixed-Ligand Poly(pyridine) Complexes of ruthenium(II). Resonance Raman Spectroscopic Evidence for Selective Population of Ligand-Localized ^{3}MLCT Excited States. *J. Am. Chem. Soc.* **1985**, *107*, 4853–4860.

36. Mabrouk, P.; Wrighton, M. Resonance Raman Spectroscopy of the Lowest Excited State of Derivatives of Tris(2,2´-bipyridine)ruthenium(II): Substituent Effects on Electron Localization in Mixed-Ligand Complexes. *Inorg. Chem.* **1986**, *25*, 526–531.

37. Bruker AXS (2009). Apex II. Bruker AXS, Madison, Wisconsin.

38. Sheldrick, G. M. Experimental Phasing with SHELXC/D/E: Combining Chain Tracing with Density Modification. *Acta Cryst.* **2010**, *66*, 479-485.

39. Holder, P. G.; Pizano, A. A.; Anderson, B. L.; Stubbe, J.; Nocera, D. G. Deciphering Radical Transport in the Large Subunit of Class I Ribonucleotide Reductase. *J. Am. Chem. Soc.* **2011**, *134*, 1172–1180.

40. Powers, D. C.; Anderson, B. L.; Nocera, D. G. Two-Electron HCl to H_2 Promoted by Ni(II) Polypyridyl Halide Complexes. *J. Am. Chem. Soc.* **2013**.

41. Loh, Z.-H.; Miller, S. E.; Chang, C. J.; Carpenter, S. D.; Nocera, D. G. Excited-State Dynamics of Cofacial Pacman Porphyrins. *J. Phys. Chem. A* **2002**, *106*, 11700–11708.

42. Neese, F. The ORCA Program System. *Comput. Mol. Sci.* **2012**, *2*, 73–78.

43. Schäfer, A.; Horn, H.; Ahlrichs, R. Fully Optimized Contracted Gaussian Basis Sets for atoms Li to Kr. *J. Chem. Phys.* **1992**, *97*, 2571–2577.

44. Weigend, F.; Ahlrichs, R. Balanced Basis Sets of Split Valence Triple Zeta Valence and Quadruple Zeta Valence Quality for H to Rn: Design and Assessment of Accuracy. *Phys. Chem. Chem. Phys.* **2005**, *7*, 3297–3305.

45. Lee, C.; Yang, W.; Parr, R. G. Development of the Colle-Salvetti Correlation-Energy Formula into a Functional of the Electron Density. *Phys. Rev. B* **1988**, *37*, 785–789.

46. Becke, A. D. A New Mixing of Hartree–Fock and Local Density-functional Theories. *J. Chem. Phys.* **1993**, *98*, 1372–1377.

47. Becke, A. D. Density-Functional Thermochemistry. III. The Role of Exact Exchange. *J. Chem. Phys.* **1993**, *98*, 5648–5652.

48. Muller, P.; Brettel, K. $[Ru(bpy)_3]^{2+}$ as a Reference in Transient Absorption Spectroscopy: Differential Absorption Coefficients for Formation of the Long-Lived ^{3}MLCT Excited State. *Photochem. Photobiol. Sci.* **2012**, *11*, 632–636.

49. Lewandowska-Andralojc, A.; Polyansky, D. E. Mechanism of the Quenching of the Tris(bipyridine)ruthenium(II) Emission by Persulfate: Implications for Photoinduced Oxidation Reactions. *J. Phys. Chem. A* **2013**.

50. Kober, E. M.; Caspar, J. V.; Lumpkin, R. S.; Meyer, T. J. Application of the Energy Gap Law to Excited-State Decay of osmium(II)-Polypyridine Complexes: Calculation of Relative Nonradiative Decay Rates from Emission Spectral Profiles. *J. Phys. Chem.* **1986**, *90*, 3722–3734.

51. Striplin, D. R.; Reece, S. Y.; McCafferty, D. G.; Wall, C. G.; Friesen, D. A.; Erickson, B. W.; Meyer, T. J. Solvent Dependence of Intramolecular Electron Transfer in a Helical Oligoproline Assembly. *J. Am. Chem. Soc.* **2004**, *126*, 5282–5291.

Chapter 6: Electron Transfer in Cobalt Cubane WOC Model Systems

6.1 Introduction

A barrier to widespread utilization of water splitting as an energy storage mechanism in a solar-to-fuels cycle is one of economics: water splitting is a proton coupled electron transfer (PCET) process which requires the management of 4 protons and 4 electrons in addition to managing the formation of an O–O bond, thus requiring finely tuned catalysts to operate without wasting excessive amounts of energy.[1-3] Compounding the problem is the requirement that these catalysts operate for long durations in the highly corrosive conditions of water oxidation.[4] The vast majority of water oxidation catalysts (WOCs) are based on metal oxides due to their robust nature. In contrast to the earth abundant manganese found in the OEC,[5] most commercial catalysts with acceptable current densities and overpotentials are based on precious metals including platinum, iridium, and ruthenium.[6] While these materials make effective catalysts, the rarity of the precious metals makes them impractical to utilize on the grid scale.

In an effort to find scalable catalysts, significant scientific effort has been focused on developing WOCs based on earth abundant transition metals.[7] Cobalt oxide phosphate (CoP_i) catalysts have showed significant promise: with low overpotentials and the ability to work at neutral pH, cobalt based WOCs have been used in novel ways including its usage as a biologically compatible catalyst for the storage of hydrogen in biomass.[8,9] While the cobalt WOC has been probed using a variety of electrochemical and spectroscopic methods, it is a heterogeneous thin film which makes characterization of the catalytic active sites difficult.

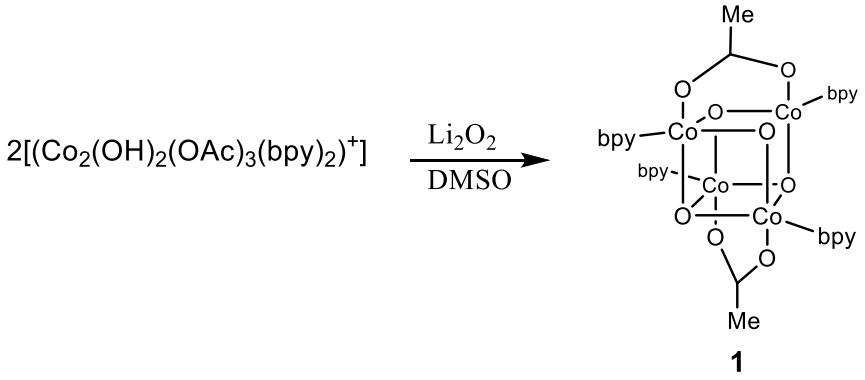

Figure 6.1. Synthesis of the Christou-cube by condensation of two cobalt dimers.

A common strategy for studying heterogeneous chemical systems is to study molecular models that mimic the functionality of the target system.[10] In the context of cobalt WOCs, two families of molecules are known which possess a $Co(III)_4(\mu_3\text{–}O)_4$ core in a cubane arrangement, a structural relative of the cobalt WOC.[11] The first example was synthesized by Christou and coworkers in 1993 by fusion of two $[Co_2(OH)_2(OAc)_3(bpy)_2]^+$ monomers to form the $[Co_4O_4(OAc)_2(bpy)_4]^{2+}$ cubane **1** (Christou-cube, Figure 6.1).[12] This initial report noted the structural similarities of the cubane to the Mn_4O_4 OEC of photosystem II (PSII). Later research explored the redox chemistry of the cobalt cubane and reported a single reversible 1 e^- oxidation at 0.69V vs $Fc^{+/0}$.[13]

A second cubane model was synthesized by Das and coworkers in 2007 by oxidation of Co^{2+} salts in the presence of pyridine and acetate to generate the neutral cubane molecule $Co_4O_4(OAc)_4(Py)_4$ **2** (Das-cube, Figure 6.2).[14] Electrochemistry experiments revealed a reversible electron transfer (ET) at 0.73 V vs Ag/AgCl in MeCN. The authors reasoned that the relatively low oxidation potential of the cubane would make it a good oxidant of organic compounds to their corresponding ketones and carboxylates. The initial report confirmed

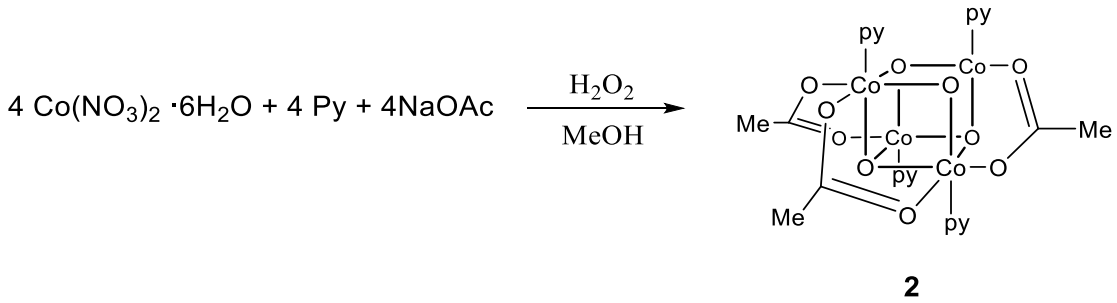

Figure 6.2. Synthesis of Das-cube by oxidation of Co^{2+} salts with H_2O_2.

its ability to oxidize organic substrates including *p*-xylene and ethylbenzene while subsequent work explored the effect of substation of the pyridine para position on oxidation of organic alcohols.[15] What has escaped the literature thus far is the second oxidation wave of the cubane. While evidence for the second oxidation can be found in the supporting information of work by Berardi *et al*.[16] the literature lacks a detailed discussion.

Due to the structural similarity of the cubanes cobalt oxide core to the edge sites of the CoP_i WOC, the cubanes have been evaluated as water oxidation catalysts. In 2011 Symes et. al reported PCET studies of the Christou-cube system in acidic aqueous solutions. Using bimolecular techniques a stepwise process was observed for bidirectional PCET in solution or at an electrode and concerted PCET for the unimolecular self-exchange reaction.[11] Initial reports claimed the observation of catalytic behavior for the Das-cube under neutral pH conditions[17,18] which were subsequently shown to be attributable to Co^{2+} impurities.[19] However, continued investigation of the Das-cube at elevated pH has provided evidence that while isolated cubanes are not themselves catalytically active, they may act as a precatalyst which is chemically activated at high pH.[20,21] Chemical and electrochemical evidence that the Das-cube is capable of oxygen evolution has been presented and it was

hypothesized that the acetate ligands can be partially displaced by a highly nucleophilic hydroxide to form a functional edge site mimic.

Theoretical studies of cobalt oxide systems have been performed. Wang et al have proposed that the oxygen-oxygen (O–O) bond forming step, widely considered to be the rate determining step of water oxidation, occurs from the radical coupling of two terminal oxygen atoms after two oxidation events.[22] Combined experimental and theoretical results by Smith *et al.* propose that the ability of the extended structure to delocalize holes is critical to the cobalt WOC: without a sufficient number of cobalt centers oxidation of the cobalt centers is too thermodynamically challenging to be catalytically relevant.[23]

In order to gain better insight into the role electronic structure plays in the cobalt WOC catalytic cycle, this Chapter reports the application of experimental and theoretical methods to probe the nature of charge transfer in the cubane model systems described above. Picosecond transient absorption (TA) has been utilized to measure the rate of charge transfer across a series of cobalt cubane model systems modified with an appended 1,8-naphthalimide (NMI) photo sensitizer. The experimental results in conjunction with density functional theory (DFT) calculations are used to analyze the effects of electronic structure on the ET properties of these cubane model systems.

6.2 Results

6.2.1. Photosensitization of Co_4O_4 Model Systems

Initial work in our lab showed that the excited state of $Re(phen)(CO)_3(MePy)PF_6$ compounds, a potent photooxidant,[24,25] exhibits bimolecular quenching with **1** with a rate constant of $k_q = 1.3\times10^9\ M^{-1}s^{-1}$, close to the diffusion limit.[26] Furthermore, covalent

attachment of the rhenium moiety resulted in complete quenching of the rhenium emission. Unfortunately, TA failed to detect any intermediates on the nanosecond or picosecond timescale prohibiting further evaluation.

In light of the failure to observe intermediates using rhenium based photooxidants we have shifted our attention to organic based sensitizers. Due to our interest in exploring the second oxidation of the cubane systems photochemically, NMI was chosen due to its highly energetic excited state, ease of synthesis, extensive characterization, and favorable photophysical properties.[27–30] An important quality of the NMI radical anion is that it exhibits strong spectral features in the optical spectral region,[29–32] facilitating observation of the charge separated state. On the picosecond timescale the prompt spectrum of the singlet excited state is characterized by a broad absorption centered at 475 nm (Figure 6.3, —, black). After ~200 ps in CH_3CN the singlet has completely decayed to the triplet state which is characterized by a TA spectrum that qualitatively resembles that of the singlet

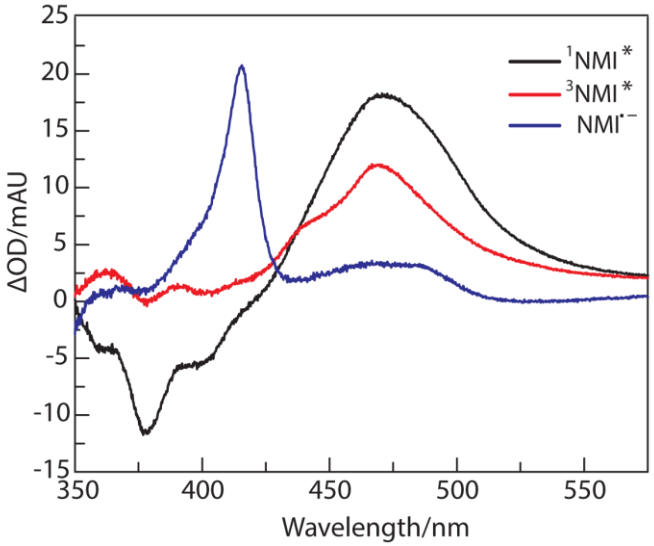

Figure 6.3. Transient absorption spectra of the NMI singlet (—, black), triplet (—, red), and radical anion (—, blue) in CH_3CN. Samples were pumped at 330 nm. NMI radical anion was generated by adding 10% triethylamine to a sample of NMI.

excited state with the exception of a shoulder at 440 nm (Figure 6.3, —, red). When triethylamine is introduced as a sacrificial reductant, a dramatic change is observed in the TA spectrum due to the rapid formation of the NMI radical anion, characterized by a strong and sharp absorption centered at 415 nm (Figure 6.3, —, blue).

6.2.2. Covalent Attachment of NMI to the Cubane Models

In contrast to the long lived excited states of the rhenium photooxidants, the lifetime of the NMI singlet excited state is on the order of a hundred picoseconds in CH_3CN[27] rendering it is unsuitable as a bimolecular photooxidant. In order to circumvent the relatively slow process of diffusion, the NMI photosensitizer was covalently attached to the cubane moiety. In analogy to the synthesis of naphthalenediimides, NMI can be synthesized in high yield by condensation of a primary amine with 1,8–naphthalic anhydride.[33,34] Due to the diversity of primary amines suitable for the NMI synthesis multiple strategies for appending the photo sensitizer to the cubane are possible. The two synthetic handles for covalently binding the NMI to the cubane are through the pyridyl or acetate groups. The acetate ligands of **1** are known to be labile at elevated temperatures, therefore we reasoned that the acetate ligands **2** of should also be labile. Under refluxing conditions both **1** and **2** are amenable to acetate substitution providing a synthetic route to the photosensitized cubanes **3** through **8**, enumerated in Table 6.1**.** Single crystal X-ray diffraction afforded the structure of **7**, displayed in Figure 6.4. The crystal structure reveals the flexibility of the ethyl linking group: in the crystal structure the NMI fragment is folded back toward the cubane core, minimizing the complexes total volume. The crystal structure of **7** allows us to inspect the perturbations of the NMI moiety on the cubane core. Consistent with the reported structure of **1**, the Co–Co distances of **7** fall into two classes: 2.665 Å and 2.844 Å for cobalt atoms

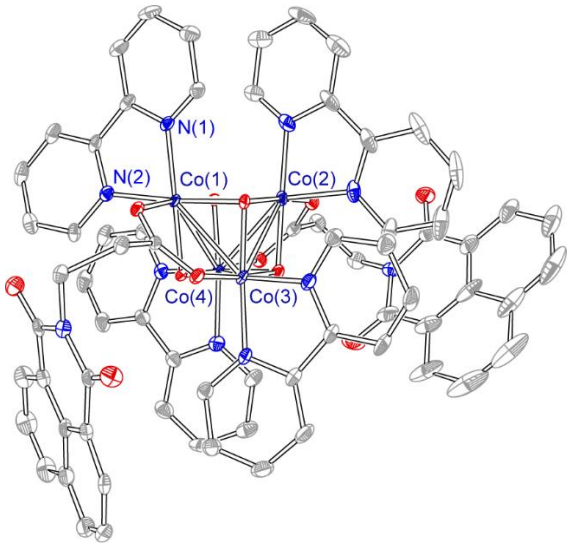

Figure 6.4. Crystal structure of **7**. Solvent molecules, PF_6 anions, and hydrogen atoms omitted for clarity.

Table 6.1. Compound numbers of the cubane model systems.

Compound	Cubane	R–COO⁻ R Group	py-para Group
1	Christou	CH_3	–
2	Das	CH_3	H
3	Das	NMI-MeBz	H
4	Das	NMI-MeBz	OMe
5	Das	NMI-$(CH_2)_2$	H
6	Das	NMI-$(CH_2)_5$	H
7	Christou	NMI-$(CH_2)_2$	–
8	Christou	NMI-$(CH_2)_5$	–

that do and don't share an acetate, respectively. Similarly, the cobalt to cubane oxygen distances are partitioned into two classes with average distances of 1.875 Å and 1.896 Å. The close agreement between the bond metrics of **7** and its parent compound **1** show that

covalent attachment of the NMI through the acetate ligand has minimal effect on the cubane moiety.

6.2.3. Thermodynamics of Photoinduced Charge Transfer

In order to interrogate the effect of thermodynamic properties of the system on the rates of charge transfer the energetics of both the cubanes and the photosensitizer have been characterized. While it is not possible to directly measure the reduction potential of the NMI singlet excited state, it can be calculated using a Latimer diagram (Figure 6.5).[35,36] The fluorescence spectrum of NMI is nearly a mirror image of the absorption spectrum[31] facilitating the determination of the E_{00} transition energy. In the case of mirrored emission and absorption spectra the E_{00} energy can be approximated from the mean energy of the absorption and emission maxima[37] which was determined to be 3.50 eV for NMI in CH_3CN. The one-electron reduction potential of NMI has been reported to be –1.80 V vs $Fc^{+/0}$.[38] By use of a Latimer diagram the one electron reduction potential of NMI singlet excited state was determined to be 1.70 V vs $Fc^{+/0}$.

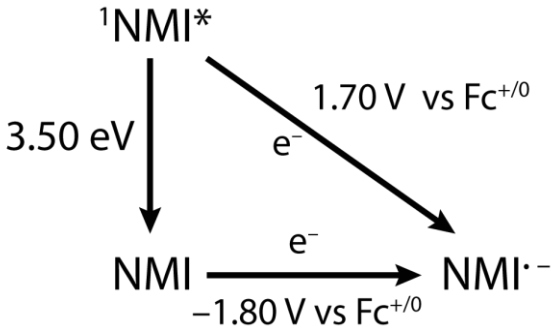

Figure 6.5. Determination of the excited state reduction potential using a Latimer diagram of the NMI in CH_3CN. Calculation of the excited state reduction potential is accomplished by taking the difference of the excited state energy, E_{00}, and the ground state reduction potential.

The potentials of the first one-electron oxidation of the cubanes (peaks (a) of Figure 6.6) have been measured using standard electrochemical techniques to be 0.70 V and 0.29 V vs $Fc^{0/+}$ for the **1** and **2** family of cubanes, respectively. The second oxidation (peak (b) of Figure 6.6) of **2** was measured to be 1.44 V vs $Fc^{+/0}$ while a second oxidation wave for **1** was not observed within the CH_3CN solvent window. In order to probe the effect of driving force on ET rates the electron donating py-OMe was used in the synthesis of the Das-cube to afford complex **2-py-OMe**. Modification of ligands with electron withdrawing or donating groups has been a highly successful strategy for exploring the effect of driving force on ET[39] and the redox properties of the Christou-cube have been shown to be sensitive to modification of both the acetate and pyridine ligand groups.[13,15] Use of the electron donating para-OMe pyridines results in a reduction of the cubane oxidation potentials by 80 and 70 mV for the first and second oxidations, respectively of **2-py-OMe** with respect to the parent molecule, **2**.

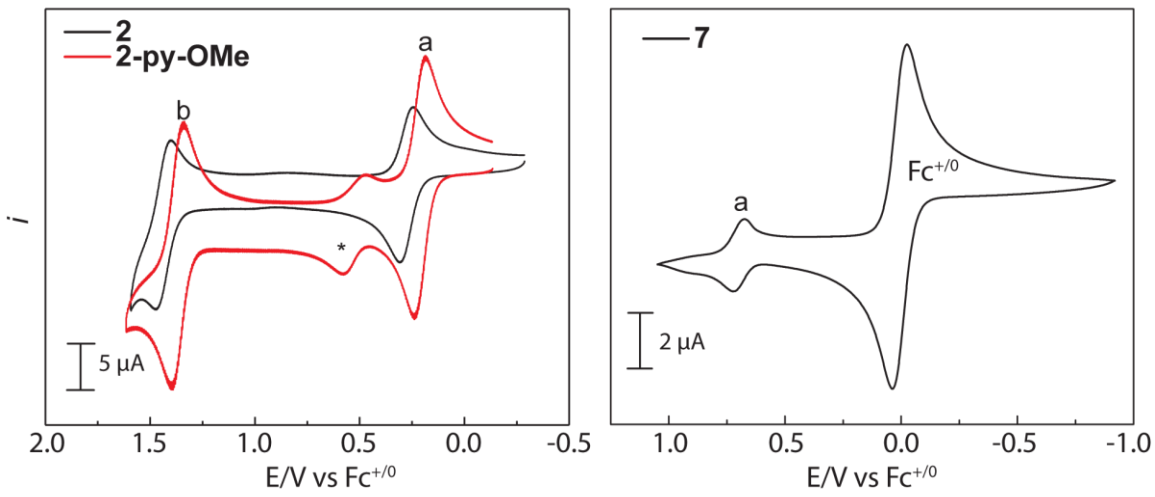

Figure 6.6. Representative cyclic voltammograms if compounds **2**, **2-py-OMe**, and **7**. First reversible oxidation waves: (a), second wave: (b), and contamination signal: (*).

$$-\Delta G^{\circ\prime} = \mathrm{e}\left(E^{*}_{NMI} + E_{(\mathrm{NMI/NMI^{-}})} - E_{(\mathrm{Cube^{+}/Cube})}\right) + w^{p} - w^{r} \qquad (1)$$

Using the thermodynamic properties obtained from characterization of the cubane and NMI moieties, the driving forces ($-\Delta G^{\circ\prime}$) for charge separation (CS) and recombination are summarized in Table 6.2 along with measured ET time constants (*vide infra*). These values take into account the electrostatic work term associated with the creation or loss of an ion pair during charge separation charge recombination (CR) (Equation 6.1). The center to center distance was assumed to be 10 Å based on the crystal structure of **7** with the NMI rotated about the C–N bond of the alkyl linker as it is unlikely that the compact orientation observed in the crystal structure would be representative of the dominant orientation of the complex in solution. While this approximation will undoubtedly introduce some uncertainty into the reported driving forces, the corrections do to the electrostatic work term are on the order of 50 mV and are therefore negligible compared to the overall driving force, rendering error introduced by uncertainty in the ion pair distance irrelevant.

Table 6.2. Summary of rate constants and driving forces of the photosensitized cubane models.

Compound	$\tau_{CR/ps}$	$\tau_{singlet/ps}$	CS Driving Force/eV	CR Driving Force/eV
3	41± 1	2.7 ± 0.1	1.45	2.05
4	93 ± 1	~1.2 (biexp)	1.53	1.97
4⁺	46 ± 1	~1.3 (biexp)	0.34	3.16
5	15 ± 1	1.2 ± 0.1	1.45	2.05
6	63 ± 3	4.8 ± 0.1	1.45	2.05
6⁺	35 ± 5	3.9 ± 0.1	0.34	3.16
7	5 ± 1	~ 1	1.12	2.38
8	> 5	2.4 ± 1	1.12	2.38

6.2.4. Ultrafast Photooxidation of Co_4O_4 Model Systems

Picosecond TA was used to interrogate the rate of charge transfer in the cubane model systems. Interestingly, initial experiments on **5** show that the formation of NMI radical anion (Figure 6.7a) is complete after ~1 ps followed by its rapid decay with a time constant of 15±1 ps (Figure 6.7b). The decay of the signal attributable to the singlet occurs with a time constant of 1.2±0.4 ps, consistent with the rapid growth of the NMI radical anion signal.

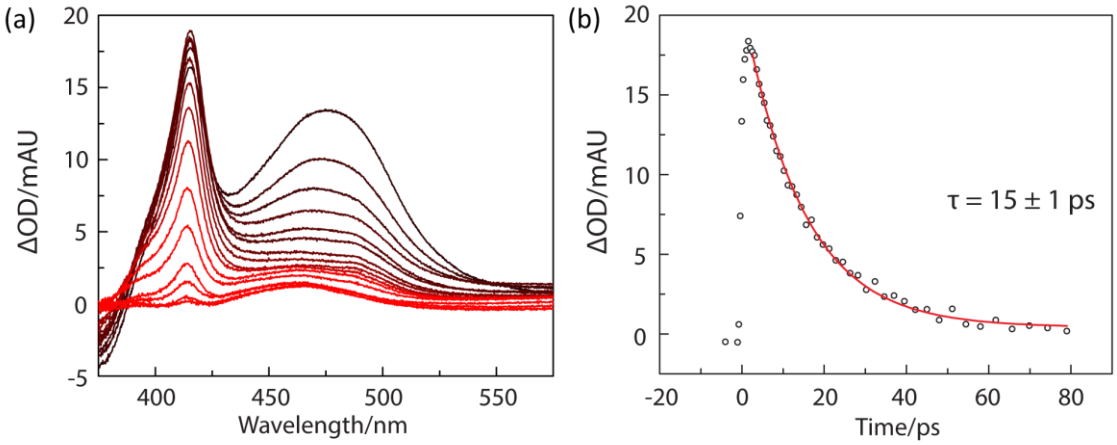

Figure 6.7. Picosecond TA of compound **5:** (a) Full spectrum series acquired over 80 ps. Signal of the NMI radical anion is observed within in the instrument response period. (b) Single wavelength kinetics of charge recombination observed at 414 nm.

The effect of perturbing the length of the alkyl chain tethering the NMI sensitizer to the cubane core is manifested in the TA of **6** (Figure 6.8), which contains five methylene groups in the alkyl linker. The growth of the NMI radical anion has been retarded with respect to the ethyl linked complex **5**, and is now resolvable while the decay of the singlet has also been slowed. The rate of charge recombination has also decreased by more than four-fold with respect to **5**.

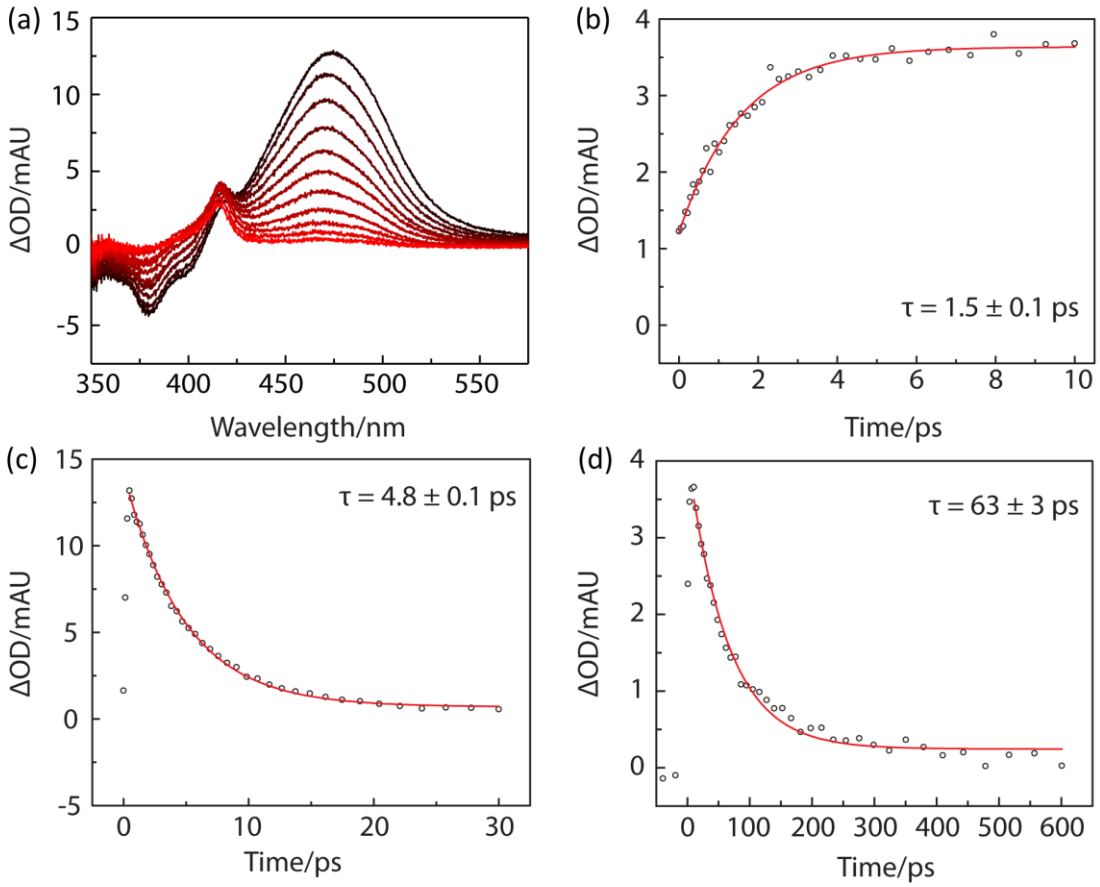

Figure 6.8. TA of compound **6**: (a) Full spectrum view over 30 ps duration. (b) Growth of 414 nm NMI radical anion peak. (c) Decay of NMI singlet excited state observed at 474 nm. (d) Decay of the NMI radical anion observed at 414 nm.

The effect of driving force on the charge transfer rates was probed by comparing the CT rates of the py-OMe complex **4** with its parent cubane, **3** (Figure 6.9). The decrease in CR driving force by 80 mV results in a twofold decrease in the rate of charge recombination.

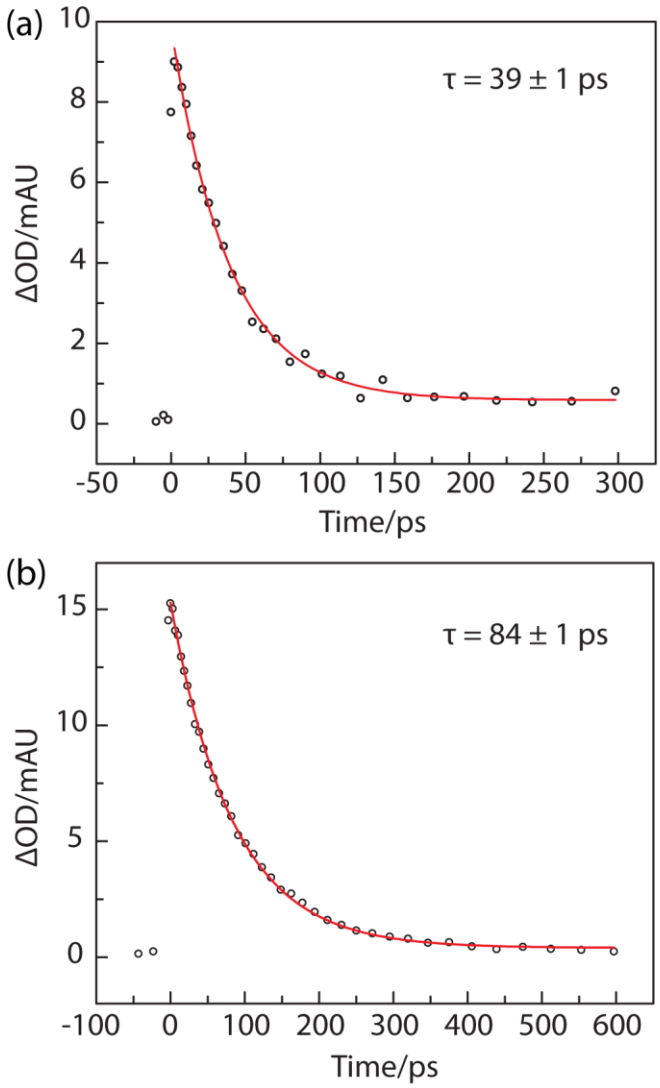

Figure 6.9. NMI radical anion decay observed at 415 nm for compounds (a) **3** and (b) **4**. Decreasing the reduction potential by 80 mV results in a decrease in the charge recombination rate by a factor of two.

TA was also performed on photosensitized Christou-cube systems. While the cubane moiety of the derivatives of **2** are all spectrally silent by TA, bleaching of the 420 nm ground state d–d transition (*vida infra*) can be seen superimposed with the NMI radical anion signal with net bleach signals occurring at 430 nm (Figure 6.10a). In comparison to the charge transfer rates of the Das cubes, the electron transfer kinetics of the Christou cube are significantly faster. In the case of **7**, oxidation is complete on the timescale of the instrument response and CR proceeds with a lifetime of 5.9±0.3 ps (Figure 6.10b).

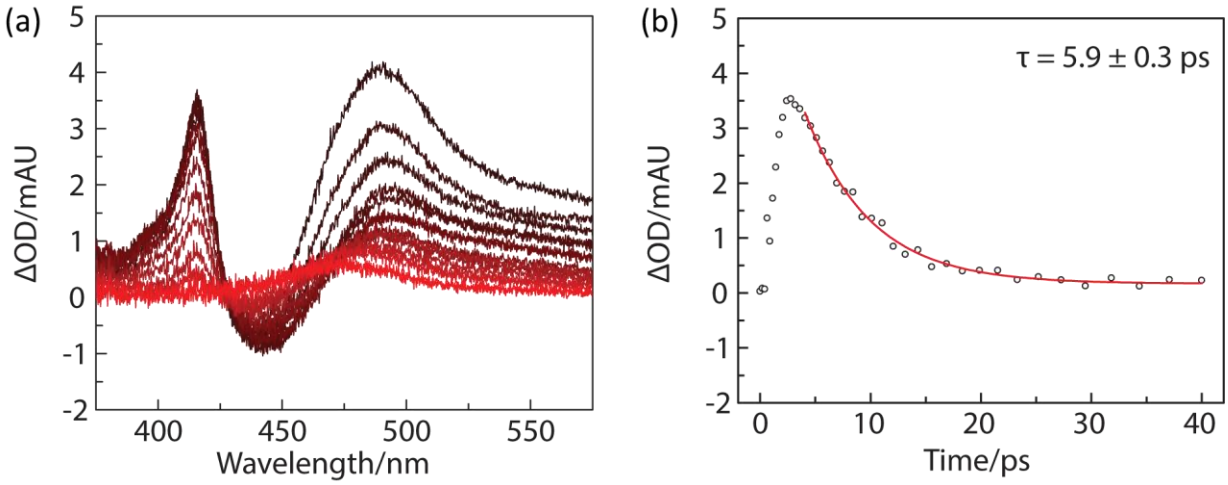

Figure 6.10. TA of **7**, (a) full spectrum TA series over 40 ps. (b) 415 nm kinetic trace with 5.9±0.3 ps lifetime.

As observed with **5** and **6**, by extending the alkyl linker from two (complex **7**) to five (complex **8**) methylene groups the rate of charge separation is significantly decreased as evidenced by the increase in singlet lifetime from ~1 to 2.4±0.1 ps (Figure 6.11). The decreased charge separation rate results in insufficient accumulation of NMI radical anion to obtain an accurate measurement, although the NMI radical anion is qualitatively discernable from the full spectrum TA and can be seen at delays as long as 20 ps. The

presence of NMI radical at long delays shows that the recombination is also suppressed by extending the alkyl linker.

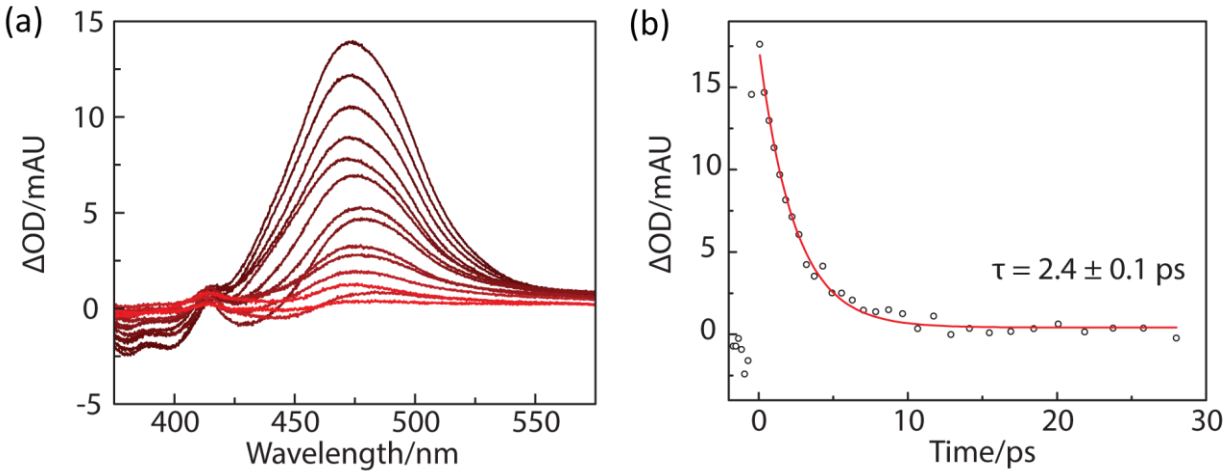

Figure 6.11. TA of **8**. Extension of the alkyl linker from two to five carbons dramatically reduces the charge transfer rate. (a) Full spectrum TA over 30 ps, (b) single wavelength intensities observed at 468 nm.

6.2.5. Second Oxidation of the Cobalt Cubanes

In order to probe the properties of the second electron transfer, the cubane model systems were chemically oxidized by one electron using Ce(IV) or NO^+. Upon oxidation the broad absorption of **7** centered at 418 nm is replaced by the tail of a broad UV absorption while the sharp peak at 293 nm appears to have undergone a bathochromic shift to 317 nm in $\mathbf{7}^+$ (Figure 6.12a). Spectral changes in the family of cubes derived from **2** are less pronounced, in part due to the weak of spectral features of **2**. Upon oxidation only a slight bathochromic shift of the UV features is observed. In both cubane models the two characteristic spectral features of the NMI sensitizer at 347 nm and 330 nm are unperturbed by chemical oxidation.

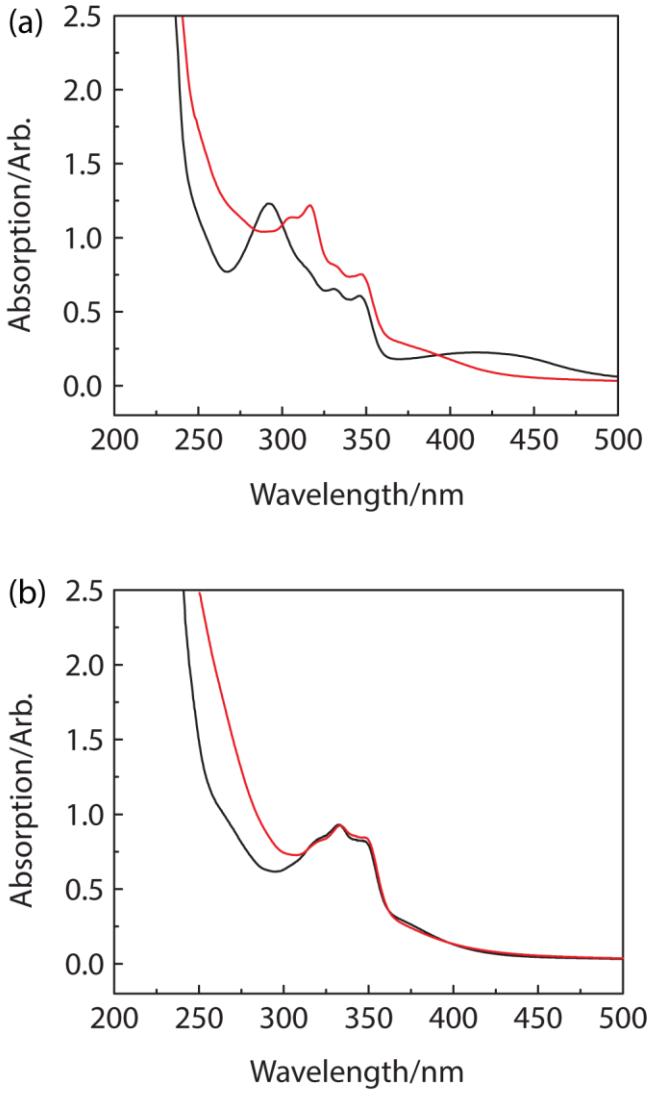

Figure 6.12. Ground state UV-Vis absorption spectra of (a) **7** (—, black), **7**$^{+}$ (—, red) and (b) **4** (—, black), **4**$^{+}$ (—, red). NMI features are preserved in both systems (~347 and 330 nm) while features attributable to the cubane core are perturbed.

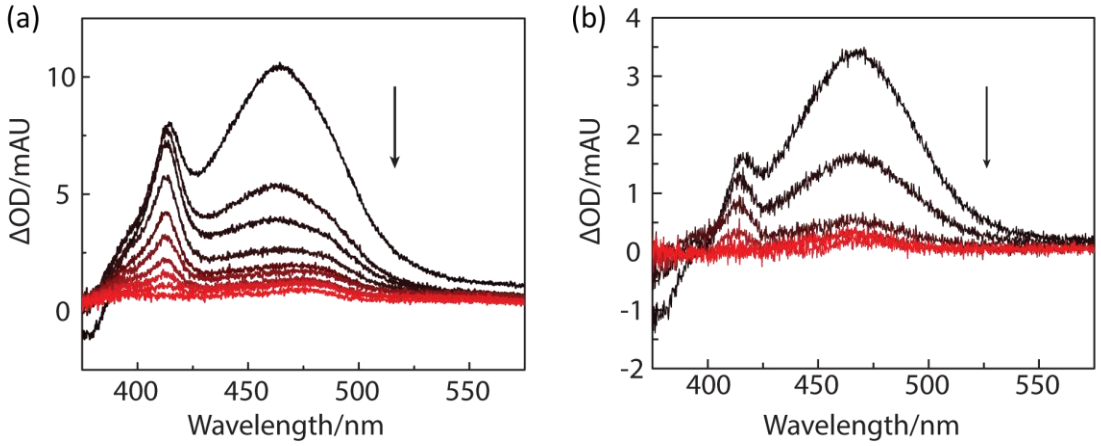

Figure 6.13. Full spectrum TA of (a) **4**$^+$ and (b) **6**$^+$ in CH_3CN acquired over 600 ps.

TA of the oxidized cubane models **4**$^+$ and **6**$^+$ show the growth of the NMI radical anion at 415 nm (Figure 6.13). While changes in the rate of charge separation are small and difficult to resolve, in both **4**$^+$ and **6**$^+$ the oxidized cubane shows faster charge recombination kinetics (Figure 6.14a and Figure 6.14b, respectively). TA of **7**$^+$ shows a very faint spectral

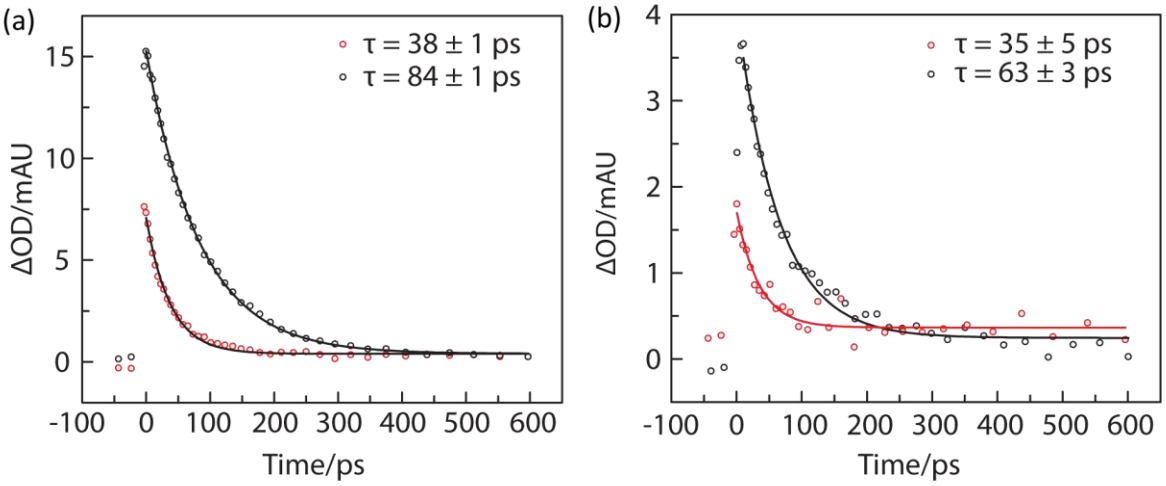

Figure 6.14. Kinetic traces of charge recombination for (a) **4** (—, black) and **4**$^+$ (—, red), (b) **6** (—, black) and **6**$^+$ (—, red) observed at 414 nm.

signature of the radical anion at 415 nm (Figure 6.15) but an insufficient buildup of radical occurs to allow deconvolution from the growth of the singlet prohibiting an accurate kinetic analysis.

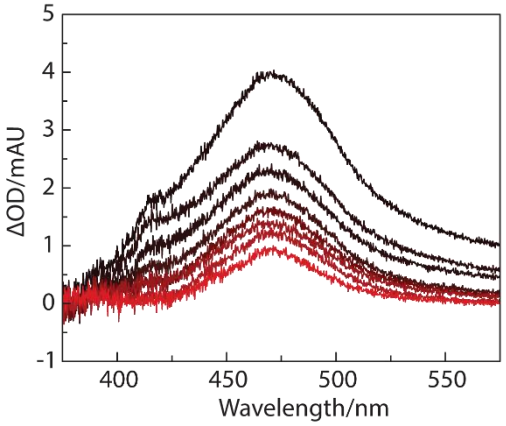

Figure 6.15. Series of full spectrum TA of **7**$^{+}$ over 300 ps exhibits signs of the NMI radical anion but insufficient buildup for kinetic analysis.

6.2.6. DFT Calculation of the Cubane Excited State Manifold

DFT and TD-DFT calculations of the cubane model systems **1**, **1**$^{+}$, **2**, and **2**$^{+}$ were performed to learn more about their ground and excited state electronic structures. Computational results of **2** and **2**$^{+}$ show that the occupied frontier orbitals are highly delocalized over the cubane core. Upon one electron oxidation the LUMO of **2**$^{+}$ is computed to be nearly superimposable with the HOMO of **2** (Figure 6.16). Spin density calculations also show extensive delocalization of spin about the cubane core and closely mirrors the

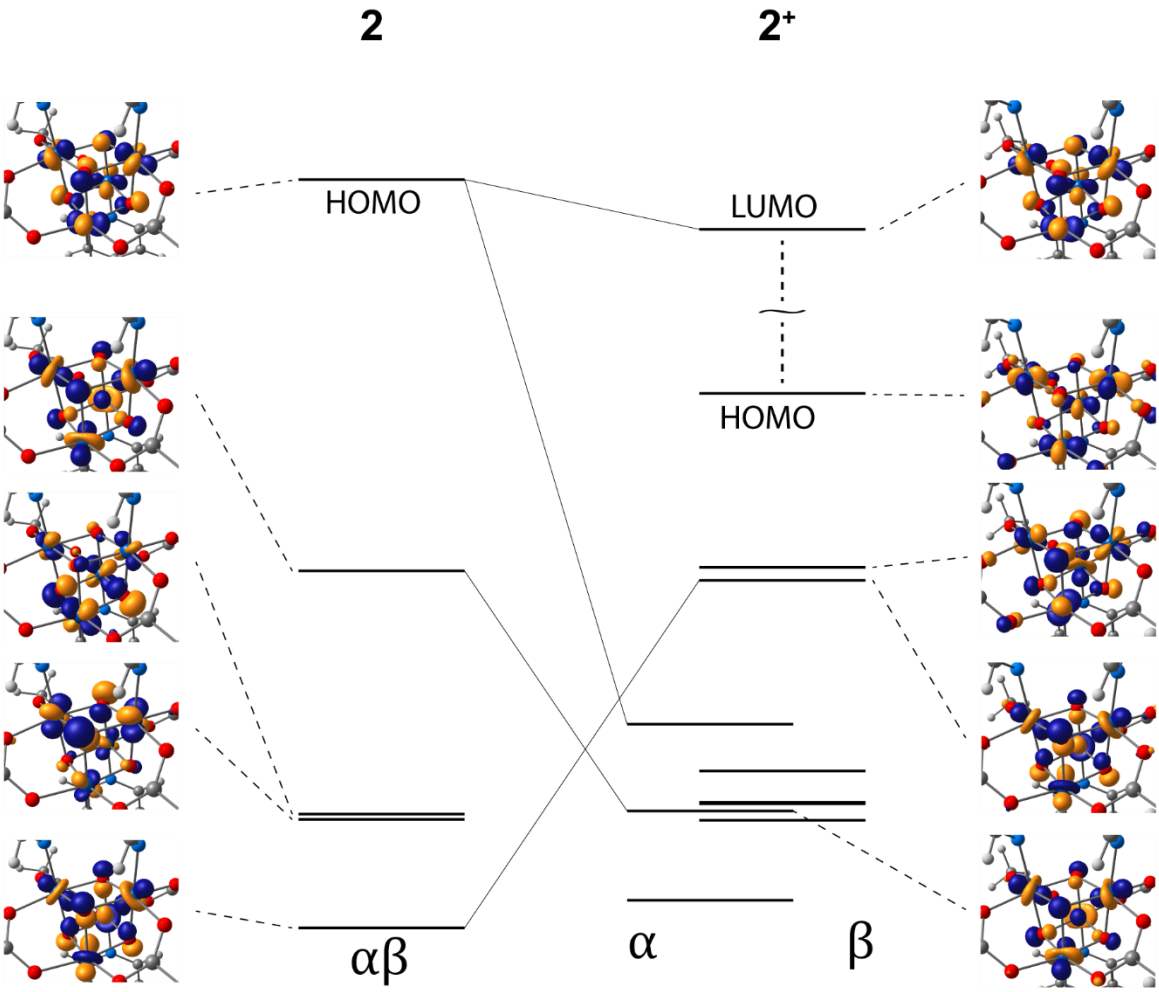

Figure 6.16. Contour plots and relative energy levels of compounds **2** and **2**$^{+}$.

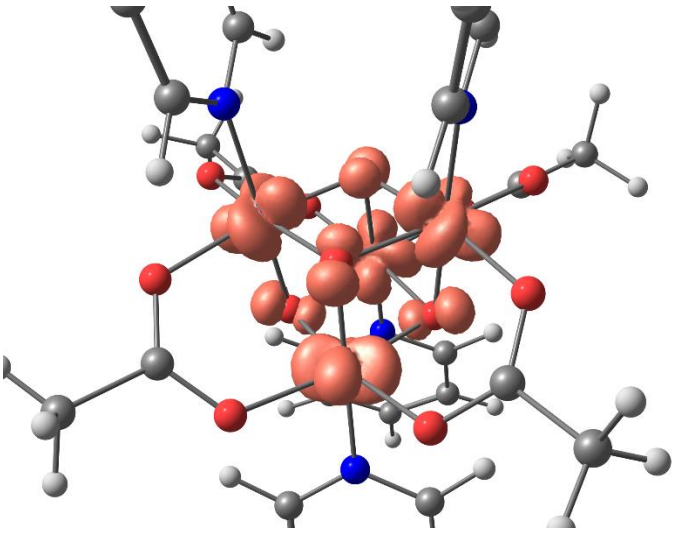

Figure 6.17. Computed spin density of $\mathbf{2}^{+}$. The spin density closely mirrors the form of the HOMO and LUMO orbitals of **2** and $\mathbf{2}^{+}$, respectively.

form of the HOMO and LUMO orbitals (Figure 6.17), consistent with delocalization of the resulting hole among the atoms of the cubane moiety. Mulliken charges are nearly identical for the four oxygens and four cobalt atoms of the cubane with each type of atom possessing a charge of –0.85 and 1.32, respectively. Upon oxidation, the charges of all the core oxygen and cobalt atoms remain evenly distributed amongst their respective types, becoming –0.80 and 1.33 respectively, further evidence of electronic delocalization of the cubane core. Oxidation has a negligible effect on the geometry of the cubane cores. For example, the distance between cobalt's sharing an acetate ligand of compound **2** contracts from 2.728 Å to 2.700 Å. Similar results are obtained for the electronic structure calculations of **1** and $\mathbf{1}^{+}$ which also show negligible geometric changes and symmetric charge distributions among the atoms composing the cubane moiety.

To gain a better understanding of the excited state electronic structure of the cubane systems TD-DFT calculations were performed on **1**, $\mathbf{1}^{+}$, **2**, and $\mathbf{2}^{+}$. To assess the validity of

the computational results they have been compared with experimentally observed transitions. TD-DFT predicts three significant transitions for **1** in the 350–1000 nm region: a d–d transition at 567 nm, a pair of nearly degenerate d–d transitions at 421 and 419 nm, and a pair of degenerate MLCT transitions at 370 nm. The d–d transitions at 570 and 420 nm match very well with the observed transitions at 543 and 438 nm, respectively while the MLCT band observed at 288 nm is at significantly higher energy than predicted. Examination of the predicted transitions of $\mathbf{1}^{+}$ predicts a significant decrease in the intensity of the 420 nm band, consistent with experimental observations.

The TD-DFT calculation of **2** predicts three optical excitations with non-negligible intensity: two nearly degenerate d–d transitions at 592 nm, another weak d–d transition at 397 nm, and strong MLCT feature at 365 nm. The two sets of d–d features agree well with the observed transition at 640 nm, and a shoulder to the intense MLCT which is assigned to 450 nm. In contrast to the case of **1**, the energy of the MLCT band is almost perfectly predicted by TD-DFT with the observed peak centered at 362 nm. Examination of the predicted excitations of $\mathbf{1}^{+}$ show relatively scattered pattern of weak absorptions consistent with the slight grey color of the material in the solid phase.

While there are few transitions predicted to have significant oscillator strength, the calculations predict a rich manifold of electronic excited states. The excited state manifolds of **1**, **1**$^{+}$, **2**, and **2**$^{+}$ are plotted in Figure 6.18. It can be seen that the excited state manifolds of **1** and **2** both consist of similar clusters of states while the **1**$^{+}$ and **2**$^{+}$ form essentially continuous manifolds that possess a significant number of states below 1 eV. As expected, TD-DFT predicts these low lying transitions of the oxidized cubanes **1**$^{+}$ and **2**$^{+}$ to be d–d excited states.

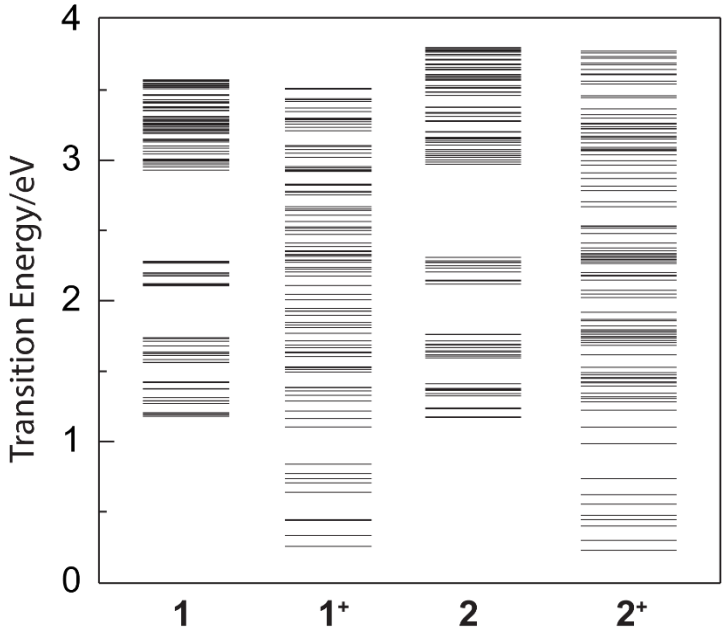

Figure 6.18. TD-DFT computed excited state manifolds of the parent cubane species and their oxidized forms.

6.3 Discussion

The nature of the resultant holes in the cobalt t_{2g} orbitals upon oxidation of the cubane models has implications for its potential as a water oxidation catalyst. Computations by Tilley and coworkers have suggested that the second oxidation of a cubane moiety

produces what is best described as a ferromagnetically coupled Co(IV)-oxyl radical.[20] In contrast to these results, our DFT calculations of **1**$^{+}$ and **2**$^{+}$ predict a delocalized hole in agreement with experimental EPR results[40] and calculations performed by Seigbahn[41] on Co_4O_4 clusters. This is discrepancy may be explained by the differences of the cubane models: Tilley and coworkers performed calculations using a model of the activated cubane which contains a terminal hydroxide. The predicted hole delocalization is important for redox leveling which may help lower catalytic overpotentials by avoiding the formation of high energy intermediates.[42–44]

An important consideration for catalysis is the rate of charge transfer. It has been shown that charge hopping in cobalt oxide films plays an important role in the rate of catalysis.[45] This is particularly interesting in the case of cobalt species as its been shown that the cobalt (II/III) exchange rates can be very slow,[46,47] too slow for efficient catalysis. In contrast to the charge transfer rates observed for cobalt (II/III) charge transfers, oxidation rates of the Co(III) cubane moieties by an appended NMI photosensitizer have been observed to be on the order of no more than a few picoseconds and often dip into the femtosecond timescale, below the instrument response time of the system used in this study. While the observed electron transfer rates are very fast, they are not unprecedented.[48–51] The speed of oxidation demonstrates that oxidation of the cubane systems is not hindered by excessive reorganization energies nor the requirement of an inner sphere mechanism. Crystal structure data shows that the cubane core undergoes negligible geometric changes upon oxidation,[12] consistent with the geometric changes calculated by the DFT. This is consistent with the Co(III/IV) self-exchange rates being significantly faster than the more commonly reported Co(II/III) self-exchange, although the species available for comparison are limited.[52]

In order to gain a better understanding of the properties governing photo-initiated electron transfer a series of perturbations was performed. To probe the effect of electronic coupling the alkyl chain linking the photooxidant to the cubane was extended from two to five methylene groups. As expected, extending the linker causes a decrease in the rate of both charge separation and charge recombination, k_{CS} and k_{CR}, respectively. This is a consequence of lowering the electronic overlap of the donor and acceptor wavefunctions, $|H_{ab}|$. While limitations imposed by the instrument response time limits our ability to quantitatively measure k_{CS}, we can draw the qualitative conclusion that the rate of ET is modulated for both charge separation and charge recombination.

Modulation of driving force, $-\Delta G°'$, also has an effect on the rate of charge transfer. Comparing **3** and **4** shows that decreasing the charge recombination driving force from 2.05 eV to 1.97 eV slows charge recombination by a factor of two. These driving forces are significantly higher than 1 eV, a typical value for many electron transfer reactions, which can lead to the observation of the Marcus

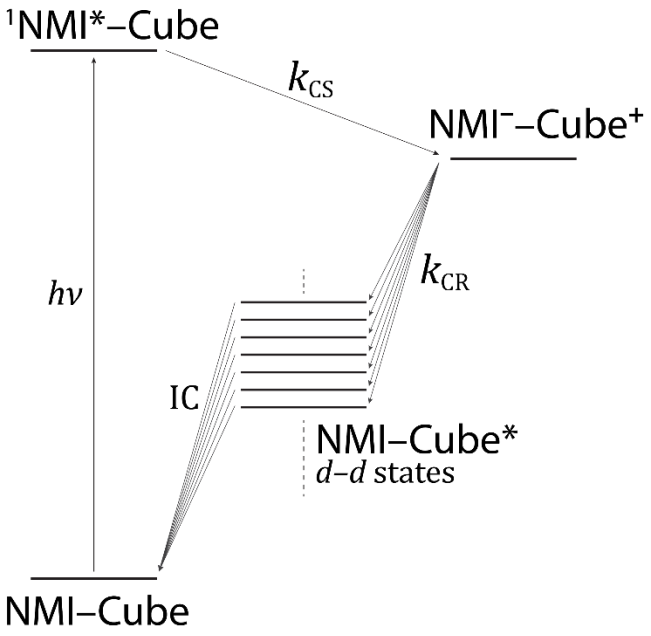

Figure 6.19. Energy level diagram of the photosensitized cubane system.

inverted region where increasing driving forces result in decreasing ET rates.[53] The same result is observed when examining the ET rates of the chemically-oxidized cubanes to their parent compound: comparisons of **4** to **4**$^{+}$ and **6** to **6**$^{+}$ both show that increased driving force results in an increase in the charge recombination rates in both cubane models. This observation is likely attributable to charge recombination to an cubane d–d excited state (Figure 6.19). This phenomena of charge recombination into electronic excited states[53,54] is well known and results in the suppression of inverted regime kinetics. Consistent with this interpretation, the TD-DFT calculations predict a rich manifold of excited states for all the cubanes studied with the oxidized cubanes exhibiting a nearly continuous manifold of excited states.

6.4 Conclusion

Cubanes are important model systems of the cobalt oxide WOC catalyst due of the difficulty of probing heterogeneous systems. In this work we have studied the electron transfer kinetics and electronic structure of two cubane model systems in order to understand the role of electronic structure on charge transfer. Time resolved photooxidation on the ultrafast timescale shows charge transfer to be extremely fast for oxidation and subsequent reduction of the cubane moiety. The reasons for this observation can be understood by examining the electronic structure of the cubane. Oxidation of the cubanes doesn't impart a significant structural change, therefore limiting the internal reorganization energy associated with ET. Observation of the Marcus inverted region is circumvented by a rich manifold of ET pathways enabled by low lying d–d excited states, common to first row transition metal complexes. DFT calculations predict a highly delocalized MO structure for the cubane model systems. This may have implications for the

ability of catalysts to perform 'redox leveling' circumventing the formation of high energy intermediates in a catalytic cycle.

6.5 Experimental

Cubane synthesis was performed in collaboration with Dr. Andrew Ullman M. Ullman and Casey N. Brodsky. Electrochemistry was performed in collaboration with Casey N. Brodsky. X-ray structure determination was performed by Seung Jun Hwang.

General Considerations

$Co(NO_3)_2 \cdot 6H_2O$ (Alfa Aesar), sodium acetate (Sigma-Aldrich), sodium propionate (Sigma-Aldrich), pyridine (Sigma-Aldrich), 4-methoxypyridine (Sigma-Aldrich), methyl isonicotinate (Sigma-Aldrich), ethylenediaminetetracarboxylic acid tetrasodium salt dehydrate (Sigma-Aldrich), β-alanine (Sigma-Aldrich), 6-aminocaproic acid (Sigma-Aldrich), 1,8-Naphtahalic anhydride (Sigma-Aldrich), and ammonium cerium(IV) nitrate (Sigma-Aldrich) were purchased and used as received. Buffer solutions were made from KH_2PO_4 (Mallinckrodt) using 18 MΩ cm distilled water from a MilliPore purification system. Complexes **1**[12] and **2**[18,23] were prepared according to literature procedures.

Synthesis of N-(2-ethanoic acid)-1,8-naphthalenimide, N-(4-aminomethyl benzoic acid)-1,8-naphthalenimide, and N-(5-caproic acid)-1,8-naphthalenimide was performed according to the literature procedure.[55] Proton nuclear magnetic resonance (^{1}H NMR) spectra were acquired on an Agilent DD2-600 (600 MHz) or Varian instrument and chemical shifts are referenced to residual protium in the NMR solvent (HDO = δ 4.79, CDH_2CN = δ 1.94, $CDHCl_2$ = δ 5.32). Mass spectroscopic (MS) data were acquired on a Bruker micrO-TOF-QII LCMS ESI-TOF mass spectrometer in the positive ion mode. All mass

spectra were externally calibrated with sodium formate. Elemental analysis was performed by Midwest Microlabs (Indianapolis, IN).

Synthesis of NMI-MeBz-Das (3)

$Co(NO_3)_2 \cdot 6H_2O$ (0.97 g, 3.3 mmol, 1 eq.) and NaOAc (5 mmol, 0.68 g, 1.5 eq.) were added to 10 mL MeOH and heated. In a separate container NaOMe (1.7 mmol, 90 mg, 0.5 eq.) and N-(4-aminomethyl benzoic acid)-1,8-naphthalenimide (550 mg, 1.7 mmol, 0.3 eq.) were dissolved in 5 mL MeOH and added to the first solution. Pyridine (266 µL, 3.3 mmol, 1.00 eq.) was added to the mixture and the solution was heated for 15 minutes. The flask was removed from the oil bath long enough that the solution stopped refluxing. Then, in very careful and control manner a solution of 30 % H_2O_2 (1.7 mL, 40 mmol, 5 eq.) was added to the mixture. Refluxed the dark green mixture for 2 h at 90 °C. At the end of this time, the mixture was concentrated to remove the MeOH. Loaded in 10 mL DCM onto 425 mL of silica, which had been equilibrated with 100 % DCM. Eluted with the following: 500 mL (DCM), 500 mL (1% MeOH/DCM), 500 mL (2% MeOH/DCM), 1000 mL (4% MeOH/DCM), and finally 500 mL (8% MeOH/DCM). ^1H NMR (CD_2Cl_2): 8.59 (d, 2H), 8.52 (m, 8H), 8.26 (d, 2H), 7.85 (m, 2H), 7.77 (t, 2H), 7.52 (m, 4H), 7.37 (d, 2H), 7.04 (m, 8H), and 5.33 (s, integration obscured by solvent peak).

Synthesis of NMI-MeBz-Das-py-OMe (4)

$Co(NO_3)_2 \cdot 6H_2O$ (2.4 g, 8.3 mmol, 1 eq.), p-OMe-py (845 µL, 8.3 mmol, 1.00 eq.), NaOAc (5.5 mmol, 1.925 g, 1.7 eq.), N-(4-aminomethyl benzoic acid)-1,8-naphthalenimide (827 mg, 2.5 mmol, 0.3 eq.), and NaOMe (2.5 mmol, 135 mg, 0.3 eq.) were added to a 50 mL round bottom flask in 25 mL of MeOH and refluxed at 90 °C until homogeneous. The flask

was removed from the oil bath long enough that the solution stopped refluxing. Then, in very careful and control manner a solution of 30 % H_2O_2 (4.15 mL, 70 mmol, 5 eq.) was added to the mixture. Refluxed the dark green mixture for 2 h at 90 °C. At the end of this time, the mixture was concentrated to remove the MeOH, and the aqueous layer was extracted into DCM. The organic layer was dried with $MgSO_4$, and filtered. Concentrated the DCM extracted, and ran the residue material through a plug of silica with 10% MeOH/DCM to collect only the green bands. Concentrated and found 375 mg of green solid. Loaded in 20 mL DCM onto 300 mL of silica, which had been equilibrated with 100 % DCM. Eluted with the following: 100 mL (1% MeOH/DCM), 500 mL (2% MeOH/DCM), 500 mL (5% MeOH/DCM), and finally 500 mL (5% MeOH/DCM). Collected the third green band and concentrated to get the product. ^{1}H NMR (CD_3CN+CD_3OD): 8.54 (d, 2H), 8.34 (d, 2H), 8.13 (m, 8H), 7.80 (t, 2H), 7.77 (d, 2H), 7.35 (d, 2H), 6.68 (m, 8H), 5.32 (s, 2H), and 2.03 (s, 3H).

Synthesis of NMI-C2-Das (5)

$Co(NO_3)_2 \cdot 6H_2O$ (1.45 g, 5.00 mmol, 1 eq.), py (402 µL, 5.00 mmol, 1.00 eq.), NaOAc (7.5 mmol, 1.02 g, 1.5 eq.), N-(2-ethanoic acid)-1,8-naphthalenimide (673 mg, 2.5 mmol, 0.5 eq.), and NaOMe (2.5 mmol, 135 mg, 0.5 eq.) were added to a 50 mL round bottom flask in 15 mL of MeOH and refluxed at 90 °C until homogeneous. The flask was removed from the oil bath long enough that the solution stopped refluxing. Then, in very careful and control manner a solution of 30 % H_2O_2 (2.5 mL, 25 mmol, 5 eq.) was added to the mixture. Refluxed the dark green mixture for 4 h at 90 °C. At the end of this time, the mixture was concentrated to remove the MeOH, and the aqueous layer was extracted into DCM. The organic layer was dried with $MgSO_4$, and filtered. Concentrated the DCM extracted, and ran the residue material through a plug of silica with 10% MeOH/DCM to collect only the green

bands. Concentrated and found 835 mg of green solid. Loaded in 20 mL DCM onto 500 mL of silica, which had been equilibrated with 100 % THF. Eluted with the following: 1000 mL (100% THF), 1800 mL (1% H_2O/THF), 1000 mL (2% H_2O/THF), and finally 1000 mL (4% H_2O/THF). Collected the third green band. Concentrated then ran a quick silica column eluting with 10% MeOH/DCM to remove the BHT inhibitor that was present in the THF solvent used in the first column. Concentrated and found 35.1 mg (0.0331 mmol, 2.65 % yield) of green solid. ^{1}H NMR (CD_3CN): 8.50 (d, 2H), 8.40 (d, 8H), 8.32 (d, 2H), 7.79 (t, 2H), 7.58 (q, 4H), 7.10 (q, 8H) 4.23 (m, 2H), 2.65 (m, 2H), 2.01 (s, 6H), and 2.00 (s, 3H).

Synthesis of NMI-C5-Das (6)

2 (300 mg, 0.352 mmol, 1 eq.) and NMI$(CH_2)_5$COOH (73.0 mg, 0.246 mmol, 0.7 eq.) were added to a flask with 17 mL of CH_3CN. Sparged solution with N_2 then refluxed at 95 C for 6 h under an N_2 atmosphere. Concentrated mixture then loaded onto a silica column (300 mL of SiO_2, equilibrated with 2 % MeOH/DCM) in 6 mL of 2 % MeOH/DCM. Eluted with the following: 600 mL (2 % MeOH/DCM) and then 2000 (4 % MeOH/DCM). There were two major green bands and the first of the two of these was collected. Concentrated and found 71.4 mg (0.0647 mmol, 26.3 % yield).

Synthesis of NMI-C2-Christou (7)

1 (75 mg, 0.06 mm, 1 eq.) and NMI$(CH_2)_2$COOH (130 mg, 0.5 mmol, 8 eq.) were added to a flask with 4 mL H2O and 4 mL CH_3CN. The mixture was brought to reflux for 2.5 hours. The reaction was cooled and most of the solvent was extracted by rotovap to yield a brown suspension. The particulates were collected on a filter made from a pipette packed with paper. Removed brown residue from filter with CH_3CN and filtered again to remove a white precipitate. The filtrate was dry loaded onto a silica gel column (~3 inch height) and eluted

with 300 mL (10% MeOH/2%HOAc/DCM). A single band was collected and concentrated. ^{1}H NMR (CD_3CN): 8.54 (d, 4H), 8.47 (d, 2H), 8.43 (d, 4H), 8.21 (d, 2H), 8.17 (t, 4H), 7.90 (t, 2H), 7.00 (t, 4H), 3.42 (t, 2H), and 1.86 (t, 2H).

Synthesis of NMI-C5-Christou (8)

1 (75 mg, 0.06 mm, 1 eq.) and NMI$(CH_2)_5$COOH (150 mg, 0.5 mmol, 8 eq.) were added to a flask with 4 mL H_2O and 4 mL CH_3CN. The mixture was brought to reflux for 2.5 hours. The reaction was cooled and most of the solvent was extracted by rotovap to yield a brown suspension. The particulates were collected on a filter made from a pipette packed with paper. Removed brown residue from filter with CH_3CN and filtered again to remove a white precipitate. The filtrate was dry loaded onto a silica gel column (~3 inch height) and eluted with 300 mL (10% MeOH/2%HOAc/DCM). A single band was collected and concentrated. ^{1}H NMR (DMSO): 8.87 (d, 4H), 8.51 (d, 2H), 8.48 (d, 2H), 8.44 (d, 4H), 8.27 (t, 4H), 7.93 (t, 2H), 7.14 (t, 4H), 3.56 (t, 2H), 1.13 (t, 2H), 0.96 (m, 2H), 0.53 (m, 2H), and 0.47 (m, 2H).

Electrochemical Methods

All electrochemical experiments were recorded at ambient temperature with a CH Instrument 760D or 730C potentiostat. CVs were performed in a N_2-atmosphere glovebox or N_2-perged cell, using Ag wire pseudo reference in conjunction with a Fc external reference. In the cyclic voltammogram (CV) experiments the counter electrode was a Pt wire. In the CV experiments, 3 mm diameter glassy carbon working electrodes were used. These were cleaned by polishing on felt with 1 μm alumina followed by 0.3 μm alumina, and then sonication in 18 MΩ cm distilled water, rinsing with acetone and drying with compressed air. Thin-layer UV–vis spectroelectrochemistry experiments were performed using a 0.5 mm path length quartz cell with an Ocean Optics USB4000 spectrophotometer

and a DT-Mini-2GS UV–vis–NIR light source in conjunction with the CH electrochemical workstation.

Transient Absorption Measurements

Picosecond transient spectroscopy was performed on a home-built system constructed around a Coherent Libra HE Ti: Sapphire Amplifier System. The Libra HE incorporates a Coherent Vitesse oscillator that serves as the seed laser for the system. The Vitesse includes the mode-locked Ti:Sapphire oscillator cavity pumped by a Coherent Verdi, a continuous-wave diode-pumped green laser. The Libra system also includes a Coherent Evolution diode pump second harmonic Q-switched laser. The Evolution operates at a 1 kHz repetition rate and provides the pump power to the amplifier module. The Libra-HE has an average output power of 3.5 W and a pulse width of 50 fs. 99.5% of the 800 nm output wavelength is directed into a Coherent OPerA SOLO optical parametric amplifier with the remainder being focused into a calcium fluoride (CaF_2) substrate for continuum generation by. Time resolution was achieved by propagating the excitation beam along a computer-controlled 1.70 m optical delay line with 1 μm precision (Aerotech ATS 62150). The pump and probe beams were focused collinearly at the continuously stirred sample with beam diameters of ~500 μm and ~250 μm respectively. The power of λ_{ex} was kept between 1-2μJ/pulse at the sample. All samples were pumped at the 330 nm band of NMI. Laser power was measured using either a Coherent J-25MB-HE meter coupled to a Coherent Labmax Top or an Ophir Laser Measurement Group ORION/PD Power Meter (PD300-UV-SIR-ROITS) fitted with an ORION head (#572775). A 2 mm quartz cuvette was used for all samples.

TA spectra were recorded at discrete times after excitation with 325 nm pump pulses. The spectrum was then resolved in the monochromator (ISA Instruments, TRIAX 320). For both full spectrum and single wavelength kinetic measurements, signal light entering the spectrometer was dispersed by a 300 × 500 blazed grating onto a Princeton Instruments PIXIS 100B CCD camera calibrated using a mercury argon pen lamp. Resulting spectra were averages of three replicates of 2000 sequences consisting of the four combinations of pump and probe used to correct for ambient and emissive signals for each time point, averaged together. Single wavelength kinetics where obtained by averaging 20 nm spectral windows about the wavelength of interest for each time point. In house developed software written in Python was used for acquisition control.

Crystallographic Details.

Single crystals of **7** were obtained from a CH_2Cl_2 solution layered with toluene. Crystals of **7** were obtained from slow diffusion of Et_2O into a CH_3CN solution saturated with **7**. Diffraction data were collected on a vertically mounted Bruker D8 three-circle platform goniometer equipped with an Apex II CCD and an Oxford Diffraction Helijet cooling device (100 K) with synchrotron radiation (0.41328 Å) supplied to ChemMatCARS located at Advances Photon Source (APS), Argonne National Laboratory (ANL). Crystals were mounted on a glass fiber pin using Paratone N oil. Data was collected as a series of φ and/or ω scans. Data was integrated using SAINT and scaled with multi-scan absorption correction using SADABS.[56] The structures were solved by intrinsic phasing using SHELXT (Apex2 program suite v2014.1) and refined against F^2 on all data by full matrix least squares with SHELXL-97.[57] All non-H atoms were refined anisotropically. H atoms were placed at idealized positions and refined using a riding model. Crystal data and refinement

statistics are summarized in Table 6.3 and thermal ellipsoid plots are collected in Figure 6.4.

Table 6.3. Crystal data and structure refinement metrics.

	$[Co_4O_4(NMI(CH_2)_2OAc)_2(py)_4]$, (**7**)
formula	$C_{77}H_{63.5}Co_4F_{12}N_{13.3}O_{12.5}P_2$
CCDC #	-------
fw, g/mol	1900.82
temp, K	100
cryst system	monoclinic
space group	C2/c
color	yellow
a, Å	31.8444 (15)
b, Å	18.9837 (9)
c, Å	27.0590 (12)
α, deg	90
β, deg	109.108 (1)
γ, deg	90
V, Å^3	15456.6 (12)
Z	8
R1[a]	0.0559
wR2[b]	0.1730
GOF[c] (F^2)	1.08
R_{int}	0.069

[a] $R1 = \Sigma||F_o| - |F_c||/\Sigma|F_o|$. [b] $wR2 = (\Sigma(w(F_o^2 - F_c^2)^2)/\Sigma(w(F_o^2)^2))^{1/2}$. [c] $GOF = (\Sigma w(F_o^2 - F_c^2)^2/(n - p))^{1/2}$ where n is the number of data and p is the number of parameters refined.

Computational methods

Density functional theory (DFT) calculations were performed using Gaussian ® version 09, Revision D.01.[58] Structure optimizations were performed using the BP86 functional[59,60] and Pople basis sets: C H: 6-31G(d); Co O N: 6-311G(d).[61] Single point energies were computed using the B3LYP hybrid functional[62] and aforementioned basis sets as implemented in Gaussian 09. TD-DFT calculations were performed using the aforementioned functional and basis sets as single point energies and computed the first 100 excited states. Cartesian coordinates of the optimized structures are listed below.

Table 6.4. Cartesian coordinates of DFT optimized geometry for the S = 1 model of **1**.

Atom	x	y	z
Co	0.920592	-0.980761	-1.080952
Co	-0.934343	0.948912	-1.076710
Co	1.002393	0.953976	1.042211
Co	-0.922911	-0.908494	1.117544
O	0.930272	0.885704	-0.866741
O	-0.937492	-0.907450	-0.792810
O	-0.861005	0.953956	0.833411
O	0.937203	-0.907584	0.825538
O	-0.736049	-0.733589	3.061893
O	0.893794	0.834930	3.003537
O	0.770013	-0.838371	-3.034391
O	-0.799109	0.791767	-3.031248
C	-0.046946	-0.050613	-5.122771
H	0.919256	-0.366631	-5.521453
H	-0.323833	0.928317	-5.519458
H	-0.802562	-0.775606	-5.448752
C	0.078758	0.127493	5.121500
H	-0.642312	0.889982	5.440129
H	1.062491	0.412821	5.499873
H	-0.231945	-0.829978	5.544669
C	0.085879	0.065526	3.608023
C	-0.016599	-0.024199	-3.608533
C	2.171593	-3.472261	-1.609839
C	-0.148688	-3.699744	-1.571762

Table 6.4 (Continued)

C	2.329144	-4.827095	-1.912833
C	-0.065657	-5.051201	-1.902317
H	-1.090248	-3.180705	-1.433994
C	1.195418	-5.626218	-2.054126
H	3.315039	-5.249686	-2.068172
H	-0.970979	-5.632425	-2.040320
H	1.298793	-6.677779	-2.303638
C	3.719871	-0.190893	-1.620316
C	3.268182	-2.479015	-1.616969
C	5.057206	-0.409894	-1.946218
H	3.294633	0.799910	-1.505117
C	4.602560	-2.772205	-1.909884
C	5.507743	-1.723690	-2.069654
H	5.723354	0.432059	-2.100300
H	4.928869	-3.797243	-2.042262
H	6.545202	-1.933358	-2.311376
C	-2.317077	3.362654	-1.652123
C	-0.010284	3.702429	-1.643240
C	-2.541911	4.700234	-1.988032
C	-0.160514	5.039028	-2.008504
H	0.957536	3.232676	-1.508242
C	-1.449256	5.548926	-2.160537
H	-3.548213	5.070880	-2.144978
H	0.714568	5.658514	-2.172541
H	-1.605532	6.587513	-2.435549
C	-3.704465	0.011906	-1.551909
C	-3.363101	2.317016	-1.626350
C	-5.051987	0.156309	-1.876988
H	-3.230687	-0.952007	-1.405339
C	-4.710679	2.536851	-1.922959
C	-5.565425	1.442041	-2.042965
H	-5.677857	-0.721082	-1.999141
H	-5.085596	3.540270	-2.088217
H	-6.612425	1.593676	-2.286933
N	0.941333	-2.943003	-1.405738
N	2.862069	-1.199877	-1.435434
N	-1.061505	2.899869	-1.443619
N	-2.894166	1.065695	-1.405505
C	-3.404269	-2.136646	1.716856
C	-3.621049	0.184768	1.666013
C	-4.752812	-2.285486	2.050668
C	-4.965144	0.110489	2.027296
H	-3.099445	1.122056	1.510620
C	-5.542849	-1.146507	2.201353
H	-5.176941	-3.268108	2.221812

Table 6.4 (Continued)

H	-5.538622	1.019663	2.172228
H	-6.589130	-1.242557	2.474857
C	-0.132230	-3.707460	1.635934
C	-2.416777	-3.239038	1.705972
C	-0.348903	-5.039940	1.982043
H	0.856618	-3.290423	1.480719
C	-2.708114	-4.568182	2.023593
C	-1.660867	-5.479134	2.156406
H	0.493076	-5.710791	2.113901
H	-3.729958	-4.885812	2.195737
H	-1.869169	-6.512375	2.416648
C	2.469142	3.338445	1.539445
C	0.176447	3.759196	1.513404
C	2.741383	4.680036	1.819549
C	0.373703	5.103406	1.824018
H	-0.807513	3.319203	1.396696
C	1.679773	5.573329	1.956238
H	3.760543	5.021230	1.959329
H	-0.478866	5.759796	1.960765
H	1.873014	6.616387	2.187297
C	3.738852	-0.059131	1.554500
C	3.478311	2.257391	1.552606
C	5.087739	0.048512	1.888588
H	3.232740	-1.010548	1.436817
C	4.829859	2.439529	1.856653
C	5.644606	1.319960	2.019408
H	5.680944	-0.846033	2.044671
H	5.238006	3.433855	1.995981
H	6.693892	1.442631	2.269774
N	-1.141260	-2.844288	1.477484
N	-2.874270	-0.910418	1.491144
N	1.197974	2.911606	1.349106
N	2.967553	1.017154	1.366254

Table 6.5. Cartesian coordinates of DFT optimized geometry for the S = 2 model of **1**$^{+}$.

Atom	x	y	z
Co	-0.002671	-1.297810	-1.119673
Co	0.002687	1.295516	-1.121018
Co	1.362490	-0.002784	1.083281
Co	-1.360800	0.002975	1.084361
O	1.340282	-0.004004	-0.812904
O	-1.340131	0.002125	-0.812441
O	0.003491	1.266117	0.799125
O	-0.002139	-1.266249	0.799844
O	-1.137891	0.000027	3.009014
O	1.141584	-0.002666	3.008091
O	0.000259	-1.135179	-3.048161
O	0.002643	1.130462	-3.049287
C	-0.036074	-0.003456	-5.153489
H	0.451973	-0.906814	-5.548857
H	0.444758	0.903222	-5.549940
H	-1.089730	-0.008216	-5.486828
C	0.002649	0.038167	5.103301
H	-0.000758	1.092714	5.434101
H	0.909502	-0.442239	5.499782
H	-0.901035	-0.447777	5.500391
C	0.002103	0.001386	3.590008
C	-0.000933	-0.002672	-3.641933
C	-0.745189	-3.967134	-1.621675
C	-2.612763	-2.540530	-1.595617
C	-1.559167	-5.072026	-1.922750
C	-3.472816	-3.595536	-1.925387
H	-2.955616	-1.510174	-1.470352
C	-2.940289	-4.885618	-2.071073
H	-1.117684	-6.060730	-2.073292
H	-4.538832	-3.400428	-2.071390
H	-3.585585	-5.732988	-2.322914
C	2.601020	-2.552873	-1.597004
C	0.726740	-3.970688	-1.621904
C	3.455797	-3.611858	-1.927798
H	2.948735	-1.524096	-1.472487
C	1.535222	-5.079323	-1.923935
C	2.917112	-4.899398	-2.073227
H	4.522522	-3.421619	-2.075023
H	1.088916	-6.065827	-2.074677
H	3.558213	-5.749713	-2.325855
C	0.745984	3.963506	-1.629011
C	2.612469	2.535477	-1.603622
C	1.560112	5.067041	-1.934588

Table 6.5 (Continued)

C	3.472593	3.589004	-1.937992
H	2.954656	1.505038	-1.477345
C	2.940792	4.879173	-2.085445
H	1.119041	6.055653	-2.086949
H	4.538027	3.392557	-2.086408
H	3.586175	5.725393	-2.340908
C	-2.601187	2.551427	-1.596403
C	-0.725954	3.967854	-1.627047
C	-3.455831	3.610411	-1.927453
H	-2.949468	1.523166	-1.469032
C	-1.534245	5.076504	-1.929569
C	-2.916488	4.897303	-2.076237
H	-4.523017	3.420755	-2.072101
H	-1.087528	6.062471	-2.082591
H	-3.557437	5.747626	-2.329224
N	-1.288587	-2.728493	-1.419608
N	1.276210	-2.734807	-1.419466
N	1.288961	2.725101	-1.424577
N	-1.275833	2.732556	-1.421889
C	-4.012832	0.745678	1.654691
C	-2.585351	2.611791	1.588193
C	-5.108516	1.561106	1.984919
C	-3.629360	3.473836	1.945802
H	-1.556905	2.952089	1.437952
C	-4.915955	2.942117	2.126506
H	-6.093600	1.121536	2.162769
H	-3.430150	4.539640	2.087797
H	-5.755285	3.588695	2.400996
C	-2.597079	-2.599601	1.590386
C	-4.016234	-0.727096	1.655127
C	-3.644863	-3.456561	1.949236
H	-1.570096	-2.944541	1.440969
C	-5.115477	-1.537214	1.986519
C	-4.929062	-2.918943	2.129480
H	-3.450238	-4.522997	2.092819
H	-6.098475	-1.093012	2.164391
H	-5.771188	-3.561476	2.404904
C	4.019127	0.727089	1.648664
C	2.601256	2.600500	1.582328
C	5.119685	1.537259	1.975552
C	3.650478	3.457609	1.936516
H	1.574362	2.946015	1.433531
C	4.934638	2.919452	2.115484
H	6.102829	1.092800	2.151961
H	3.457130	4.524660	2.077251

Table 6.5 (Continued)

H	5.777883	3.562065	2.387264
C	2.586269	-2.611012	1.589930
C	4.015064	-0.745673	1.650816
C	3.630230	-3.472976	1.947942
H	1.557312	-2.950821	1.442270
C	5.110694	-1.561089	1.981225
C	4.917421	-2.941724	2.125707
H	3.430434	-4.538289	2.092738
H	6.096245	-1.121782	2.157126
H	5.756701	-3.588289	2.400386
N	-2.785303	-1.275243	1.418107
N	-2.779256	1.287987	1.417836
N	2.787884	1.275444	1.413557
N	2.781015	-1.287790	1.416300

Table 6.6. Cartesian coordinates of DFT optimized geometry for the S = 1 model of **2**.

Atom	**x**	**y**	**z**
Co	-0.896494	1.105057	-0.907398
Co	-0.903356	-1.096476	0.909369
O	-0.945715	0.770930	0.927447
O	-0.959936	-0.761703	-0.925160
O	-0.727144	1.167791	-2.842508
O	-0.714715	-1.169698	2.842752
O	0.730906	2.840301	1.166942
O	-0.699525	3.014895	-0.620909
N	-2.824477	1.350112	-1.055140
N	-2.832802	-1.323088	1.072931
C	0.010310	-0.335936	3.492295
C	0.046384	-0.511951	5.000224
C	-0.008535	0.330695	-3.494008
C	-0.018097	0.457097	-5.007438
C	-3.471569	2.109376	-0.139296
H	-2.859789	2.475625	0.687532
C	-4.835798	2.398633	-0.245128
H	-5.313754	3.025240	0.513725
C	-5.560564	1.882646	-1.329659
H	-6.627099	2.101962	-1.444828
C	-4.889745	1.079018	-2.263392
H	-5.410692	0.648395	-3.123599
C	-3.523514	0.832548	-2.092232
H	-2.949642	0.224563	-2.793614
C	-3.515343	-0.808674	2.122422

Table 6.6 (Continued)

H	-2.928699	-0.208891	2.820472
C	-4.881268	-1.046286	2.308509
H	-5.388491	-0.618086	3.178081
C	-5.569403	-1.837360	1.376807
H	-6.636030	-2.049859	1.503283
C	-4.861893	-2.349625	0.279159
H	-5.353925	-2.966473	-0.478657
C	-3.497044	-2.069635	0.158738
H	-2.898335	-2.432707	-0.678874
C	0.025603	3.494838	0.320949
C	0.064371	5.008687	0.430062
H	0.651460	5.415352	-0.412940
H	0.527967	5.317164	1.378222
H	-0.954731	5.419716	0.346644
O	0.715840	-0.610559	-3.012054
O	0.723884	0.612822	3.009623
Co	0.892020	-0.914967	-1.100176
Co	0.904799	0.906663	1.097110
O	0.947516	-0.930310	0.766226
O	0.955428	0.920932	-0.769082
O	-0.731454	-3.009076	0.613178
O	0.695862	-2.844670	-1.178042
N	2.818898	-1.123346	-1.298246
N	2.834896	1.101107	1.295092
C	3.472142	-2.042425	-0.548354
H	2.863427	-2.565579	0.191867
C	4.837417	-2.298877	-0.711015
H	5.320244	-3.058290	-0.088864
C	5.557001	-1.578378	-1.676023
H	6.624351	-1.765294	-1.832985
C	4.879373	-0.613453	-2.435633
H	5.395475	-0.021766	-3.197453
C	3.512516	-0.412069	-2.217606
H	2.934257	0.317242	-2.787513
C	3.521840	0.400467	2.227441
H	2.938847	-0.319047	2.804911
C	4.888075	0.600874	2.450686
H	5.397961	0.017719	3.223190
C	5.572514	1.553959	1.682451
H	6.639285	1.740691	1.843463
C	4.860298	2.263043	0.703608
H	5.348664	3.012989	0.074374
C	3.495478	2.007884	0.536219
H	2.893161	2.521428	-0.215757
C	-0.028704	-3.493013	-0.342515

Table 6.6 (Continued)

C	-0.070667	-5.000014	-0.522721
H	-0.660772	-5.238017	-1.425975
H	-0.532529	-5.482556	0.350728
H	0.947277	-5.389468	-0.685821
H	1.014520	0.565920	-5.379415
H	-0.425657	-0.469008	-5.448364
H	-0.622024	1.320058	-5.321863
H	0.469315	0.380108	5.484360
H	-0.965586	-0.717223	5.384038
H	0.673113	-1.388532	5.244149

Table 6.7. Cartesian coordinates of DFT optimized geometry for the S = 2 model of **2**$^{+}$.

Atom	**x**	**y**	**z**
Co	-0.896494	1.105057	-0.907398
Co	-0.903356	-1.096476	0.909369
O	-0.945715	0.770930	0.927447
O	-0.959936	-0.761703	-0.925160
O	-0.727144	1.167791	-2.842508
O	-0.714715	-1.169698	2.842752
O	0.730906	2.840301	1.166942
O	-0.699525	3.014895	-0.620909
N	-2.824477	1.350112	-1.055140
N	-2.832802	-1.323088	1.072931
C	0.010310	-0.335936	3.492295
C	0.046384	-0.511951	5.000224
C	-0.008535	0.330695	-3.494008
C	-0.018097	0.457097	-5.007438
C	-3.471569	2.109376	-0.139296
H	-2.859789	2.475625	0.687532
C	-4.835798	2.398633	-0.245128
H	-5.313754	3.025240	0.513725
C	-5.560564	1.882646	-1.329659
H	-6.627099	2.101962	-1.444828
C	-4.889745	1.079018	-2.263392
H	-5.410692	0.648395	-3.123599
C	-3.523514	0.832548	-2.092232
H	-2.949642	0.224563	-2.793614
C	-3.515343	-0.808674	2.122422
H	-2.928699	-0.208891	2.820472
C	-4.881268	-1.046286	2.308509
H	-5.388491	-0.618086	3.178081
C	-5.569403	-1.837360	1.376807

Table 6.7 (Continued)

H	-6.636030	-2.049859	1.503283
C	-4.861893	-2.349625	0.279159
H	-5.353925	-2.966473	-0.478657
C	-3.497044	-2.069635	0.158738
H	-2.898335	-2.432707	-0.678874
C	0.025603	3.494838	0.320949
C	0.064371	5.008687	0.430062
H	0.651460	5.415352	-0.412940
H	0.527967	5.317164	1.378222
H	-0.954731	5.419716	0.346644
O	0.715840	-0.610559	-3.012054
O	0.723884	0.612822	3.009623
Co	0.892020	-0.914967	-1.100176
Co	0.904799	0.906663	1.097110
O	0.947516	-0.930310	0.766226
O	0.955428	0.920932	-0.769082
O	-0.731454	-3.009076	0.613178
O	0.695862	-2.844670	-1.178042
N	2.818898	-1.123346	-1.298246
N	2.834896	1.101107	1.295092
C	3.472142	-2.042425	-0.548354
H	2.863427	-2.565579	0.191867
C	4.837417	-2.298877	-0.711015
H	5.320244	-3.058290	-0.088864
C	5.557001	-1.578378	-1.676023
H	6.624351	-1.765294	-1.832985
C	4.879373	-0.613453	-2.435633
H	5.395475	-0.021766	-3.197453
C	3.512516	-0.412069	-2.217606
H	2.934257	0.317242	-2.787513
C	3.521840	0.400467	2.227441
H	2.938847	-0.319047	2.804911
C	4.888075	0.600874	2.450686
H	5.397961	0.017719	3.223190
C	5.572514	1.553959	1.682451
H	6.639285	1.740691	1.843463
C	4.860298	2.263043	0.703608
H	5.348664	3.012989	0.074374
C	3.495478	2.007884	0.536219
H	2.893161	2.521428	-0.215757
C	-0.028704	-3.493013	-0.342515
C	-0.070667	-5.000014	-0.522721
H	-0.660772	-5.238017	-1.425975
H	-0.532529	-5.482556	0.350728
H	0.947277	-5.389468	-0.685821

Table 6.7 (Continued)

H	1.014520	0.565920	-5.379415
H	-0.425657	-0.469008	-5.448364
H	-0.622024	1.320058	-5.321863
H	0.469315	0.380108	5.484360
H	-0.965586	-0.717223	5.384038
H	0.673113	-1.388532	5.244149

6.6 References

1. Cukier, R. I.; Nocera, D. G. Proton-Coupled Electron Transfer. Annual Review of Physical Chemistry 1998, 49 (1), 337–369.
2. Meyer, T. J.; Huynh, M. H. V.; Thorp, H. H. The Possible Role of Proton-Coupled Electron Transfer (PCET) in Water Oxidation by Photosystem II. *Angewandte Chemie International Edition* **2007**, *46* (28), 5284–5304.
3. Hammes-Schiffer, S. Theory of Proton-Coupled Electron Transfer in Energy Conversion Processes. *Acc. Chem. Res*. **2009**, *42* (12), 1881–1889.
4. Lutterman, D. A.; Surendranath, Y.; Nocera, D. G. A Self-Healing Oxygen-Evolving Catalyst. *J. Am. Chem. Soc*. **2009**, *131* (11), 3838–3839.
5. Yano, J.; Kern, J.; Yachandra, V. K.; Nilsson, H.; Koroidov, S.; Messinger, J. Light-Dependent Production of Dioxygen in Photosynthesis. In Sustaining Life on Planet Earth: Metalloenzymes Mastering Dioxygen and Other Chewy Gases; Kroneck, P. M. H., Torres, M. E. S., Eds.; Metal Ions in Life Sciences; Springer International Publishing, 2015; pp 13–43.
6. Dau, H.; Limberg, C.; Reier, T.; Risch, M.; Roggan, S.; Strasser, P. The Mechanism of Water Oxidation: From Electrolysis via Homogeneous to Biological Catalysis. *ChemCatChem* **2010**, *2* (7), 724–761.
7. Du, P.; Eisenberg, R. Catalysts Made of Earth-Abundant Elements (Co, Ni, Fe) for Water Splitting: Recent Progress and Future Challenges. *Energy Environ. Sci.* **2012**, *5* (3), 6012–6021.
8. Kanan, M. W.; Nocera, D. G. In Situ Formation of an Oxygen-Evolving Catalyst in Neutral Water Containing Phosphate and Co^{2+}. *Science* **2008**, *321* (5892), 1072–1075.
9. Torella, J. P.; Gagliardi, C. J.; Chen, J. S.; Bediako, D. K.; Colón, B.; Way, J. C.; Silver, P. A.; Nocera, D. G. Efficient Solar-to-Fuels Production from a Hybrid Microbial–water-Splitting Catalyst System. *PNAS* **2015**, *112* (8), 2337–2342.
10. Copéret, C.; Chabanas, M.; Petroff Saint-Arroman, R.; Basset, J.-M. Homogeneous and Heterogeneous Catalysis: Bridging the Gap through Surface Organometallic Chemistry. *Angewandte Chemie International Edition* **2003**, *42* (2), 156–181.
11. Symes, M. D.; Surendranath, Y.; Lutterman, D. A.; Nocera, D. G. Bidirectional and Unidirectional PCET in a Molecular Model of a Cobalt-Based Oxygen-Evolving Catalyst. *J. Am. Chem. Soc.* **2011**, *133* (14), 5174–5177.
12. Dimitrou, K.; Folting, K.; Streib, W. E.; Christou, G. Dimerization of the $[Co_2III(OH)_2]$ Core to the First Example of a [Co4IIIO4] Cubane: Potential Insights into Photosynthetic Water Oxidation. *J. Am. Chem. Soc*. **1993**, *115* (14), 6432–6433.

13. Dimitrou, K.; Brown, A. D.; Concolino, T. E.; Rheingold, A. L.; Christou, G. Mixed-Valence, tetranuclearcobalt(III,IV) Complexes: Preparation and properties of $[Co_4O_4(O_2CR)_2(bpy)_4]^{3+}$ Salts. *Chem. Commun*. **2001**, *14*, 1284–1285.

14. Chakrabarty, R.; Bora, S. J.; Das, B. K. Synthesis, Structure, Spectral and Electrochemical Properties, and Catalytic Use of Cobalt(III)−Oxo Cubane Clusters. *Inorg. Chem*. **2007**, *46* (22), 9450–9462.

15. Chakrabarty, R.; Sarmah, P.; Saha, B.; Chakravorty, S.; Das, B. K. Catalytic Properties of Cobalt(III)−Oxo Cubanes in the TBHP Oxidation of Benzylic Alcohols. *Inorg. Chem.* **2009**, *48* (14), 6371–6379.

16. Berardi, S.; La Ganga, G.; Natali, M.; Bazzan, I.; Puntoriero, F.; Sartorel, A.; Scandola, F.; Campagna, S.; Bonchio, M. Photocatalytic Water Oxidation: Tuning Light-Induced Electron Transfer by Molecular Co4O4 Cores. *J. Am. Chem. Soc*. **2012**, *134* (27), 11104–11107.

17. McCool, N. S.; Robinson, D. M.; Sheats, J. E.; Dismukes, G. C. A Co4O4 "Cubane" Water Oxidation Catalyst Inspired by Photosynthesis. *J. Am. Chem. Soc*. **2011**, *133* (30), 11446–11449.

18. Ganga, G. L.; Puntoriero, F.; Campagna, S.; Bazzan, I.; Berardi, S.; Bonchio, M.; Sartorel, A.; Natali, M.; Scandola, F. Light-Driven Water Oxidation with a Molecular Tetra-cobalt(III) Cubane Cluster. *Faraday Discuss*. **2012**, *155* (0), 177–190.

19. Ullman, A. M.; Liu, Y.; Huynh, M.; Bediako, D. K.; Wang, H.; Anderson, B. L.; Powers, D. C.; Breen, J. J.; Abruña, H. D.; Nocera, D. G. Water Oxidation Catalysis by Co(II) Impurities in Co(III)4O4 Cubanes. *J. Am. Chem. Soc*. **2014**, *136* (50), 17681–17688.

20. Nguyen, A. I.; Ziegler, M. S.; Oña-Burgos, P.; Sturzbecher-Hohne, M.; Kim, W.; Bellone, D. E.; Tilley, T. D. Mechanistic Investigations of Water Oxidation by a Molecular Cobalt Oxide Analogue: Evidence for a Highly Oxidized Intermediate and Exclusive Terminal Oxo Participation. *J. Am. Chem. Soc*. **2015**, *137* (40), 12865–12872.

21. Smith, P. F.; Hunt, L.; Laursen, A. B.; Sagar, V.; Kaushik, S.; Calvinho, K. U. D.; Marotta, G.; Mosconi, E.; De Angelis, F.; Dismukes, G. C. Water Oxidation by the $[Co_4O_4(OAc)_4(py)_4]^+$ Cubium Is Initiated by OH^- Addition. *J. Am. Chem. Soc*. **2015**, *137* (49), 15460–15468.

22. Wang, L.-P.; Van Voorhis, T. Direct-Coupling O_2 Bond Forming a Pathway in Cobalt Oxide Water Oxidation Catalysts. *J. Phys. Chem. Lett*. **2011**, *2* (17), 2200–2204.

23. Smith, P. F.; Kaplan, C.; Sheats, J. E.; Robinson, D. M.; McCool, N. S.; Mezle, N.; Dismukes, G. C. What Determines Catalyst Functionality in Molecular Water Oxidation? Dependence on Ligands and Metal Nuclearity in Cobalt Clusters. *Inorg. Chem*. **2014**, *53* (4), 2113–2121.

24. Dattelbaum, D. M.; Omberg, K. M.; Schoonover, J. R.; Martin, R. L.; Meyer, T. J. Application of Time-Resolved Infrared Spectroscopy to Electronic Structure in Metal-to-Ligand Charge-Transfer Excited States. *Inorg. Chem*. **2002**, *41* (23), 6071–6079.

25. Reece, S. Y.; Nocera, D. G. Direct Tyrosine Oxidation Using the MLCT Excited States of Rhenium Polypyridyl Complexes. *J. Am. Chem. Soc*. **2005**, *127* (26), 9448–9458.

26. Symes, M. D.; Lutterman, D. A.; Teets, T. S.; Anderson, B. L.; Breen, J. J.; Nocera, D. G. Photo-Active Cobalt Cubane Model of an Oxygen-Evolving Catalyst. *ChemSusChem* **2013**, *6* (1), 65–69.

27. Wintgens, V.; Valat, P.; Kossanyi, J.; Biczok, L.; Demeter, A.; Bérces, T. Spectroscopic Properties of Aromatic Dicarboximides. Part1.—N—H and N-Methyl-Substituted Naphthalimides. *J. Chem. Soc., Faraday Trans*. **1994**, *90* (3), 411–421.

28. Samanta, A.; Ramachandram, B.; Saroja, G. An Investigation of the Triplet State Properties of 1,8-Naphthalimide: A Laser Flash Photolysis Study. *Journal of Photochemistry and Photobiology A: Chemistry* **1996**, *101* (1), 29–32.

29. Aveline, B. M.; Matsugo, S.; Redmond, R. W. Photochemical Mechanisms Responsible for the Versatile Application of Naphthalimides and Naphthaldiimides in Biological Systems. *J. Am. Chem. Soc.* **1997**, *119* (49), 11785–11795.

30. Rogers, J. E.; Weiss, S. J.; Kelly, L. A. Photoprocesses of Naphthalene Imide and Diimide Derivatives in Aqueous Solutions of DNA. *J. Am. Chem. Soc*. **2000**, *122* (3), 427–436.

31. Rogers, J. E.; Kelly, L. A. Nucleic Acid Oxidation Mediated by Naphthalene and Benzophenone Imide and Diimide Derivatives: Consequences for DNA Redox Chemistry. *J. Am. Chem. Soc*. **1999**, *121* (16), 3854–3861.

32. Abraham, B.; Kelly, L. A. Photooxidation of Amino Acids and Proteins Mediated by Novel 1,8-Naphthalimide Derivatives. *J. Phys. Chem. B* **2003**, *107* (45), 12534–12541.

33. Pengo, P.; Pantoş, G. D.; Otto, S.; Sanders, J. K. M. Efficient and Mild Microwave-Assisted Stepwise Functionalization of Naphthalenediimide with α-Amino Acids. *J. Org. Chem*. **2006**, *71* (18), 7063–7066.

34. Tambara, K.; Ponnuswamy, N.; Hennrich, G.; Pantoş, G. D. Microwave-Assisted Synthesis of Naphthalenemonoimides and N-Desymmetrized Naphthalenediimides. *J. Org. Chem*. **2011**, *76* (9), 3338–3347.

35. Rehm, D.; Weller, A. Kinetics of Fluorescence Quenching by Electron and H-Atom Transfer. *Isr. J. Chem.* **1970**, *8* (2), 259–271.

36. Kavarnos, G. J.; Turro, N. J. Photosensitization by Reversible Electron Transfer: Theories, Experimental Evidence, and Examples. *Chem. Rev.* **1986**, *86* (2), 401–449.

37. Lakowicz, J. R. *Principles of Fluorescence Spectroscopy*; Springer Science & Business Media, 2007.

38. Bullock, J. E.; Vagnini, M. T.; Ramanan, C.; Co, D. T.; Wilson, T. M.; Dicke, J. W.; Marks, T. J.; Wasielewski, M. R. Photophysics and Redox Properties of Rylene Imide and Diimide Dyes Alkylated Ortho to the Imide Groups. *J. Phys. Chem. B* **2010**, *114* (5), 1794–1802.

39. Kalyanasundaram, K. Photophysics, Photochemistry and Solar Energy Conversion with tris(bipyridyl)ruthenium(II) and Its Analogues. *Coordination Chemistry Reviews* **1982**, *46*, 159–244.

40. McAlpin, J. G.; Stich, T. A.; Ohlin, C. A.; Surendranath, Y.; Nocera, D. G.; Casey, W. H.; Britt, R. D. Electronic Structure Description of a [Co(III)3Co(IV)O4] Cluster: A Model for the Paramagnetic Intermediate in Cobalt-Catalyzed Water Oxidation. *J. Am. Chem. Soc.* **2011**, *133* (39), 15444–15452.

41. Li, X.; Siegbahn, P. E. M. Water Oxidation Mechanism for Synthetic Co–Oxides with Small Nuclearity. *J. Am. Chem. Soc.* **2013**, *135* (37), 13804–13813.

42. Cady, C. W.; Crabtree, R. H.; Brudvig, G. W. Functional Manganese Model Chemistry Relevant to the Oxygen-Evolving Complex of Photosystem II: Oxidation of a Mn(III,IV) Complex Coupled to Deprotonation of a Terminal Water Ligand. In *Photosynthesis. Energy from the Sun*; Allen, J. F., Gantt, E., Golbeck, J. H., Osmond, B., Eds.; Springer Netherlands, 2008; pp 377–381.

43. Graham, D. J.; Dogutan, D. K.; Schwalbe, M.; Nocera, D. G. Hangman Effect on Hydrogen Peroxide Dismutation by Fe(III) Corroles. *Chem. Commun.* **2012**, *48* (35), 4175–4177.

44. Isobe, H.; Tanaka, K.; Shen, J.-R.; Yamaguchi, K. Water Oxidation Chemistry of a Synthetic Dinuclear Ruthenium Complex Containing Redox-Active Quinone Ligands. *Inorg. Chem.* **2014**, *53* (8), 3973–3984.

45. Bediako, D. K.; Costentin, C.; Jones, E. C.; Nocera, D. G.; Savéant, J.-M. Proton–Electron Transport and Transfer in Electrocatalytic Films. Application to a Cobalt-Based O2-Evolution Catalyst. *J. Am. Chem. Soc.* **2013**, *135* (28), 10492–10502.

46. Habib, H. S.; Hunt, J. P. Electron-Transfer Reactions between Aqueous Cobaltous and Cobaltic Ions1,2. *J. Am. Chem. Soc.* **1966**, *88* (8), 1668–1671.

47. Ullman, A. M.; Nocera, D. G. Mechanism of Cobalt Self-Exchange Electron Transfer. *J. Am. Chem. Soc.* **2013**, *135* (40), 15053–15061.

48. Rehm, J. M.; McLendon, G. L.; Nagasawa, Y.; Yoshihara, K.; Moser, J.; Grätzel, M. Femtosecond Electron-Transfer Dynamics at a Sensitizing Dye–Semiconductor (TiO2) Interface. *J. Phys. Chem.* **1996**, *100* (23), 9577–9578.

49. Wang, D.; Xiang, J.; Jiang, H.; Xu, G.; Gong, Q. Photoinduced Electron Transfer between Dye IR-140 and TiO 2 Colloids by Femtosecond Pump Supercontinuum Probing. *J. Opt. A: Pure Appl. Opt.* **2003**, *5* (2), 123.

50. He, T.-F.; Guo, L.; Guo, X.; Chang, C.-W.; Wang, L.; Zhong, D. Femtosecond Dynamics of Short-Range Protein Electron Transfer in Flavodoxin. *Biochemistry* **2013**, *52* (51), 9120–9128.

51. Natali, M.; Orlandi, M.; Berardi, S.; Campagna, S.; Bonchio, M.; Sartorel, A.; Scandola, F. Photoinduced Water Oxidation by a Tetraruthenium Polyoxometalate Catalyst: Ion-Pairing and Primary Processes with $Ru(bpy)_3^{2+}$ Photosensitizer. *Inorg. Chem.* **2012**, *51* (13), 7324–7331.

52. Byrne, E. K.; Theopold, K. H. Redox Chemistry of tetrakis(1-Norbornyl)cobalt. Synthesis and Characterization of a cobalt(V) Alkyl and Self-Exchange Rate of a Co(III)/Co(IV) Couple. *J. Am. Chem. Soc.* **1987**, *109* (4), 1282–1283.

53. Marcus, R. A.; Sutin, N. Electron Transfers in Chemistry and Biology. *Biochimica et Biophysica Acta (BBA) - Reviews on Bioenergetics* **1985**, *811* (3), 265–322.

54. Wallace, W. L.; Bard, A. J. Electrogenerated Chemiluminescence. 35. Temperature Dependence of the ECL Efficiency of tris(2,2'-bipyridine)rubidium^{2+} in Acetonitrile and Evidence for Very High Excited State Yields from Electron Transfer Reactions. *J. Phys. Chem.* **1979**, *83* (10), 1350–1357.

55. Rogers, J. E.; Abraham, B.; Rostkowski, A.; Kelly, L. A. Mechanisms of Photoinitiated Cleavage of DNA by 1,8-Naphthalimide Derivatives. *Photochemistry and Photobiology* **2001**, *74* (4), 521–531.

56. Bruker AXS (2009). Apex II. Bruker AXS, Madison, Wisconsin.

57. Sheldrick, G. M. Experimental phasing with *SHELXC*/*D*/*E*: combining chain tracing with density modification. *Acta Cryst.* **2010**, *D66*, 479.

58. Gaussian 09, Revision D.01, M. J. Frisch, G. W. Trucks, H. B. Schlegel, G. E. Scuseria, M. A. Robb, J. R. Cheeseman, G. Scalmani, V. Barone, B. Mennucci, G. A. Petersson, H. Nakatsuji, M. Caricato, X. Li, H. P. Hratchian, A. F. Izmaylov, J. Bloino, G. Zheng, J. L. Sonnenberg, M. Hada, M. Ehara, K. Toyota, R. Fukuda, J. Hasegawa, M. Ishida, T. Nakajima, Y. Honda, O. Kitao, H. Nakai, T. Vreven, J. A. Montgomery, Jr., J. E. Peralta, F. Ogliaro, M. Bearpark, J. J. Heyd, E. Brothers, K. N. Kudin, V. N. Staroverov, T. Keith, R. Kobayashi, J. Normand, K. Raghavachari, A. Rendell, J. C. Burant, S. S. Iyengar, J. Tomasi, M. Cossi, N. Rega, J. M. Millam, M. Klene, J. E. Knox, J. B. Cross, V. Bakken, C. Adamo, J. Jaramillo, R. Gomperts, R. E. Stratmann, O. Yazyev, A. J. Austin, R. Cammi, C. Pomelli, J. W. Ochterski, R. L. Martin, K. Morokuma, V. G. Zakrzewski, G. A. Voth, P. Salvador, J. J. Dannenberg, S. Dapprich, A. D. Daniels, O. Farkas, J. B. Foresman, J. V. Ortiz, J. Cioslowski, and D. J. Fox, Gaussian, Inc., Wallingford CT, 2013.

59. Perdew, J. P. Density-functional approximation for the correlation energy of the inhomogeneous electron gas. *Phys. Rev. B*. **1986**, *33*, 8822-8824.

60. Becke, A. D. Density-functional exchange-energy approximation with correct asymptotic behavior. *Phys. Rev. A.* **1988**, *38*, 3098-3100.

61. Hehre, W. J.; Random, L.; Schleyer, P. v. R.; Pople, J. A. Ab Initio Molecular Orbital Theory; John Wiley: New York, 1986.

62. Lee, C.; Yang, W.; Parr, R. G. Development of the Colle-Salvetti correlation-energy formula into a functional of the electron density. *Phys Rev. B* **1988**, *37*, 785.